Spin Valve Systems for Angle Sensor Applications

vom
Fachbereich Material- und Geowissenschaften
der Technischen Universität Darmstadt
genehmigte

Dissertation

zur Erlangung des akademischen Grades eines
Doktors der Ingenieurswissenschaften
(Dr.-Ing.)

eingereicht von
M. Sc. Andrew Johnson
aus Cincinnati, Ohio
USA

Referent:	Prof. Dr.-Ing. Horst Hahn
Korreferent:	Prof. Dr.-Ing. Hartmut Fuess
Tag der Einreichung:	25. Juli 2003
Tag der mündlichen Prüfung:	20. Januar 2004

Darmstadt 2004

D17

Table of Contents

Introduction

Research on the Giant Magneto-Resistance (GMR) effect, large resistance changes due to an applied magnetic field, began with the experimental observation of antiferromagnetic coupling in Fe/Cr magnetic multilayers by Grünberg, et al. [Grü86], in 1986. Magnetic multilayers consist of the multiple repetition of a FerroMagnetic (FM) layer separated by a Non-Magnetic (NM) spacer layer. The simultaneous discovery of the GMR effect by Baibich, et al. [Bai88], and Binasch, et al. [Bin89], followed in the late 1980's. The description "giant" was coined by Binasch, et al. [Bin89], to describe the difference in the resistance change caused by the GMR effect when comparing the effect size to that of the well-known Anisotropic Magneto-Resistance (AMR). These discoveries unleashed a wave of new research in the area of magneto-resistance effects such as GMR, Colossal Magneto-Resistance (CMR) [Sun98] and Tunnel Magneto-Resistance (TMR) [Moo96], and lead to the birth of a new research field: magneto-electronics. The field of magneto-electronics encompasses any application that utilizes the spin-dependent nature of electrons to induce a variation in the electrical resistance due to a change of the applied magnetic field. Many new possible applications were seen in the area of magnetic sensors and for a new type of non-volatile memory: Magnetic Random Access Memory (MRAM).

The first technological application of the GMR effect was the use of spin valves, a special type of magnetic multilayers, in the read heads of Hard-Disk Drives (HDD). Dieny, et al. [Die91], were the first to propose the spin valve system in 1991. A spin valve consists of a FM/NM/FM trilayer where the magnetization of one of the FM layers is pinned in one direction. The most common method for irreversibly pinning the magnetization in one direction is through the exchange coupling of an AntiFerroMagnetic (AFM) layer with a neighboring FM layer in the spin valve stack. The exchange coupling of the antiferromagnet with a ferromagnet is referred to as the "exchange bias" effect, which was first observed by Meikljohn and Bean in 1956 [Mei56]. The inherently higher effect size and sensitivity at the zero field of a spin valve read head, compared to AMR read heads, allowed for a dramatic increase in the storage density from 1 Gbit/in^2 in 1995 to 100 Gbit/in^2 (present) [Kan01]. There was an intensive race between the data storage companies, e.g. IBM, Seagate, Toshiba, etc., to be the first to master this new technology and bring it to market. High volume production of spin valve read heads first began in 1998, and is now the standard read head in every HDD used today.

GMR-technology will also be widely used in the near future for sensor applications in the automotive industry. Typical applications are wheel speed sensors for the Anti-locking Brake System (ABS), Vehicle Dynamics Controls (VDC), speed and position sensors for engine control, as well as incremental angular encoders for various other applications. Sensors based on the Hall or AMR effect allow close-to-zero speed measurement, and deliver additional information such as standstill detection and the direction of rotation. GMR sensors currently under development offer higher signal amplitudes, better sensitivity and improved resolution than the existing Hall and AMR sensors. This allows for new cost saving concepts in devices with larger fitting tolerances.

One specific type of GMR sensor of particular interest to the automotive industry is a GMR 360° angle sensor based on the spin valve system. A GMR angle sensor has many inherent advantages over the existing AMR angle sensors. This includes the ability for absolute angle detection over a 360° range, due to the cosine dependence of the GMR effect, rather than only over a 180° range. Another advantage is the larger size of the GMR effect in a spin valve (8-10% vs. 3%) which allows for a higher signal to noise ratio and therefore larger airgap tolerances. Spong, et al. [Spo96], of IBM were the first to present results of a GMR sensor in a Wheatstone bridge configuration based on a spin valve system in 1996. Clemens, et al. [Cle97], were the first to develop a functioning GMR 360° angle sensor in 1997. This angle sensor has been available commercially from Infineon since 1998 as the GMR C6 angle sensor [Inf02]. The GMR C6 angle sensor uses a Synthetic AntiFerromagnet (SAF) without an exchange biasing AFM layer to pin the magnetization in one direction.

The development of a demonstrator GMR 360° angle sensor based on a spin valve system was an important milestone in the "BMBF Leitprojekt Magneto-Elektronik" and provided the primary motivation for this dissertation. The demonstrator angle sensor has to operate in a specified temperature range [–40° to 150°C] and survive for short periods of time (several hours) at temperatures up to 190°C. The sensor must achieve an angular error below ±1° and operate in a magnetic field range of 10-100 mT. A large obstacle in the development of this sensor was the lack of a practical method for reorienting the bias direction in the spin valve meanders of a Wheatstone bridge circuit. The sensor design of a GMR 360° angle sensor consists of two Wheatstone bridge circuits with two opposing bias directions in each circuit: total of four different bias directions. The relationship needed to be examined between the magnetic parameters of a spin valve and the observed deviations from the cosine dependence of the GMR effect. The temperature dependence of these parameters and the GMR effect of the spin valve needed to be determined in order to select the appropriate spin valve system for the angle sensor application. A method had to be developed for the reorientation of the bias direction in a spin valve on a μm scale in order to fabricate the sensor element of the angle sensor.

The research work began with a systematic study of the deviation from the cosine dependence of the GMR effect in a spin valve. This included the quantification of the amount of cosine deviation as a function of the applied field strength and the determination of the possible physical effects that cause the cosine deviation. The physical origins of the cosine deviation factors were confirmed by detailed comparison between experimental and simulated MR rotation curves. The MR rotation curves were simulated through the use of a program [May02] based on a free energy model for magnetic multilayers proposed by Dieny, et al. [Die00], and further refined by Tietjen, et al. [Tie02]. This program allowed the simulation of both resistance changes and the magnetization direction in each layer as a function of applied field strength and direction and provided a useful tool in confirming the validity of the experimental results. The experimental results were used to identify the critical magnetic parameters for the angle sensor application and in optimizing the layout of the sensor element.

The magnetic properties (GMR effect, exchange bias, etc.) of the of the following spin valve systems (NiO, FeMn, IrMn, PtMn, PtMn with SAF) were examined to determine the appropriate spin valve system for the angle sensor application. The spin valve system must have sufficient GMR effect and exchange bias over the given operating temperature range [–40°C to 150°C] and the bias direction of the spin valve must remain completely stable up to 190°C for short periods of time. The magnetic properties of each spin valve system were determined through field-dependent magnetoresistance measurements. The crystal structure was determined with X-Ray Diffraction (XRD). The temperature dependence of the GMR and exchange bias effect of each system was determined in the temperature range of 25°C to 170°C. A detailed comparison was made between the different spin valve systems upon the conclusion of the aforementioned measurements.

The most challenging of the research goals was the development of a method for local reorientation of the bias direction on the μm scale. Three different methods (lift-off, ion irradiation, laser-writing) were analyzed in terms of their effectiveness in reorienting the bias direction on a μm scale without inducing any degradation in the magnetic properties of the spin valve. The lift-off method (multiple deposition of the spin valve stack) was tested at the "Institut für Festkörperphysik and Werkstoffwissenschaft Dresden" (IFW-Dresden). The ion irradiation method, first described by Mougin, et al. [Mou01a], and Fassbender, et al. [Fas02], was analyzed in a collaborative work with the "Universität Kaiserslautern" and "Institut für Physikalische Hoch Technologie Jena" (IPHT-Jena). The effectiveness of the laser-writing method was tested at the Corporate R&D Center of Robert Bosch GmbH with a KrF excimer laser. The method that induced the least amount of degradation in the magnetic properties of the spin valve and was compatible with a production setting was selected for fabrication of a demonstrator GMR 360° angle sensor.

The laser-writing method was found to induce changes in the magnetic and electrical properties of a spin valve prior to complete loss of the GMR and exchange bias effects. The laser irradiation of a spin valve led to a reduction in the GMR effect prior to complete intermixing of the spin valve layers while the exchange bias effect remained constant in the same laser energy range. The GMR and exchange bias effects usually reduce simultaneously in magnitude as seen long-term anneal studies conducted on spin valves [Led99]. Analysis of the spin valves with XRD, Auger Electron Spectroscopy (AES) and X-Ray Reflectometry (XRR) provided a detailed picture of the microstructural changes induced by the laser irradiation. The relationship between the microstructural changes and the divergent behavior of these two physical effects could be explained by the interface dependence of the GMR effect and through use of the domain state model for exchange bias [Now00].

This dissertation lead to a more complete understanding of the spin valve system in relation to the angle sensor application. The physical effects that caused deviations from the cosine dependence of the GMR effect were found and directly correlated to the resulting angular error of a GMR angle sensor. An optimized sensor layout was designed using guidelines developed from the characterization of the cosine deviation factors. The PtMn spin valve with SAF was found to have the high GMR and exchange bias effects over the specified temperature range. The laser-writing was found to be the preferred method for imprinting the bias direction in the different spin valve meanders of the Wheatstone bridge circuit of an angle sensor. The detailed analysis of the laser irradiated spin valves lead to additional scientific support for the interface dependence of spin-dependent scattering and the domain state model for exchange bias. A demonstrator of a spin valve-based GMR 360° angle sensor was successfully fabricated using the laser-writing method.

Theory

2.1 Electrical Resistance and Magnetoresistance

The source of the electrical resistance R or specific electric resistivity ρ of metals stems from the scattering of conduction electrons during electron transport. The dominant scattering sites in polycrystalline metals are from grain boundaries, but also include interstitial defects, vacancies, impurity atoms or dislocations. Phonons lead to additional scattering of the conduction electrons and to a temperature dependence of electrical resistance.

Magneto-Resistance (MR) is the resistance change in a material induced by the application of a magnetic field. This is defined by the following expression:

$$MR = \frac{R_{max} - R_{min}}{R_{min}} = \frac{\Delta R}{R_{min}} \tag{2.1}$$

where R_{max} is the maximum measured resistance, R_{min} is the minimum measured resistance and ΔR the amount of resistance change. MR is commonly expressed as a percent value. This convention will be used throughout this dissertation.

The MR effect has been observed in nonmagnetic metals upon application of an applied magnetic field more than half a century ago [Koh49] [Jan57]. This resistance change stems from the Lorentz force of magnetic field acting on the conduction electrons. The Lorentz force changes the trajectory of the conducting electron, therefore increasing its scattering potential. The MR effect, due to the Lorentz force, is two orders of magnitude smaller in comparison to the AMR and GMR effects, and its contribution to the overall MR effect is typically ignored.

2.2 Anisotropic Magneto Resistance (AMR)

The AMR effect is a current-induced MR that exists in ferromagnetic metals such as Ni, Co or Fe upon application of an applied field H. The physical origin of the AMR effect is spin-orbital coupling on the 3d orbitals caused by an applied magnetic field [Smi51]. This increases the scattering potential of the electrons during conduction in ferromagnetic materials. The magnitude of the AMR effect is dependent on the angle between the current flow I and the angle of the magnetization M in the ferromagnetic metal as shown in Figure 2.1. θ_M is usually the same as the angle of the applied field θ_H, but can be influenced by other factors such as a form or crystalline anisotropy in the ferromagnetic thin film [McG75]. θ_j is the direction of the current flow.

The resistance of a ferromagnetic thin film is at a maximum when the current is parallel to the magnetization direction $R_{//}$ and is at a minimum when the current is perpendicular to the magnetization direction $R_{\perp}$. The magnetic field dependence of the AMR effect for a ferromagnetic thin film is shown Figure 2.2. There is no difference in resistance at zero field between the two current-field orientations. Upon application of a magnetic field, the difference in resistance between the // and $\perp$ become immediately apparent. The resistance with the current set perpendicular to magnetic field direction decreases while the resistance increases with the current set parallel to the field direction. The difference in resistance between the two orientations quickly reaches a maximum with increase in magnetic field, e.g. 1-2 mT for $Ni_{81}Fe_{19}$ [McG75], also known as permalloy.

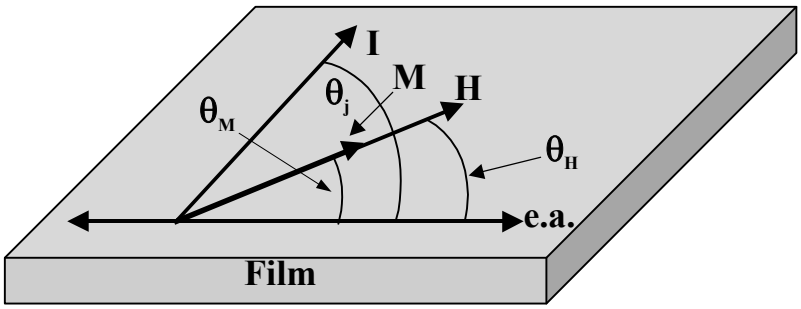

Figure 2.1: Orientation of the current in relation to the magnetization direction of a ferromagnetic thin film and the applied magnetic field.

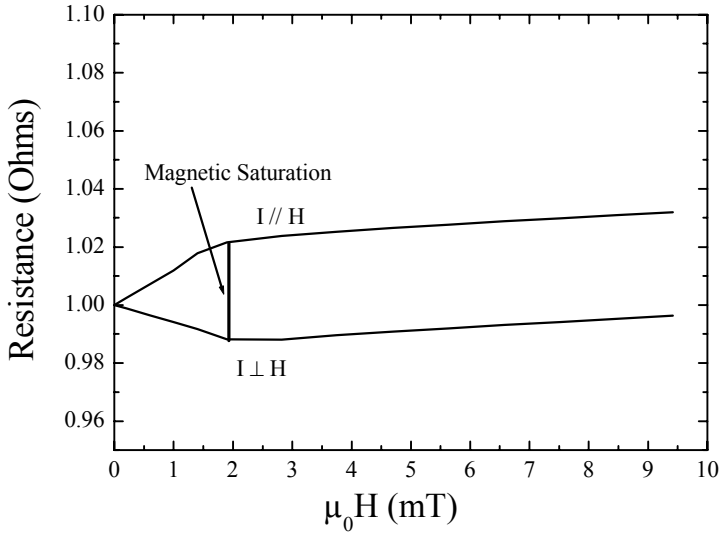

Figure 2.2: Field dependence of the resistance in a ferromagnetic thin film measured with the current direction set parallel and perpendicular to the applied field direction.

The angle dependence of the resistance change due to the AMR effect can be expressed as follows:

$$R(\theta) = R_{min} + \Delta R_{AMR} \times \cos^2(\theta_M - \theta_j) \tag{2.2}$$

where ΔR_{AMR} is the resistance change due to the AMR effect.

This relationship is expanded to include the terms, $R_{\perp}$ and $R_{//}$:

$$\begin{aligned} \Delta R_{AMR} &= R_{//} - R_{\perp} \\ R_{min} &= R_{\perp} \\ R(\theta) &= R_{\perp} + (R_{//} - R_{\perp}) \times \cos^2(\theta_M - \theta_j) \end{aligned} \tag{2.3}$$

According to Eq. (2.2) the resistance changes from the AMR effect should then have 180° periodicity when the ferromagnetic is rotated in a constant applied magnetic field as seen in Figure 2.3. The AMR effect must be taken into consideration when analyzing GMR thin film systems, because they all contain ferromagnetic metals. Substantial resistance changes can be created through the AMR effect in ferromagnetic thin films. The AMR effect can be as high as 2.5% for a 30 nm thick NiFe film [McG75] and up to 1% of the total MR effect in a spin valve [Koo96].

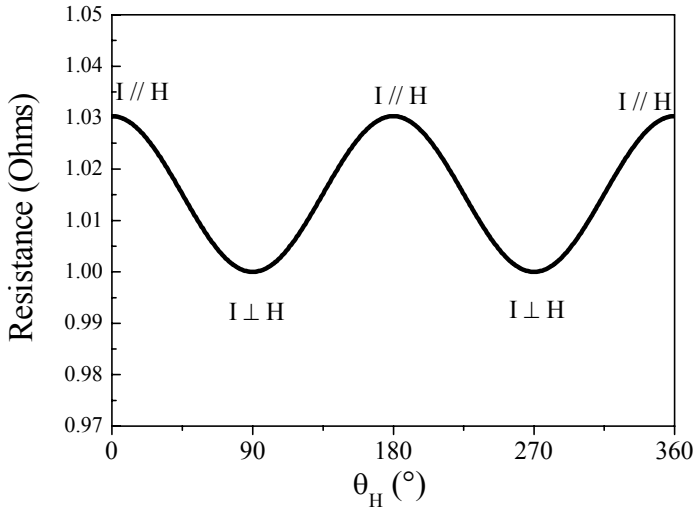

Figure 2.3: Rotation curve illustrating the cosine-squared periodicity of the AMR effect when a ferromagnetic thin film is rotated in an applied magnetic field.

2.3 Giant Magneto Resistance (GMR)

Grünberg, et al. [Grü86], was the first to report the existence of exchange interlayer coupling in magnetic multilayers with the discovery of antiferromagnetic coupling in the Fe/Cr/Fe system. The exchange coupling changed from antiferromagnetic to ferromagnetic as in the Cr spacer layer thickness changed. This discovery was followed in the late 1980's by the simultaneous observance of the GMR effect by Baibich, et al. [Bai88], and Binasch, et al. [Bin89]. The GMR effect was observed during resistance measurements made on antiferromagnetically coupled multilayers at liquid nitrogen temperature. The resistance of a magnetic multilayer dropped to zero upon application of an applied magnetic field that was sufficient to overcome the antiferromagnetic coupling as seen in Figure 2.4.

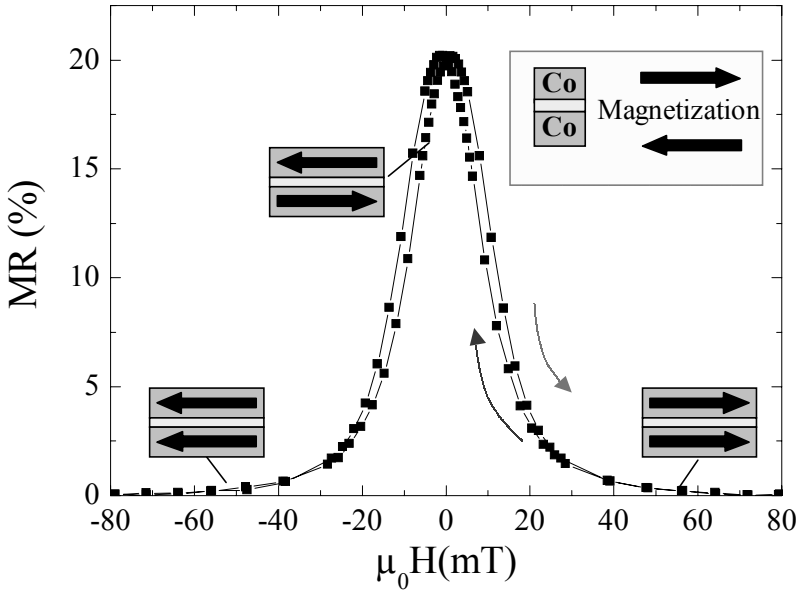

Figure 2.4: MR curve measured from a Co/Cu multilayer showing the field dependence of the GMR effect and magnetization directions in the ferromagnetic layers.

Parkin, et al. [Par90], was the first to publish results on the oscillatory nature of the GMR effect and exchange interlayer coupling in different magnetic multilayers. The oscillatory period of the GMR effect is defined as the change in spacer layer thickness that results in the switch from ferromagnetic to antiferromagnetic exchange interlayer coupling in a magnetic multilayer. Observance of the GMR effect allowed one to easily determine the oscillatory period of the exchange coupling. In the case of Cu, the 1st antiferromagnetic maximum was found at 1 nm, the 2nd at 2.2 nm and the 3rd at 3.5 nm, as seen in Figure 2.5.

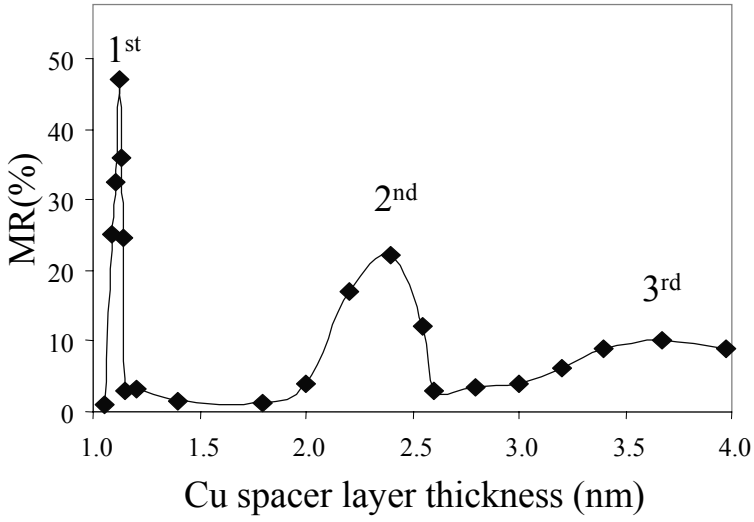

Figure 2.5: Antiferromagnetic maxima of the exchange coupling in the Co/Cu multilayer system [Sch98].

Parkin, et al. [Par91a], was also the first to systematically study the oscillatory nature of the exchange coupling in other magnetic multilayers containing 3d, 4d and 5d transition metals. The true breakthrough for the possible application of the GMR effect in industry came with the report of 65% MR effect measured at room temperature in the Co/Cu system

deposited by the sputter deposition [Par91b]. Magnetic multilayers previously were only deposited with Molecular Beam Deposition (MBE), which has too slow of a deposition rate to be economical. High MR values had only been previously reported at liquid nitrogen temperatures. The GMR effect has since been measured in many other magnetic multilayer systems grown by sputter deposition including NiFe/Cu [Par92], CoFe/Cu [Kat93] and NiFe/Au [Par96].

The strength of the exchange coupling is dependent upon the angle between the magnetization directions of the different ferromagnetic layers. Taking the simplest case of one NM spacer layer between the two FM layers with magnetizations M_1 and M_2 as seen in Figure 2.6, the energy E_i of the exchange coupling can be described phenomenologically by the following relationship [Bru93]:

$$E_i = -J_1 \frac{M_1 \times M_2}{|M_1||M_2|} = -J_1 \cos(\Delta\theta) \tag{2.4}$$

where J_1 is the coupling coefficient and $\Delta\theta$ is the angle between M_1 and M_2. The type of coupling (antiferromagnetic or ferromagnetic) is dependent upon the sign of the coupling coefficient.

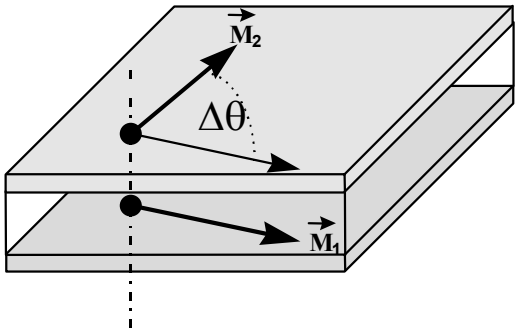

Figure 2.6: Schematic showing the orientation of the magnetization direction in two ferromagnetic layers separated by a nonmagnetic spacer layer.

J_1 can be determined directly from a MR measurement as shown below:

$$J_1 = \frac{\mu_o M H_s t_{FM}}{2} \tag{2.5}$$

where H_s is the saturation field of the magnetic multilayer, field value at which the MR is at a minimum, μ_0 is the induction constant, and t_{FM} is the thickness of the FM layer. The exchange coupling energy coefficient as a function of spacer layer can be calculated in the above expression as shown in Figure 2.7.

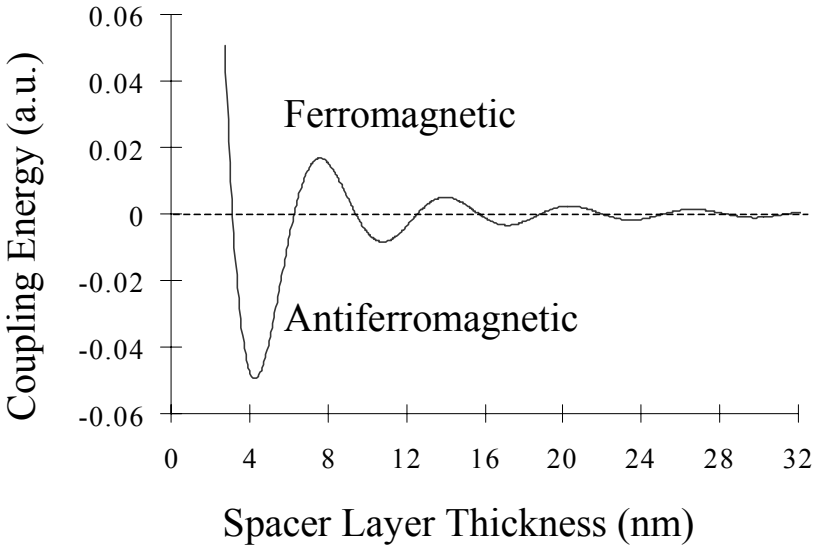

Figure 2.7: Exchange coupling energy as a function of the Cu spacer layer thickness in Co/Cu multilayer system.

Many models have been developed to explain the oscillatory nature of the exchange coupling in multilayers,. The Ruderman-Kittel-Kasuya-Yosida (RKKY) theory gave the best results for the theoretical calculation of the oscillating exchange coupling [Bru93]. The physical origin of the oscillations in this model is attributed to quantum interference, which is due to spin-dependent confinement of the electrons in the spacer layer. The periods of the oscillations are determined by the Fermi bandgap at the interface of the spacer layer as experimentally confirmed by Parkins, et al. [Par91a]. The exchange coupling is often referred to as RKKY-coupling in literature due to the success of this model at predicting the oscillatory period of the exchange coupling.

2.4 Spin-Dependent Scattering

At first the existence of the GMR effect was thought to be directly coupled on the antiferromagnetic exchange coupling present in a magnetic multilayer. This was disproved by studies done by Barnaś, et al. [Bar90], and Dupas, et al. [Dup90], on Co/Au/Co tri-layers with Co layers of different thicknesses and thus different coercivities. The layer with the lower coercivity, smaller layer thickness, would follow the applied magnetic field before the thicker Co layer. The spacer layer thickness was selected to prevent any exchange interlayer coupling. A GMR effect of 1.4% at room temperature was observed in the Co/Au/Co tri-layer. Only the anti-parallel alignment of the magnetization directions between the two layers was necessary for the existence of the GMR effect. Another physical effect was responsible for the large resistance changes seen in magnetic multilayers, spin-dependent scattering.

2.4.1 Co/Cu Bandgap Structure

The presence of spin-dependent scattering in magnetic multilayers was seen as a possible explanation for the existence of the GMR effect without the presence of antiferromagnetic interlayer coupling. Spin-dependent scattering can be explained by close examination of the electronic structure of ferromagnetic transition metals and the bandgap structure at the FM/NM interface in magnetic multilayers. Conduction in ferromagnetic transition metals

comes mainly from electrons in the 4s and 3d outer shell. The 3d electrons are localized in transition metals resulting in a high electron mass in comparison to 4s electrons. This greatly reduces their contribution to conduction, but does increase the scattering potential. The scattering probability is expected to be the largest for the spin direction with the largest density of states at the Fermi level, such as the 3d states in the magnetic transition metals. In the case of transition metals such as Ni and Co, the 3d electrons are highly spin-polarized resulting in only minority spin electrons at the band gap [Pri95]. The magnetic moment in Ni and Co is due to the spin-polarized state of electrons in the 3d shell.

The bandgap structure in an antiferromagnetically coupled Co/Cu/Co multilayer system is presented in Figure 2.8 [Pri95]. The charge carriers in a magnetic system are separated into two categories: majority and minority carriers. Majority carriers have their spin in the direction of the magnetic moment, whereas minority carriers have their spin anti-parallel to the magnetic moment. In the left Co layer, the majority carriers have a spin-up orientation, and the minority carriers have a spin-down orientation. During electron transport, a majority carrier from the Co layer will travel unhindered through the Cu since its band structure is similar to that of Co. The majority carrier will, however, be scattered upon reaching the other Co/Cu interface, because it is now a minority carrier in the other Co layer while the magnetization in this layer has the opposite orientation. A Co minority carrier from the first Co layer, spin-down, will reach the first Cu/Co interface and be scattered upon finding no free state in the Cu layer. It will not be scattered upon reaching the 2nd Co/Cu interface, as it is now majority carrier. The electrons of both the spin-up and spin-down orientation would be scattered at every 2nd Co layer in a magnetic multilayer of several NM/FM periods. This leads to a strong increase in the measured resistance of the magnetic multilayer. This is based on the assumption that the mean free path of the electron is much larger than the spacer layer thickness of the multilayer. The spin information of the electron is retained upon reaching the opposite Co/Cu interface, and is not lost due to spin-independent scattering.

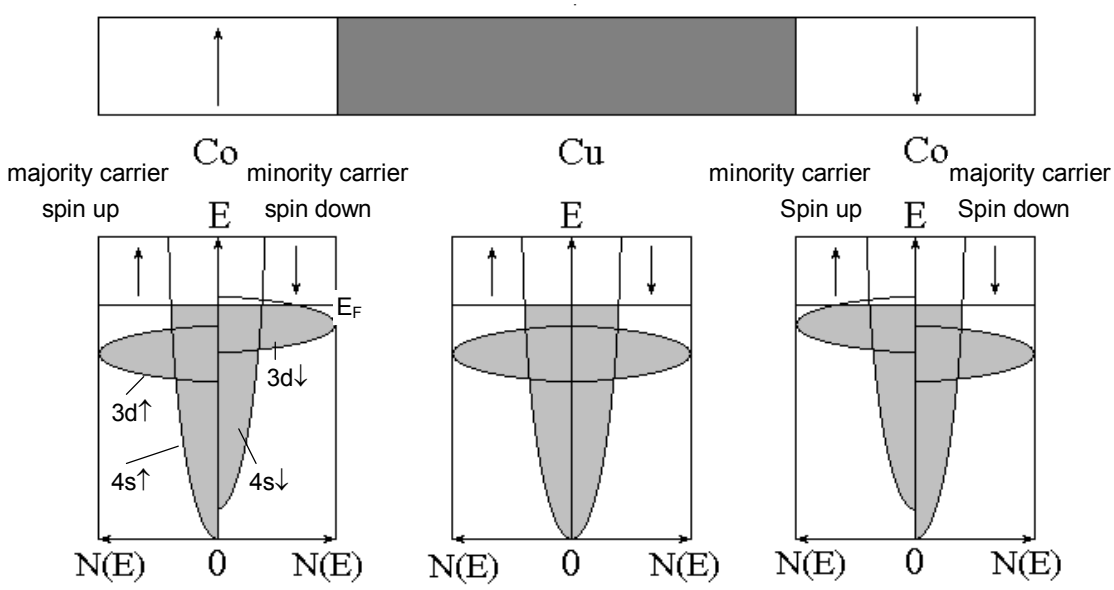

Figure 2.8: Bandgap structure for the Co/Cu/Co interface of magnetic multilayer with anti-parallel alignment of the magnetization directions.

The GMR effect exists due to the difference in spin-dependent scattering that exists at zero and large applied magnetic fields. First, the two different scattering must be defined states: parallel state at zero field at large fields and the anti-parallel state as illustrated in Figure 2.9. In the left part of the figure, the applied field has pulled all magnetization of each layer into

In the left part of the figure, the applied field has pulled all magnetization of each layer into the parallel state. On the right side the zero field case is shown where the magnetization of each ferromagnetic layer are anti-parallel to one another. Only scattering at the interfaces is indicated, as interface scattering dominates the scattering potential in multilayers. The arrows indicating the magnetization direction of the FM layer also indicate the spin direction of the majority carrier in that layer.

In the parallel magnetization case, scattering is strong for the electrons with spin anti-parallel, minority carriers, to the magnetization of the FM layer and weak for electrons with spin parallel, majority carriers. The electron mean-free path for one spin direction is larger than the multilayer period and much smaller for the other spin direction. The anti-parallel alignment of the magnetic layers results in appreciable scattering from electrons of both spin directions. The lower amount of scattering events in the parallel case leads to a lower resistance state than in the anti-parallel case.

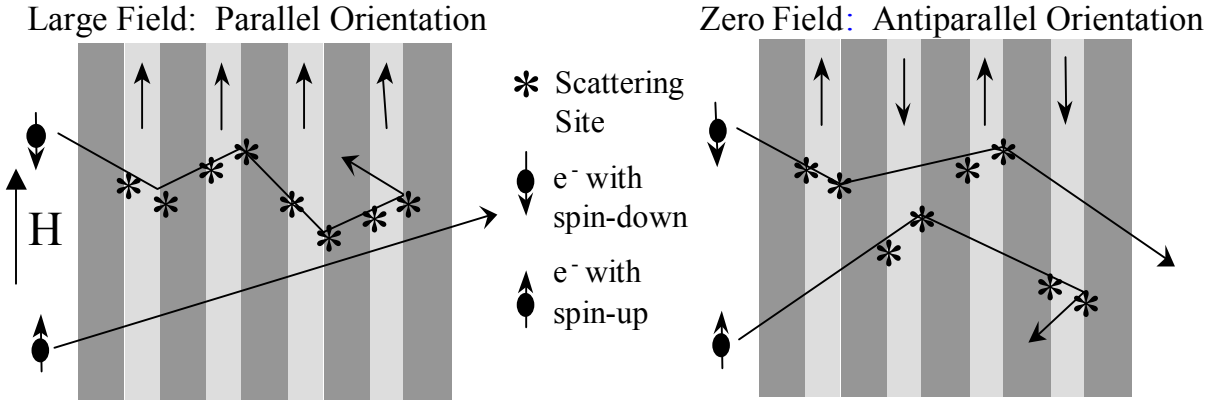

Figure 2.9: Diagram illustrating the scattering events occurring in the layers at large magnetic fields, parallel state, (left) and at zero field, anti-parallel state (right). The Current in Plane (CIP) configuration for measuring the MR of magnetic multilayers is assumed in this case.

2.4.2 Mott Two-Current Model

Levy and Zhang [Lev95] proposed a model for the electrical conductivity in magnetic multilayer systems based upon the previously described situation for spin-dependent scattering and using the Mott two-current model [Mot36]. An important assumption of this model is that the total resistance can be expressed as the sum of the separate contributions from the spin-up and spin-down electrons. The scattering events for the spin-up electrons $S^{\uparrow}$ and spin-down electrons $S^{\downarrow}$ can be viewed as separate channels that are added in parallel.

This two-current model is presented in Figure 2.10 for both the parallel and anti-parallel state. In both channels, two resistors are present to represent scattering events at two different interfaces. A large resistor represents large amounts of scattering while a small resistor represents no scattering. In the parallel state (see Figure 2.10a) the spin down electrons are scattered at every interface, while the spin up electrons are not scattered. This results in a low total resistance for the parallel state. The spin up and spin down electrons are scattered at every other interface in the anti-parallel state resulting in a large resistor component in both spin channels and a high resistance state (see Figure 2.10b).

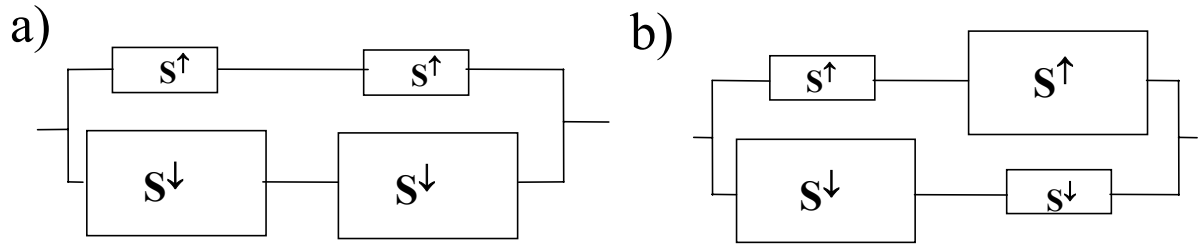

Figure 2.10: Circuit diagram for the Mott two-current model representing the a) parallel state and b) anti-parallel state.

If $R^{\uparrow}$ and $R^{\downarrow}$ are the resistance for the spin-up and spin down channels respectively, the resistance for the parallel state R_p can be expressed as:

$$R_p = \frac{R^{\uparrow} \cdot R^{\downarrow}}{R^{\uparrow} + R^{\downarrow}} \tag{2.6}$$

and the resistance for the anti-parallel state R_{ap} as:

$$R_{ap} = \frac{R^{\uparrow} + R^{\downarrow}}{4} \tag{2.7}$$

defining the scattering asymmetry as $\alpha = R^{\uparrow} / R^{\downarrow}$, the MR ratio can be defined as:

$$\frac{\left(R_{ap} - R_p\right)}{R_p} = \frac{\left(1-\alpha\right)^2}{4\alpha} \tag{2.8}$$

The GMR effect can be increased drastically by increasing the ΔR between the spin-up and spin-down channels. A study of the Fermi Band bandgap structure at the interface of FM/NM layers predicted the highest GMR effects in the Co/Cu and Fe/Cr systems [Coe96]. This was experimentally confirmed by the report of the highest GMR effects to date in the Co/Cu system [Par91b] and the Fe/Cr system [Sch94]. The Fermi bandgap structure plays a deciding role in the magnitude of the GMR effect, but microstructural features such as grain size and texture must be taken into account when attempting to optimize the GMR effect of the magnetic multilayers [Har00].

2.5 Spin Valve System

Dieny, et al. [Die91], were the first to propose the spin-valve system in 1991. A spin-valve structure is the combination of a FM/NM/FM tri-layer with an AFM layer in contact to one of the FM layers as illustrated in Figure 2.11. This basic spin valve structure is referred to as a simple spin valve. The magnetization of the FM layer adjacent to the AFM layer is pinned in one direction through the exchange bias effect, which occurs across the interface AFM/FM. The FM layer in contact with the AFM layer is referred to as the pinned layer and the direction of the pinned layer magnetization as the bias direction of the spin valve. The exchange bias is also referred to as a unidirectional anisotropy due to the unidirectional nature of the effect [Coe96].

The AFM layer can either be deposited at the bottom of the spin valve stack, Bottom Spin Valve (BSV), as seen in Figure 2.11 or at the top of the spin valve stack, Top Spin Valve (TSV). One variation of the simple spin valve is a double or symmetric spin valve. This is essentially a combined top and bottom spin valve, which has a GMR effect almost double that of the simple spin valve e.g. 21% (double) vs. 12 % (simple) [Ege93].

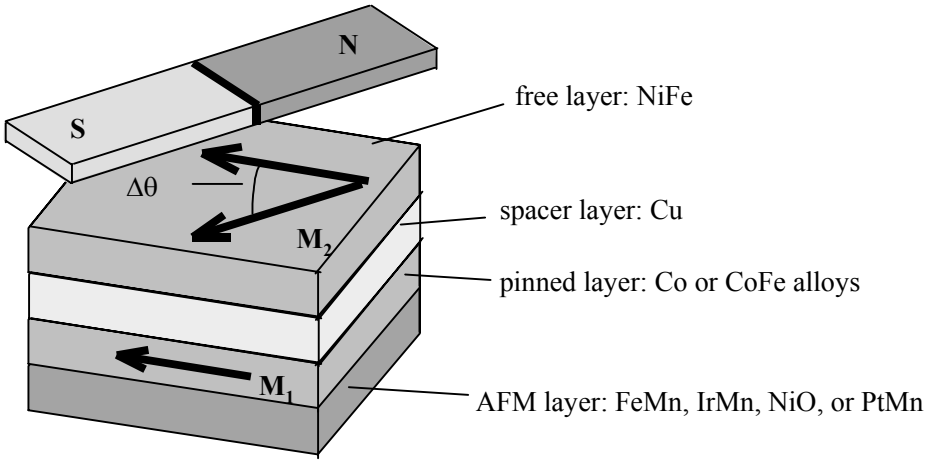

Figure 2.11: Structure of a simple bottom spin valve.

The complexity of the spin valve system and the involved physical effects (uniaxial anisotropy, interlayer coupling, exchange bias) requires the separation of the background theory into five distinct sections to allow a detailed explanation of each topic:

- Phenomenological description of the applied magnetic field and angle dependence magnetoresistance of a spin valve (see Section 2.5.1)
- Uniaxial anisotropy in the free and pinned layer (see Section 2.5.2)
- Interlayer coupling between the free and pinned layer (see Section 2.5.3)
- Exchange bias in the spin valve system (see Section 2.5.4)
- Standard spin valve materials (see Section 2.5.5).

2.5.1 Magnetoresistance Characteristics of a Spin Valve

The magnetoresistance characteristics of a spin valve are very different from those of the previously described magnetic multilayers. The MR plot from a magnetic multilayer (see Figure 2.4) is symmetric in form, while the spin-valve is asymmetric as depicted in Figure 2.12. This asymmetry in the MR curve is due the unidirectional anisotropy of the pinned layer. The positive field direction is the same as the bias direction of the spin valve. The magnetization of the free layer and of the pinned layer have a parallel orientation for $\mu_0 H > 0$ in the major loop of the MR curve: large field measurement (e.g. max. field value ±100 mT). The resistance is at a minimum at this point due to the parallel alignment between the magnetization direction of the free layer (FL) and pinned layer (PL).

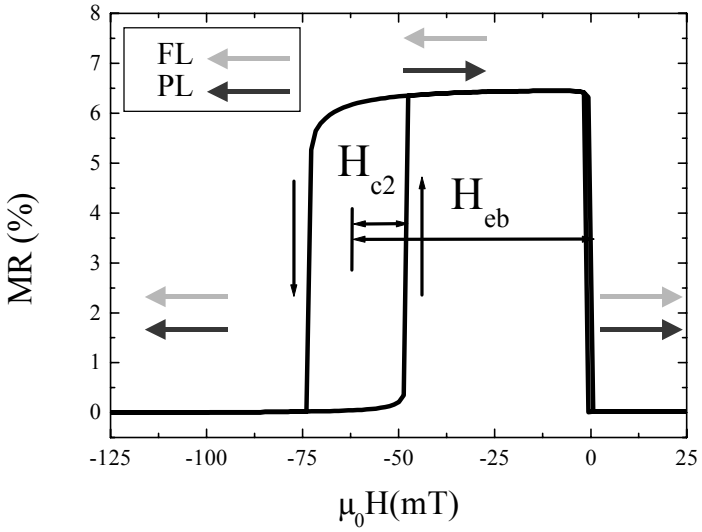

Figure 2.12: Major loop of an MR curve measured from a spin valve.

After the field direction switches to a negative polarity, the magnetization of the free layer reverses direction, while the magnetization of the pinned layer remains fixed. The resistance now rises to the maximum value, because the magnetization of the free and reference layers are now in the anti-parallel state. Only upon application of a field greater than the exchange bias field H_{eb} does the magnetization of the pinned layer rotate in the direction of the applied field. The measured MR drops to zero at this point. The H_{eb} is determined at the halfway point in the hysteresis of the major loop and at half the MR value as seen in Figure 2.12. After the exchange bias effect is overcome by the applied field, the magnetization of the free and pinned layers are again in the parallel orientation.

Numerous other magnetic parameters, such as the interlayer coupling between the free and pinned layer H_e and coercivity of the free layer H_{c1} and the pinned layer H_{c2} can also be extracted directly from an MR measurement. H_e is the shift in the minor loop of an MR or magnetization curve from the zero field (see Figure 2.13). A positive shift is an indication of ferromagnetic interlayer coupling and a negative shift of anti-ferromagnetic interlayer coupling.

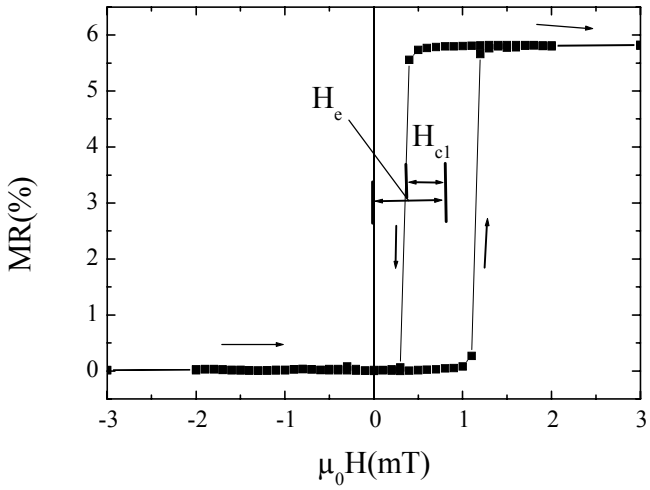

Figure 2.13: Minor loop of an MR curve measured from a spin valve.

The coercivity is a measure of the uniaxial anisotropy of the ferromagnetic layer and is represented by the hysteresis seen in the closed loop of the MR curve (see Figure 2.12). H_{c1} is measured from the half-way point of hysteresis in the minor loop of an MR curve and is

determined at half the maximum MR value as shown in Figure 2.13. The minor loop of an MR curve is defined as an MR or magnetization measurement made near zero field with a maximum field range of only a few mT, e.g. ±5 mT. H_{c2} is the hysteresis measured in the major loop of the MR curve as shown in Figure 2.12 and is determined in the same manner as H_{c1}.

The unidirectional nature of the GMR effect is even more evident when the spin valve is rotated under a constant applied field. The resistance change in the spin valve shows a cosine dependence that can be described by the following relationship [Coe96]:

$$R(\Delta\theta) = 0.5 \times (R_{ap} - R_p) + R_p + 0.5 \times (R_{ap} - R_p) \times \cos(\Delta\theta) \qquad (2.9)$$

where $\Delta\theta$ is the angle between the magnetization directions of the pinned and free layer, R_p is the resistance when the magnetization in the free layer is aligned parallel to that of the pinned layer, and R_{ap} is the resistance when the magnetization directions between the free and pinned layer are in the anti-parallel orientation.

The cosine dependence of the GMR effect exists only at field values below the H_{eb} of the spin valve. H_{eb} also defines the theoretical limit of the maximum operating magnetic field of a GMR 360° angle sensor. A resistance measurement as a function of $\Delta\theta$ is presented in Figure 2.14.

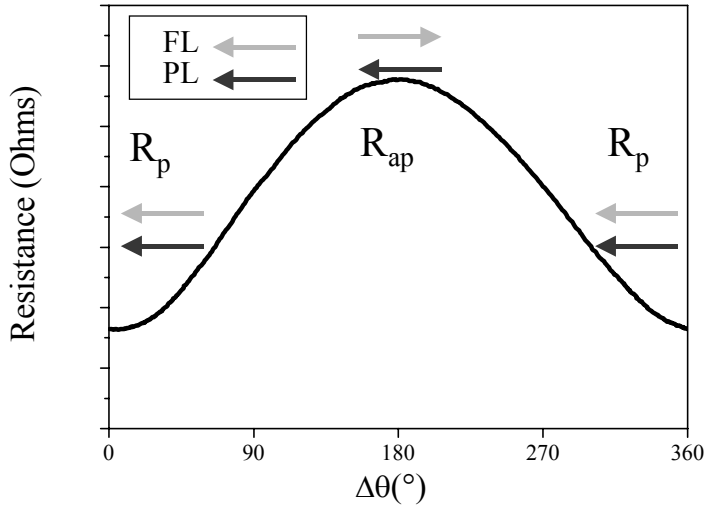

Figure 2.14: Resistance as a function of the applied field direction in a spin valve.

2.5.2 Uniaxial Anisotropy in the Free Layer and Pinned Layer

H_{c1} and H_{c2} are a measure of the uniaxial anisotropy or coercivity in the free layer and pinned layer. There exists an intrinsic uniaxial anisotropy in all ferromagnetic materials, but a uniaxial anisotropy of larger magnitude can be induced either by growth in an applied magnetic field or by anneal in an applied magnetic field [Wil68]. The ferromagnetic layer must be annealed or deposited while the layer is in saturation to induce the uniaxial anisotropy. This induced uniaxial anisotropy in ferromagnetic thin films is thought to originate from the directional ordering of a fraction of the magnetic pairs during deposition or anneal under a magnetic field [Née54]. The high coercivity in the pinned layer of a spin valve is not induced by a field anneal or deposition under a field, but rather through contact with the neighboring AFM layer [Ber99].

The uniaxial anisotropy coefficient of the free layer $K_f^{uniaxial}$ can be determined as shown in the following equation [Tie02]:

$$K_f^{uniaxial} = \frac{H_{c1} M_f t_f}{2} \tag{2.10}$$

where M_f is the saturation magnetization for the free layer and t_f the thickness of the free layer. All free energy coefficients are given in energy per unit area, e. g. J/m^2.

The uniaxial anisotropy coefficient of the pinned layer $K_p^{uniaxial}$ can be calculated in the same manner:

$$K_p^{uniaxial} = \frac{H_{c2} M_p t_p}{2} \tag{2.11}$$

where M_p is the saturation magnetization of the pinned layer and t_p is the thickness of the pinned layer.

The 180° periodicity of the uniaxial anisotropy is best shown in the corresponding free energy term as given below:

$$E_f^{uniaxial} = K_f^{uniaxial} \sin^2\left(\theta_f - \theta_f^{uniaxial}\right) \tag{2.12}$$

where θ_f is the direction of the magnetization in the free layer, $E_f^{uniaxial}$ is the free energy term for the uniaxial anisotropy in the free layer and $\theta_f^{uniaxial}$ is the direction of the uniaxial anisotropy in the free layer.

The free energy term for the uniaxial anisotropy of the pinned layer is calculated in a similar manner:

$$E_p^{uniaxial} = K_p^{uniaxial} \sin^2\left(\theta_p - \theta_p^{uniaxial}\right) \tag{2.13}$$

where $E_p^{uniaxial}$ is the free energy term per unit area for the uniaxial anisotropy in the pinned layer, θ_p is the direction of the magnetization in the pinned layer, and $\theta_p^{uniaxial}$ is the direction of the uniaxial anisotropy in the pinned layer.

2.5.2.1 Crossed Anisotropy Axis

For most sensor applications it is preferable that the switching of the free layer be free of any hysteresis. If the uniaxial anisotropy axis in the free layer is placed parallel to the bias direction as shown in Figure 2.15a, the minor loop of the MR curve will show a relatively large hysteresis. The magnetization reversal in parallel axis orientation is by domain wall movement, which results in the large hysteresis [Rij94] [McC96]. As shown by Riijks, et al. [Rij94], the hysteresis can be reduced by placing the magnetic uniaxial anisotropy axis perpendicular to the bias direction of the pinned layer as shown in Figure 2.15b. In the crossed anisotropy case, the magnetization in the free layer will coherently rotate 90° in the direction of uniaxial anisotropy axis and then be pulled in the direction of the applied field. This eliminates the domain formation normally associated with a magnetization reversal and greatly reduces the hysteresis in the minor loop.

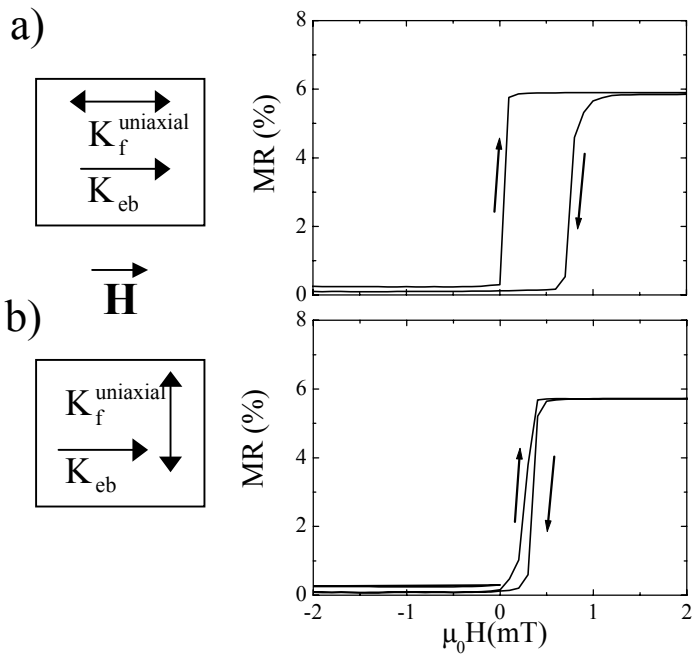

Figure 2.15: Orientation of the uniaxial anisotropy in the free layer in relation to the bias direction of the spin valve where the anisotropy axes are in the a) parallel axis orientation and b) crossed axis orientation and the resulting minor loop measurements for both orientations.

2.5.3 Interlayer Coupling in a Spin Valve System

In theory there is no interlayer coupling between the free layer and pinned layer of a spin valve, but in reality there is always some residual interlayer coupling present. This residual coupling can either be exchange interlayer coupling [Spe91] [Ant94] (see Section 2.3) or magnetostatic or "orange-peel" interlayer coupling induced by interface roughness at the FM/NM interface [Koo95] or a superposition of the two effects [Hos94]. There can also be ferromagnetic coupling due to pinholes through the spacer layer, but this only occurs if the layer thickness is below a critical value, less than 2 nm in the case of a Cu spacer layer [Koo95]. All of the spin valves studied in this dissertation had a Cu spacer layer thickness t_{Cu} of greater than 2 nm.

If the interlayer coupling is due to exchange coupling, it would show an oscillatory nature with a change in t_{Cu} the same as seen in magnetic multilayers [Spe91][Hos94] (see Figure 2.7). If the interface roughness is high, the ferromagnetic, orange-peel coupling would dominate over the antiferromagnetic RKKY-coupling at the 1st, 2nd and 3rd antiferromagnetic maxima at the appropriate layer thicknesses and only ferromagnetic coupling would be present in the system. The interlayer coupling energy plotted as a function of layer thickness will show an oscillatory nature with a change in t_{Cu} if the two interlayer coupling components are of the same magnitude.

The interlayer coupling coefficient J_{int} is determined as shown in the following equation [Koo96]:

$$J_{int} = H_e M_f t_f \tag{2.14}$$

The interlayer coupling is always found to be parallel to the unidirectional anisotropy and also has a cosine dependence as seen below:

$$E_{int} = J_{int}\cos(\theta_p - \theta_f) \tag{2.15}$$

where E_{int} is the free energy term per unit area for the interlayer coupling.

Orange-peel interlayer coupling is the result of correlated interface roughness as illustrated in Figure 2.16. The correlated interface roughness results in the formation of magnetic poles in the FM layer at the FM/NM interface. The magnetic poles created in the other FM layer have the opposite orientation, resulting in a ferromagnetic coupling between the two FM layers across the NM spacer layer. The orange-peel coupling has been modeled for the spin valve system using the original Neél Model [Née62] by Kools [Koo95]. The relationship is summarized below:

$$J_{int} = \frac{\pi^2}{\sqrt{2}}\frac{h^2}{L}\mu_0 M_{fr}^2 \exp\left(-\frac{2\pi\sqrt{2}t_{Cu}}{L}\right) \tag{2.16}$$

where h is the amplitude of a two-dimensional interface waviness, L is the lateral correlation length, and t_{Cu} is the Cu spacer layer thickness. L is associated with the average grain diameter, which is about the same size in most spin valve systems.

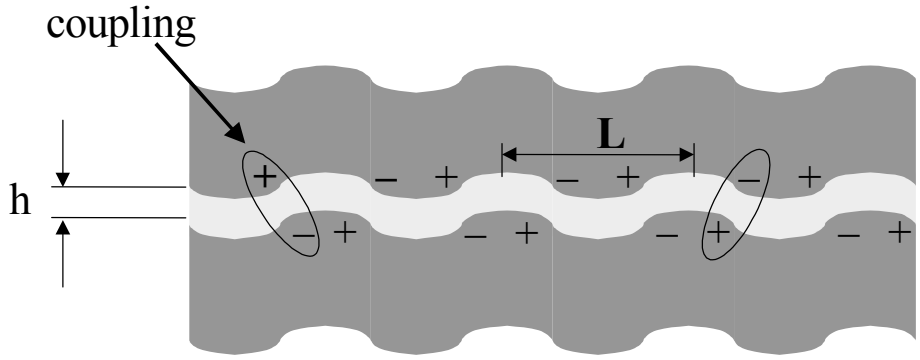

Figure 2.16: Cross-section of FM/NM/FM tri-layer where the interface roughness causes magnetostatic or "orange-peel " coupling between the ferromagnetic layers.

2.5.4 Unidirectional Anisotropy: Exchange Bias

2.5.4.1 Phenomenological Description

Discovered in 1956 by Meiklejohn and Bean [Mei56], exchange bias refers to the unidirectional pinning of the magnetization of a ferromagnetic layer by an adjacent antiferromagnet. Ferromagnetic films typically have a preferred magnetization axis, an easy *axis, due to a uniaxial anisotropy and the spins tend to align along this axis. There are two equally stable easy spin directions rotated by 180° along this axis that require the same energy and applied magnetic field to align the spins along either easy direction. The magnetization loop of a single ferromagnetic thin film is therefore symmetric about zero on the magnetic field axis as shown in Figure 2.17a.

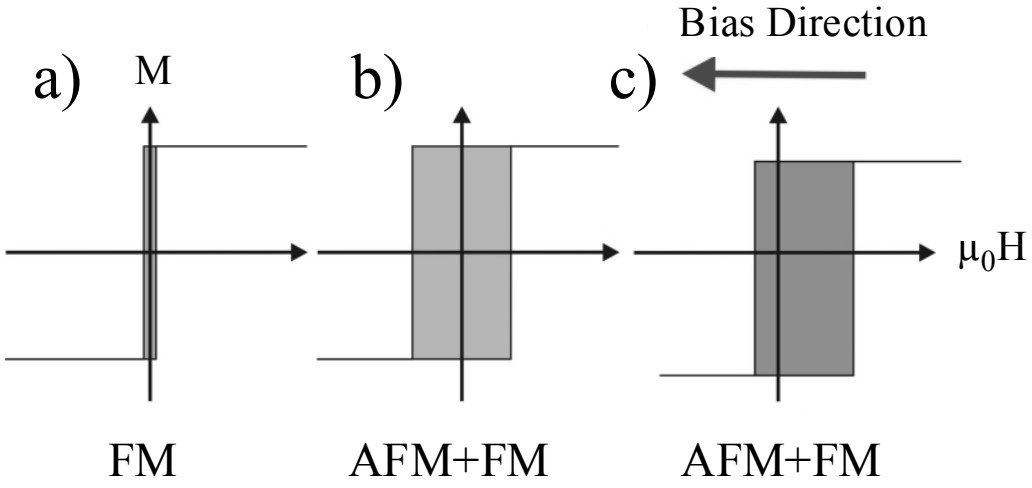

Figure 2.17: Easy axis magnetization loops of a) an FM film, b) an FM film grown on an AFM, and c) an FM/AFM sandwich grown in a field or annealed in a field above the Neél temperature.

When a FM layer is grown on an AFM layer, the ferromagnetic hysteresis loop is still symmetric, indicating two equivalent easy directions, but the exchange coupling between the two layers leads to an increased coercivity of the FM layer (Figure 2.17b). The bias direction has a random distribution at the macroscopic level in the AFM/FM sandwich when grown under no applied magnetic field. If, on the other hand, the AFM-FM system is grown in a magnetic field, or annealed in an applied magnetic field after growth to temperatures above the AFM Néel temperature T_N, temperature above which the exchange bias effect disappears [Neé67]), the bias direction is now uniform throughout the FM layer. The hysteresis loop becomes asymmetric and is shifted from zero as seen in Figure 2.17c. The ferromagnet is pinned by the antiferromagnet into this easy (left) direction that is opposite to the direction of the bias shift (right). This unidirectional shift is called exchange bias and reflects the fact that there is now a preferred easy magnetization direction for the FM layer. The use of an anneal and subsequent cool down in an applied field to change the bias direction is referred to as a "field cool" [Rij94].

The exchange bias or unidirectional anisotropy coefficient K_{eb} is a more convenient quantity to allow the direct comparison between different spin valve systems. This is determined as shown below [Koo96]:

$$K_{eb} = H_{eb} M_p t_p \tag{2.17}$$

It is difficult to determine H_{eb} or H_{c2} when the $H_{c2} \geq H_{eb}$. This creates a large hysteresis in the major loop of the MR curve, which tends to suppress the appearance of the exchange bias effect in a MR curve.

The cosine dependence of the exchange bias effect is illustrated below [Koo96]:

$$E_{eb} = K_{eb} \cos(\theta_p - \theta_{eb}) \tag{2.18}$$

where E_{eb} is the free energy term per unit area for the unidirectional anisotropy and θ_{eb} is the direction of the unidirectional anisotropy.

2.5.4.2 Néel Temperature of Antiferromagnet Thin Films

The T_N [Née67] of an AFM thin film is often referred to as a blocking temperature T_b since T_N is often lower than in the bulk material. Exchange bias is said to be an interface effect, however a minimal thickness of the AFM layer is required for observation of the exchange bias effect in many natural antiferromagnets at room temperature. For example, FeMn at 5 nm layer thickness has a T_b of 50°C, which rises to 150-160°C at thicknesses above 8 nm [Hos94]. Other microstructural factors, such as the change in grain size of the AFM thin film, appear to correlate with changes the T_b, but no definitive relationships have yet been established [Nog99].

The exchange biasing effect of a natural anti-ferromagnet will disappear above T_b due to loss of magnetic order from thermal excitation and will lose the defined bias direction if not cooled down in a magnetic field. The macroscopic magnetic order can be restored in true antiferromagnets such as FeMn or NiO if the material is heated above the T_b in a furnace of the antiferromagnet and then cooled down in a magnetic field (see Figure 2.18). The AFM layer is after the field cool again coupled on the FM layer as indicated by the dashes placed at the AFM/FM interface. A field cool is the only widely known method by which one can change the bias direction of an AFM/FM bilayer after deposition.

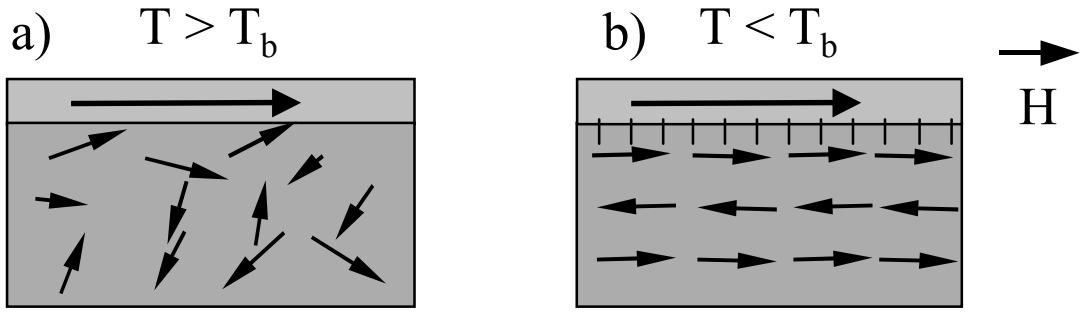

Figure 2.18: Cross section of AFM/FM bilayer showing a) the loss of magnetic order in the AFM upon heating above the T_b of the AFM and b) the pinning of the magnetization of the FM layer in one direction upon cooling the AFM down to room temperature under an applied field.

2.5.5 Spin Valve Systems: Standard Materials and Microstructure.

The standard materials used in spin valve systems can be divided into three different categories: ferromagnetic, nonmagnetic and antiferromagnetic. The standard ferromagnetic materials used in spin valves come exclusively from the fcc range of the NiFeCo ternary phase diagram [Koo96]. A NiFe binary alloy, $Ni_{81}Fe_{19}$ (also known as permalloy) has become the established material for the free layer [Koo96]. This is due to soft magnetic response of permalloy, lower M_f, in comparison to other ferromagnetic materials such as Co (NiFe: 1.09 T, Co 1.795 T) [Jil91]. A lower M_f in the free layer leads to reduction in $H_{c1,}$, as seen in Eq.(2.10), and H_e in Eq. (2.14),which allows for a higher sensitivity of the MR response near the zero field.

Co or CoFe alloys are the standard ferromagnetic materials used in the pinned layer of spin valves [Koo96]. Co or CoFe alloys, are most often selected for the pinned layer to increase the H_{eb} of the spin valve. The higher the M_p of the pinned layer the higher the exchange biasing at the FM/AFM interface as seen in Eq. (2.18). The equilibrium structure for Co is the hcp crystal structure, but in thin films it has been found to grow in the fcc crystal structure when grown on the appropriate buffer layer and only to a few nm thickness [Ben95].

CoFe alloys are often used instead of Co due to the higher spin polarization that can be achieved, thus reaching a higher GMR effect [Moo96] and establishing a better thermal stability of the spin valve. [Zel98]. NiFe is selected as the pinned layer material when a lower H_{c2} is desired in the pinned layer [Koo96].

The primary criteria for the selection of the non-magnetic spacer is (1) matching between the conduction band of the spacer layer with the spin-up channel of the neighboring ferromagnetic layer and (2) a high electrical conductivity in order to achieve high MR effects [Coe96]. Only Ag, Au, and Cu are the only materials come into question as spacer materials due to the prevalent use of fcc NiFeCo alloys in spin valves based on these two conditions [Die94]. Cu is the most logical candidate material due to its lattice matching with the fcc NiFeCo alloys (fcc-Cu: a_0 = 0.361 nm; fcc-Co: a_0 = 0.354 nm; fcc-NiFe: a_0 = 0.357 nm) [Koo96]. It has since become the standard spacer material used in every spin valve system [Coe96].

The insertion of a thin Co or CoFe barrier layer (e.g. 0.3 nm) between the free layer and the spacer layer is common practice in the design of spin valve structures resulting in a higher GMR effect. The Fermi bandgap structure at Co/Cu interfaces has been found to have a larger mismatch at the minority spin 3d bands than at the NiFe/Cu interface, which results in a higher amount of minority carrier scattering at the interface [Coe96]. This was experimentally confirmed by Parkin, et al. [Par93], where the placement of a Co layer at the NiFe/Cu interfaces in a NiFe/FeMn spin valve system increased the MR effect from 2.9% to 6%. An additional advantage of a Co barrier layer is the reduction in the intermixing of Ni with Cu during deposition, Co/Cu is a phase separating system, which results in less intermixing during deposition [Nic94]. The intermixing forms a nonmagnetic dead layer at the interface, which results in an increase in spin-independent scattering thus reducing the MR effect. The thermal stability of the spin valve is increased through use of a Co barrier layer for the same reason.

A buffer or seed layer is a standard part of any spin valve stack. The purpose of the buffer layer to induce a (111) texture in the spin valve stack and the growth of Co in the fcc phase [Koo96]. A (111) texture has been found to coincide with an increase in the GMR effect in spin valve systems [Coe96]. Various refractory metals Ta [Die93], Ti, Zr, Hf [Joo95], Mo and W [Duc96] have been tested as buffer layers and found to induce the desired texture (111) [Nak94]. The increase in the GMR effect can be understood by close examination of the microstructure and the Fermi bandgap structure resulting from the (111) texture. First columnar grain growth through the spin valve stack and large grain sizes (5 nm without Ta buffer layer; 10 nm with buffer layer) have been found to coincide with the appearance of the (111) texture [Coe96]. The columnar grain growth and larger grain size minimizes the number of grain boundaries in the spin valve, which reduces the amount of spin independent scattering. Secondly the perfect matching of the band structures of the majority spin carriers for a Co/Cu or CoFe/Cu interface when grown in the (111) orientation further increases the scattering potential difference between the majority and minority carriers. [But02].

Ta is the most commonly used buffer layer for spin valve stacks seen in literature [Coe96]. Ta normally has a bcc crystal structure [JCP96], but has an amorphous structure with regions of nanocrystallites, regions of crystallites (d < 2nm) when grown by sputter deposition to only a few tens of nm in thickness [Len97]. The structural relationship between the use of a Ta buffer layer and the growth in the (111) texture of the NiFe layer is not yet understood despite the multitude of studies [Coe96]. Ta is also deposited at the top of the spin valve stack to act as a passivation layer and oxidizes quickly to form upon exposure to air a Ta_2O_5 oxide layer.

A wide variety of different antiferromagnets have been studied in the past forty years since the discovery of the exchange bias effect [Bek99] [Nog99]. Band matching between the AFM and FM layers is not possible with the existing AFM materials. This leads to additional spin-independent scattering at the AFM/FM interface, which reduces the expected MR effect

[Koo96]. Each class of antiferromagnets has both advantages and disadvantages that must be taken in consideration. Most of the present research on AFM materials used in spin valves has concentrated on three different families of AFM materials listed below:

- fcc metallic monoxides: CoO, $Ni_xCo_{1-x}O$, NiO [Car92]
- fcc disordered Mn-alloys: FeMn [Die91], IrMn [Fuk97] [Nak97]
- fct ordered Mn-alloys: NiMn [Lin95], PtMn [Sai97]

The oxide antiferromagnets (NiO, CoO) have the advantage of low shunting (higher MR effect), and a high corrosion resistance typical of oxides [Car92]. The highest MR values to date have been reported in symmetric NiO spin valves (21%) [Ege93]. NiO also has a reported T_b of 200°C while CoO has a low T_b of only 33°C [Car92]. NiO and CoO have the disadvantage of low H_{eb} values (20 mT) and a need for precise control of the argon partial pressure during sputter deposition to cause growth in the correct (111) orientation.

FeMn and IrMn are from the disordered fcc-alloys Mn-alloy class of AFMs. FeMn is the most widely studied AFM material in spin valves due to low cost of the target and ease of deposition in the antiferromagnetic phase [Koo96]. FeMn equilibrium structure's is the α-phase (bcc), but it can grow in the antiferromagnetic fcc phase through growth on a buffer layer [Len97]. Unfortunately, FeMn has poor corrosion resistance and low T_b of only 150°C [Hos94]. The low T_b of FeMn made it the perfect test system in various experiments presented in the Results and Discussion. IrMn has a higher reported T_b of 190°C and had a superior corrosion resistance to FeMn [Led99].

The fourth and most promising class of AFM materials studied for high temperature operation is the ordered face-centered-tetragonal (fct) alloys. Both NiMn, T_b of 400°C [Lin95], and PtMn, T_b of 380°C [Mao00], have much higher blocking temperatures than the previously mentioned antiferromagnets. Both NiMn and PtMn grow in the disordered nonmagnetic fcc phase when deposited by sputter deposition and require a high temperature anneal of 200-300°C for several hours in order to transform into the antiferromagnetic fct phase [Lin95][Sai97]. The following AFM materials (NiO, FeMn, IrMn, PtMn) will be covered in more detail in Section 6.2 of the Results and Discussion. The reader is referred to the following reviews [Ber99] [Nog99] for a complete overview of all existing AFM materials.

2.6 Exchange Bias Models

The origin of the exchange bias effect is still widely debated after more than forty years of research on the subject. Central to the debate are the importance of the interfacial spin structure, the existence of uncompensated "interfacial spins" and the role of magnetic domains in the appearance of the exchange bias phenomenon. Important questions remain relating to the origin of uncompensated interfacial spins and their role in the observed coercivity in a FM in contact with AFM layer. This is despite the intensive study of the AFM/FM sandwiches with methods such as Mössbauer [Ter87][Jun95] and neutron diffraction [Lin93][Bor95][Iji98]. At present there are no generally accepted models that provide a complete explanation of the exchange bias effect due to the difficulty associated with the determination of the magnetic interfacial structure and it's relation to the domain structures in an AFM layer [Bek99]. The importance of the antiferromagnetic domain structure is that, on a microscopic level, the exchange coupling across the AFM/FM interface is expected to proceed domain by domain. Therefore the correlation of the AFM domain structure with that of the FM is of crucial importance to establishment of any exchange bias model [Nol00].

The three earliest exchange bias models will be reviewed to introduce the concepts central to the explanation of the exchange bias effect. These models are the ideal interface model [Mei57], partial wall model of uncompensated interface [Mau87], and random-field model [Mal87] [Mal88]. More progress has been made in recent years towards the development of models, which realistically reproduce the characteristics of the exchange bias effect. One recent exchange bias model one presented by Koon [Koo97] explains the exchange bias effect through perpendicular coupling across the AFM/FM interface. Another well developed model by Schulthess and Butler [Sch99] uses defect-based explanation similar to the random field model combined with a spin-flop coupling mechanism to explain the exchange bias effect and coercivity increase. The reader is referred to the previously mentioned references for a detailed review of these exchange bias models.

One exchange bias model, the domain state model, proposed recently by Nowak, et al. [Now00], has particularly been successful at predicting the magnitude and behavior of the exchange bias effect in different experimental results published in literature. Nowak proposed a defect-based model which related the number of defects in the volume of the AFM to the number of domain walls and their interplay with the spin arrangement at the AFM/FM interface to explain the existence of the exchange bias effect. This model was very helpful in explaining ion irradiation experiments (Section 6.4) and laser-writing experiments (Section 6.5) presented in the Results and Discussion.

2.6.1 Ideal Interface Model

Meikljohn and Bean [Mei57] proposed that the exchange bias effect arose from a fully uncompensated AFM interface layer at the AFM/FM interface. They examined the situation for Co FM layer on a CoO AFM layer at an ideally flat AFM/FM interface to provide a detailed explanation. The exchange bias was said to arise from short-range interaction between the nearest neighbors at the FM/AFM interface in this uncompensated layer. For the case of fully compensated interface (see Figure 2.19a), the AFM sublattice is such that there are equal numbers of opposite spin directions in the AFM volume resulting in a net magnetic moment of zero [Nog99]. This is the definition of a true antiferromagnet. A fully uncompensated AFM layer interface (see Figure 2.19b) has all of the spin directions in AFM interface layer in the same orientation as the neighboring FM layer. This results in an interfacial energy difference across the AFM/FM interface. Exchange interaction occurs across the interface pinning the magnetization of the pinned layer due to the interfacial energy difference. During the reversal of the FM layer the spins of the FM rotate coherently, but the spins of the AFM layer remain pinned in one direction.

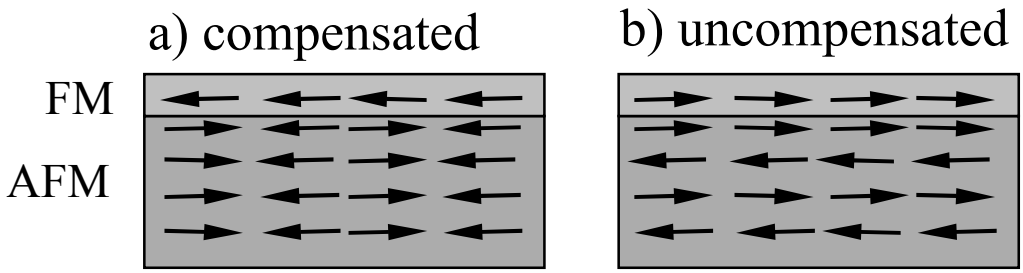

Figure 2.19: Side view of AFM/FM interface showing the spin orientation in the a) compensated and b) the uncompensated state.

The energy needed to rotate the spins in the FM layer can be calculated by considering the case of the Co atom in the FM and the neighboring Co in the AFM layer. The exchange

interaction will favor the parallel alignment of the spins between the Co in the FM layer, S_{FM}, and the AFM layer, S_{AFM}. The energy cost per pair of Co atoms is $J_{ex} \cdot S_{FM} \cdot S_{AFM}$ where J_{ex} is the exchange parameter. The exchange bias energy K_{eb} is given by dividing the energy cost by the number of Co atom pairs per unit area a^{-2} (lattice parameter) [Mei57]:

$$K_{eb} = \frac{2J_{ex}S_{FM}S_{AFM}}{a^2}$$
$$H_{eb} = \frac{K_{eb}}{M_{FM}t_{FM}} = \frac{2J_{ex}S_{FM}S_{AFM}}{a^2 M_{FM}t_{FM}} \quad (2.19)$$

M_{FM} and t_{FM} are the same as M_p and t_p mentioned earlier in Eq (2.11). The major problems associated with this model are the prediction of exchange bias fields that are two orders of magnitude larger than the observed values, failure to explain the exchange biasing observed at fully compensated interfaces and not taking into account the existence of interface roughness which exists in sputtered polycrystalline thin films [Mal87].

2.6.2 Partial Domain Wall Model

Mauri, et al. [Mau87], proposed the existence of a planar domain wall parallel to the AFM-FM interface as a modification to ideal interface model. This dramatically lowers the energy required for the reverse magnetization of the pinned layer. A planar domain will form upon reversal of the magnetization as shown in Figure 2.20.

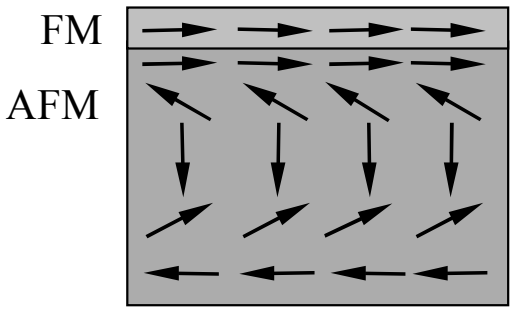

Figure 2.20: Side view of AFM/FM bilayer showing the fully uncompensated spin state at the AFM/FM interface, which results in the formation of a domain parallel to the interface.

The energy cost per area to rotate the FM layer is now spread over the width of the domain wall and is given by the following equation [Mau87]:

$$K_{eb} = 2\sqrt{A_{AFM}K_{AFM}}$$
$$H_{eb} = \frac{2\sqrt{A_{AFM}K_{AFM}}}{M_{FM}t_{FM}} \quad (2.20)$$

where A_{AFM} is the exchange stiffness parameter and K_{AFM} is the magnetocrystalline anisotropy of the AFM layer.

K_{eb} is reduced by a factor of 100 by spreading the energy over an entire domain wall rather than over an atomically sharp interface, as in the ideal interface model. This step provides results consistent with observed values [Mau87]. This model does not explain the

origin of exchange bias at compensated interfaces or offer insights in the mechanism responsible for the reduced exchange energy. The domain wall length required for this reduction is usually larger than the actual thickness of the AFM layer [Mal87]. The partial domain wall model does introduce the important concept of domain formation in the AFM layer as a factor in determining the magnitude of the exchange bias effect.

2.6.3 Random-Field Model

Malozemoff, [Mal87][Mal88], explained the source of the exchange bias effect as originating from the imbalance in the interfacial spins at the AFM/FM interface caused by the interface roughness. The interface roughness results in frustrated bonds at the AFM/FM interface as shown in Figure 2.21a and high interfacial energy. The cross marks represent the frustrated bonds. The amount of the interfacial energy is reduced through the parallel arrangement of the spins in AFM interface layer to the FM layer as seen in Figure 2.21b.

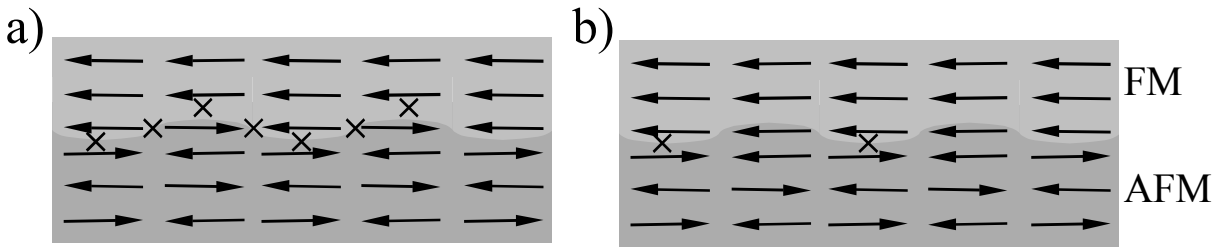

Figure 2.21: Schematic side view of AFM/FM bilayer showing the creation of uncompensated spins at the AFM/FM interface due to interface roughness. a) The anti-parallel alignment results in high energy state, which is reduced through the b) ferromagnetic coupling of the spins in the AFM interface layer to the FM layer.

A net average interfacial energy will exist when averaged over a small number of sites. The magnetization of the AFM film will divide in domain regions to further minimize the amount of interfacial energy. The domain forms perpendicular to the interface in this model in contrast to the partial domain wall model (see previous section). The interfacial energy difference or exchange bias energy is spread over the area of the domain (πaL) where L is the length of the domain wall. The energy per unit area for the reversal of magnetization in the FM layer is given by:

$$K_{eb} = \frac{4zJ_{ex}}{\pi aL} \tag{2.21}$$

where z is the number of order unity for the AFM. With $J_{ex} \approx A_{AFM}/a$ and $L \approx \pi (A_{AFM}K_{AFM})^{1/2}$, equilibrium domain size [Mal87], H_{eb} is changed to the following equation:

$$H_{eb} = \frac{2z\sqrt{A_{AFM}K_{AFM}}}{\pi M_{FM}t_{FM}} \tag{2.22}$$

The random-field model also explained the reduction in the exchange bias energy, but was only applied to case of a single crystal AFM layer. It did nothing to explain the situation in polycrystalline thin films where grain boundaries, vacancies, and other defects are present. The model has also never been experimentally confirmed. It did however introduce the

concept of domain interaction in the AFM layer with defects in the AFM that would be central to later exchange bias models.

2.6.4 Domain State Model

The domain state model proposed by Nowak, et al. [Now00][Now02], explained the existence of the exchange bias effect through the interaction between nonmagnetic defects and the domain walls in the volume of the AFM and subsequent exchange coupling with the neighboring FM layer. The basis theory for the domain state model originated from the study of domain formation and interaction of these domains with defects in diluted Ising antiferromagnets in an external magnetic field [Kle93][Ble93]. According to these studies, it is energetically favorable for the walls of domains to pass through the nonmagnetic defects to reduce the energy for domain wall formation as shown in Figure 2.22.

The domain wall is represented by a solid line where the domain wall passes through the defects represented by the black dots. The magnetization of the individual atoms in the domain, represented by gray arrows. The domain has a total of three uncompensated spins, which leads to surplus magnetization in this part of the diluted antiferromagnet. This domain is surrounded by domains, represented by the black arrows, which have a net magnetization direction that is reversed with respect to the first domain. If this picture is extended to include an infinitely long thin film, the average of the surplus magnetization will however be zero. The domain state in the antiferromagnet can be oriented if the defects in the volume are created under an applied field or if the sample is cooled down below the T_b of the AFM while under an applied magnetic field. This leads to a net macroscopic magnetization in the volume of the AFM.

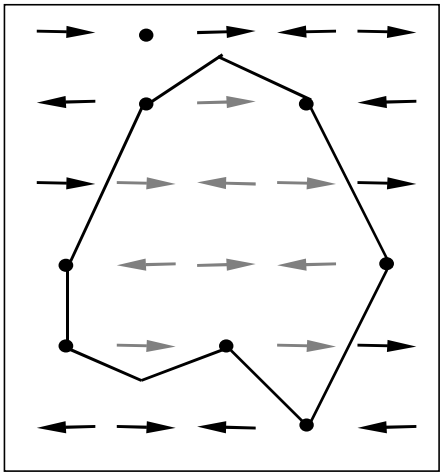

Figure 2.22: Planar overview of diluted Ising antiferromagnet showing the role of defects in domain formation and the creation of uncompensated spins.

The situation becomes even more complex when a FM layer is deposited on top of a diluted Ising antiferromagnet as seen in Figure 2.23. The domains in the AFM layer will now extend from the AFM/FM interface to the bottom of the AFM layer. The spins that are coupling within a domain are represented by the dashed lines. The resulting domain state in the volume of AFM changes the spin arrangement at the interface of the AFM/FM resulting in uncompensated spins at the interface. The uncompensated spins in the domain at the interface, seen in Figure 2.22 will couple with the spins of the neighboring atoms in the FM layer due to a interfacial energy difference. The coupling between the AFM and FM is represented by a solid line. A net surplus magnetization exists at the AFM/FM interface

when the magnetization is averaged over a set number of domains. This leads to the observance of the exchange bias effect. Magnetic linear dichroism has been used to image the domains in both the FM and the AFM layer of AFM/FM bilayers to confirm this hypothesis [Nol00] [Ohl01]. The domains in both layers were found to coincide locally with one another an indication of exchange coupling across the AFM/FM interface.

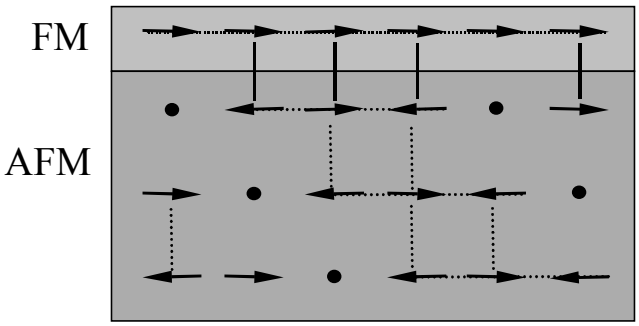

Figure 2.23: Side view of AFM/FM bilayer illustrating the role of defects in domain formation in the volume of the AFM and the subsequent exchange coupling at the AFM/FM interface.

The defect density in the volume of the AFM determines the number of domain walls, the size of the surplus magnetization and the resulting magnitude of the exchange bias effect. The defects present at the AFM/FM interface, such as interface roughness, do not have any influence on the size of the exchange bias effect. The microstructure, which determines the defect density in the volume of the AFM, is the deciding factor that influences the strength of the exchange bias field. This physical model formed the basis of Monte-Carlo simulations that were able to reproduce the magnitude and temperature dependence of the exchange bias effect, and dependence on AFM layer thickness. The algorithms used in the Monte-Carlo simulation and the subsequent simulation results are discussed in detail by Nowak et. al [Now02]

This model was confirmed experimentally by observing the change in H_{eb} as function of volume defect density in a CoO/Co bilayer grown by MBE [Mil00] [Kel02a]. Defects were introduced into the CoO AFM by changing the oxygen partial pressure during the deposition to allow for an excess or deficiency of oxygen in the CoO or by the substitution of Mg for Co during the growth of the bilayer. The interface was protected from a change in defect density by the growth of 0.4 nm thick CoO layer at the interface Co/CoO. This was done prior to the substitution of the Mg for Co or increase in oxygen partial pressure. The H_{eb} was found to increase to a maximum with increase in defect density and then decrease as the loss of long-range order in the crystal lattice destroyed the antiferromagnetic nature of the CoO layer. This model was also experimentally confirmed by the irradiation of NiFe/FeMn bilayers with the He^+ ions [Mew00a] [Mou01a]. The H_{eb} of the of NiFe/FeMn bilayers was found to also increase with the defect density in the AFM and subsequently disappear with further increase in defect density after the loss of long-order in the crystal lattice.

2.7 Synthetic Anti-Ferromagnet (SAF)

The Synthetic Anti-Ferromagnet (SAF) was developed as a variant of the simple spin valve structure to increase the H_{eb} of the spin valve [Hei95][Lea98] [Bea00]. A SAF consists of two ferromagnetic layers separated by a nonmagnetic spacer layer set at 1st antiferromagnetic maximum for the interlayer exchange coupling. The FM layer adjacent to

the AFM layer is still referred to as the pinned layer. The other FM layer in the SAF is referred to as the reference layer. Ru is the standard spacer layer used in the SAF due its higher interlayer exchange coupling in comparison to Cu [Park91c] (see Figure 2.24). The bias direction in the spin valve is now defined by the direction of the magnetization in the reference layer and not that by the pinned layer as is the case with a simple spin valve. The antiferromagnetic coupling between the reference and pinned layer will greatly increase the field required to rotate the pinned layer magnetization in the direction of the applied field. For example an IrMn simple spin valve with an H_{eb} of 45 mT increased to 175 mT upon the incorporation of a SAF in the spin valve stack (see Section 6.2.3.1 and 6.5.7).

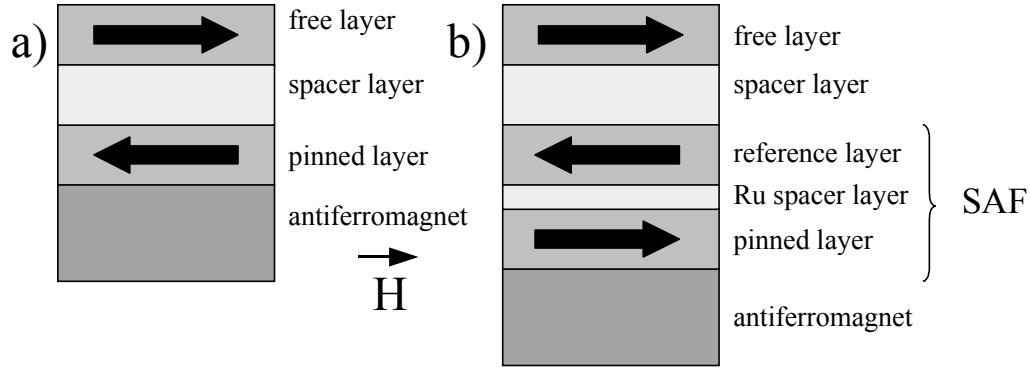

Figure 2.24: Comparison between the structure of a) a simple spin valve and b) a spin valve with SAF.

The source of the increase in H_{eb} of a spin valve with SAF is due to the antiferromagnetic coupling energy J_{SAF} of the SAF. J_{SAF} is usually three to four times larger than K_{eb} of a normal spin valve, which correspondingly leads to the need for a higher field value to change the magnetization direction in the spin valve. H_{eb} had previously described the magnitude of the asymmetry in the MR curve (see Figure 2.12), but this term exclusively applies to the field value necessary to fully rotate the pinned layer magnetization in the direction of the applied field. The bias shift is largely determined by the strength of the antiferromagnetic interlayer coupling on the reference layer. H_{ex} is the measure of the asymmetry of an MR curve measured from a spin valve with SAF and is determined in the same manner as the H_{eb} in a simple spin valve (see Figure 2.25). H_{eb} is now given by the halfway point of the bump in the MR curve as seen in Figure 2.25. The exchange biased pinned layer is still necessary in the SAF, since the bias direction of an unbiased SAF can be reversibly changed upon going into magnetic saturation.

The MR and magnetization behavior as a function of applied field is much more complex than in the case of simple spin valve. The analysis must take into account the magnetization direction of three different FM layers, the pinned layer (PL), the reference layer (RF) and the free layer (FL), exchange biasing of the pinned layer and antiferromagnetic coupling between the reference and pinned layer. The magnetic parameters of the spin valve with SAF, such as H_{eb} or H_e, can be determined from the major loop and minor loop of a MR Curve. The typical MR curve for a spin is presented in Figure 2.25. The positive field direction is the same as the bias direction of the SAF.

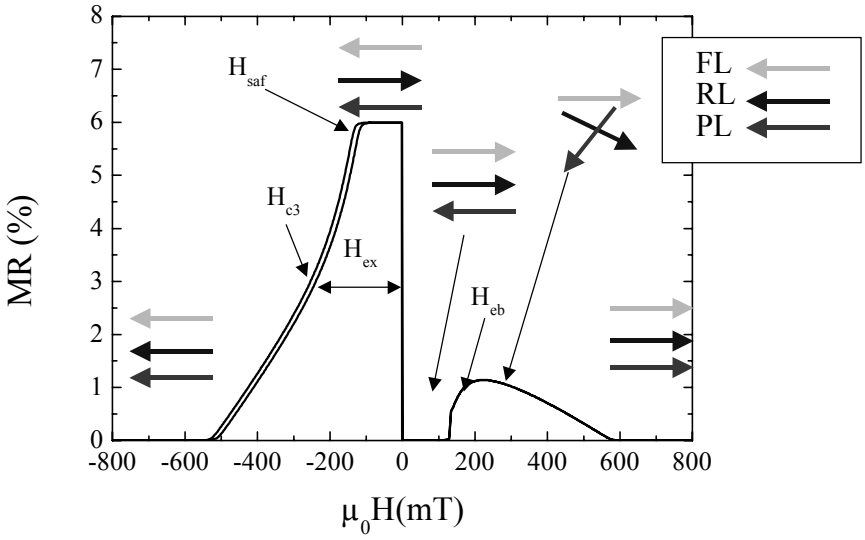

Figure 2.25: MR curve measured from a spin valve incorporating a SAF.

For $\mu_0 H$>-600 mT, the magnetization of each layer are parallel due to the high applied field as shown in Figure 2.25. The MR is at a minimum at this point. As the applied field decreases to intermediate field values, the magnetization in the reference layer goes anti-parallel to the free and pinned layer. The pinned layer remains fixed due to exchange bias effect and the antiferromagnetic interlayer coupling forces the reference layer into the anti-parallel position. The MR rises to a maximum until it levels off. The point at which the plateau region in the MR curve ends is referred to as the antiferromagnetic interlayer coupling field value H_{saf} of the spin valve (see Figure 2.25).

After the field direction switches to positive field direction, the magnetization of the free layer reverses while the magnetization of the reference and pinned layers remains fixed (see Figure 2.25). The MR drops again to minimum while the free and reference magnetizations are parallel to one another. The pinned layer remains fixed by the exchange bias effect. At intermediate field values, the MR begins to rise as seen in Figure 2.25. The H_{eb} of the spin valve has been reached at this point and the pinned layer magnetization begins to follow the direction of the applied field. The reference and pinned layers go through a "scissoring" motion at intermediate fields due to this rotation of the pinned layer while the reference layer will rotate in the opposite direction of the pinned layer due to the antiferromagnetic interlayer coupling across the Ru spacer layer (J_{SAF}> K_{eb}). As the applied field increase to higher values the antiferromagnetic interlayer coupling is overcome by the applied field and the magnetization of the free, reference, and pinned layers are aligned in the direction of the applied field. The MR again drops to a minimum at this point.

Other important magnetic parameters of a spin valve with SAF can be determined from the major loop and minor loop of a MR Curve. The coercivity of the free layer, H_{c1}, and the interlayer coupling H_e are determined the same as with a simple spin valve (see Figure 2.13.) It is important note that H_e is measure of the residual interlayer coupling between the free and reference layers across the Cu spacer layer, not pinned and free layer as in the case of the simple spin valve. The hysteresis measured in the major loop of the MR curve is the coercivity of the reference layer, H_{c3}, and not of the pinned layer (see Figure 2.25). The coercivity of the pinned layer, H_{c2}, can now only be determined from a magnetization measurement as shown in Figure 2.26. The majority of the spin dependent resistance changes occur between the reference and free layer. The coercivity of the pinned layer cannot be directly measured from the MR curve due to this fact.

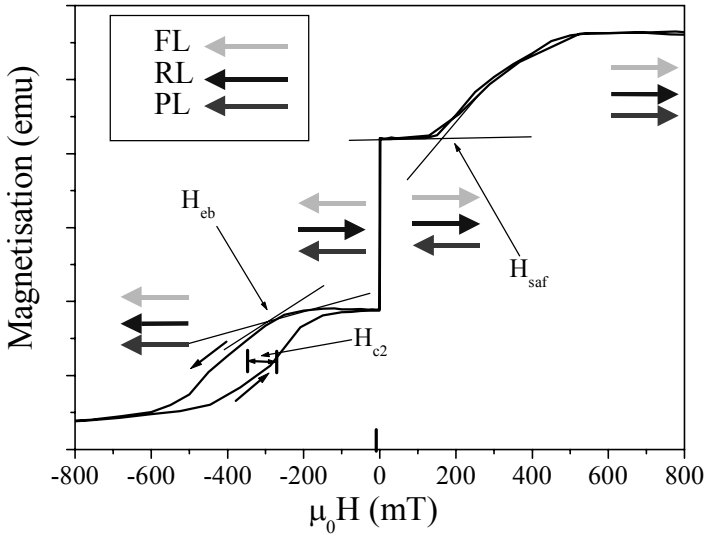

Figure 2.26: Magnetization curve measured from a spin valve incorporating an SAF.

2.8 GMR 360° Angle Sensor

2.8.1 Design of GMR 360° Angle Sensor

Metals typically have a large temperature coefficient resistance, e.g. on the order of 0.1%/K, due to the increase in lattice vibration with the rise in temperature. A wheatstone bridge configuration is used to eliminate the temperature dependence of metallic thin films such as those in a spin valve system and to remove the signal offset typical of single resistance element. Automotive sensors must function in a temperature range from –40°C to 150°C and therefore the resistance changes due to temperature must be taken into consideration. A wheatstone bridge has four identical elements, R_1, R_2, R_3 and R_4 as shown in Figure 2.27. V_B is the applied bias voltage and V_{out} is the output signal from the Wheatstone bridge. The use of four elements with identical resistances compensates for any resistance changes induced by a temperature change.

The V_{out} of a Wheatstone bridge can be described as follows:

$$V_{out} = V_b\left(\frac{R_1 \cdot R_4 - R_2 \cdot R_3}{(R_1 + R_2)(R_3 + R_4)}\right) \tag{2.23}$$

when $R_1 = R_2 = R_3 = R_4$, then V_{out} is zero. A change in a V_{out}, in the ideal case, can therefore only be due to resistance changes induced from effects other than temperature changes

The Wheatstone bridge circuit of a spin valve angle sensor has one important difference to that of a previously described Wheatstone bridge circuit. Each adjacent element in the Wheatstone bridge has the same resistance, but the bias directions in two elements are 180° to the two other elements as shown in Figure 2.27. As a result, this bridge has a bipolar output with the full signal amplitude of a single element.

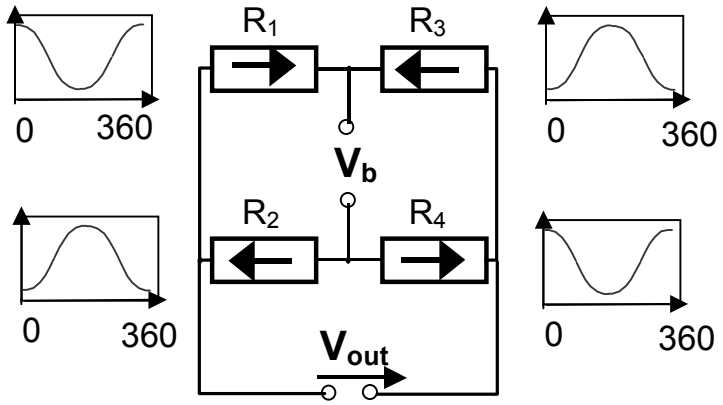

Figure 2.27: Wheatstone bridge circuit design of a GMR angle sensor based on the spin valve system.

Let us now consider the resistance change as a function of θ_H. Since the bias direction in two elements is 180° to one another then two assumptions can be made:

$$\begin{aligned} R_2(\theta_H) &= R_1(\theta_H + 180°) \\ R_1 &= R_4 \text{ and } R_2 = R_3 \end{aligned} \tag{2.24}$$

Inserting this into Eq. (2.23) gives us:

$$V_{out} = V_b\left(\frac{R_1(\theta_H)\cdot R_1(\theta_H) - R_1(\theta_H + 180°)\cdot R_1(\theta_H + 180°)}{[R_1(\theta_H) + R_1(\theta_H + 180°)]\cdot[R_1(\theta_H) + R_1(\theta_H + 180°)]}\right) \tag{2.25}$$

which simplifies to:

$$V_{out} = V_b\left(\frac{R_1(\theta_H) - R_1(\theta_H + 180°)}{R_1(\theta_H) + R_1(\theta_H + 180°)}\right) \tag{2.26}$$

For a 360° angle sensor two Wheatstone bridge elements are required each with two different exchange bias directions. The one Wheatstone bridge is 90° rotated in relation to the other bridge so that one bridge gives cosine output and the other bridge a sine output signal as seen in Figure 2.28. The absolute angle measured by the sensor can then be determined through a standard arctan analysis as follows:

$$\alpha = \arctan\left(\frac{V_{sin}}{V_{cos}}\right) \tag{2.27}$$

where α is the measured angle, V_{cos} is the cosine output signal and V_{sin} is the sine output signal. The sensor error is determined by subtracting the calculated angle from a reference angle.

The output signal from a GMR angle sensor allows the absolute measurement of the angle over 360° while the standard AMR sensors only allow the determination of the angle over 180° [Haa00]. This is due to the π periodicity of the AMR effect as a function of θ_H as seen in Eq. (2.2). This is obvious advantage of a GMR angle sensor.

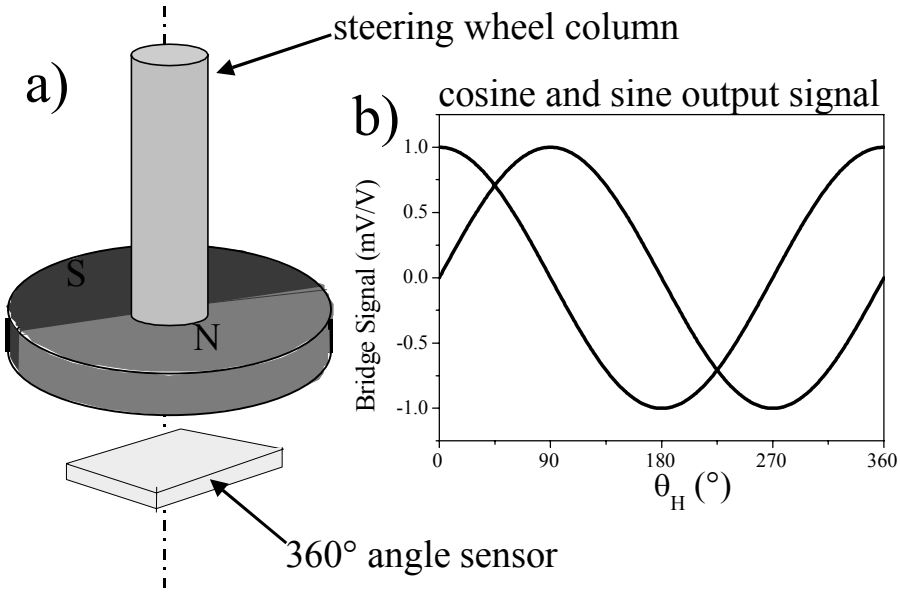

Figure 2.28: a) GMR 360° angle sensor measuring the angle of a steering wheel column and b) cosine and sine output signal of the sensor.

2.8.2 Previous Research on GMR Angle Sensors

A GMR sensor based on a spin valve system has already been explored by many other research groups and companies. These most important milestones in the previous research work are summarized below. Daughton, et al. [Dau94], of Nonvolatile Electronics (NVE) was the first to present results of a GMR sensor based in the Wheatstone bridge configuration using a hard-soft multilayer system [Dau93] in 1994. A Wheatstone bridge configuration was realized by shielding two of the elements with permalloy magnetic shields which acted simultaneously as flux concentrators for the other two elements. The output is unfortunately halved since two of the four elements are inactive and therefore do not contribute to the output signal.

The GMR angle sensors were first reported by Clemens, et al. [Cle97], in 1997. These sensors are based on a hard-soft-multilayer pinned by an Artificial Anti-Ferromagnet (AAF) [dBe96]. An AAF is also referred as an unbiased SAF, which lacks the AFM layer in order to exchange bias one of the FM layers. GMR angle sensors from Infineon, GMR B6 and C6, have been commercially available since 1998 [Inf02]. It is possible to change the bias direction locally in a bridge element via application of a local magnetic field with a write-head similar to those used in HDD. The SAF in the spin valve is brought into magnetic saturation by a write-head, which gives the spin valve the desired bias direction. The bias direction in an SAF however can be reversibly changed by overcoming the antiferromagnetic interlayer exchange coupling between the two FM layers. This limits the operation of the sensor to fields below 20 mT making it unusable in the automotive industry.

Spong, et al. [Spo96], was the first to propose a method for fabricating a GMR sensor based on a spin valve system with a true antiferromagnet. A full Wheatstone bridge configuration is achieved by setting the bias direction of different elements in opposite direction by heating the elements with conductor stripes are deposited on top of a passivation layer. The stripes are set in such a way as to induce a magnetic field in opposite directions in different elements of the bridge. When a large current is sent through the conductor, it simultaneously generates a magnetic field and heats the AFM layer above its T_b. The current setting method is inherently limited by the strength of the magnetic field that can be generated and by the temperatures, only to 150°C, that can be achieved by this method.

2.8.3 Advantages of a GMR 360° Angle Sensor

A GMR 360° angle sensor based on a exchange-biased spin valve system offers several advantages over the existing AMR angle sensors. The applied magnetic field required for operation of an GMR angle sensor is five times smaller than that required for the AMR angle (20 mT vs. 100 mT) to achieve the same sensor error. A high magnetic field is required for an AMR sensor to reduce the sensor error caused by the form and crystal anisotropy. The need of a lower strength magnetic field for sensor operation allows for use of cheaper iron ferrite magnets in comparison to the more expensive NdFeB permanent magnets used in AMR sensors.

The inherent limitation of the AMR effect to an 180° angular range requires the use of a switchable magnetic field generated inside the sensor element to allow angle determination over 360°. The Application Specific Integrated Circuit (ASIC) required for the AMR 360° angle sensor is very complex due to this signal shift of the bridge signal, and is therefore high in cost. The simplicity of the output signal of the GMR angle sensor, cosine and sine with 360° periodicity, allows for a simpler ASIC and further cost reduction. The GMR 360°angle sensor also has a higher MR effect than AMR angle sensors (6% vs. 3%) giving a higher signal-to-noise ratio and allowing for larger airgap tolerances.

Experimental Methods

3.1 Sputter Deposition

Sputter deposition belongs to a class of basic deposition techniques referred to as Physical Vapor Deposition (PVD). PVD includes any deposition technique that uses evaporation or collision impact, e.g. sputtering, to cause atoms from a molten or solid source to enter the gas phase in a reduced pressure environment and subsequent deposition on a substrate [Ohr92]. Examples of other PVD methods also include MBE and Ion Beam Deposition (IBD) [Ohr92]. Sputter deposition is a cost-effective and simple method for the deposition of metallic thin films on Si substrates typically used in the semiconductor industry. This technique centers on the use of plasma to create ions, normally Ar^+ ions, which strike a negatively charged target of a certain material. Neutral atoms are dislodged from the target due to momentum transfer and are subsequently deposited on a substrate that lies in typically in line-of-sight of the target. Metallic thin film alloys grown by PVD deposition tend to form metastable phases that are homogeneous in composition with very few precipitates [Ohr92].

3.1.1 The Sputtering Process

The simplest form of a sputtering system consists of a single vacuum chamber with a single substrate holder and one target as seen in Figure 3.1. The substrate lies under the target during the deposition and usually is on a special, rotating substrate holder. Typical sputtering systems have one or more vacuum chambers and multiple targets. The first step in the sputtering process is the pumping of the vacuum chamber to a base pressure of 10^{-5} mbar. After sufficient vacuum pressure is achieved, a charge gas is necessary for formation of the plasma flows into the vacuum chamber. A noble gas, such as Ar, is typically used as the charge gas in the sputter deposition. It is possible to create plasma with Ar through the application of voltage in the 0.3-3 kV range between the cathode, target, and the anode, substrate holder.

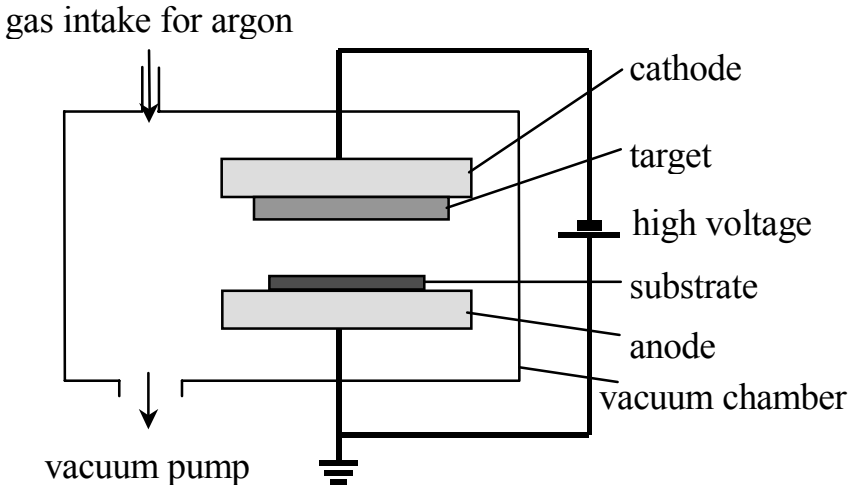

Figure 3.1: Example of a dc sputtering system.

Very little current flows at first due to the small number of charge carriers in the system after the initial application of the voltage. After there is a sufficient number charge carriers, the free electrons will strike the Ar neutrals to create an Ar^+ ions and more free electrons. The newly created free electrons can now ionize additional Ar neutrals thus multiplying the number of Ar^+ ions. The Ar^+ ions in the plasma will be accelerated in direction of the cathode and strike the target. The neutral target atoms are dislodged by the collision with the Ar^+ ions and then deposited on all surfaces in line-of-sight of the substrate. The collision processes of the Ar^+ ions with the neutral argon gas and the target create additional Ar^+ ions in the plasma. The creation of additional charge carriers makes the plasma self-sustaining. A constant voltage is only necessary for sustainment of the plasma.

Two types are mainly used in the sputtering process: Direct Current (dc) and Radio Frequency (RF). RF current refers to the application of an ac signal to the electrodes during the sputtering process. RF sputtering is necessary to sputter dielectric materials such as NiO. Dielectrics have a high resistance that results in charging of the target when only direct current is used. The application of an ac signal is achieved by capacitively coupling the electrodes to a RF generator. The RF voltages can be coupled through any kind of impedance; therefore, the electrodes need not be conductors to be used in sputter deposition.

3.1.2 Magnetron Sputtering

Magnetron sputtering was developed to increase the thin films deposition rates of sputter deposition. The simplest way to increase deposition rates is to increase the Ar partial pressure, but this leads to the incorporation of more Ar^+ ions in the deposited thin film. A second way is to increase the mean free path of the free electrons in the plasma. The longer the free electrons remain in the plasma the higher the collision probability and the number of Ar^+ ions [Ohr92]. This leads to a higher deposition rate without the need to increase the Ar partial pressure.

The mean free path of the electrons in the plasma can be lengthened by placement of permanent magnets on the backside of the target to create a magnetic field with a field direction parallel to the target as seen in Figure 3.2. This is referred to as the magnetron principle [Ohr92]. Normally the free electrons proceed in a linear path through the plasma; however, the Lorentz force of the magnetic field imparts a helical motion to the electrons. The free electrons are held near the cathode as seen in the case of a planar magnetron (see Figure 3.3). This is often visible as a halo effect around the target during sputtering. DC magnetron sputtering allows the sputter deposition at lower Ar partial pressures and lower

discharge currents than conventional DC sputtering. It also has the additional benefit of reducing the amount of bombardment of the substrate with free electrons.

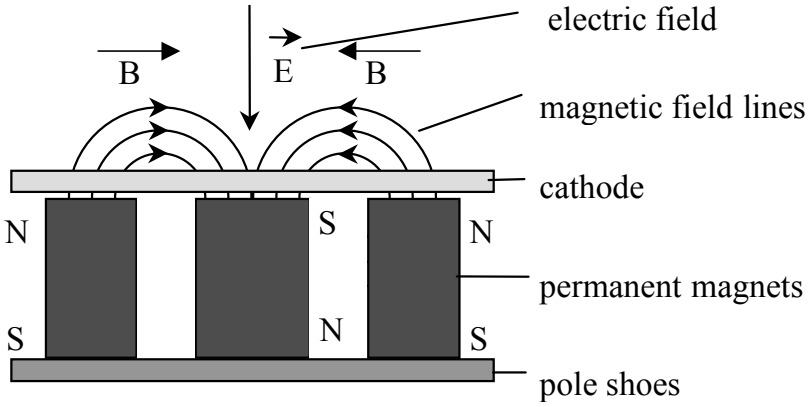

Figure 3.2: Sideview of a cathode in the dc sputtering system showing the placement of the permanent magnets in the dc magnetron configuration.

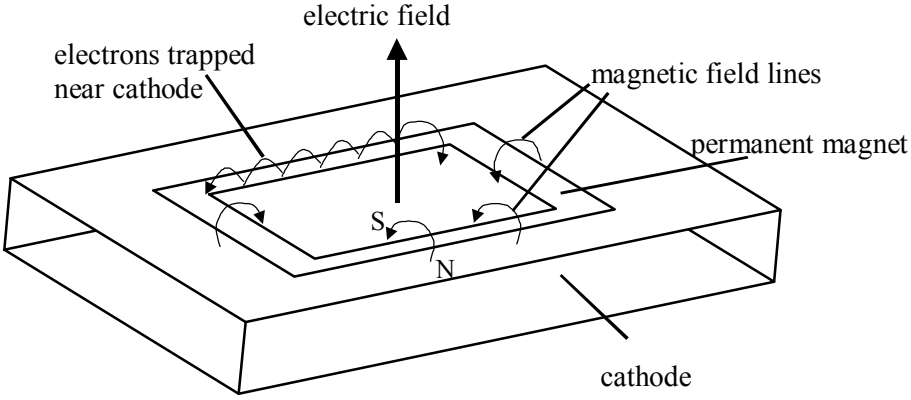

Figure 3.3: View of planar magnetron showing the helical motion of the free electrons near the permanent magnets placed in the cathode.

3.1.3 Unaxis Cyberite Sputtering System

Most of the spin valve thin films analyzed in the framework of this dissertation were deposited with a Unaxis Cyberite sputtering system (see Figure 3.3) by the project partner IPHT-Jena [Mat00]. Spin valve samples deposited on other sputtering systems will be noted in the Results and Discussion section. Most spin valve systems consist of ultrathin layers (1-10 nm) consisting of up to eight different materials which require UHV conditions prior to deposition to prevent the incorporation of detrimental contaminants in the spin valve stack. The Cyberite system was especially designed for the demands of the deposition of GMR multilayer systems used in read heads and MRAM devices. The Cyberite can be considered representative of state-of-the-art sputtering system used for the deposition of spin valve stacks.

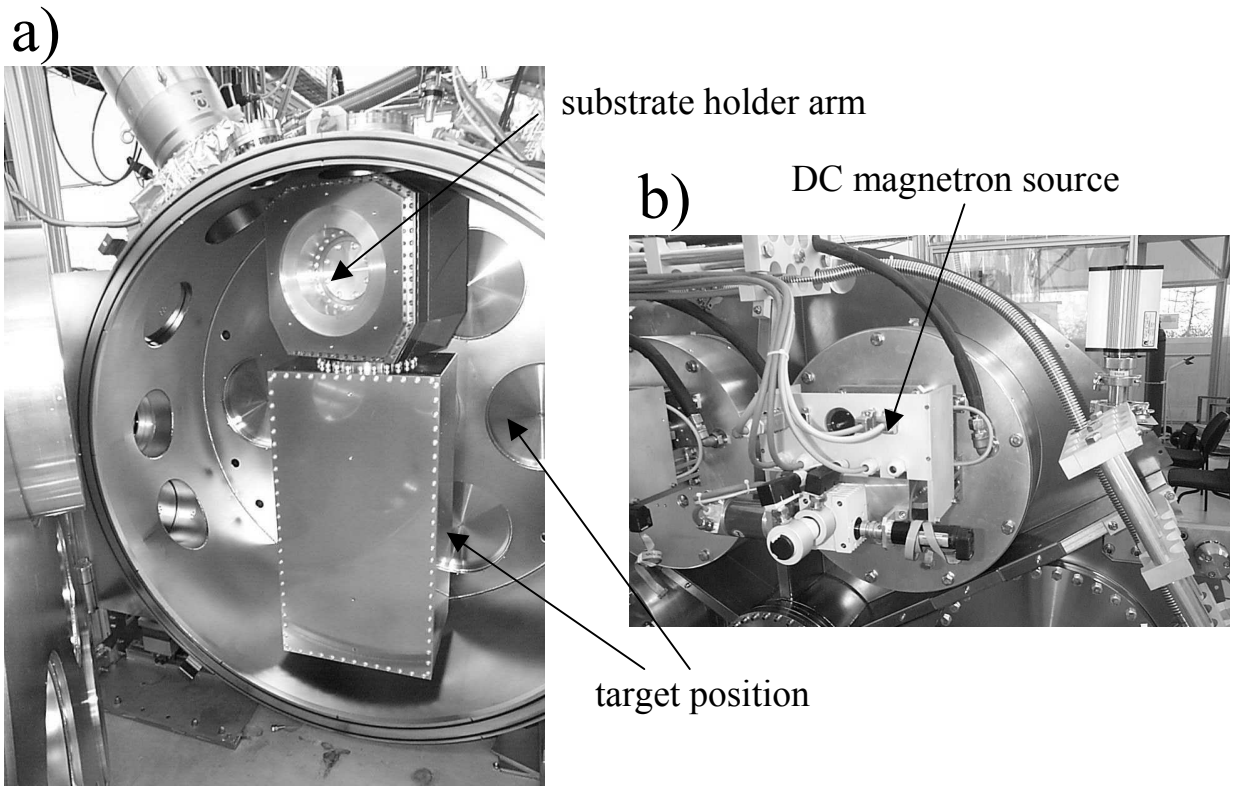

Figure 3.5: View of the Unaxis Cyberite sputtering system with a) the open sputter chamber with substrate holder arm and b) the UHV-compatible dc magnetron source.

3.1.4 Spin Valve Deposition Conditions

The spin valve samples were deposited on thermally oxidized 4" or 6" Si (100) wafers. The SiO_2 layer was approx. 1µm in thickness. Every wafer was cleaned with acetone, isopropanol, and deionized water prior to the sputter deposition. Each sample was sputtered in a magnetic bias field of 5 mT to induce a bias direction in the pinned layer and a uniaxial anisotropy in the free layer. The base pressure prior to the begin of the sputter deposition was typically on the order of 10^{-5}mbar. The base pressure during deposition was set at 5×10^{-3} mbar. $Ni_{81}Fe_{19}$ was the standard NiFe alloy composition and $Co_{90}Fe_{10}$ was the standard CoFe alloy composition used in every spin valve stack. The structure of each spin valve stack studied in the framework of this dissertation is listed in Table 9.1. Any special facts regarding the deposition of a particular spin valve stack will be discussed in relevant Section in the Chapter 6: Results and Discussion.

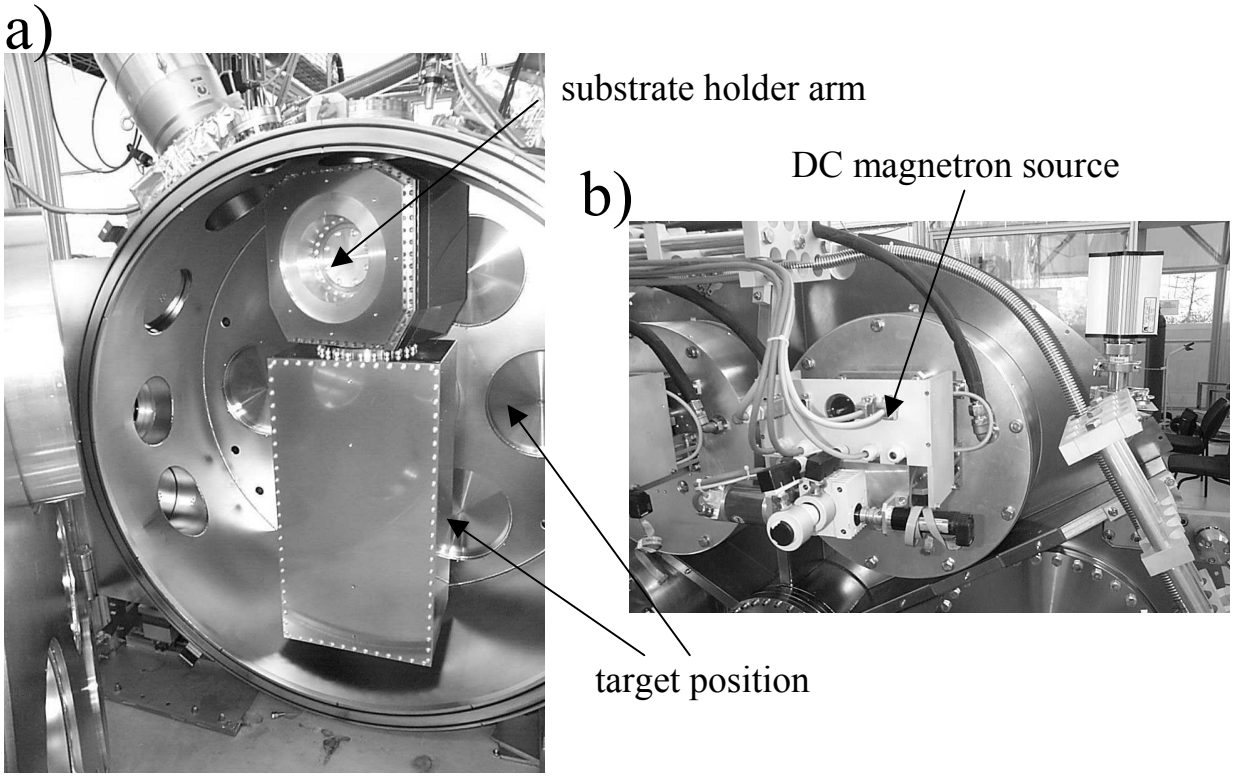

Figure 3.5: View of the Unaxis Cyberite sputtering system with a) the open sputter chamber with substrate holder arm and b) the UHV-compatible dc magnetron source.

3.1.4 Spin Valve Deposition Conditions

The spin valve samples were deposited on thermally oxidized 4" or 6" Si (100) wafers. The SiO_2 layer was approx. 1µm in thickness. Every wafer was cleaned with acetone, isopropanol, and deionized water prior to the sputter deposition. Each sample was sputtered in a magnetic bias field of 5 mT to induce a bias direction in the pinned layer and a uniaxial anisotropy in the free layer. The base pressure prior to the begin of the sputter deposition was typically on the order of 10^{-5}mbar. The base pressure during deposition was set at 5×10^{-3} mbar. $Ni_{81}Fe_{19}$ was the standard NiFe alloy composition and $Co_{90}Fe_{10}$ was the standard CoFe alloy composition used in every spin valve stack. The structure of each spin valve stack studied in the framework of this dissertation is listed in Table 9.1. Any special facts regarding the deposition of a particular spin valve stack will be discussed in relevant Section in the Chapter 6: Results and Discussion.

3.2 Excimer-Laser

3.2.1 Theory and Basic Design of a Laser

A laser is defined as a device that emits coherent and monochromatic radiation in a highly directional beam [Hec86]. A review of the physics of both spontaneous emission and stimulated emission are critical to achieving an understanding of the basic operating principles of a laser. Spontaneous emission occurs when an electron is raised from the ground state to an excited state through, for example, the application of a current, microwave excitation or the absorption of photons from a laser [Bas01]. The electron will only remain for a short time in this excited state (10^{-8} s) before dropping back down to the ground state [Bas01]. A photon will be emitted when the electron drops back to the ground state.

Stimulated emission occurs when photons interact with electrons in the excited state. This interaction causes a photon emission coherent with the initial photon. This can only occur if a population inversion exists between the electrons in the ground state and excited state [Hec86] [Bas01]. This greatly decreases the probability of the absorption of the emitted photon by neighboring atoms. This makes stimulated emission the only option for the release of the photon energy. This population inversion must be maintained and controllable over long periods of time to allow for practical application of stimulated emission, e.g. a laser.

Most of the lasers developed in the past forty years consist of four basic components as shown in Figure 3.6. These components are the laser medium, energy reservoir, the laser pump and the laser resonator. The laser medium is the material that is the source of the stimulated emission. This medium can either be a gas mixture (KrF), crystalline solid (Nd:YAG) or semiconductor thin film (GaAs) [Bas01]. The energy reservoir supplies the needed energy for excitation of the laser medium and is typically supplied directly from the main power grid. A laser pump is the discharge source for the “pumping” or excitation of the laser medium needed for stimulated emission. An UltraViolet (UV) light, microwave or rf source or voltage discharge through electrodes are typical examples of discharge sources for laser pumps [Bas01]. The energy can be directly supplied to the laser medium in the case of continuous wave lasers. This is done to enable uniform stimulated emission rather than a cascading effect in the laser medium.

A laser resonator is used to generate a coherent, highly directional laser beam. A resonator consists of an optical feedback system of mirrors. The example shown in this case consists of a front and back mirror (see Figure 3.6). The mirrors are arranged opposite to one another to force the radiation to oscillate between the two mirrors. The back mirror is totally reflective while a part of the front mirror is partially transparent to allow part of the radiation to escape to form the laser beam.

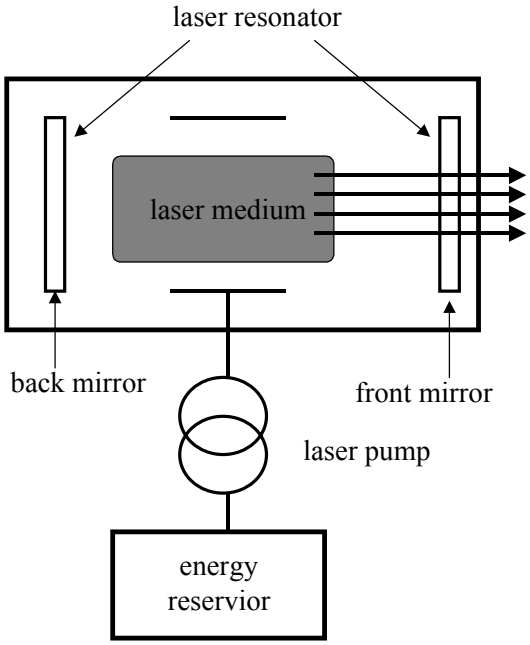

Figure 3.6: Schematic showing the four basic components of a laser.

3.2.2 Excimer Lasers

Excimer lasers are high energy pulsed gas lasers that emit photons at the ultraviolet wavelengths [Bas01]. The term "excimer" is a abbreviation for "excited dimer", which is the active medium in an excimer laser. An excited dimer is a molecule containing two identical atoms that exist only in an excited state. This definition has been expanded to include any diatomic molecule that only exists in the excited state. The excimer gas mixture consists of a 80-90% buffer gas, such as Ne, that serves as the energy transfer media and a rare-gas-halide mixture, such as Kr/F_2, as the active medium. Pulsed lasers, such as the excimer laser, require the use of a capacitor for the discharge of the energy into the laser medium. A capacitor is used so the high voltage discharge into the gas mixture can occur on a short time scale. This is necessary to achieve the short pulse times, 8-250 ns, of pulsed lasers.

The excitation process of a excimer dimer is very complex. KrF dimers are used as an example to explain this process. The outer electron shell for Kr is full at the beginning of the excitation process so it is not possible to form electron bonds between a Kr atom and F atom in the ground state. The Kr and F atoms must therefore be ionized by UV light, X-ray irradiation, or an electric discharge to allow for the bonding between Kr and F. After ionization the Kr^+ and F^- ions can bond with one another to form a dimer molecule. The creation of a KrF dimer molecule is summarized below:

$$\begin{aligned} e^- + F_2 &\rightarrow F^- + F \\ e^- + Kr &\rightarrow 2e^- + Kr^+ \\ Kr^+ + F^- + Ne &\rightarrow KrF^* + Ne \end{aligned} \tag{3.1}$$

A F^- ion, a F neutral, Kr^+ ion and an additional free electron are created in the discharge [Bas01]. The voltage difference between the cathode and anode imparts a high kinetic energy to the Kr^+ and F^- ions. Neon atoms are present in the gas mixture to act as a transfer partner for the high kinetic energy of the Kr^+ and F^- ions, otherwise a KrF molecule could not be formed. The KrF^* molecule will immediately drop back down to the ground state after molecule formation emitting a photon at the 248 nm wavelength. It is important to frequently

refill the excimer laser with the Kr/F_2 gas mixture, since Kr/F_2 gas degrades over time. A Micromachining Station Exitech 7000 equipped with a LPX 210 excimer laser (see Figure 3.7) was used to irradiate the spin valve samples. This excimer laser was located in Department FV/FLD at the corporate R&D center of Robert Bosch GmbH. The LPX 210 excimer laser can emit at two different wavelengths through the use of two different gas mixtures: argon fluoride or krypton fluoride. The two different wavelengths are 193 nm (ArF) and 248 nm (KrF). The spin valve samples were irradiated only at the 248-nm wavelength.

Figure 3.7: Micromachining Station Exitech 7000 with LPX 210 excimer laser.

3.2.2.1 Determination of the Laser Energy and Magnet Holder

The Exitech 7000 excimer laser is especially suited for the local heating of patterned spin valve samples on a µm scale. This excimer laser was originally designed for the patterning of metallic NiCr thin films for pressure sensors and the crystallization of amorphous silicon in Thin Film Transistors (TFT) for use in flat screen displays [Bas01]. The laser irradiation is done through a mask similar to those used in photolithography in the semiconductor industry. The use of sample stage with x, y, and z alignment controllers and a high resolution CCD camera allows precise control of the laser beam on a µm scale (see Figure 3.8). This allows the irradiation of selected areas on a patterned spin valve sample necessary for the later fabrication of demonstrator GMR angle sensor element.

The energy of the laser beam can be varied through use of a two-mirror attentuator placed in the path of the laser beam in Figure 3.8. The trajectory of the laser beam is modified by the transmission through the first mirror and then brought back to the correct trajectory through the use of the 2nd mirror. The energy of the laser beam is reduced through reflection at the first mirror. The laser beam has a uniform energy density due to the use of a homogenizer lens array. The lens array filters out any part of the laser beam that is not at the same trajectory as the majority of the laser beam. For determination of the laser energy density, the laser beam is projected through the energy determination window of the mask, which has a set area. The filtered laser beam is focused to ¼ the original beam size after the discharge with an objective lenses to increase the laser energy. An energy detector is placed in the path of the laser beam just below the focal to measure the energy per pulse. The energy of the laser beam is measured over 10 pulses to obtain an averaged value. The laser energy is

typically listed is as a percent value of maximum laser energy to allow direct comparison with other types of lasers.

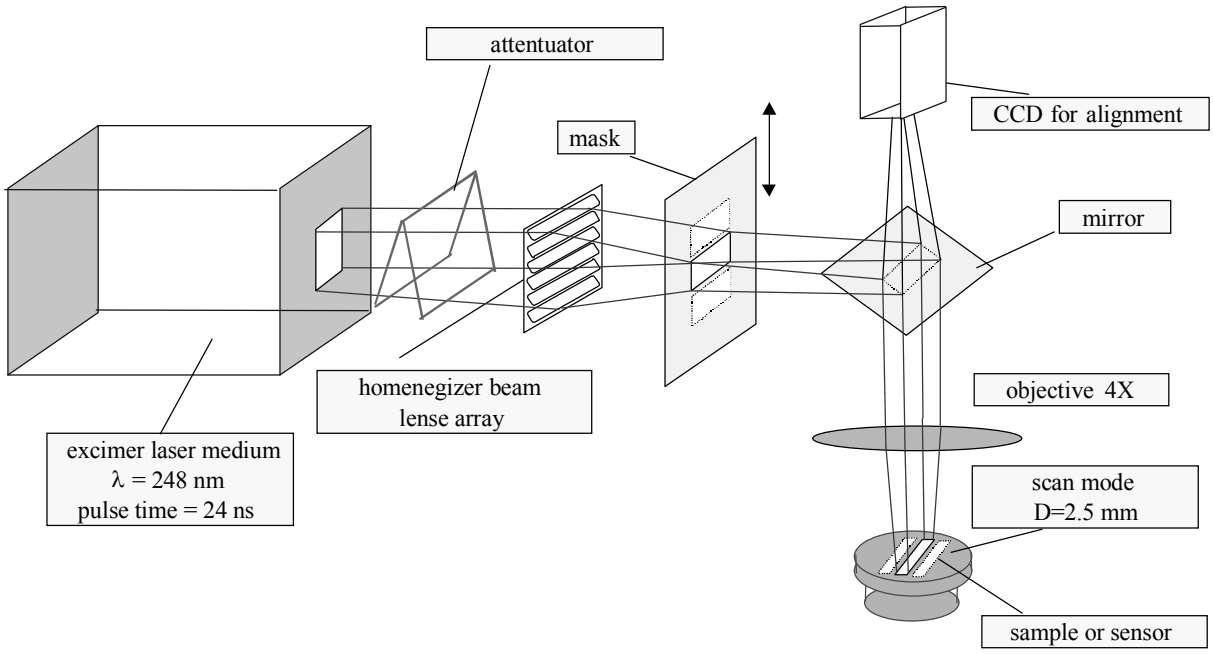

Figure 3.8: Schematic of the basic internal structure of the excimer laser illustrating the use of the attentuator, mask and scanning mode to irradiate samples accurately on the μm scale.

The only option for the application of a magnetic field during the laser irradiation was through the use of two NdFeB permanent magnets. The magnets were placed with the north and south poles in the same direction to create a magnetic field with a homogeneous field direction as seen in Figure 3.9. The wafer sample or chip is then placed between the two magnets. The field strength could be varied from 10-300 mT by adjusting the distance between the two magnets. The magnetic field strength is determined with use of a portable magnetometer. The excimer laser can scan in 2 mm steps after each laser pulse to allow the irradiation of an entire wafer sample, 10 mm by 10 mm in size. The irradiation of large wafer samples is necessary to allow the study of the changes in microstructure induced by the laser-writing with methods such as XRD or AES.

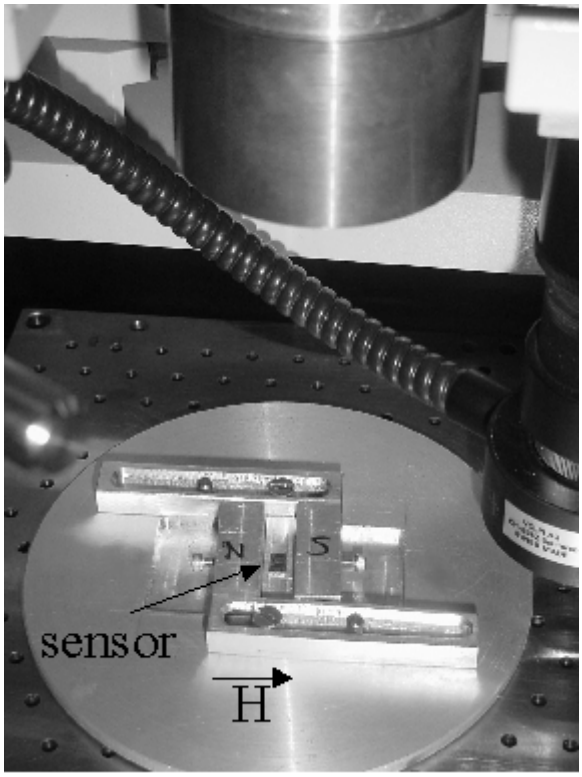

Figure 3.9: Picture of the permanent magnet holder located under the objective lenses of the excimer laser. This holder is used to supply applied magnetic field during the laser-writing. The location of the sample, in this case a sensor, is indicated in the picture.

Characterization Methods

4.1 Magnetoresistance measurements

4.1.1 Four-Point Probe

The measurement of the electrical resistance of spin valve thin films is done through the use of a four-point measurement probe. A four-point probe consists of four feather-tipped metal pins placed in a row, separated from each other by the same distance d as illustrated in Figure 4.1. A constant current I_0 is run through the outermost pins 1 and 4 and the voltage V_0 are measured at the innermost two contacts 2 and 3. According to Ohm's Law:

$$V_0 = I_0 \times R_{sample} \tag{4.1}$$

If I_0 is held constant and there is a resistance change in the sample, there will be a proportional change in the V_0. The resistance of thin films can easily be measured with this method.

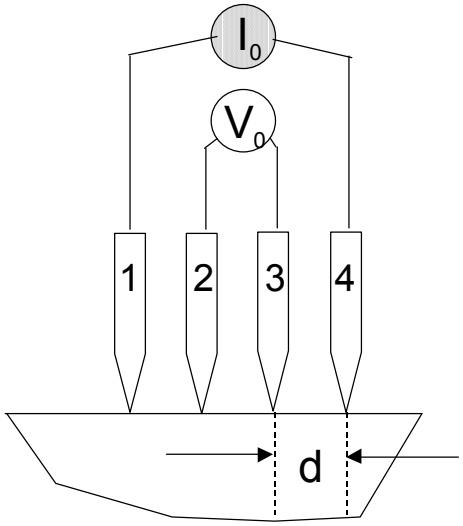

Figure 4.1: 4-point probe used for the measurement of electrical resistance in thin film samples.

This circuit arrangement can be duplicated in patterned stripes of spin valve samples structured by standard photolithography techniques. An example is shown in Figure 4.2. I_0 is applied to pads 1 and 4 while the I_0 is measured at pads 2 and 3.

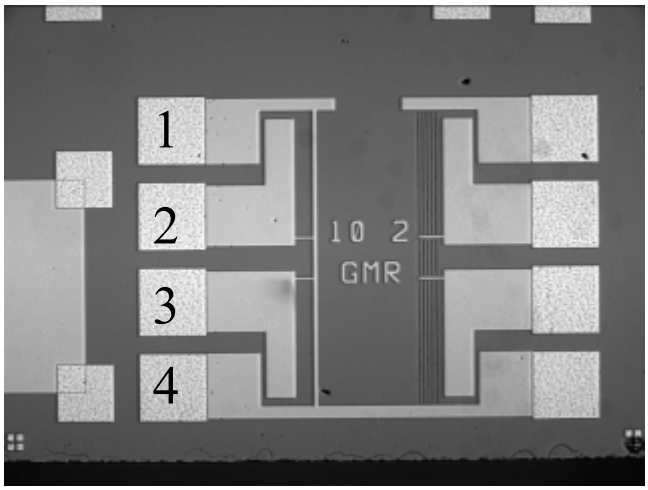

Figure 4.2: Test structure in the form of single stripes structured from a spin valve stack in the four-point probe circuit arrangement.

4.1.2 Measurement Setup

MR measurement setups at Corporate R&D center of Robert Bosch GmbH in Stuttgart were used to determine the field dependence of MR effect in a spin valve. The MR measurement is used to determine the MR effect, H_{eb}, H_e and many other magnetic parameters of a spin valve system. A MR measurement apparatus representative of those used at Robert Bosch is shown in Figure 4.3. The 4-point probe with the sample holder is placed between the electromagnet coils, and the applied magnetic field is generated by applying a current through the electromagnet coils. The applied magnetic field strength can be changed by varying the amount of current through the coils.

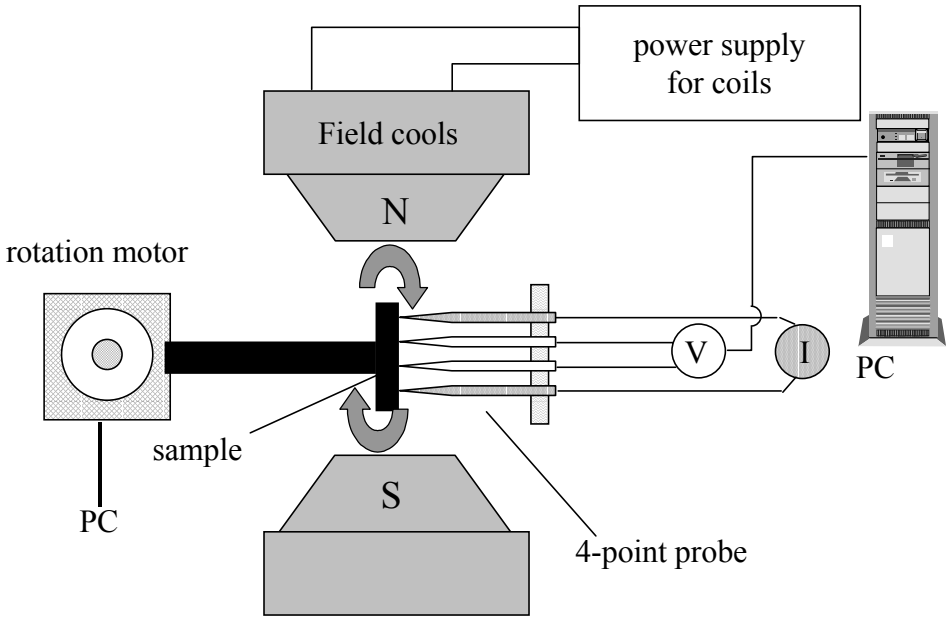

Figure 4.3: Representative setup used for measurement of the magnetoresistance of thin films sample as a function of applied magnetic field strength and direction.

Separate measurement setups w/o iron cores in the electromagnets were available for the MR measurements. The electromagnet coils with an iron core can generate fields up to 600

mT, but have the disadvantage of a high remanence of the iron core. This can introduce a hysteresis in an MR measurement near zero field, which makes it difficult to have accurate minor loop MR measurement near zero field. This problem is overcome through the use of Helmholtz coils, coils without an iron core. Helmholtz coils induce a magnetic field without this remanence effect, but can only generate magnetic fields up to 25 mT. A rotation motor attachment allowed the measurement of the resistance as a function of angle at a constant applied field. A heating stage attachment enabled the heating of a wafer sample or chip up to 170°C during the MR and MR rotation measurements.

The GMR effect can be measured in two different geometries. One geometry is with the current direction in the plane of the thin film (CIP: Current In Plane) while the other with the current direction perpendicular to the plane of thin film (CPP: Current Perpendicular to Plane). MR measurements done in the CPP geometry typically have a larger GMR effect than those measured in the CIP geometry; however, measurements in the CPP geometry are technically irrelevant due to the extremely low intrinsic resistance values [Coe96]. All MR measurements presented in this dissertation were done in the CIP geometry. The typical sample size for the MR measurements was a 10 mm by 10 mm wafer piece cut from a single wafer or test stripes 20 μm in width.

4.1.3 Analysis of the MR Rotation Curves: Amount of Cosine Deviation

An accurate determination of the amount of cosine deviation in a MR rotation curve is a critical step in the development of an angle sensor. The amount of angular error in a GMR angle sensor is direct related to the amount of cosine deviation in a MR rotation curve. The identification of the magnetic parameters of a spin valve that influence the amount of cosine deviation as a function of applied field would be an important measure in reducing the sensor error.

The analytical method used to determine the amount of cosine deviation is a variation of the arctan analysis used with AMR and GMR angle sensors to determine the angular error (see Section 2.8.1). A cosine and a sine signal are required for the arctan analysis of a signal; however, there is only a single MR rotation curve, only one signal, measured from a single sample at a given field strength. Performing two sets of rotation measurements 90° in phase to one another would simply double the amount of necessary measurements. A simpler way around this problem was to create a 2nd signal (sine signal can be created from the original MR rotation curve (cosine signal). The resistance data of the original MR rotation curve was shifted 90° in phase to the angle data in order to create a 2nd date set (sine signal).

The calculated angle θ_{cal} from the arctan analysis of the cosine and sine signal is given by first removing the offset in the resistance in both signals. The arctan of the cosine and sine signals is then taken to give θ_{cal} as shown below:

$$\theta_{cal} = \arctan\left(R_{orig+90°} \Big/ R_{orig} \right) \tag{4.2}$$

where R_{orig} is the resistance value from the original data set and the $R_{orig+90°}$, is the resistance value from the data set that was shifted 90°. This is directly analogous to Eq. (2.27), which is used to determine to measured angle from a 360° angle sensor.

The amount of cosine deviation CD is determined by the taking the difference between the reference angle θ_{ref} of the original rotation and calculated angle θ_{cal} by the arctan method at a given angle as seen in the following:

$$CD = \theta_{ref} - \theta_{cal} \tag{4.3}$$

The cosine deviation is plotted over the entire measurement range of 360° as seen in Figure 4.4. The maximum cosine deviation ΔCD is the quantity quoted throughout the text of this dissertation. The quantity ΔCD is a standard deviation term (±°) that centers around zero (see Figure 4.4). This type of analysis allows a direct comparison between MR rotation curves of different amplitudes (MR effect) and measured at different applied field strengths. Every MR rotation curve is also fitted with a cosine function based on Eq. (2.9) to allow for a better visualization of the cosine deviation. The cosine fit has no relation to determination of the cosine deviation.

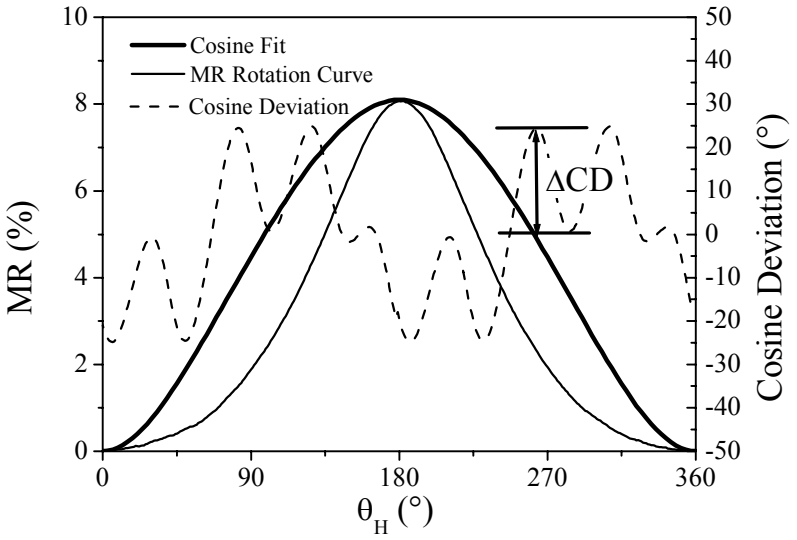

Figure 4.4: Example of a rotation curve with cosine deviation plotted as a function of applied field direction.

There are several important reasons for using the arctan analysis rather than plotting the deviation of the MR rotation curve from the cosine fit. First arctan analysis allows a comparison between the angular error from an angle sensor and the cosine deviation of an unpatterned sample or single sensor elements on a test chip. The arctan method determines the cosine deviation in terms of degrees while taking the difference from the cosine fit would only give the deviation in terms of %MR. This is not a useful quantity when relating the cosine deviation to the angular error calculated from an angle sensor. It is not possible to invert the measured signal to the deviation in terms of degrees, because of the discrete nature of the measured signal. Most importantly the arctan method determines the difference in cosine only in terms of the deviation from cosine independent of the rotation curve amplitude.

4.2 Structural Characterization

4.2.1 X-Ray Diffraction

The crystal structure, lattice constants and texture of polycrystalline thin films can be determined through the use of X-ray Diffraction (XRD). The conditions necessary for the reflection of a X-ray in a single crystal or polycrystalline material are summarized in Bragg's Law as derived by the British physicists Sir W.H. Bragg and his son Sir W.L. Bragg in 1913 [Cul78]. Bragg's Law explains how the cleavage faces of crystals appear to reflect X-ray

beams at only certain angles of incidence Θ to the surface of the crystal [Cul78]. An X-ray beam is diffracted when it strikes an atom site periodically arranged in a lattice plane as presented in Figure 4.5. At most angles of incidence destructive interference occurs between the diffracted X-ray. No X-rays will be detected at these angles of incidence. At a few angles of incidence, related to the lattice parameter of the crystal, constructive interference takes place between the diffracted X-rays (see Figure 4.5). This results in the appearance of interference maxima when the conditions, as described by Bragg's Law, are fulfilled as summarized below:

$$n\lambda = 2d_{hkl}\sin\Theta \tag{4.4}$$

where d_{hkl} is the distance between atomic layers in a crystal, lattice constant, λ is the wavelength of the incident X-ray beam and n is the order of the interference maxima.

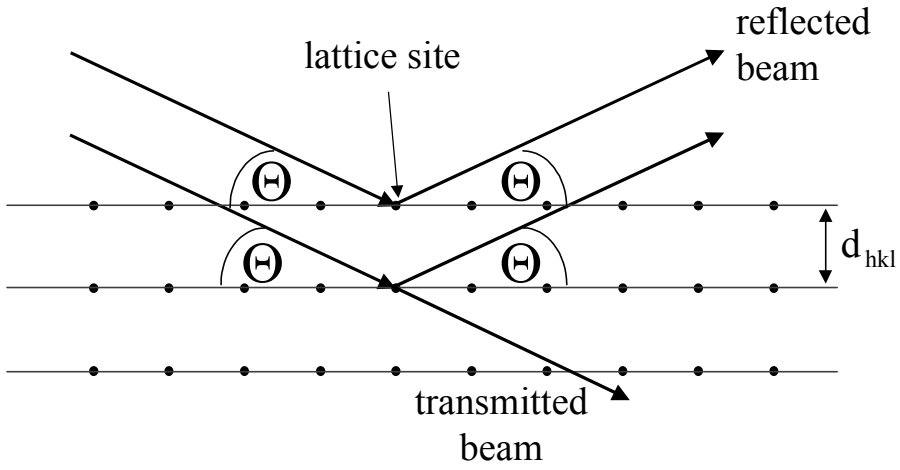

Figure 4.5: Diffraction of an X-ray beam from crystal lattice according to Bragg's Law.

One typically measures the reflected X-ray beam over a large incidence angle range (10° < 2Θ < 180°). A detector is rotated about the sample to measure the intensity of the reflected X-rays as shown in Figure 4.6. This allows one to determine to lattice constant, crystallinity, and texture of sample by comparison to tabulated diffraction spectra data [JCP96].

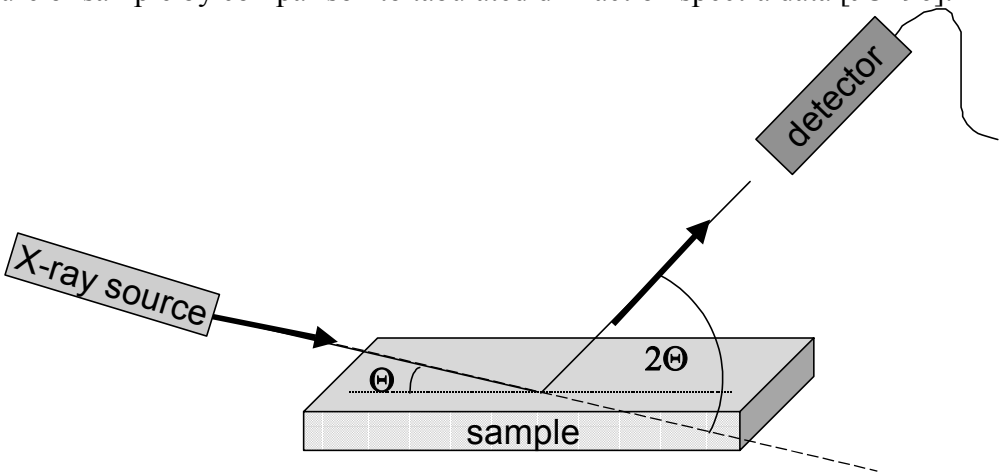

Figure 4.6: X-ray diffractometer showing the X-ray source, sample, diffraction of the X-rays from the sample and the detector.

The measurement setup used for XRD in thin films is different than the normal Bragg-Brentano geometry for normal X-ray diffractometers. The penetration depth for the normal geometry is 1-2 μm. The spin valve stacks are usually only less than 100 nm in thickness. This means that a strong substrate peak is always present in the Θ-2Θ scans in the low angle regime, which obscures the signal from a thin film. A constant angle of incidence is used during the measurement to remove this problem. Since the focus properties of the Bragg-Brentano geometry is lost, a soller slit is positioned in the diffracted beam. This arrangement allows only parallel X-rays to enter the flat monochromator in the scintillation detector. The low angle of incidence of the X-rays leads to a much lower penetration depth of the X-rays and reduction of any possible substrate signals.

The XRD diffraction patterns were made on a Siemens D5000-Diffractometer with a Cu – K_α-beam (λ = 0.154056 nm). The X-ray diffraction measurements were made at a voltage setting of 40 kV and beam current of 30 mA.

4.2.2 X-Ray Reflectometry

X-Ray Reflectometry (XRR) is a well-known, nondestructive method used to evaluate thickness, density and interfacial roughness of an ultrathin layers with very high degree of accuracy [Hua93][Zor94][dBo95]. In XRR the measurement of the reflected X-ray is made in the low angle regime, e.g. 2Θ<6° in comparison to the angle regime of normal XRD. The continual change of the beam angle in this geometry leads to the appearance of interference maxima and minima in the X-ray diffraction pattern as seen in Figure 4.7.

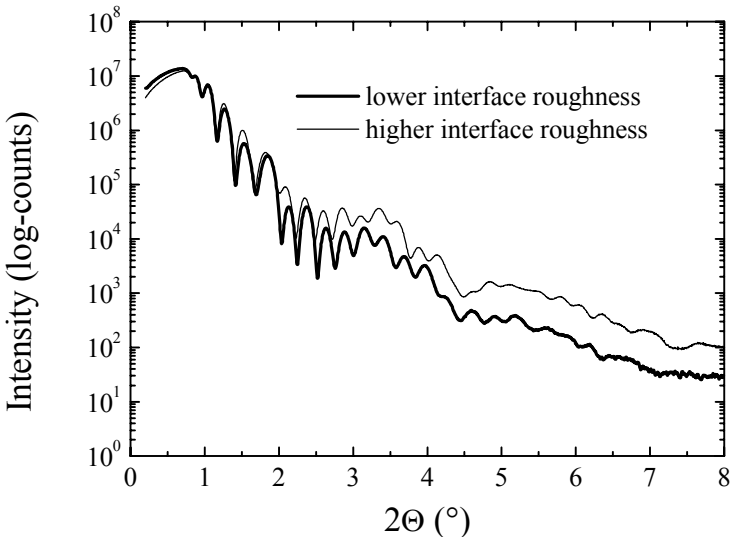

Figure 4.7: A X-ray reflectometry measurement showing the intensity difference that results from an increase in interface roughness in a spin valve sample.

The appearance of these maxima and minima can easily be explained by examining the case of a single layer on a substrate when the angle Θ is above the critical angle total reflection Θ_c. One part of the beam is transmitted through the thin film and part of this transmitted beam is reflected at the interface between the thin film and the substrate. This reflected beam interferes with the reflected beam from the surface, which results in the appearance of Kiessel fringes.

The X-ray beam in the low angle regime is very sensitive to interface layer thickness and interface roughness as long as the x-ray scattering vector is always perpendicular to the surface. A change in the layer thickness results in a change in the spacing between the maxima and minima. An increase in the interface roughness results in a loss in intensity and

clarity, peak to trough height, of the oscillation peak of the reflectometry measurement. The specularly reflected intensity ideally follows the Fresnel law of optics, which for larger angles of incidence, falls off rapidly with increase the roughness parameter [Hua93].

XRR measurements were performed with a Seifert PTS four-circle diffractometer. Primer to the sample, bend x-ray mirror, and a slit system were used to provide a parallel x-ray beam. On the secondary side another slit system and a graphite monochromator separated the Cu K_α radiation. The X-ray source operated at 40 kV and 40 mA during the measurement. A beam width of 0.1 mm, the width of the sample and the size of the slit system were taken into account to generate an adequate fit. The interface roughness σ was calculated using the Nevót-Croce model [Nev80].

4.2.3 Auger Electron Spectroscopy

Auger electron spectroscopy (AES) identifies elemental compositions of surfaces by measuring the energies of Auger electrons. It is a widespread method used for the compositional analysis of surfaces, thin films and interfaces [Bri83][Ert85]. Typical samples studied by AES include both raw semiconductor materials and finished electronic devices. Electron beams disperse into small volumes, typically 1×10^{-12} cc, when striking a material. X-rays are emitted from most of this volume. Auger electrons arise from very small volumes, about 3×10^{-19} cc [Ohr92]. Auger electrons fail to emerge with their characteristic energies if they originate from deeper than 1-5 nm in the thin film. This characteristic of the Auger process makes it very surface specific. For example AES can distinguish between Si, SiO_2, SiO and Si_3N_4 in a 10 nm layer on a silicon wafer [Ohr92].

The basic Auger process starts with removal of a inner shell electron to form a vacancy as depicted in Figure 4.8a. Several processes are capable of producing the vacancy, but bombardment with an electron beam is the most commonly used method. A second atomic electron from a higher shell fills the inner shell vacancy and energy is simultaneously released (see Figure 4.8b). A third electron, the Auger electron, escapes carrying the excess energy in a radiationless process. The process of an excited ion decaying into a doubly charged ion by ejection of an electron is referred to as the Auger process. For low atomic number elements, the most probable transitions occur when a K-level electron is ejected by the primary beam, an L-level electron drops into the vacancy, and another L-level electron is ejected. Higher atomic number elements have LMM and MNN transitions that are more probable than a KLL transition [Bri83].

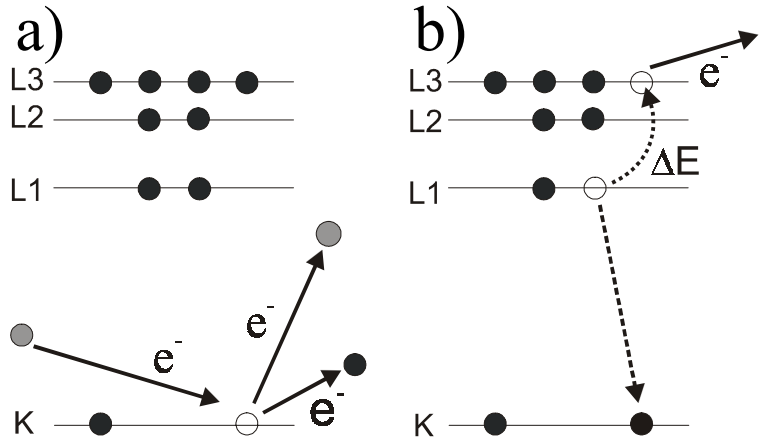

Figure 4.8: The Auger process where a K inner shell electron is removed a) by another electron and b) a L3 shell electron drops down to fill the vacancy.

Qualitative analysis by AES depends on identification of the elements responsible for the various peaks in the spectrum. The Auger electron energies are widely tabulated for all elements in the periodic table [Mul97]. Auger electron peaks are proportional to elemental concentrations; however, it is seldom possible to measure concentrations from first principles. Several instrumental factors such as primary beam energy, sample orientation and the energy resolution and acceptance angle of the analyzer influence the Auger peak heights. The chemical state of element, e.g. oxidation state, also influences the process of elemental analysis. Additionally, the secondary and backscattered electrons have broad energy distributions that tail into the Auger region. The sum of these interfering signals is much greater than the Auger signals. Auger display algorithms use differentiation to enhance the signal [Ohr92].

To analyze samples in depth, Auger instruments incorporate ion beam sputtering to remove material from the sample surface. This is referred to as AES depth profiling. One cycle of a typical depth profile consists of sputtering a small increment into the sample, stopping, measuring relevant portions of the Auger spectrum and elemental quantification of the measured AES spectrum. The sharpness of the peak signals for each element, where the transition from layer to layer appears, can be blurred due to various sputter effects such as backscattering of the elements and sputtered induced roughness. Other thin film characteristics such as interface roughness can also causing blurring of the AES signal leading to inaccuracies in the depth profiling measurements. The AES analytical detection limits for determination of the concentration is 0.01-1%.

The atomic concentration C_A of a given species in a matrix of m elements in the AES depth profiling is determined as follows :

$$C_A = 100\% \frac{I_A / RSF_A}{\sum_{i=1}^{m} I_i / RSF_i} \tag{4.5}$$

where RSF_i is the measured relative Auger sensitivity factor for that particular element and matrix, and I_i is the intensity of the Auger line.

The AES depth profiling measurements presented in this dissertation was done on a Auger Microprobe PHI1660 (Physical Electronics USA) located at IFW-Dresden. The primary electrons were set at 10 keV impinging at an angle of 30° to the surface normal and measurement area of 100x100 μm^2 during the AES depth profiling. The samples were sputtered with electron current 100 nA, incident angle of the electrons 30,. The sputtering of the samples was done with Ar^+ ions at an incidence angle of 60° with an energy of 1.5 keV. The corresponding etch rate was 3 nm/min. The sample rotation during the depth profiling was done with use of a PRE2000 sample holder. The concentration was determined with the sensitivity factors as given by the AES producer [Mul97]. An LLS fit was performed during the measurement to remove the added intensity due to the peak overlap of the 3d-transition metals (Fe, Co, Ni) [Bau01].

4.3 Magnetic Characterization

4.3.1 Alternating Gradient Magnetometer

An Alternating Gradient Magnetometer (AGM) has considerable advantages over other magnetometers such as a Vibrating Sample Magnetometer (VSM) or a Superconducting

Quantum Interference Device (SQUID) [Fla89] [Gra00]. It is 1000 times more sensitive than a VSM making it ideal for the characterization of magnetic thin films and has the same space requirements. In comparison to a SQUID, it is much easier to mount a sample in a AGM since there is no need for liquid helium to maintain the temperature of the Josephson junction in the SQUID. It is also not necessary to perform the magnetization measurement data point to data point. This considerably lessens the measurement time in comparison to SQUID [Fla89] [Gra00].

An AGM consists of, in the simplest form, a cantilevered rod incorporating a piezoelement that is mounted between two magnetic coils [Gra00]. The magnetic sample in an AGM is mounted on the end of the cantilevered rod as seen in Figure 4.9. The sample is subjected simultaneously to a dc field and a small alternating field gradient. The alternating field gradient exerts a force on the magnetic sample that is proportional to the magnetic moment of the sample and the strength of the alternating field gradient. The piezoelement in the rod detects the deflection in the sample due to the AC field and delivers an output voltage signal that is proportional to the deflection.

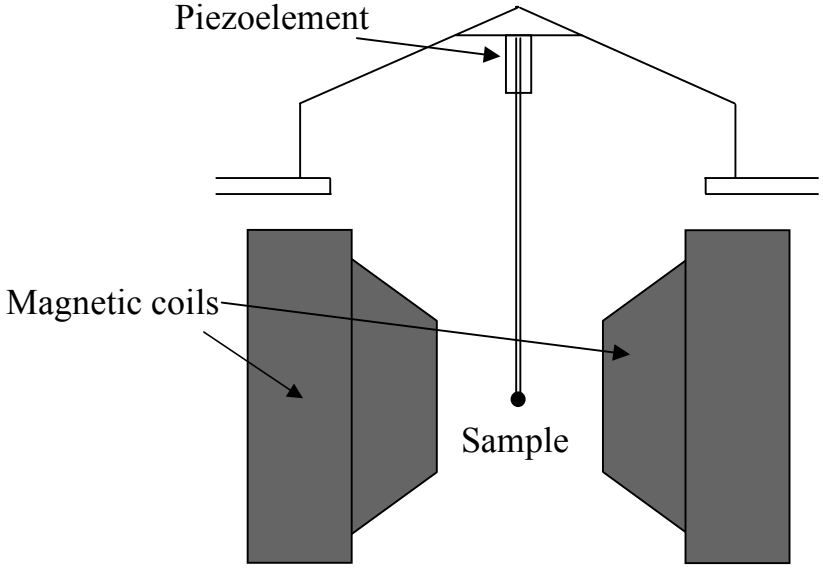

Figure 4.9: AGM measurement setup for showing the piezoelement, magnetic coils, and the placement of the sample between the coils.

The magnetic moment of individually magnetic layers can be determined through a magnetization measurement, which gives the effective magnetic layer thickness of a ferromagnetic material. Any microstructural changes that result in a change in layer thickness would result in a change in the magnetic thickness of the individual layers, which would be detected by the AGM measurement. An additional advantage of AGM is the ability to observe changes in the magnetic moment of the samples such as the magnetization reversal of the pinned layer in a spin valve with SAF at large fields.

4.3.2 Magnetic Optical Kerr Effect

The Magnetic Optical Kerr Effect (MOKE) is an optical technique that can measure, relatively, the magnetization in nm thick ferromagnetic thin films, can be easily set up on a single optical bench and has a sensitivity rivaling that of a SQUID magnetometer. This technique only requires an external magnetic field and access to the sample for the optical beam [Arn97]. The MOKE technique is based upon use of the Kerr effect, which was discovered by Kerr in 1876 [Ker77]. When polarized light propagates through a magnetized

material, off-diagonal elements of the dielectric tensor can modify the polarization state of the light. This is manifested as a rotation of the primary axis of polarization, the Kerr rotation, and a change in the ellipticity of polarization, Kerr ellipticity. The size of these effects can be related to the average sample magnetization through the matrix elements, which is related to the magneto-optical constants of the ferromagnetic thin film. Therefore, if the polarization state of the incident light is known or prepared prior to incidence, the magnetization direction can be obtained by analyzing the polarization of reflected or transmitted light.

MOKE measurements are performed in reflection geometry as shown in Figure 4.10 with an externally applied field to allow hysteresis curves to be obtained. Depending on the preferred magnetic axis of the sample, the field may be perpendicular to the film plane, with the light at normal incidence (polar geometry) or parallel to the film plane, with the light incident at 20-30° (longitudinal geometry). The incoming polarization state is prepared to be either s- or p-linear polarization by the polarizer. The reflected light goes through an analyzer, an additional polarizer, oriented to give the maximum intensity change per degree of polarization rotation.

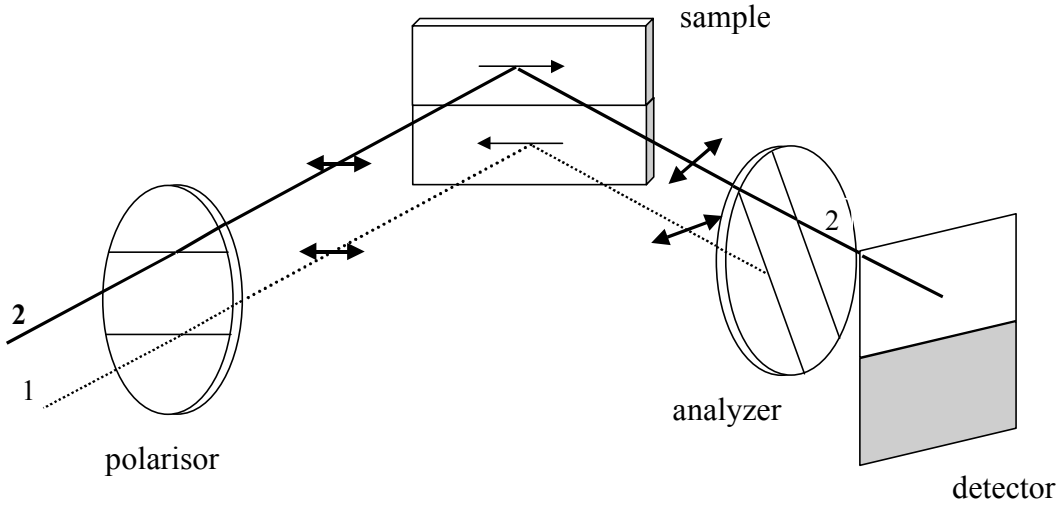

Figure 4.10: Standard MOKE measurement setup including a polarizer, analyzer and detector.

A laser usually provides the source of the polarized light, which is more than sufficient in intensity, but still requires some form of intensity stabilization. Typically a lock-in detection technique with an incident-intensity modulator is often used to improve the signal-to-noise ratio for very thin films [Arn97]. MOKE is most often used as a probe of hysteretic properties or relative magnetization trends, rather than as a quantitative measure of magnetization and not to measure the magnetic moment of spin valve thin films.

Stoner-Wohlfarth Model: Spin Valve Systems

This Chapter is devoted to a detailed description of a macroscopic magnetic model used to simulate the magnetic behavior of the spin valve system under the influence of an applied field. This model allows the calculation of the spin-dependent resistance and magnetization changes in a spin valve system as a function of both the applied field strength and direction. The first section centers on the effect of an applied field on the magnetization of a single ferromagnetic layer as a function of applied field strength. The free energy model for both a simple spin valve and spin valve with SAF are presented in the following two sections. These models formed the basis for a program that allowed the simulation of the MR curves and MR rotation curves measured from different spin valve systems studied in this dissertation [May02].

5.1 Applied Field Influence on Ferromagnetic Thin Film

The influence of a magnetic field on the magnetization in a ferromagnetic film can be simulated through use of the single domain assumption in the Stoner-Wohlfarth model [Sto48]. The magnetization of a single layer is described as a collective vector in the single domain assumption. The single domain assumption describes the magnetization reversal process for a thin ferromagnetic film through a coherent rotation rather than magnetic domain formation. During the magnetization reversal of the ferromagnetic thin film, the magnitude of the magnetization remains constant, but the direction of the magnetization is given by the free energy term.

The effect of the applied field on the magnetization of a single ferromagnetic layer, based on the above assumption, can be mathematically presented as follows:

$$E_H = \mu_0 H M_{FM} t_{FM} \cos(\theta_M - \theta_H) \tag{5.1}$$

where E_H is the free energy term per unit area for the applied field, H is the strength of the applied field, M_{FM} is the saturation magnetization of the ferromagnetic layer, θ_M is the angle of the magnetization of the ferromagnetic layer and t_{FM} the thickness of the layer. All free energy terms are given in J/m^2.

5.2 Model Description: Simple Spin Valve

A free energy model based on the one-domain assumption has been previously used to simulate the magnetic interaction between the different ferromagnetic layers in a simple spin valve [Nis95][Par95]. This model involves the summation of the free energy terms for the applied magnetic field, interlayer coupling and unidirectional anisotropy for each layer as a

function of the magnetic field. A global minimum is sought for the free energy of the entire system to determine the position of the magnetization for each ferromagnetic layer. This model was modified by Dieny, et al. [Die00], to allow the calculation of the spin-dependent resistance changes in a spin-valve, but with the external field fixed in one direction and does not include uniaxial anisotropy terms. The model was further refined by Tietjen, et al. [Tie02], to include uniaxial anisotropy free energy terms. This change in the model allowed the use of an arbitrary number of ferromagnetic layers and a variable direction of the applied field. The ability to vary the direction of the applied field allowed the simulation of MR rotation curves.

The free energy model for a simple spin valve includes the following terms: the applied field influence on the free layer E_{Hf} and pinned layer E_{Hp}, the unidirectional anisotropy in the pinned layer E_e, the interlayer coupling between the free and pinned layer E_{int} and the uniaxial anisotropy in the free layer $E_f^{uniaxial}$ and pinned layer $E_p^{uniaxial}$. This is summarized below for the case of unpatterned simple spin valves:

$$E_T = E_{Hf} + E_{Hp} + E_{eb} + E_{int} + E_f^{uniaxial} + E_p^{uniaxial} \tag{5.2}$$

where E_T is the total free energy of the entire system.

The free energy model can be expanded to show the relationship between the layer thickness of the ferromagnetic thin films and the direction and strength of the applied field by inserting appropriate equations for each free energy term: Eq. (2.18) for E_{Hf} and E_{Hp}, Eq. (2.17) for E_{eb}, Eq. (2.15) for E_{int}, Eq. (2.11) for $E_f^{uniaxial}$ and Eq. (2.13) for $E_p^{uniaxial}$. The total free energy is now expressed as follows:

$$\begin{aligned} E_T(\theta_p,\theta_f) = &-HM_p t_p \cos(\theta_p - \theta_H) - HM_f t_f \cos(\theta_f - \theta_H) \\ &- K_{eb}\cos(\theta_p - \theta_p^{unidirectional}) - J_{int}\cos(\theta_p - \theta_f) \\ &+ K_p^{uniaxial}\sin^2(\theta_p - \theta_p^{uniaxial}) + K_f^{uniaxial}\sin^2(\theta_f - \theta_f^{uniaxial}) \end{aligned} \tag{5.3}$$

The direction of the magnetization for the pinned layer and free layer can no longer be determined by finding the global minimum of the entire system. There are now several local minima in the system due to the introduction of the uniaxial anisotropy term to the model. The θ_p and θ_f must now be varied in small steps, $\delta\theta$, where the variation is represented by the vector $\vec{v} \in \{-1,0,1\}$ where –1 means to shift clockwise, 0 to remain at the same angle, and 1 to shift counterclockwise [Tie02]. The vector is chosen that reduces the entire system to the lowest free energy state. This procedure is repeated for every change in field direction and strength.

The direct calculation of a resistance change due to the spin-dependent scattering is accomplished by the incorporation of an extra scattering term proportional to $(1-\cos(\theta_{i+1}-\theta_i))$ for an unlimited number of layers [Tie02]. The spin-dependent scattering is a function of the angle between the magnetization in the i-th layer and the i+1-th layer. If there are more than two ferromagnetic layers, the scattering is assumed to be independent between the other layers. The whole system must be regarded as one material rather than as the parallel connection of single GMR resistors [Ele01]. The resistance change due to the GMR effect, ΔR_{GMR}, is therefore the sum of all of the resistance changes:

$$\Delta R_{GMR} = \sum_{i=1}^{N-1} \Delta R_{GMR}^{i} \left(1 - \cos(\theta_{i+1} - \theta_i)\right) \tag{5.4}$$

where ΔR^{i}_{GMR} are fit parameters for the resistance change due to the GMR effect between the i-th and the i+1-th layer as determined from the experiments.

The layers for Eq. (5.4) must be defined to determine the spin-dependent resistance changes. Layer 1 is the pinned layer and Layer 2 is the free layer. The resistance change due to the spin dependent scattering in a simple spin valve is given by substituting in θ_p and θ_f into Eq. 5.5 for direction of magnetization for the appropriate ferromagnetic layers, θ_1 and θ_2. $\Delta R_{GMR,}$, now becomes:

$$\Delta R_{GMR} = \Delta R^{p}_{GMR}\left(1-\cos\left(\theta_f - \theta_p\right)\right) \tag{5.5}$$

where ΔR^{p}_{GMR} is the resistance change due to spin-dependent scattering between the pinned and free layer.

5.3 Model for Spin Valve with SAF

The extension of the free energy model to a spin valve system with SAF requires the addition of another ferromagnetic layer to the model. Three new free energy terms must now be defined due to the additional ferromagnetic layer. These are free energy terms for the influence of the applied field on the reference layer E_{Hr}, antiferromagnetic coupling between the pinned and reference layer E_{SAF} and uniaxial anisotropy in the reference layer $E_r^{uniaxial}$. E_{Hr} is analogous to the applied field term presented in Eq. (5.1).

E_{SAF} is calculated in the same manner as E_{int} as seen in Eq. (2.15) as shown below:

$$E_{SAF} = J_{SAF}\cos\left(\theta_p - \theta_r\right) \tag{5.6}$$

where θ_r is the direction of the magnetization in the reference layer. J_{SAF} is always set equal to the exchange interlayer coupling coefficient for Ru at the 1st AFM (J_{SAF} = -7.3×10 Jm^{-2}).

The calculation of $E_r^{uniaxial}$ is similar to that of $E_p^{uniaxial}$ and $E_f^{uniaxial}$ (see Section 2.5.2). This is given below:

$$E_r^{uniaxial} = K_r^{uniaxial}\sin^2\left(\theta_r - \theta_r^{uniaxial}\right) \tag{5.7}$$

where $\theta_r^{uniaxial}$ is the direction of the uniaxial anisotropy in the reference layer and $K_r^{uniaxial}$ is the uniaxial anisotropy constant of the reference layer. $K_r^{uniaxial}$ is given by:

$$K_r^{uniaxial} = \frac{H_{c1}M_f t_f}{4} \tag{5.8}$$

where M_r is the saturation magnetization of the reference layer and t_r the thickness of the reference layer.

The total free energy of a spin valve system with SAF can be summarized by adding the terms E_{Hr}, E_{SAF} and $E_r^{uniaxial}$ to Eq. (5.2) as summarized below:

$$E_T = E_{Hp} + E_{Hr} + E_{Hf} + E_{eb} + E_{SAF} + E_{int} + E_p^{uniaxial} + E_r^{uniaxial} + E_f^{uniaxial} \tag{5.9}$$

The free energy model can be expanded relationship between the layer thickness of the ferromagnetic thin films and the direction and strength of the applied field by inserting appropriate equations into the summation of total free energy shown into Eq. (5.3): analogous term for E_{Hp} from Eq. (5.1), Eq. (5.7) for E_{SAF}, and Eq. (5.8) for $E_r^{uniaxial}$. The total free energy for the spin valve system with SAF can be written as:

$$\begin{aligned} E_T(\theta_p,\theta_r,\theta_f) = & -\mu_0 H M_p t_p \cos(\theta_p-\theta_H) - \mu_0 H M_r t_r \cos(\theta_r-\theta_H) \\ & - \mu_0 H M_f t_f \cos(\theta_f-\theta_H) - K_{eb}\cos(\theta_p-\theta_p^{unidirectional}) \\ & - J_{SAF}\cos(\theta_p-\theta_r) - J_{int}\cos(\theta_r-\theta_f) \\ & + K_p^{uniaxial}\sin^2(\theta_p-\theta_p^{uniaxial}) + K_r^{uniaxial}\sin^2(\theta_r-\theta_r^{uniaxial}) \\ & + K_f^{uniaxial}\sin^2(\theta_f-\theta_f^{uniaxial}) \end{aligned} \tag{5.10}$$

There is one small change to E_{int} term in Eq. (2.15). The residual interlayer coupling was always between the free and pinned layer in the simple spin valve system. In the spin valve with SAF, the residual interlayer coupling is now between the reference and free layer due to the insertion of the additional ferromagnetic layer. θ_r replaces θ_p in the Eq. (5.10) due to this change.

The coefficient K_{eb} cannot be calculated as shown in Eq. (2.17) in the case of a spin valve with SAF. Tietjen, et al. [Tie02], has shown that the antiferromagnetic interlayer coupling together with the unidirectional anisotropy determines the value of H_{eb} as shown below:

$$\begin{aligned} K_{eb} &= \mu_0 H_{eb} M_p t_p + J_{SAF} \\ H_{eb} &= \frac{K_{eb} - J_{SAF}}{\mu_0 M_p t_p} \end{aligned} \tag{5.11}$$

The interlayer coupling does not play a role in the determination of H_{eb} in a simple spin valve while $K_{eb} >> J_{int}$. The situation is different when considering the antiferromagnetic coupling of a spin valve with SAF. H_{eb} is greatly enhanced by the antiferromagnetic interlayer coupling.

Layer 1 is the pinned layer, Layer 2 is the reference layer, and Layer 3 is the free layer. The resistance change due to the spin dependent scattering in a spin valve with SAF, is given by substituting in θ_p, θ_r and θ_f into Eq. (5.2) for the appropriate layers. ΔR_{GMR} now becomes:

$$\Delta R_{GMR} = \Delta R_{GMR}^{p}\left(1-\cos(\theta_r-\theta_p)\right) + \Delta R_{GMR\,r}^{r}\left(1-\cos(\theta_f-\theta_r)\right) \tag{5.12}$$

where ΔR_{GMR}^{r} is the resistance change due to spin-dependent scattering between the reference and free layer. ΔR_{GMR}^{p} is now for the term for the spin-dependent scattering between the pinned and reference layer.

Results and Discussion

The main direction of the research presented in this dissertation was driven by the goal of developing a demonstrator 360° GMR angle sensor and the general specifications for a magnetic sensor as specified by the automotive industry. These specifications dealt with the issues of thermal stability, high signal to noise ratio, and a large magnetic field operation window of the angle sensor. The magnetic field operation window is also referred to as operation window throughout the text of the dissertation. A list of the five most important specifications for the angle sensor application are given below:

1. Operating temperature range: –40°C to 150°C.
2. Magnetic field operation window: 10-100 mT
3. Elevated Temperature: 190°C for short time periods. Sensor must not function at this temperature.
4. Higher signal-to-noise ratio than standard AMR sensors (MR>3%) in the operating temperature range.
5. Angular error: ±1°

Three primary objectives were set in this dissertation considering the goal to develop a demonstrator GMR 360° angle sensor that could operate under the aforementioned conditions. The experimental results were analyzed for both the scientific and the technological aspects necessary for the fulfillment of these objectives. These objectives are summarized below:

- Identification of the physical effects that cause a deviation from the cosine dependence of the GMR effect in a spin valve.
- Analysis of the thermal stability of five different spin valve systems (NiO, FeMn, IrMn, PtMn, PtMn with SAF).
- Development of a method for local reorientation of the bias direction on a μm scale for use in the fabrication of a demonstrator GMR 360° angle sensor.

The source of deviation factors from the cosine dependence of the angle resistance changes were determined in Section 6.1 through a detailed analysis of the MR rotation curves measured from a test FeMn spin valve system. The complex interplay between the cosine deviation factors (AMR, interlayer coupling, rotation of the pinned layer magnetization) could only be understood through comparison between simulated and experimental MR rotation curves. These experimental results were critical to identifying the magnetic parameters of a spin valve that determine the magnetic operating window in a GMR angle sensor.

In Section 6.2 five different spin valve systems (NiO, FeMn, IrMn, PtMn, PtMn with SAF) are analyzed in terms of their magnetic parameters, MR, H_{eb}, H_e etc., and the temperature dependence of the MR effect and H_{eb}. The temperature dependent measurements were necessary to find a thermally stable spin system for the angle sensor application. XRD was used to analyze the microstructure of each spin valve system. The complex magnetic

behavior of a spin valve with SAF was understood through comparison of MR curves both measured and simulated measured from a PtMn spin valve with SAF prior to and after annealing.

The lift-off (see Section 6.3), ion irradiation (see Section 6.4) and laser-writing methods (see Section 6.5) were all evaluated for their effectiveness in creating four different bias directions on a single chip. The laser-writing method was studied in further detail for later application in the fabrication of a demonstrator GMR 360° angle sensor. The changes in the magnetic properties of the spin valve induced by laser-writing were studied through characterization of the thin films with AGM, XRD, GIXR and AES. The domain state model for exchange bias effect was used to explain the behavior of the exchange bias in both the ion and laser irradiated spin valves. A detailed understanding of the different physical effects present in a PtMn spin valve with SAF (induced uniaxial anisotropy, antiferromagnetic interlayer coupling) was necessary to understand the difficulty in reorienting the bias direction in this particular spin valve system.

6.1 Cosine Dependence: Deviation Factors

The angle dependent resistance changes of a spin valve were analyzed for any possible deviation factors from the expected cosine dependence of the GMR effect. The identification and understanding of possible disturbing influences is critical in determining the maximum magnetic field operating window of a spin valve angle sensor. AMR, interlayer coupling and the rotation of the pinned layer magnetization in the direction of the applied magnetic field were seen as possible disturbing influences prior to the beginning of this study.

The experimental results were confirmed through use of a simulation program based on the previously micromagnetic model described in Chapter 5. Good agreement was found between the experimental and simulated MR rotation curves. A simulation was used to see the complex interplay between the AMR effect, interlayer coupling and rotation of the pinned layer magnetization in the deviation from the cosine dependence of the GMR effect. Both the simulation and experiment results were applied to the analysis of the simulated output signal from GMR 360° angle sensor in the Wheatstone bridge configuration.

6.1.1 AMR Effect

The cosine deviation caused by the AMR effect was studied through detailed analysis of MR rotation curves measured from a FeMn spin valve test system. deposited. This spin valve test system was deposited under a magnetic bias field on 4-inch oxidized Si(100)-wafers by a Shamrock 150 sputtering system The FeMn spin valve stack was of the following structure: $Si/SiO_2/Ta(5)/NiFe(6)/CoFe(1.5)/Cu(2.9)/CoFe(2)/NiFe(2)/FeMn(10)/Ta(5)$. The layer thicknesses are given in nm. The standard alloy composition for the FeMn layer was $Fe_{50}Mn_{50}$. The FeMn spin valve had a MR effect of 8% and a H_{eb} of 30 mT. This spin valve stack is referred to as FeMn 1 in the text to differentiate from the other FeMn spin valves presented later in this section.

6.1.1.1 Separation of the AMR and GMR effect in a Spin Valve

The AMR and GMR effects in a spin valve can be separated using a method proposed by Miller, et al. [Mil93]. This involves changing the bias direction from parallel to current flow to the perpendicular orientation with a field cool while the 4-point probe is still attached to the sample (see Figure 6.1). This removes any problems associated with the changes in the contact resistance due repositioning of the 4-point probe. The field cool method can be applied to either wafer or patterned samples. When the current is set parallel to the bias direction, this measurement orientation is referred to as the // current-bias orientation, and when the current is set perpendicular it is referred to as $\perp$ current-bias orientation. This terminology is used throughout in the rest of this dissertation. The sample needed only to be heated to above 150°C, in the case of FeMn, to change the bias direction. Other spin valve samples (IrMn and PtMn) have too high of a T_b to have the bias direction change with a field cool (sample holder heating limit = 170°C).

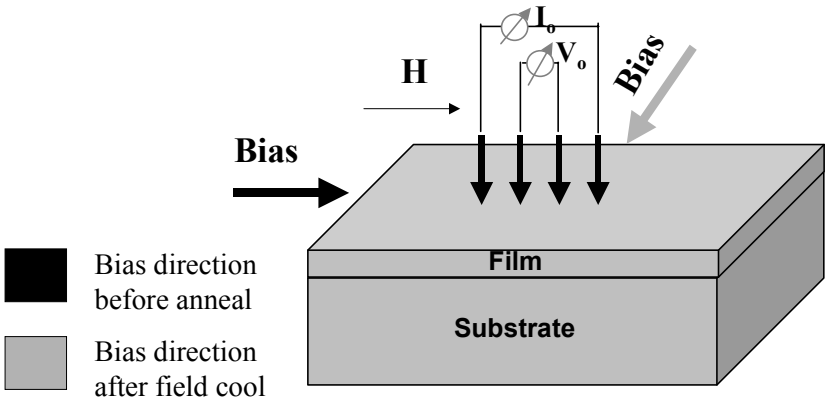

Figure 6.1: The use of a field cool to change the bias direction of a spin valve 90° with respect to the current flow for determination of AMR effect without breaking physical contact with the sample.

The combined AMR effect of the pinned and the free layer can be determined by measuring the minimum resistance in both the // current-bias orientation $R_{min//}$ and the ⊥ current-bias orientation $R_{min\perp}$. These values can be extracted from a normal MR measurement as shown in Figure 6.2a. Bias is the abbreviated term for the bias direction of a spin valve that is used in Figure 6.2 and in all of the following Figures of the Results and Discussion. The AMR effect can then be calculated as follows :

$$\frac{\Delta R}{R} = \frac{R_{min//} - R_{min\perp}}{R_{min\perp}} = \frac{\Delta R_{AMR}}{R_{min\perp}} \qquad (6.1)$$

where ΔR_{AMR} is the change in resistance due to AMR.

The MR measurements are usually made at field strengths far above the saturation field of the spin valve. An MR rotation measurement made at high fields will also give a measure of the AMR effect in a spin valve from the pinned layer and free layer. The AMR effect from only the free layer can be determined through an MR rotation measurement made in both current-bias orientations [Mil93] (see Figure 6.2b). The MR rotation measurement is made at a field strength that is much lower than the H_{eb} so the magnetization in the pinned layer remains fixed and does not contribute to the measured AMR effect.

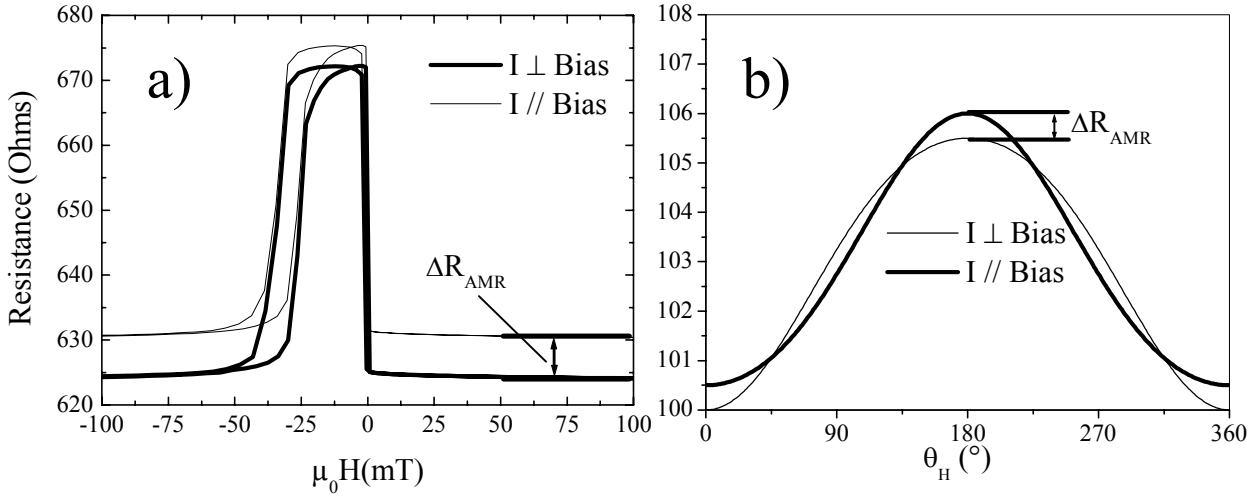

Figure 6.2: a) MR curve and b) MR rotation curve measured from a spin valve sample in both the // current-bias and the ⊥ current-bias orientations.

6.1.1.2 Determination of AMR influence on Cosine Dependence of GMR Effect

The influence of the AMR effect was studied by changing the current axis from the parallel to perpendicular to the bias direction between the rotation measurements. First MR rotation measurements were made in the // current-bias configuration in the range from 1-25 mT field range. A rotation measurement was also made at 100 mT to see the periodicity of the AMR effect in each current-bias orientation. The bias direction was then shifted 90° by a field cool and the same set of MR rotation measurements were repeated for the ⊥ current-bias orientation. The MR rotation curves measured at 3 mT in both current-bias orientations are presented in Figure 6.3. The MR rotation curves measured at 3 mT were compared since the pinned layer magnetization does not rotate in the direction of the applied field at this field strength.

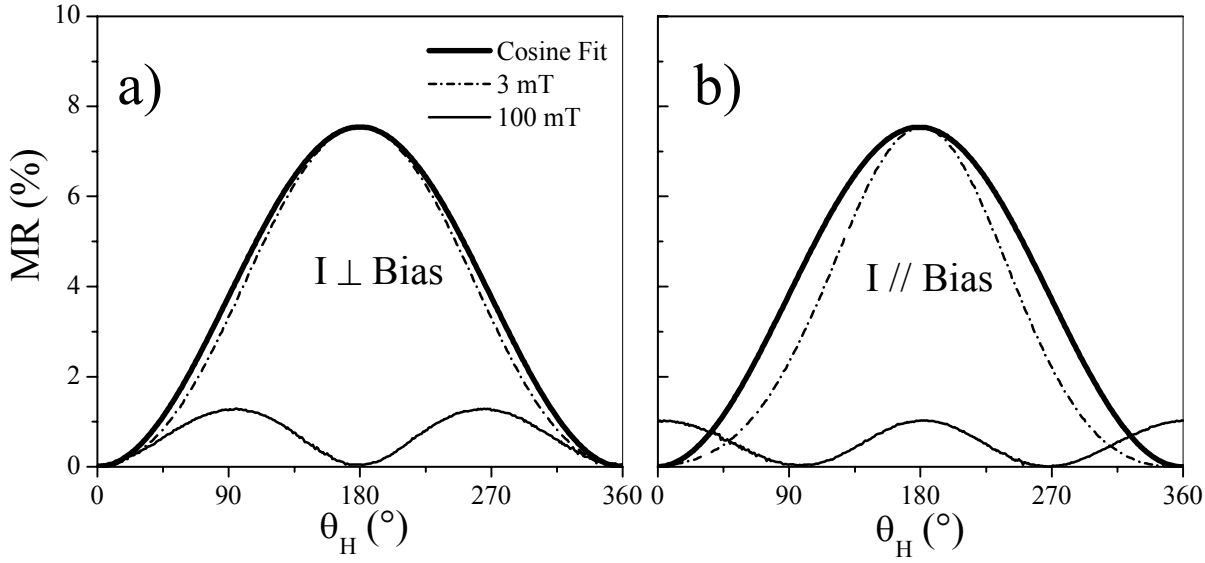

Figure 6.3: MR rotation curves measured at 3 mT and 100 mT from sample FeMn1 in both a) // current–bias orientation and b) ⊥ current–bias orientation.

The rotation curve measure in the // current-bias orientation showed a narrowing of the MR rotation curve from the cosine fit at 3 mT. The 100 mT MR rotation curve showed an MR effect of 1%, same value as measured with the field cool method, and a periodicity characteristic of the AMR effect with the maxima at 0° and 180°. The exchange bias effect is completely suppressed at an applied field strength of 100 mT. The large magnetoresistance changes in the spin valve can only originate from the AMR effect at this field value. The ⊥ current-bias orientation results in a rotation curve with minimal deviation from the cosine fit. The rotation curve measured at 100 mT shows the expected AMR periodicity with maxima at 90° and 270°, but a higher AMR effect of 1.2%.

The cosine deviation of the MR rotation curves as a function of the applied field were calculated to quantitatively determine the field dependence of the AMR influence (see Figure 6.4). At 1 mT the // current-bias orientation has approximately the same amount of deviation, ±50°, as the ⊥ current–bias orientation, ±46°. The AMR was not the dominant cosine deviation from 1-2 mT otherwise a much larger difference in the cosine deviation would have been seen between the // current-bias orientation and ⊥ current-bias orientation. From 2-20 mT, the // current-bias consistently showed a higher cosine deviation. The difference in cosine deviation, in both orientations, reached a minimum at 5 mT and began to increase as the applied field overcame the exchange bias effect in the pinned layer. The rotation of the

pinned layer magnetization in the direction of the applied field was now the dominant deviation factor, but the AMR influence was still evident (see Figure 6.4).

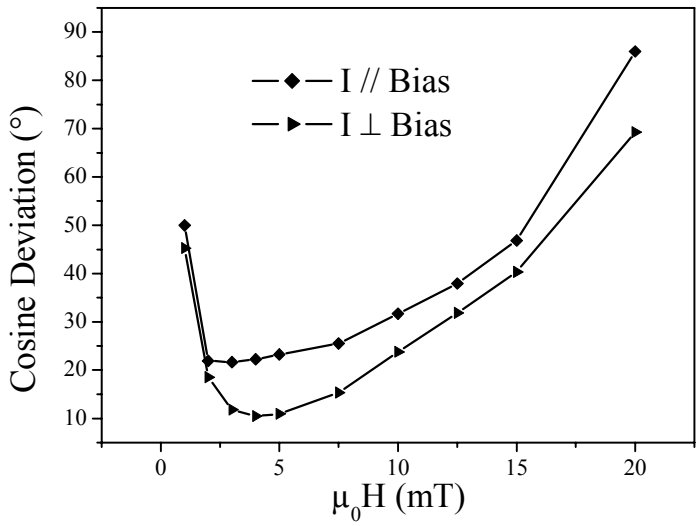

Figure 6.4: Cosine deviation as a function of field strength calculated from the MR rotation curves of spin valve FeMn1 for the // and ⊥ current-bias orientations.

6.1.1.3 Theory of AMR influence

The field dependence of the AMR contribution to the resistance changes in a spin valve has been studied by Miller, et al. [Mil93], and modeled by Rijks, et al. [Rij95], but no one has yet analyzed the influence of the AMR effect on the cosine angle dependence of the GMR effect. A simple equation can be derived to theoretically study the influence of the AMR effect. AMR and GMR effects can be added in series. This is possible since both can be regarded as separate scattering effects and the layer thicknesses in a spin-valve are usually smaller than the mean free path of electrons for such a system [Rij95]. The AMR component of the total resistance changes can be seen by adding a cosine-squared AMR term as seen in Eq. (2.2) to angle dependence equation for the GMR effect in Eq. (2.9) as indicated below:

$$R(\theta) = 0.5 \times (R_{ap} - R_p) + R_p + 0.5 \times (R_{ap} - R_p) \times \cos(\Delta\theta) + \Delta R_{AMR} \times \cos^2(\theta_M - \theta_j) \quad (6.2)$$

A cosine deviation due solely to the AMR effect should be symmetric in the absence of other cosine deviation factors according to Eq. (6.2) [Joh02a]. This symmetric deviation was seen by adding together the separate resistance changes from AMR and GMR effect as function of θ_H. The AMR part of the overall MR effect was set at 0.5% and the GMR effect at 8% for the addition of the two signals. Data sets for MR rotation curves in both the // and ⊥ current-bias orientations were created. A combined AMR+GMR MR rotation curve was created from each data set.

The addition of a cosine-squared signal (only AMR effect) with a cosine signal of much larger amplitude (only GMR effect) leads to a narrowing of the rotation curve (AMR+GMR) from an overall cosine dependence in the // current-bias orientation as seen in Figure 6.5. This occurs since the maximum value of the AMR cosine-squared signal, at 0° and 180°, coincides with the GMR maximum at 180° and minimum at 0°. The opposite case is true for the ⊥ current-bias orientation. This current-bias direction orientation leads to a broadening of the rotation curve from a cosine dependence. There is a minor difference in the resistance between the two current-bias orientations, but the curves are normalized to allow a direct

comparison of the deviation from the cosine fit. The experimental results do not show the same symmetrical cosine deviations (see Figure 6.3). The additional influence of a ferromagnetic interlayer coupling on the magnetization in the free layer could explain this difference between experiment and theory.

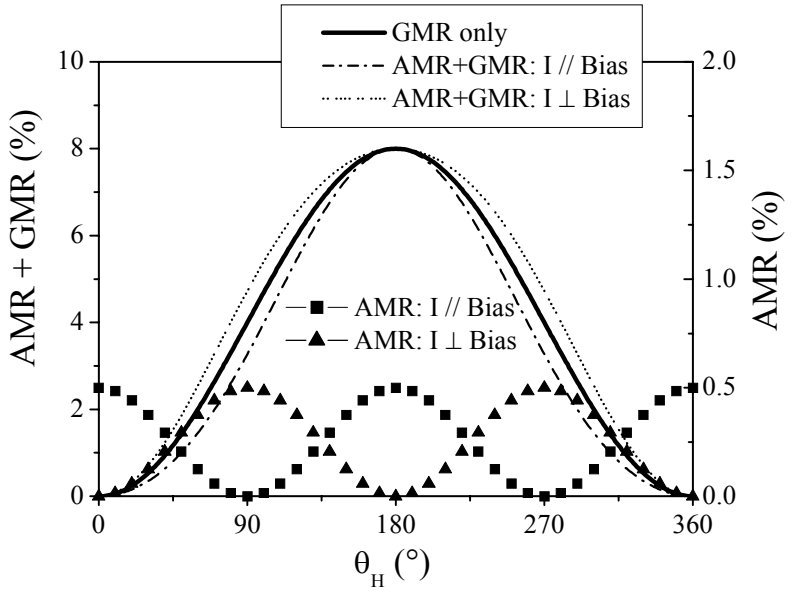

Figure 6.5: MR rotation curve illustrating the effect of adding a signal with a cosine-squared periodicity to a signal with a cosine periodicity and much larger amplitude in both current-bias orientations. AMR MR rotation curves refer to the right-hand axis. The combined AMR+GMR MR rotation curves refer to the left-hand axis.

6.1.2 Interlayer Coupling

The free layer magnetization being pulled into a parallel orientation with the pinned layer magnetization by the ferromagnetic interlayer coupling would be a good explanation for this discrepancy between theory and experiment. The influence of interlayer coupling on the free layer magnetization is commonly thought to be suppressed above the H_e of a spin valve. Tietjen, et al. [Tie02], has shown in simulations that switching off the ferromagnetic interlayer coupling in the aforementioned free energy model (see Chapter 5) results in a dramatic reduction of the deviation from cosine of the MR rotation curves. Ferromagnetic coupling could therefore still have an effect despite the fact that the MR rotation measurements were made at 3 mT ($\mu_0 H > H_e$).

The magnetization direction of the free layer is tilted with respect to the direction of the applied field as a result of the interlayer coupling as illustrated in Figure 6.6. The angle between M_p and M_f would be smaller than the angle between M_p and H in the case of a ferromagnetic coupling in the spin valve. The actual resistance in the spin valve at this angle would therefore be lower than the expected resistance value as given by Eq. (6.2). This leads to an overall narrowing of the rotation curve in reference to the cosine fit. Performing the same MR rotation measurements on FeMn samples with different interlayer coupling strengths tested this hypothesis.

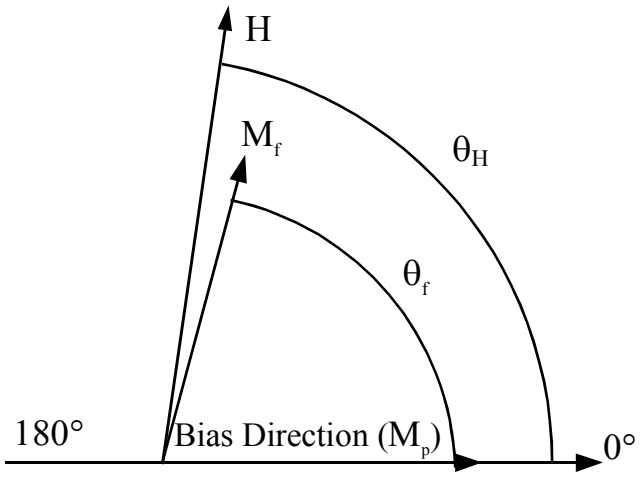

Figure 6.6: The orientation of the applied field in relation to the magnetization in the free layer and reference layer. In this case the applied field has not completely overcome the effect of the interlayer coupling on the free layer.

Three different FeMn spin-valve systems were deposited on 4-inch oxidized Si(100)-wafers under a magnetic bias field by a Shamrock 150 sputtering system to specifically study the influence of interlayer coupling on the cosine dependence of the GMR in spin valves. The Cu layer thickness was varied to change the strength of the interlayer coupling [Koo95]. The three FeMn spin valves were of the following structure: Si/SiO_2/Ta(5)/NiFe(6)/CoFe(1.5)/Cu(X)/CoFe(2)/NiFe(2)/FeMn(8)/Ta(5). The layer thicknesses are given in nm. The only difference between the different FeMn spin valves was a change in the Cu layer thickness where X is 2.9, 2.6 and 2.2 nm, respectively. The spin valve stacks are referred to as FeMn 2, FeMn3 and FeMn4 respectively in the text. The spin valve stack FeMn1 was also used in this study. All of the important magnetic properties such as of each spin valve sample is summarized in Table 6.1. J_{int} was calculated according to Eq. (2.14).

Table 6.1: Summary of the magnetic properties for spin valve samples FeMn1-FeMn4.

Sample	t_{Cu}	MR	H_{eb}	H_{c1}	H_{c2}	H_e	J_{int}
-	nm	%	mT	mT	mT	mT	Jm^{-2}
FeMn1	2.9	8	29	0.1	1.5	0.4	3.74×10^{-6}
FeMn2	2.9	7.9	25	0.1	1.5	0.73	6.82×10^{-6}
FeMn3	2.6	8.5	25	0.1	1.5	0.89	8.31×10^{-6}
FeMn4	2.2	9.4	23	0.1	1.5	1.42	1.33×10^{-5}

6.1.2.1 Magnetoresistance Rotation Measurements

The MR rotation curves were measured in both current orientations in the range from 1-25 mT for samples FeMn 1-4. All of the MR rotation curves were normalized to allow a direct comparison between the different rotation measurements. The direct effect of the change in ferromagnetic interlayer coupling strength on the MR rotation curves was observed in Figure 6.7. The MR rotation curve is closest to the cosine fit at the lowest J_{int}, of 3.74×10^{-6} Jm^{-2} (FeMn1). The narrowing of the rotation curve increased as the ferromagnetic coupling increased from $6.82\times10^{-6}Jm^{-2}$ (FeMn2) to 8.31×10^{-6} Jm^{-2} (FeMn3). The MR rotation curve from sample FeMn4 shows the largest deviation with a J_{int} of $1.33\times10^{-5}Jm^{-2}$. The increase in

cosine deviation was directly proportional to the increase of the ferromagnetic interlayer coupling.

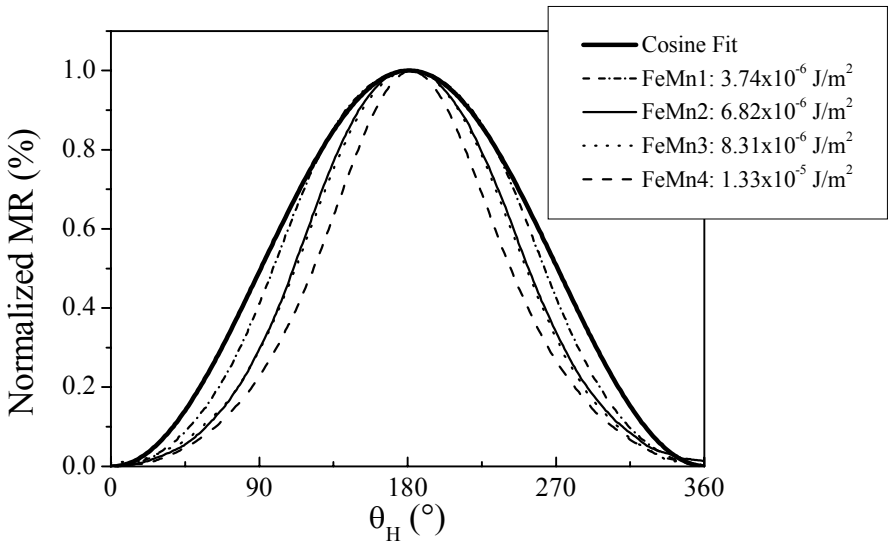

Figure 6.7: Normalized MR rotation curves measured from samples FeMn1-FeMn4 each with different interlayer coupling measured at 3 mT. All of the samples were in the ⊥ current-bias direction orientation.

The cosine deviation as a function of the field strength is presented in Figure 6.8 for samples FeMn 1-4. The cosine deviation starts at maximum value at 1 mT and then decreases to a minimum in the 4-5 mT range for every interlayer coupling strength and current-bias orientation. This decrease in cosine deviation is due to the applied field overcoming the influence of the ferromagnetic interlayer coupling on the free layer magnetization. After 5 mT the error begins to increase to a maximum as the pinned layer begins to rotate in the direction of the applied field.

The cosine deviation in the // current orientation was always larger than that of the perpendicular current orientation (see Figure 6.8). This is due to the AMR contribution. The cosine deviation began to increase in both current bias orientations starting in the 5-7 mT field range. This is due to the rotation of the pinned layer in the direction of the applied field. This will be explained in more detail in Section 6.1.3. The difference in cosine deviation reduces with increasing applied field, $\mu_0 H > 15$ mT. The influence of the ferromagnetic interlayer coupling was being continually reduced by the increasing applied field strength. At 20 mT the cosine deviation is on the order of 80° regardless of current-bias orientation or strength of the interlayer coupling.

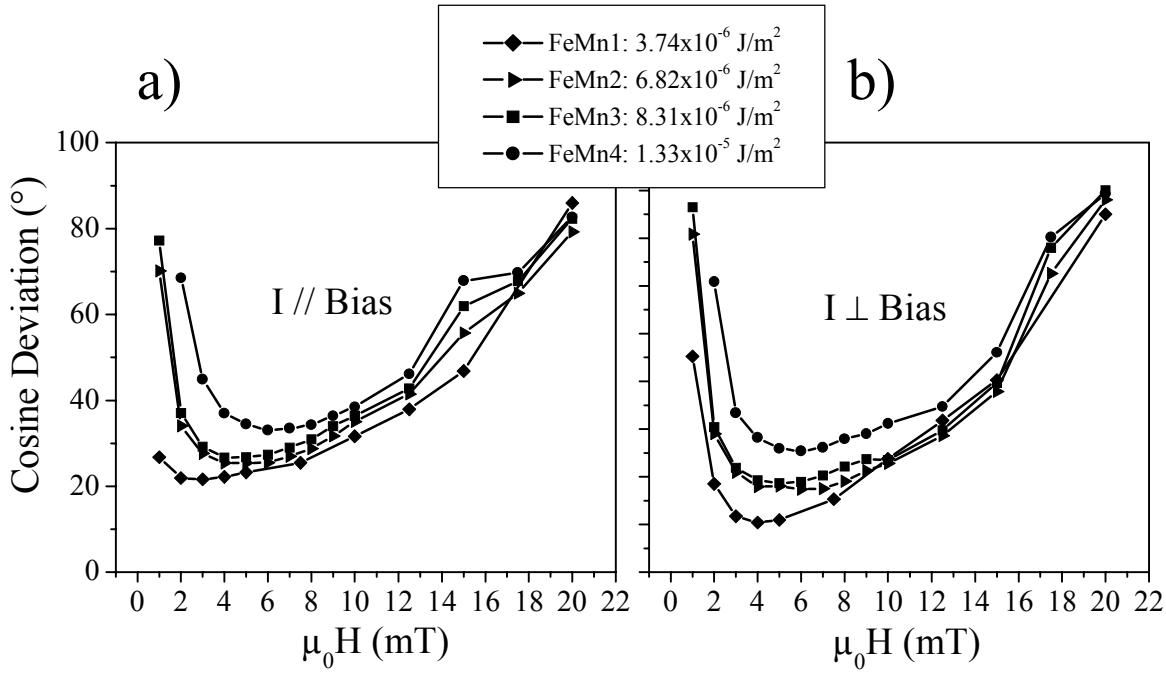

Figure 6.8: The cosine deviation determined from the MR rotation measurements of samples FeMn1-FeMn4 as a function of the applied field strength measured in the a) // current-bias orientation and b) for the ⊥ current-bias orientation.

6.1.2.2 Antiferromagnetic Interlayer Coupling

Most of the studied spin valve systems showed the presence of ferromagnetic interlayer coupling between the pinned layer and free layer. Only one spin valve system had a antiferromagnetic interlayer coupling across the Cu spacer layer. This was a PtMn spin valve with SAF where the Cu layer thickness was set close to the 2nd antiferromagnetic exchange coupling maximum to compensate any ferromagnetic coupling due to interface roughness. Also the orange-peel coupling had been minimized through reduction of the interface roughness due to better process control during deposition. The result was an antiferromagnetic coupling between the free layer and reference layer on the same order of magnitude as the rest of the previously as ferromagnetic coupling Section 6.1.2.1. The spin valve stack structure was otherwise the same as that described in Section 6.2.5. The presence of the antiferromagnetic coupling is indicated through the negative shift of the minor loop of the MR curve as seen in Figure 6.9. The H_e of this system was measured to be -0.7 mT, which corresponds to an interlayer coupling of -4.07×10^{-6} Jm^{-2}.

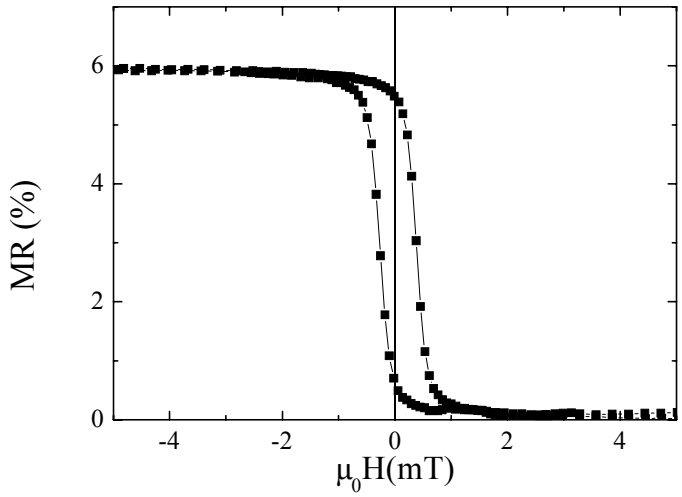

Figure 6.9: Minor loop of PtMn spin valve with SAF that exhibits antiferromagnetic coupling between the free layer and pinned layer.

The MR rotation curves were measured in both current orientations in the field range of 1-25 mT. These are the same measurement conditions as in the ferromagnetic coupling study (see previous Section). The presence of antiferromagnetic coupling creates the opposite case with the // and ⊥ current-bias orientations as in the ferromagnetic coupling case (see Figure 6.10). The antiferromagnetic coupling pulls the magnetization towards the anti-parallel alignment with the pinned layer rather than towards the parallel alignment. The result is the opposite that of the ferromagnetic coupling case seen in Figure 6.6 and Figure 6.7. The MR measured was greater than that predicted by a pure cosine dependence of the GMR effect from Eq. (6.2) (see Figure 6.10).

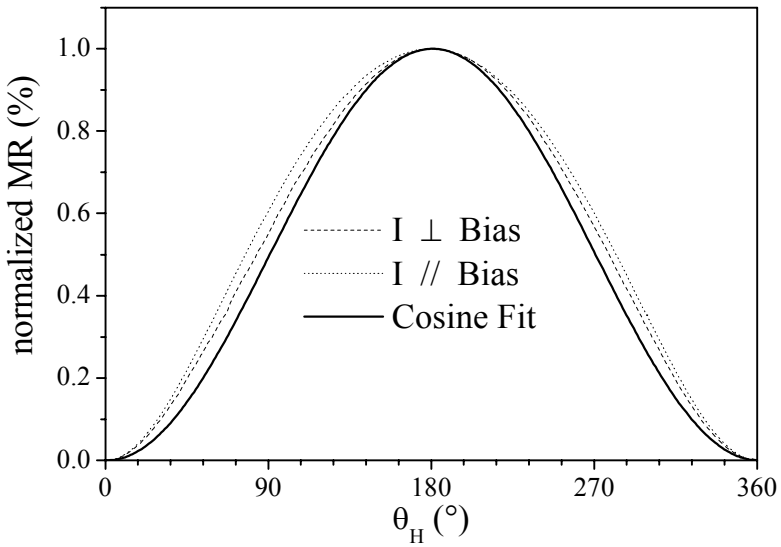

Figure 6.10: MR rotation measurement made at 3 mT from a PtMn spin valve with SAF in the a) // current-bias orientation and b) ⊥ current-bias orientation.

The cosine deviation caused by the antiferromagnetic coupling showed a field dependence similar to that of the ferromagnetic coupling (see Figure 6.8). The cosine deviation dropped from 17.5° at 1 mT to 5.2° at 25 mT in the ⊥ current-bias orientation as seen in Figure 6.11. In the // current-bias orientation the cosine deviation dropped from 12.9° at 1 mT to 1.1° at 25 mT. As with the ferromagnetic coupling, the increase in the applied magnetic field gradually

reduced the influence of the antiferromagnetic coupling on the free layer magnetization. The cosine deviation in the ferromagnetic coupling case in a FeMn simple spin valve began to increase at 7 mT, while the cosine deviation continually decreased with increasing applied field in a spin valve with SAF. The pinned layer magnetization remains completely stable up to a field strength of 25 mT in spin valve with SAF. The H_{eb} of the PtMn spin valve with SAF is six times larger than the H_{eb} of the sample FeMn1 (180 mT vs. 30 mT).

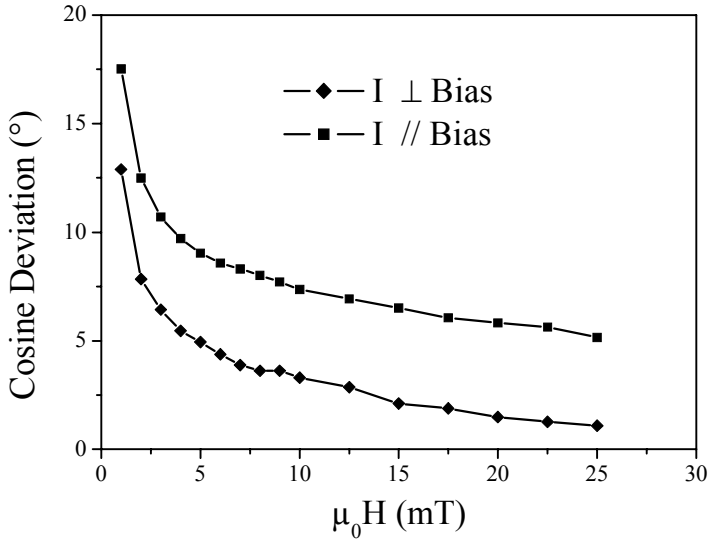

Figure 6.11: Cosine deviation as a function of field strength from the measured rotation curves from PtMn spin valve with SAF in the // current-bias orientation and ⊥ current-bias orientation.

6.1.3 Rotation of the Pinned Layer Magnetization

The cosine deviation begins to rise after reaching a minimum value at 5-7 mT for the FeMn spin valves (see Figure 6.4 and Figure 6.8). This is due to the rotation of the pinned layer magnetization at oblique angles to the bias direction at field values below the H_{eb} of a spin valve. The pinned layer magnetization is supposed to remain fixed in relation to θ_H up to the H_{eb} of a spin valve. In reality it will begin to follow the applied direction at field values much lower than H_{eb} (see Figure 6.12a). This leads to a reduction in the resistance changes that is directly analogous to that of ferromagnetic coupling as described in Section 6.1.2. An lower applied strength to overcome the exchange bias effect and rotate the pinned layer magnetization when the field direction is set 90° to the bias direction than when the field direction is set 180° to bias direction. This is seen in the MR measurements made in the parallel and perpendicular to the bias direction (see Figure 6.12b and Figure 6.12c).

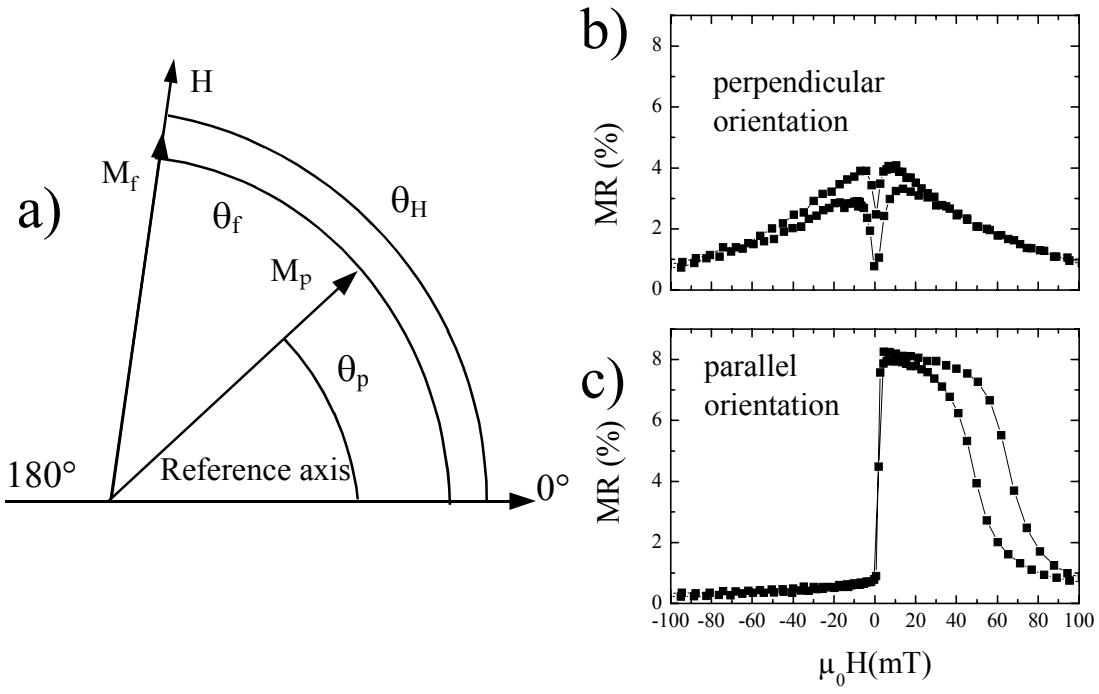

Figure 6.12: a) The orientation of applied field in relation to the magnetization in the free layer and pinned layer at a field strength of ½th the H_{eb} of the spin valve. MR curve measured with the field direction b) 90° to the bias direction and c) parallel to the bias direction of a spin valve.

6.1.3.1 MR Rotation Measurements

Examination of the MR rotation curves measured from sample FeMn1 measured at 5, 10, 15, 20, 25 and 40 mT clearly showed the influence of the applied field on the pinned layer magnetization (Figure 6.13). The MR rotation measurements were made in the ⊥ current-bias orientation. The difference in MR, ΔMR, between the cosine fit and measured rotation curve is plotted in the rotation curves to better illustrate the amount of cosine deviation. At 5 mT the pinned layer magnetization is stable and the rotation curve shows little deviation from the cosine fit as seen in arctan error (see Figure 6.4 and Figure 6.13). At 10 mT the rotation curve has begun to deviate most visibly at 90° and 270° from the cosine fit (see Figure 6.13). The rotation curve measured at 20 mT shows the largest deviation from the cosine fit at angles close to 180°. At 25 mT the pinned layer magnetization no longer remains fixed by the exchange bias effect and the rotation curve has begun to assume the 180° periodicity of typical of an AMR effect.

The exchange bias effect is completely overcome by the applied magnetic field at 40 mT. The MR rotation curve is similar to the rotation curves measured from a single ferromagnetic thin film exhibiting the AMR effect except in the MR effect size. The MR due to the AMR effect is typically 1% in spin valves (see Figure 6.3). The reason for the high MR effect is the continued influence of the exchange bias effect on the pinned layer magnetization angle. The exchange bias effect is not nonexistent above the H_{eb} of the spin valve and still pulls the pinned layer magnetization in the bias direction.

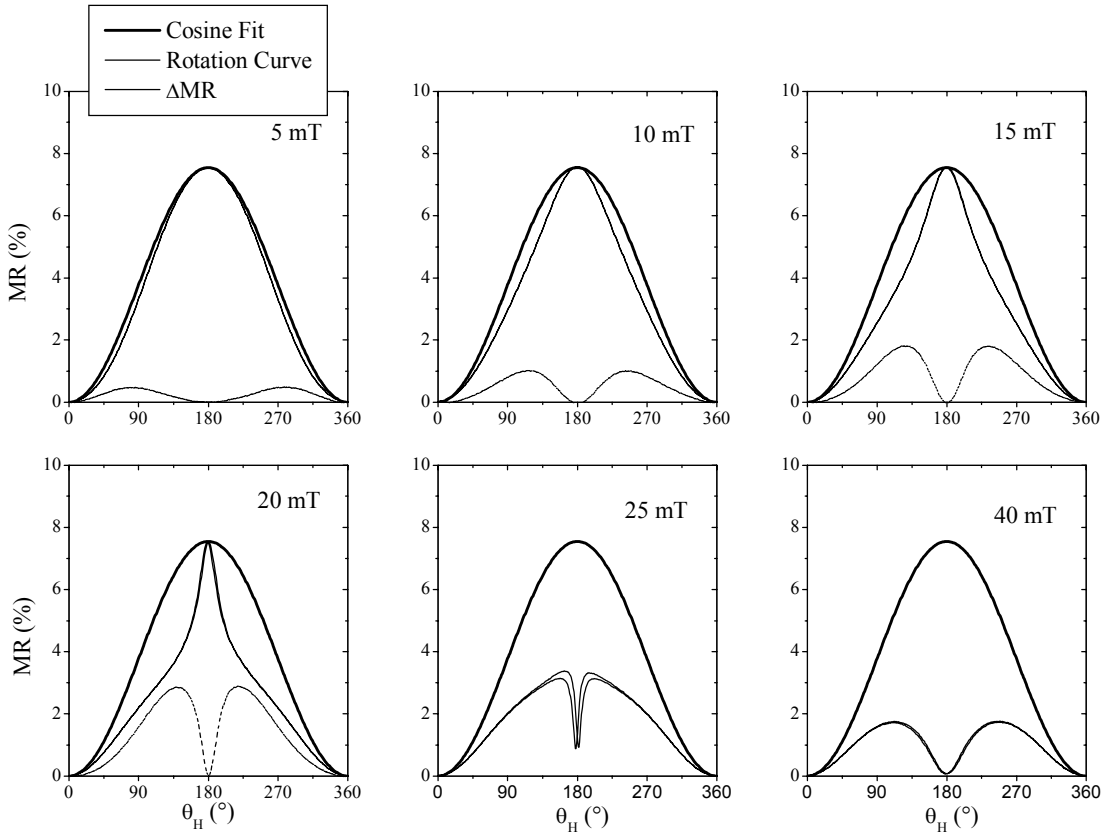

Figure 6.13: MR rotation curves measured from sample FeMn1 at 5 mT, 10 mT, 15 mT, 20 mT, 25 mT and 40 mT.

6.1.3.2 Cosine Deviation: Comparison Between Simple Spin Valve and Spin Valve with SAF

H_{eb} is the magnetic parameter of a spin valve that determines the magnetic operating window of a GMR 360° angle sensor. The need for a large H_{eb} and therefore a large operating window was shown by comparison of MR rotation curves measured from a FeMn simple spin valve (H_{eb}=55 mT) and PtMn spin valve with SAF (H_{eb}=180 mT). MR rotation curves were measured in the 1-120 mT field range from both the FeMn simple spin valve (see Section 6.2.2) and a PtMn spin valve with SAF (see Section 6.2.5). It is important to note that this comparison is not between spin valve systems with different antiferromagnets, but between spin valve systems with a large difference in H_{eb}.

The arctan analysis was performed on each MR rotation curve and the cosine deviation for each spin valve system plotted as a function of field strength as seen in Figure 6.14. In the case of the simple spin valve, the cosine deviation was ±55° at 1 mT and decreased to a minimum of ±22° at 10 mT as the applied field overcame the influence of ferromagnetic coupling on the free layer (see Figure 6.14). As the applied field increased in strength, the cosine deviation rose to a maximum of ±76° at 40 mT. The cosine deviation of the spin valve with SAF reached a minimum of ±9°in the 10-30 mT range and then began to increase to a maximum error of ±20° at 110 mT.

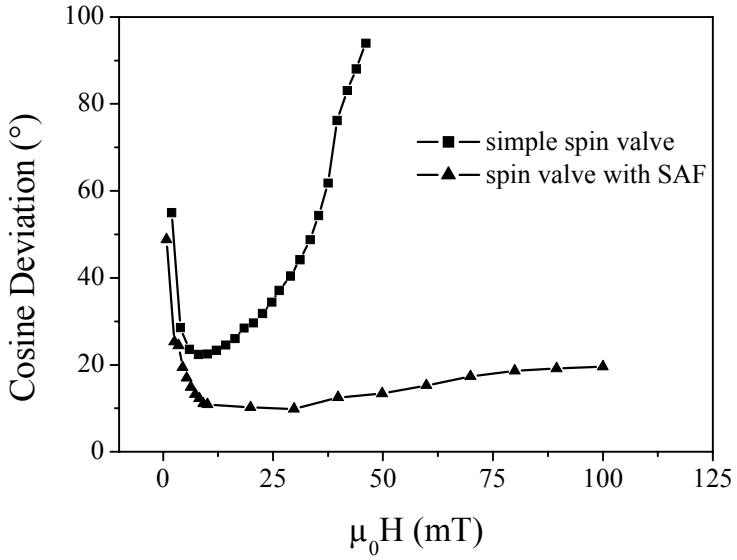

Figure 6.14: Comparison between the field dependence of the cosine deviation calculated from rotations curve measured from a simple spin valve and a spin valve with SAF.

A general rule for the cosine deviation caused by the rotation of the pinned layer in the direction of the applied field can be distilled from these rotation measurements (see Figure 6.14) and those from samples FeMn1-4 samples (see Figure 6.8). In the case of the FeMn1-4 samples, (H_{eb} = 30 mT) the cosine deviation due to the pinned layer the rotation of the pinned layer magnetization begins in the 5-6 mT range (see Figure 6.8). The cosine deviation started in the 9-10 mT range in the simple spin valve system (H_{eb}=55 mT) and in the 25-30 mT range for the spin valve with SAF (H_{eb}=180 mT) (see Figure 6.14). The cosine deviation due to rotation of the pinned layer magnetization onset at approx. $1/6^{th}$ the H_{eb} value for both types of spin valve systems. The incorporation of SAF in the spin valve stack significantly increases the H_{eb} of a spin valve and subsequently the field range over which the cosine deviation is kept at a minimum.

6.1.4 Overview of the Cosine Deviation Factors

The AMR effect, ferromagnetic interlayer coupling and rotation of the pinned layer magnetization below the H_{eb} of the spin valve were found to be the source of the deviations from the cosine dependence of GMR effect in unpatterned spin valves. The relationship of the cosine deviation factors to one another can be shown by the direct comparison between an MR measurement and the corresponding MR rotation measurements as shown in Figure 6.15. The interlayer coupling was found to be the dominant cosine deviation factor at field strengths up to $1/6^{th}$ of the H_{eb} as seen in MR rotation curve measured at 1 mT (see Figure 6.15b). At 5 mT the MR rotation curve shows the least deviation from the cosine fit while the pinned layer magnetization remains fixed and the interlayer coupling influence is mostly suppressed. The 20 mT MR rotation curve is a good example of the cosine deviation caused by the rotation of the pinned layer magnetization. At 40 mT only the AMR component of the resistance change is still present in the rotation curve. The AMR effect is a constant deviation factor that is present in the spin valve at any field strength.

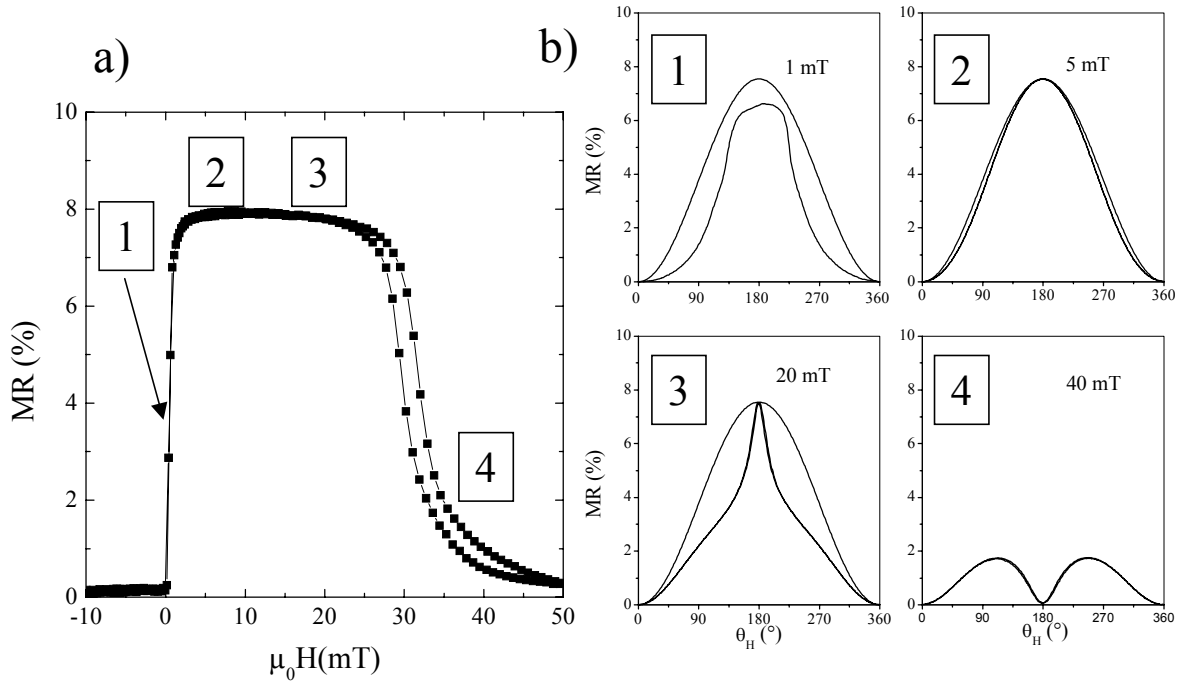

Figure 6.15: a) MR curve measured from sample FeMn1 with the corresponding b) MR rotation curves measured at 1 mT, 5 mT, 20 mT, and 40 mT. This figure shows the direct relation between an MR curve and cosine deviation in the MR rotation curves.

A short description and the field dependence of each cosine deviation factor is given below:

I. Interlayer coupling
Description: Causes deviation of direction of the free layer magnetization from the applied field direction. It is dependent upon the sign and strength of coupling.
Field Range: $\mu_o H \leq 1/6^{th}$ of H_{eb}

II. Rotation of the pinned layer magnetization
Description: Magnetization of the pinned layer rotates in the direction of the applied field below H_{eb} of the spin valve
Field Range: $\mu_o H \geq 1/6^{th}$ of H_{eb}

III. AMR
Description: Additional resistance change added as a cosine-squared signal to the overall resistance change dependent upon the angle between the magnetization direction in the pinned and free layer respectively
Field Range: present at every field value.

6.1.5 Simulation of MR Rotation Curves

The previous experimental results had shown that AMR, interlayer coupling and the rotation of the pinned layer magnetization played the largest role in the deviation of the GMR effect from a cosine dependence. The simulation of the experimental results presented in the previous sections posed an excellent opportunity to check the accuracy of the model proposed by Tietjen, et. al [Tie02,]. Only the addition of an AMR term to the overall resistance change (see Eq. (2.4)) was necessary to correctly simulate MR rotation curves. The same MR

rotation measurements from Sections 6.1.1, 6.1.2, and 6.1.3 were simulated and then compared directly with the experimental.

6.1.5.1 Addition of AMR Term to Simulation

An AMR term must be added to the resistance change equation, Eq. (5.4), to correctly simulate the MR rotation curves for a spin valve system. As shown experimentally (see Section 6.1.2), the AMR effect creates additional resistance changes in the spin valve system separate from the GMR effect that must be taken into consideration. The AMR effect originates from each ferromagnetic layer in the spin valve and is dependent on the angle between the magnetization in each layer and the current direction. It is therefore important to add the AMR term as a function of θ_i, rather than θ_H, since the magnetization direction is not always the same as that of the applied field. The magnetization direction of the free layer is influenced, to a degree, by the interlayer coupling between the pinned layer and free layer (see Sections 6.1.2 and 6.1.3). Also the pinned layer magnetization rotates in the direction of the applied field direction below the H_{eb} of the spin valve.

Dieny, et al. [Die00] had already proposed a resistance change equation that included separate terms for the AMR effect in each layer of a spin valve as a function of the magnetization direction in each ferromagnetic layer. This same principle is used to describe the resistance changes caused by the AMR effect, but for an undetermined number of ferromagnetic layers as given below:

$$\Delta R_{AMR} = \sum_{i=1}^{N} \Delta R^{i}_{AMR} \cos^2\left(\theta_i - \theta_j\right) \tag{6.3}$$

where ΔR^{i}_{AMR} is the fit parameter for the resistance change due to the AMR effect for each i-th layer as determined from experiment.

The AMR term can be added to the Eq. (5.2) for ΔR_{GMR} to give the total resistance changes, ΔR_T, in a spin valve due to magnetoresistance effects:

$$\begin{aligned} \Delta R_T &= \Delta R_{GMR} + \Delta R_{AMR} \\ \Delta R_T &= \sum_{i=1}^{N-1} \Delta R^{i}_{GMR}\left(1 - \cos\left(\theta_{i+1} - \theta_i\right)\right) + \sum_{i=1}^{N} \Delta R^{i}_{AMR} \cos^2\left(\theta_i - \theta_j\right) \end{aligned} \tag{6.4}$$

This simple addition to the model allows one to simultaneously see the combined influence of AMR effect, interlayer coupling and rotation of the pinned layer magnetization on the angle dependent resistance changes in spin-valves.

The resistance change equation given in Eq. (5.5) for the simple spin valve model is reworked to include the influence of the AMR effect. This is done by inserting θ_p and θ_f into Eq. (5.5) for the appropriate layers. Again Layer 1 is the pinned layer and Layer 2 is the free layer. ΔR_T now becomes:

$$\Delta R_{GMR} = \Delta R^{p}_{GMR}\left(1 - \cos\left(\theta_f - \theta_p\right)\right) + \Delta R^{p}_{AMR} \cos^2\left(\theta_p - \theta_j\right) + \Delta R^{f}_{AMR} \cos^2\left(\theta_f - \theta_j\right) \tag{6.5}$$

where ΔR^{p}_{AMR} and ΔR^{f}_{AMR} are the resistance changes due to the AMR effect in the pinned layer and free layer respectively.

6.1.5.2 Simulated MR Rotation Curves: AMR Influence

The MR rotation curves from spin valve sample FeMn1 were simulated using the model described in section 5.2 to test the AMR addition to the simulation. The overall AMR effect was measured to be 1.0% based on the 100 mT MR rotation curves (see Figure 6.3). At 100 mT the pinned and free layer contribute to the overall AMR effect. At 3 mT the quantity (θ_p - θ_j) remains constant since the magnetization in the pinned layer is fixed by the exchange bias effect [Dim98]. The AMR was estimated to be 0.8 % for the free layer and 0.2% for the pinned layer. The saturation magnetization values for the free layer M_s and pinned layer M_p are averaged values from the bulk saturation magnetization for NiFe (1.08 T) and CoFe (1.91 T) [Jil91]. This is necessary since both the free layer and pinned layer in sample FeMn1 are CoFe/NiFe sandwich layers which must be regarded as one layer in the simulation.

The magnetic properties of sample FeMn1 were used as the input parameters for the determination of the free energy terms (see Table 6.1). The free energy terms for each layer are summarized below to give an overview of the simulation parameters:

Layer 1: Pinned Layer
Saturation Magnetization (M_p): 1.49 T
Unidirectional Anisotropy (K_{eb}): 1.73×10^{-4} J/m^2
Direction of the Unidirectional Anisotropy: 0°
Interlayer coupling (J_{int}): 3.74×10^{-6} J/m^2 (Orange-peel coupling)
Uniaxial Anisotropy ($K_p^{uniaxial}$): 5.97×10^{-6} J/m^2
Direction of the Uniaxial Anisotropy: 0°

Layer 2: Free Layer
Saturation Magnetization (M_f): 1.25 T
Uniaxial Anisotropy ($K_f^{uniaxial}$): 2.33×10^{-7} J/m^2
Direction of the Uniaxial Anisotropy: 90°

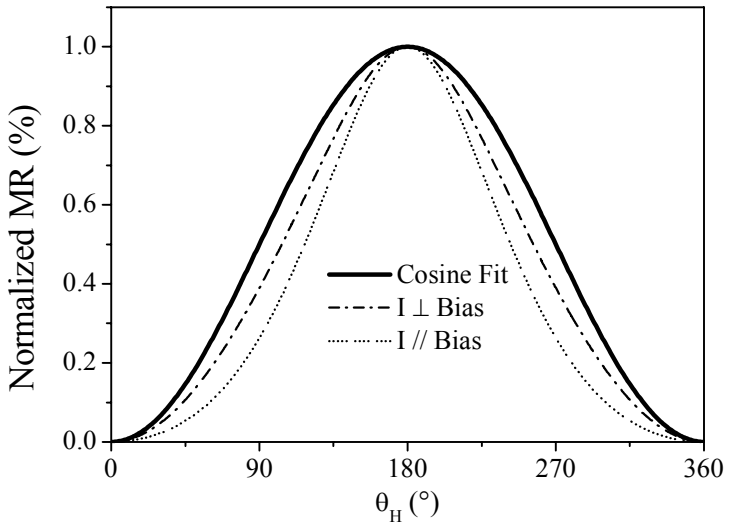

Figure 6.16: Simulated MR rotation curves of sample FeMn1 with the current ⊥ bias direction orientation and current // bias orientation.

The MR rotation curves measured at 3 mT from sample FeMn1 were simulated first in the // current-bias orientation and then ⊥ current-bias orientation. The θ_{eb} was shifted 90° in the model to correspond to the 90° change in the bias direction in the experiment caused by the field cool. Both different MR rotation curves are plotted together in Figure 6.16 together with

a cosine fit. The cosine deviation is greater in the // orientation than in the ⊥ current orientation. This matches the behavior seen in the experimental rotation curves (see Figure 6.3). The improved model qualitatively duplicates the cosine deviation trends caused by the change in current- bias orientation with a added influence of the ferromagnetic coupling present in the spin valve.

6.1.5.3 Simulated MR Rotation Curves: Interlayer Coupling

The influence of the interlayer coupling on the cosine dependent resistance changes could also be duplicated with the free energy model presented in Section 5.2. The MR rotation curves in Figure 6.17 were simulated using the model parameters extracted from samples FeMn1-FeMn4 as listed in Table 6.2. The only difference is the substitution of the model parameters for samples FeMn 2-4 in place of those for sample FeMn1. The current direction is set ⊥ to the unidirectional anisotropy in each simulated MR rotation curve.

Table 6.2: Summary of model parameters used for the simulation of AMR and interlayer coupling influence on angle dependent resistance changes.

Sample	K_{eb}	J_{int}	$K_p^{uniaxial}$	$K_f^{uniaxial}$
-	Jm^{-2}	Jm^{-2}	Jm^{-2}	Jm^{-2}
FeMn1	1.73×10^{-4}	3.74×10^{-6}	5.97×10^{-6}	2.33×10^{-7}
FeMn2	1.49×10^{-4}	6.82×10^{-6}	4.48×10^{-6}	2.33×10^{-7}
FeMn3	1.49×10^{-4}	8.31×10^{-6}	4.48×10^{-6}	2.33×10^{-7}
FeMn4	1.49×10^{-4}	1.33×10^{-5}	4.48×10^{-6}	2.33×10^{-7}

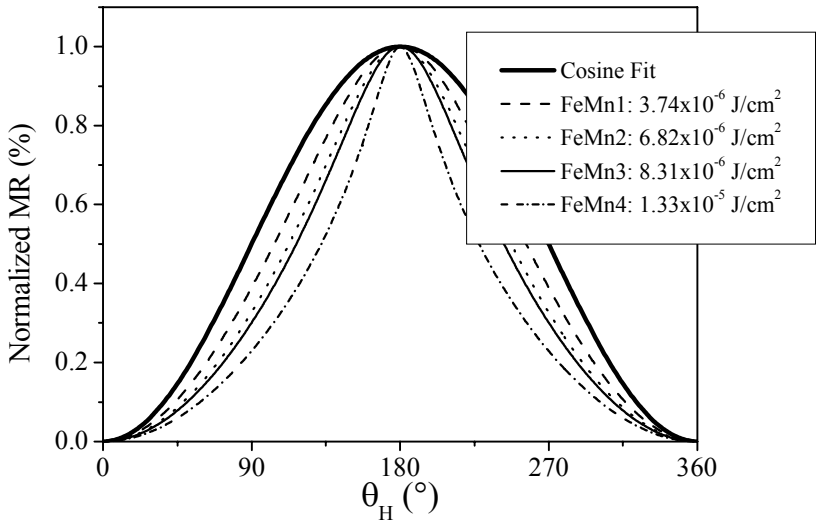

Figure 6.17: Simulated MR rotation curves from samples FeMn1-FeMn4 with different interlayer coupling measured at 3 mT.

The simulated MR rotation curve from sample FeMn1 showed the least deviation from cosine as shown in Figure 6.17. Sample FeMn1 had the lowest J_{int} of 3.49×10^{-6} Jm^{-2} of all of the studied samples (see Table 6.2). The simulated MR rotation curve becomes narrower with the increase in J_{int}, $6.37\times10^{-6}Jm^{-2}$ to 1.24×10^{-6} Jm^{-2}, for samples FeMn2-FeMn4. This matches the trend in the cosine deviation seen in the experimental rotation curves from Figure 6.7. The only difference is the amount of cosine deviation from cosine fit observed in the experimental and simulated MR rotation curves (Figure 6.7 and Figure 6.17). The experimental curves have less amount of deviation from the cosine fit than the simulated

curves. The reason for this difference is not yet clear. Possibly the AMR component in the free layer is actually more than the measured 0.8 %.

The influence of the interlayer coupling on the free layer magnetization becomes clearer upon examination of the difference in angle between θ_f and θ_H. As seen in Figure 6.18, magnetization direction in the free layer deviates from the applied field direction at every angle. Only at 0° and 180° there was no deviation of the free layer magnetization from the applied field direction. The point of maximum deviation is found to shift in angle as a function of the interlayer coupling strength (see Figure 6.18). For example at 3.74×10^{-6} Jm^{-2} (FeMn1) the θ_H-θ_f is at minimum of +9° at 111° while it increases to +36.2° at 139° at an interlayer coupling of 1.33×10^{-5} Jm^{-2} (FeMn4). The deviation is largest for angles close to θ_H = 90° and 270°. If θ_H <180° then the θ_f lags behind the applied field and if θ_H >180° then the θ_f precedes the applied field direction. The simulated MR rotation curves confirmed the hypothesis that the ferromagnetic coupling pulls the magnetization in the free layer away from the applied field direction.

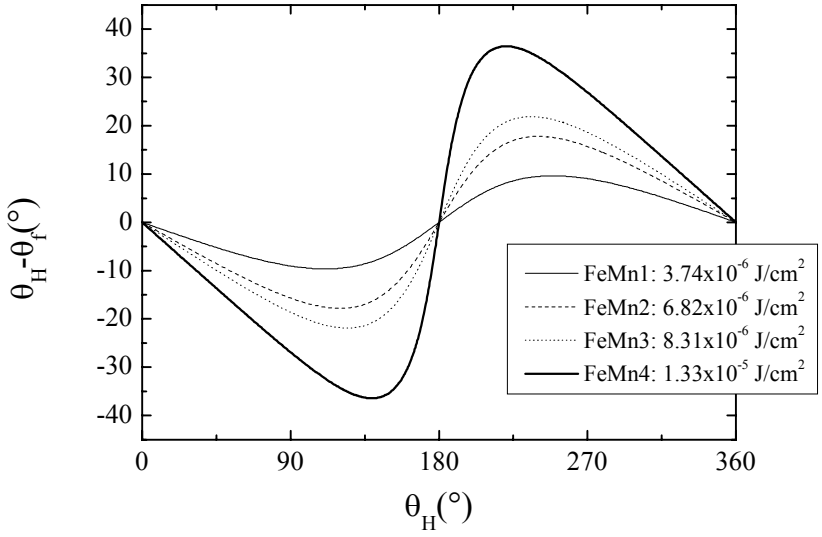

Figure 6.18: Deviation of the magnetization angle vector of the free layer from the applied field direction for samples FeMn1-4 as determined from the simulated MR rotation curves.

6.1.5.4 Simulated MR Rotation Curves: Rotation of the Pinned Layer Magnetization

The simulation program could also duplicate the cosine deviation caused by the rotation of the pinned layer magnetization in the applied field direction at field values below the H_{eb} of a spin valve. The current direction is set in the ⊥ current-bias orientation in the simulation. The MR rotation curves shown in Figure 6.13 were simulated using the same model parameters for sample FeMn1 in section 6.1.5.2. The MR rotation curves measured at 5, 10, 15, 20, 25 and 40 mT were generated by the simulation program (see Figure 6.19). The increasing cosine deviation in the MR rotation curves with increase in applied field is duplicated with one major discrepancy. Major differences are evident in the MR rotation curves for 20 and 25 mT. The 20 mT rotation curve in experiment (see Figure 6.13) showed a much larger deviation than in the simulation. The experimental rotation curve at 25 mT had 180° periodicity of the AMR effect while the simulated curve had a 360° periodicity expected of the GMR effect. Both the 40 mT simulated and experimental rotation curves showed the 180° periodicity of the AMR effect.

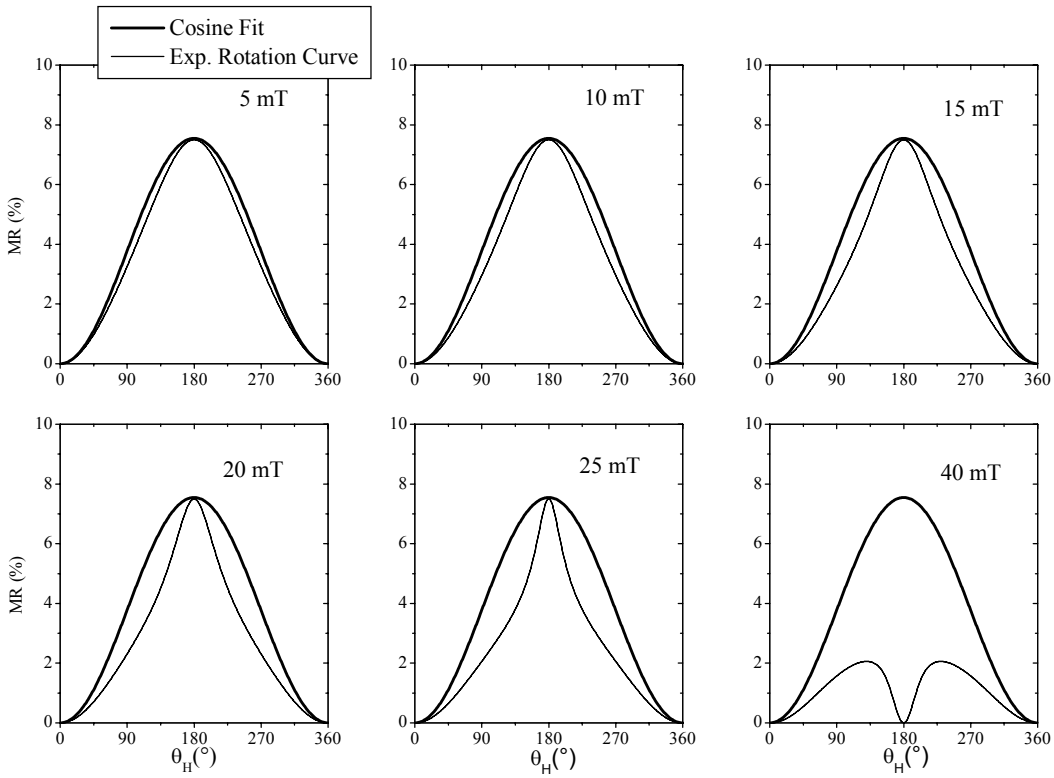

Figure 6.19: MR rotation curves from spin valve FeMn1 simulated at 5 mT, 10 mT, 15 mT, 20 mT, 25 mT, and 40 mT.

The simulated rotation curves first showed the onset of the cosine-squared periodicity when the applied field was above 30 mT, the H_{eb} of the spin valve system. This discrepancy between simulation and experiment could be explained through the onset of domain formation in the pinned layer close to the H_{eb} value, which has been observed by Kerr microscopy in FeMn spin valves [dHa02]. This is due to a H_{eb} distribution in the AFM layer of the spin valve. The simulation program does not take into account domain formation but uses the one-domain assumption (see Chapter 5).

The rotation of the magnetization of the pinned layer with increasing applied field is quantifiable by examining the difference between the expected and actual magnetization vector of the pinned as a function of the applied field direction (see Figure 6.20). The magnetization in the pinned layer deviates up to 9° from the expected bias direction even at 5 mT. The simulation seems to indicate that the rotation of the pinned layer magnetization also plays a role in the deviation from cosine in the low field range: 1-5 mT. As applied field increases to 25 mT, the H_{eb} of the spin valve is 29 mT, the cosine deviation increases to 50°. The largest deviation occurs when the applied field direction is nearest to 180°. These simulated results supported the hypothesis that the pinned layer magnetization rotates in the direction of the applied field rotation at field values much lower than the H_{eb} of a spin valve system.

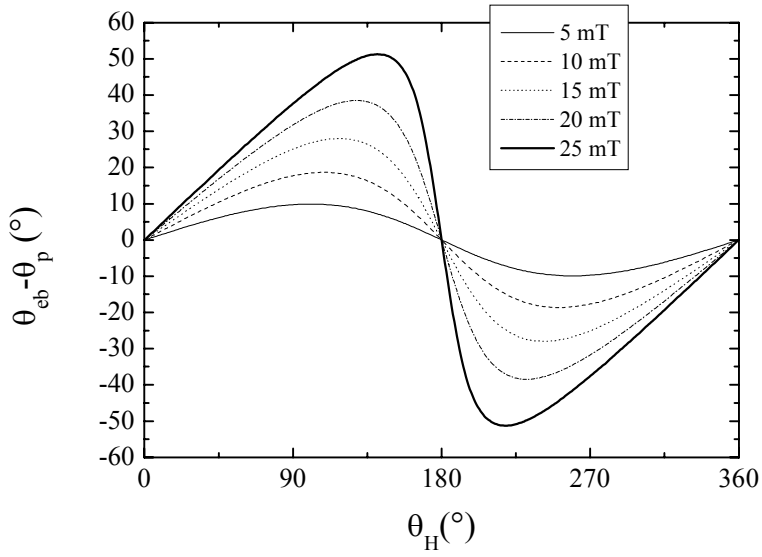

Figure 6.20: Deviation of the magnetization vector of the pinned layer from the expected bias direction for sample FeMn1 at 5 mT, 10 mT, 15 mT, 20 mT and 25 mT.

6.1.6 Cosine Deviation Factors: Implications for a 360° Angle Sensor

The cosine deviation caused by the AMR effect, interlayer coupling, and the rotation of the pinned layer magnetization has already been experimentally determined in an MR rotation curve measured from a spin valve. The influence of these cosine deviation factors on the angular error of a 360° angle sensor could be studied by simulating the output signals from the Wheatstone bridge circuits of a 360° angle sensor. This can be done by using the data set from a single MR rotation measurement. First the resistance data from the rotation measurement is shifted 180° in phase. The original data set is referred to as resistance R_1 and the shifted data set as resistance R_2. This represents two different bias directions in the Wheatstone bridge circuit as shown in Eq. (2.24). V_{out} is calculated at every θ_H value using Eq. (2.26) and the data sets of R_1 and the R_2 signals. The V_{out} is shifted 90° in relation to the reference angle to simulate the sine output signal from the GMR 360° angle sensor. The first output signal is the V_{cos} and the shifted bridge signal is V_{sin}. The angle α measured by the angle sensor is calculated by taking the arctan from cosine and sine signals as shown in Eq 2.26. The angular error is calculated by taking the difference between the measured angle and reference angle.

MR rotation curves measured from a patterned PtMn spin valve with SAF stack, 20 μm wide stripe (see Figure 4.2), in the field range of 0-100 mT were used to simulate rotation curves from a GMR 360° angle sensor. This patterned sample is referred to as a test stripe throughout the rest of the dissertation. The cosine deviation, angular error in the case of the simulated bridge signal, was calculated as a function of applied field from the simulated rotation curves and plotted in Figure 6.21. The cosine deviation from the original MR rotation measurements (see Figure 6.14) is plotted for comparison in Figure 6.21. There was a drastic reduction in the cosine deviation from the simulated bridge signal in comparison to the cosine deviation from the unpatterned samples. For example, the cosine deviation at 10 mT dropped from 10° for the unpatterned sample to 2.6° for the bridge signal (see Figure 6.21). The increase in cosine deviation caused by the rotation of the pinned layer magnetization was still evident, but was not as drastic in comparison to the cosine deviation in the MR rotation curves measured from the test stripe.

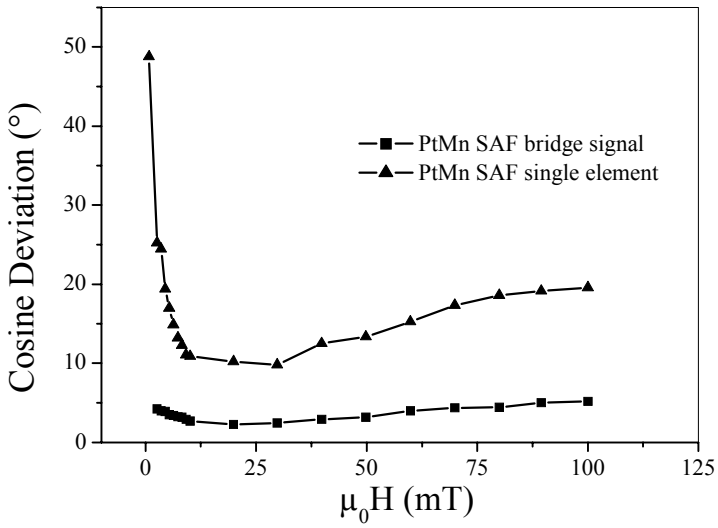

Figure 6.21: Comparison of the cosine deviation calculated from the rotation measured from a test stripe patterned from PtMn spin valve with SAF sample and the 360° angle sensor out signal generated from the MR rotation measurement.

The reason for the improvement in the sensor error becomes evident upon direct comparison of normalized rotation curves from a single test stripe and from the bridge signal (see Figure 6.22a). The improvement in the cosine deviation is due to normalization of the rotation curve at 0°, 90°, 180° and 270° points by the Wheatstone bridge circuit. This leads to drastic reduction in the cosine deviation in the bridge signal as seen in Figure 6.22b. The reduction of the cosine deviation was an unexpected benefit of the use of the Wheatstone bridge circuit in the angle sensor design.

Temperature dependence of the cosine deviation factors must also be taken into account in this study. The AMR effect [Kit02] and the interlayer coupling due to interface roughness [Koo96] will reduce in magnitude with increasing temperature thus decreasing the amount of cosine deviation caused by these effects. The cosine deviation caused by the rotation of the pinned layer magnetization; however, increases with rise in temperature due to the reduction of the exchange bias effect. The operating window for a GMR 360° angle sensor will shrink with rise in temperature. The temperature dependence of the exchange bias effect is therefore the most critical parameter of the spin valve system in regards to angle sensor application.

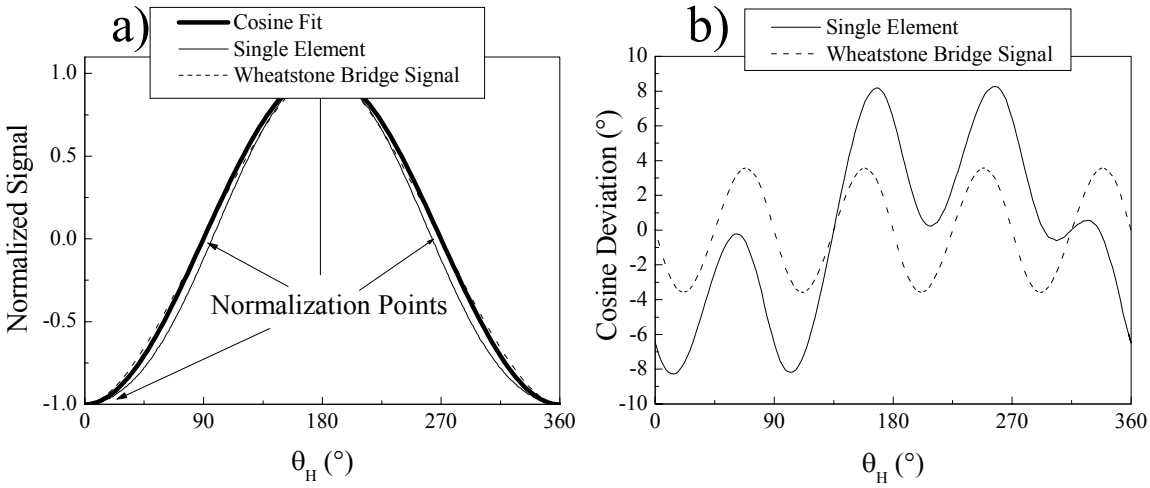

Figure 6.22: a) Normalized rotation curve measured at 20 mT from a single test strip and the simulated bridge signal from a Wheatstone bridge circuit and b) the resulting cosine deviation for both measurements plotted as function of applied field direction.

6.1.7 Summary: Cosine Deviation Factors

The magnetoresistance changes due to spin-dependent scattering in a spin valve are dependent on the angle between the magnetization direction of the pinned layer and the free layer. In the ideal case the GMR effect measured from a spin valve shows a cosine dependence when rotated in an applied magnetic field. This occurs when the free layer follows perfectly the applied field direction and the pinned layer magnetization remains fixed in one direction. In reality there are numerous deviation factors from this expected cosine dependence. The identification and understanding of these disturbing influences was critical to the determination of the magnetic field operating window of a spin valve based angle sensor. The major highlights of these experimental results are summarized below:

- AMR effect was found to be a significant portion of the overall MR effect in a spin valve and to cause appreciable deviation from a cosine dependence of the GMR effect. The resistance changes cause by the AMR effect can be added as a cosine-squared signal to the overall resistance change. It is dependent upon the angle between the current and the magnetization direction of the pinned layer and free layer respectively.

- Interlayer coupling was seen to influence the direction of the free layer magnetization during the rotation of a spin valve in an applied magnetic field above the measured H_e of the spin valve and up to $1/6^{th}$ the field value of the measured H_{eb} of the spin valve. The amount of cosine deviation was found to depend on the strength and type (antiferromagnetic or ferromagnetic) interlayer coupling.

- The pinned layer magnetization was found to rotate in the direction of the applied field at field values much lower than the H_{eb} of a spin valve ($\mu_o H > 1/6^{th}$ of H_{eb}) This was identified as the most important magnetic parameter of spin valve in regards to determining the magnetic operating window for the angle sensor application.

- The validity of a macro-magnetic model of a spin valve system developed by Dieny, et al. [Die00], and Tietjen, et al. [Tie02], was confirmed through comparison between experiment and simulation.

- The reduction in the cosine deviation in the output signal of a 360° angle sensor, in comparison to the MR rotation measurement from a single element or wafer, is due to the design of the Wheatstone bridge circuit. The Wheatstone bridge circuit causes a normalization of the MR signal from a half-bridge element, which leads to a reduction of the cosine deviation.

6.2 Selection of Spin Valve System

A wide range of spin valves with different antiferromagnets (NiO, FeMn, IrMn, PtMn) were studied with standard MR measurements to determine the size of the MR effect and other magnetic parameters such as the H_{eb}, H_e, H_{c1}, and H_{c2} of each spin valve system. The X-ray diffraction measurements were made to analyze the crystal structure and texture of each spin valve system. The temperature dependence of MR effect and H_{eb} of each spin valve was determined up to 170°C. These measurements were necessary to determine which spin valve system had a sufficient MR effect (MR>3%) and H_{eb} (H_{eb} >100 mT) over the following temperature range [–40°C to 150°C]. The T_b of each spin valve system was determined from the MR temperature-dependent measurements. The T_b of the spin valve must be greater than 190°C to insure the stability of the bias direction up to 150°C. A direct comparison was made between the studied spin valve systems upon conclusion of the previously mentioned experiments.

6.2.1 NiO Spin Valve System

The first antiferromagnet analyzed was a fcc metallic monoxide, NiO. NiO spin valves were first studied by Carey, et al. [Car92], and have been of continued interest over past ten years [Ant94] [Hwa98]. NiO has the typical advantages of a metallic oxide antiferromagnetic, which includes the reduction of the MR loss due to shunting and a high corrosion resistance. The NiO AFM has a reported T_b of 220°C [Car92].

The NiO spin valve stack was of the following structure: Si/SiO_2/NiO(50)/NiFe(5)/ Cu(2.5)/NiFe(5). All layer thicknesses are given in nm. NiO bottom spin-valve system was deposited on 4-inch oxidized Si(100)-wafers under a magnetic bias field by rf magnetron sputtering at IFW-Dresden. NiFeB permanent magnets built into the substrate holder were used to supply the magnetic bias field during the sputter deposition. NiO is mostly deposited by reactive sputtering of Ni in an Ar/O_2 gas mixture [Ber99], but in this case a NiO target of stoichiometric composition was used in the sputter deposition. No Ta buffer layer was used in the spin valve stack due to the availability of only three cathodes in the sputtering system.

6.2.1.1 Magnetoresistive Characteristics

This NiO spin valve system had a MR effect of 4.1% and H_{eb} of 9 mT (Figure 6.23). These values were much lower in comparison to the literature values of 8% MR effect and 20 mT for the H_{eb} [Yam99]. The low MR effect can be partially explained by the use of NiFe rather than Co in the pinned layer and the lack of Co interface layer in the free layer [Par93]. The H_e was measured to be 0.8 mT, which is an indication of ferromagnetic coupling in the spin valve. H_{c1} was 0.1 mT, which was unusual considering the uniaxial anisotropy of the free layer is set parallel to the bias direction during the deposition. This should result in a much higher hysteresis value, e.g. 0.5 mT (see Section 2.5.2.1). H_{c2} was 1.5 mT for the pinned layer, which is higher than the coercivity of the free layer. The coercivity increase is due to the induced uniaxial anisotropy from the adjacent NiO AFM layer [Car92].

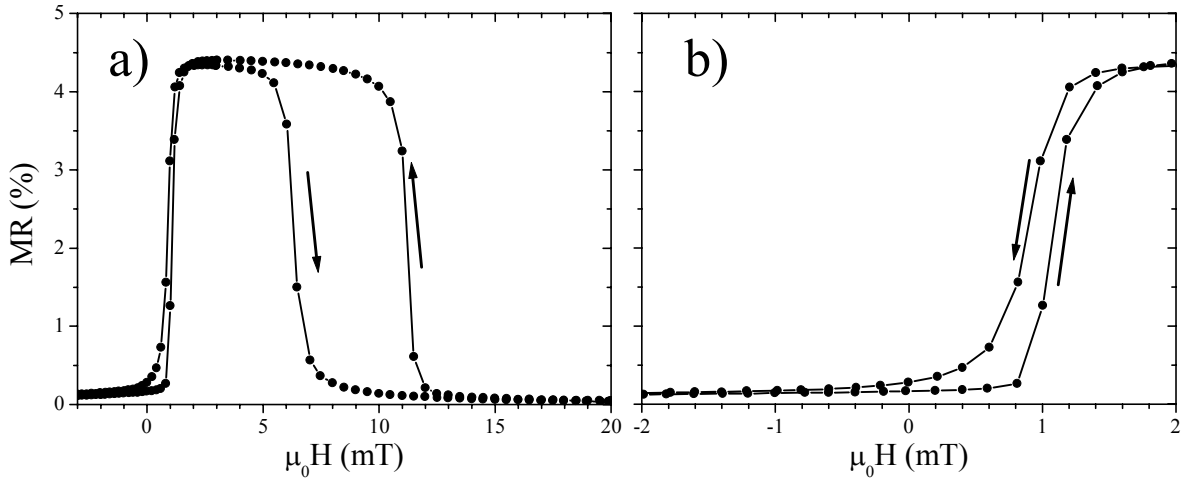

Figure 6.23: MR curve measured from a NiO spin valve showing the a) major loop and b) minor loop.

6.2.1.2 Crystal Structure

The X-Ray diffraction pattern of the NiO spin valve (see Figure 6.24) showed the presence of three different cubic NiO orientations: (200), (111) and (220) at 36.7°, 43.0° and 62.2° respectively. These are the same peak positions as reported in literature [Car92][She96]. The calculated peak positions assuming a lattice parameter of 0.4177 nm [JCS89], were 37.26° for the (200) reflection, 43.25° for the (111) reflection and 62.88° for the (220) reflection as shown in Figure 6.24 by the position of the solid line markers. This shift in the NiO peak from the calculated peak position has also been observed in other NiO thin films deposited by sputter deposition [Car92].

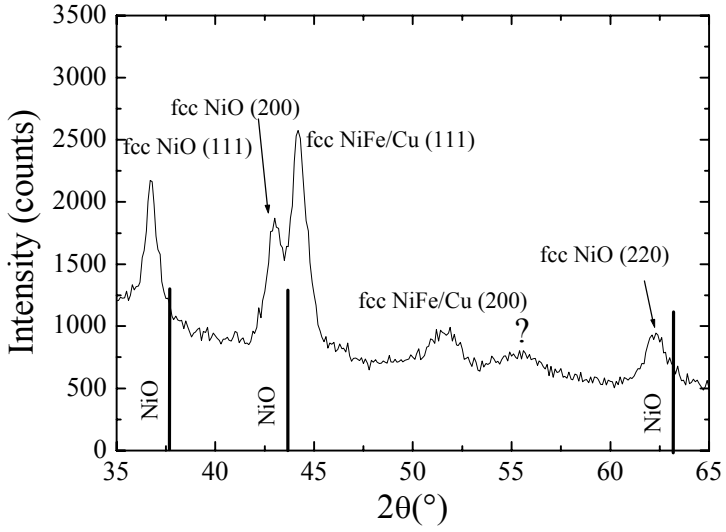

Figure 6.24: X-ray diffraction pattern measured from a NiO spin valve. The markers indicated the expected positions of the NiO reflections [JCP96].

The peaks at 44.24° and 51.6° were identified as the combined reflection for NiFe/Cu (111) and (200) (see Figure 6.24). The presence of a single reflection for NiFe and Cu is not unusual considering minimal difference in lattice parameters between fcc-Cu (a_0 = 0.3620 nm) and fcc-NiFe (a_0= 0.357 nm). This allows for coherent growth between the layers [Koo96]. The combined NiFe/Cu (111) reflection should have been located between the

expected peak positions for NiFe, 43.9°, and Cu, 43.37°, as seen in Figure 6.26. Instead the peak position was shifted almost 0.7° in relation to the expected peak position. The reason for the peak shift as well as growth in two different orientations, (111) and (200), was probably related to growth directly on NiO layer. The NiO layer grew in three different orientations: (111), (200) and (220).

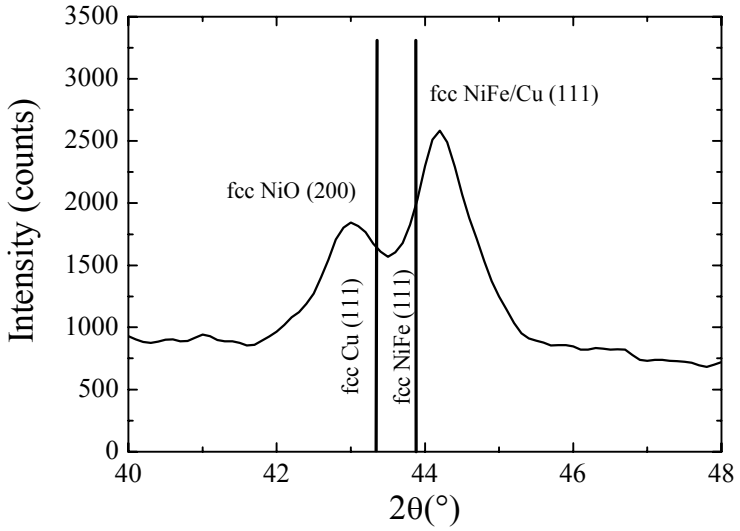

Figure 6.25: Close-up of the X-ray diffraction peak for (111) NiFe/Cu and (200) NiO. The markers indicated the expected positions of the Cu and NiFe (111) reflections [JCP96].

The presence of three different NiO orientations rather a single (111) peak was explained by poor control of the Ar partial pressure during the sputter deposition. A (111) texture is preferred due to the relation between a high GMR effect and the (111) texture (see Section 2.5.5). X-ray diffraction studies on NiO/NiFe bilayers have shown a transition in the crystal texture from (111) to (220) when increasing the Ar partial pressure (from 0.75×10^{-3} mbar to 3×10^{-3}mbar) during the sputter deposition [Tie00]. The growth mode and nucleation rate of the NiO thin film depends greatly on the Ar partial pressure. A small shift in the argon partial pressure during the deposition could change the growth mode or the nucleation rate.

The low GMR effect, in comparison to literature, is partially explained by the use of NiFe in the pinned and free layer, but the presence of two different orientations in the NiFe/Cu layer also leads to additional reduction of the GMR effect. A (111) texture coincides with a coherent columnar grain growth between the pinned, spacer, and free layers [Koo96]. A decrease in the grain size is seen with a lack of columnar growth and this raises the number of grain boundaries in the spin valve stack [Koe96]. This increases then number of possible scattering sites thus increasing the spin-independent scattering and further decreasing the size of the MR effect. The presence of two different NiFe/Cu (111) and (200) orientations was not indicative of columnar grain growth. A high H_{eb} has also been shown to coincide with the presence of a (111) texture in the spin valve [Lai96] [Hwa98], but the relationship between a (111) texture and increased H_{eb} in NiO spin valves is not yet understood.

6.2.1.3 Temperature Dependence of the MR and Exchange Bias Effect

The temperature dependence of the MR and H_{eb} was determined by MR measurements made from 25°C to 170°C. The point at which H_{eb} dropped to zero in the MR plot is defined

as the T_b of the AFM as illustrated in Figure 6.26. NiO was found to have a T_b of 145°C, which is lower than the reported T_b of 220°C [Car92] (Figure 6.26). This lower T_b was probably related to the lack of (111) texture in the spin valve (see Figure 6.24). The MR effect dropped from 4.1% at room temperature to 0.2% at 160°C (Figure 6.26). The loss in MR was linear up to 100°C and then showed a more abrupt loss up to 140°C.

The linear portion is associated with increased lattice vibration due to thermal agitation while the abrupt drop in MR is associated with the loss of the exchange bias effect. The main limiting factor for the blocking temperature in this case was the loss of magnetic order in the antiferromagnet with increase in temperature and not interdiffusion in the spin valve stack [Koo96]. There was no interdiffusion in the NiO sample, since the resistance in the wafer sample remained unchanged after the high temperature MR measurement. The NiO spin valve system did not have sufficient MR or H_{eb} over the specified temperature range.

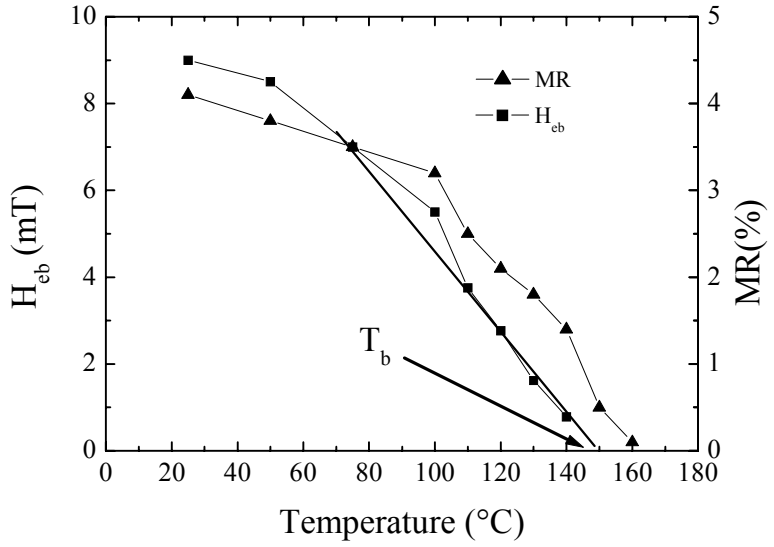

Figure 6.26: Temperature dependence of the MR effect and H_{eb} of a NiO spin valve.

6.2.2 FeMn Spin Valve System

The FeMn spin valve system was the first spin valve structure to be reported in literature [Die91]. The equilibrium bulk crystal structure of FeMn is normally the α-phase (bcc), but FeMn grown on a lattice-matched fcc buffer layer (Cu or NiFe) has a fcc structure up to few tens of nm in layer thickness. The antiferromagnetic ordering of the fcc FeMn-phase occurs from 33-55% Mn at room temperature [Umb66]. The standard alloy composition of $Fe_{50}Mn_{50}$ was used in this FeMn spin valve system. This particular FeMn spin valve was of the following structure: Si/SiO_2/Ta(5)/NiFe(4)/Co(1)/Cu(2.6)/Co(1.4)/FeMn(8)/Ta(5)/Cu(0.5). The deposition conditions are summarized in Section 3.1.4.

A Ta/NiFe buffer layer was included in the spin valve stack to induce the growth of a (111) orientation in the entire spin valve stack and the FeMn layer in the fcc phase [Len97]. The NiFe layer in the buffer also functions as the free layer in the spin valve stack in the top spin valve configuration. The uniaxial anisotropy of the free layer is set perpendicular to the bias direction in the free layer by a 90° rotation of the magnetic bias field before deposition of the pinned layer. This crossed anisotropy axis orientation reduced the H_{c1} of the spin valve(see Section 2.5.5.5).

6.2.2.1 Magnetoresistive Characteristics

This FeMn spin valve system had a MR effect of 7.9% and a H_{eb} of 55 mT as seen in Figure 6.27. The FeMn spin valve was a vast improvement in comparison to the NiO spin valve in terms of the measured MR effect and H_{eb}. The H_e was 1.1 mT, which was an indication of ferromagnetic coupling in the spin valve due to interface roughness. H_{c1} was 0.1 mT for the free layer due to the crossed anisotropy axis orientation between free and pinned layer. H_{c2} was measured to be 6 mT, which was a sizable increase in comparison to the H_{c2} of the NiO spin valve, 1.5 mT. This is due to use of a Co pinned layer, which has a higher saturation magnetization than NiFe [Jil91] and the induced uniaxial anisotropy from the adjacent (111) textured FeMn layer.

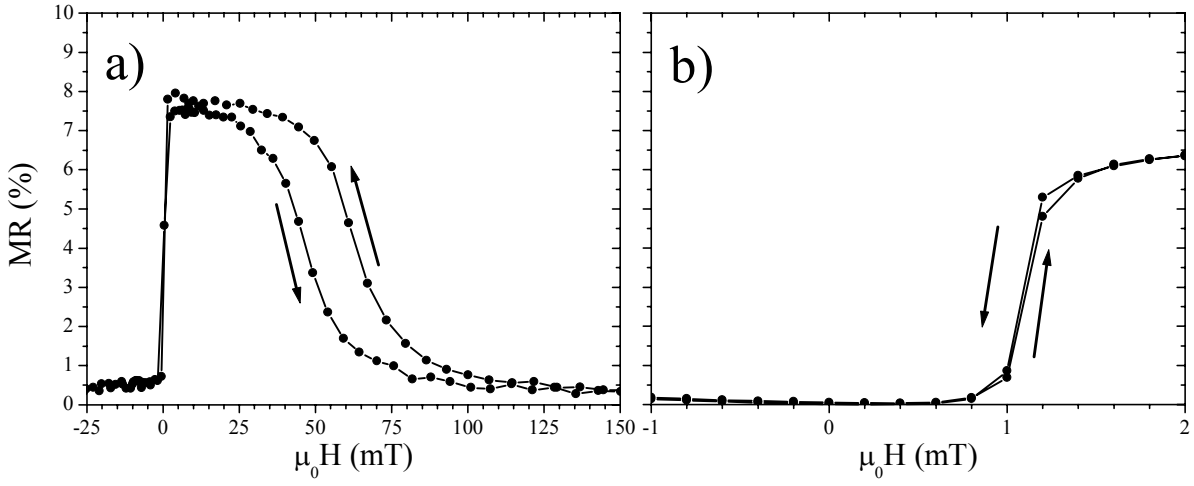

Figure 6.27: MR curve measured from a FeMn spin valve showing the a) major loop and b) minor loop.

6.2.2.2 Crystal Structure

The X-ray diffraction pattern of the FeMn spin valve showed the presence of only a single reflection at 43.7°(see Figure 6.28). This was identified as the combined (111) reflection for fcc FeMn, Co, Cu and NiFe. The existence of a (111) texture in the spin valve stack was important to ensure a high GMR effect in the spin valve system [Cho97] [Gup98] [Cho98]. The (111) reflection at 43.7° corresponded to a lattice parameter of 0.358 nm, which is close to the lattice parameter of the NiFe buffer layer. Growth of the spin valve stack on the NiFe buffer layer lead to the existence of strained lattice through the rest of the spin valve structure. The semicoherent growth between NiFe, Cu, Co, and FeMn layers was possible due to the minimal variation of the lattice parameter between the different materials (fcc-Cu: a_0 = 0.361 nm; fcc-Co: a_0 = 0.354 nm; fcc-NiFe: a_0 = 0.357 nm; fcc-FeMn: a_0 = 0.363 nm) [Koo96]. Semicoherent growth between the layers in a spin valve stack has already been seen in High Resolution Transmission Electron Microscopy (HR-TEM) pictures taken of a FeMn top spin valves of a similar structure [Koo96]. The lattice parameter was therefore the average of all four materials.

The two small satellite peaks, at 42.5° and 45.3°, flanking the (111) peak were attributed to constructive interference between the NiFe/Co free and Cu spacer layers and the NiFe/Co free and Co pinned layer. Kamuguchi, et al. [Kam96], concluded this from XRD diffraction patterns measured from a spin valve samples that sequentially deposited. No reflection was seen for the Ta buffer or passivation layer.

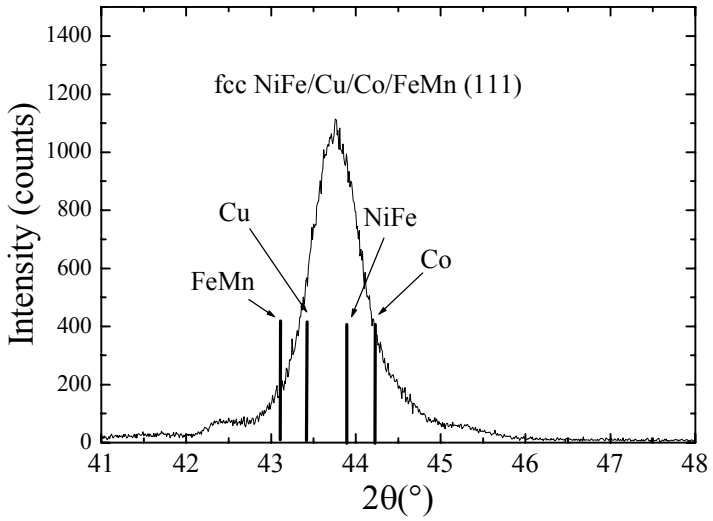

Figure 6.28: X-ray diffraction pattern of an FeMn spin valve. The expected positions for (111) reflection of fcc FeMn, fcc-Cu, fcc-NiFe and fcc-Co are also indicated in the pattern [JCP96].

6.2.2.3 Temperature Dependence of GMR and Exchange Bias Effect

The blocking temperature of FeMn was determined to be 140°C (see Figure 6.29). A T_b of 150°C has been reported in spin valves with a 10 nm thick FeMn layer. A spin valve with a 8 nm thick FeMn layer should have a T_b lower than 150°C according to the relationship between the layer thickness and the T_b of the FeMn antiferromagnet [Hos94]. The MR effect of the FeMn spin valve dropped to 1.2% at 160°C from 7.9% at room temperature (see Figure 6.29). The loss in MR was linear up to 140°C and suddenly dropped 2.5% in the MR effect at 140°C. The behavior of the MR effect with mimicked that of the NiO spin valve system. The MR loss up to 140°C, the linear portion of the MR loss, was due to increased vibration in the lattice and an abrupt drop in the measured MR occurred with the complete loss of the exchange bias effect at 140°C. The FeMn spin valve system did not have sufficient MR or H_{eb} up to 150°C.

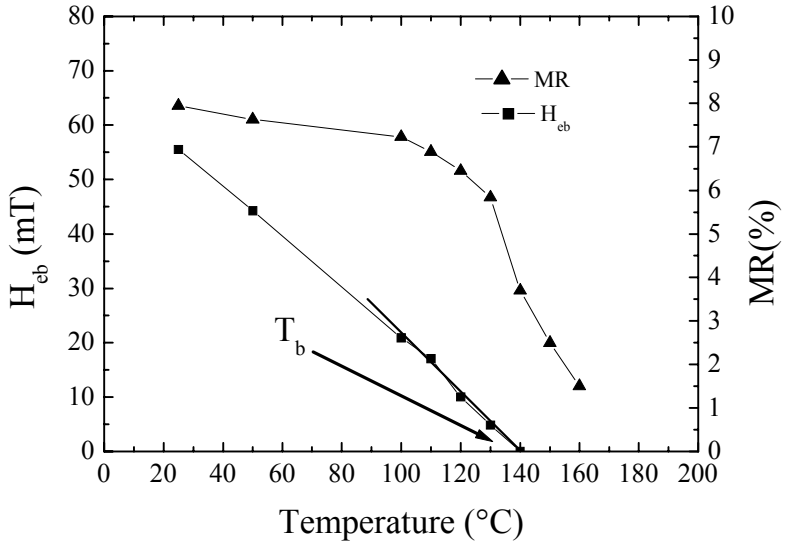

Figure 6.29: Temperature dependence of the MR and H_{eb} of FeMn spin valve.

6.2.3 IrMn Spin Valve System

IrMn was considered a better candidate for the automotive sensor applications due to it's higher reported T_b of 230°C [Led99] and better corrosion resistance in comparison to FeMn. IrMn is a disordered solid-solution alloy with a fcc structure [Fuk97][Nak97]. The antiferromagnetic IrMn phase exists from 10 to 30 atm% Ir [Yam71]. $Ir_{20}Mn_{80}$ was the standard alloy composition used in these spin valves. The deposition conditions are summarized in Section 3.1.4. An IrMn top spin valve of the following structure was used for the experiments described in the following section: Si/SiO_2/Ta(5)/NiFe(7.2)/Co(1)/Cu(3)/ CoFe(2)/IrMn(10)/Ta(5). All layer thicknesses are given in nm. The uniaxial anisotropy of the free layer is set perpendicular to the unidirectional anisotropy in the free layer during deposition. A Ta/NiFe buffer layer was used in this case to only induce (111) texture and not to stabilize to the IrMn in the fcc phase as with FeMn [vDr00]

6.2.3.1 Magnetoresistive Characteristics

The magnetoresistive characteristics of the IrMn spin valve at room temperature were slightly inferior to those of the FeMn spin valve (MR = 7.9% and H_{eb} = 55 mT). The IrMn spin valve was found to have an MR effect of 7.5% and a H_{eb} of 45 mT as seen in Figure 6.30. The H_e was measured to be 0.8 mT, which was again an indication of ferromagnetic coupling in the spin valve due to high interface roughness. H_{c1} was 0.1 mT for the free layer, again a result of the crossed anisotropy axis orientation. The induced uniaxial anisotropy from the adjacent IrMn layer raised the H_{c2} to 6.5 mT.

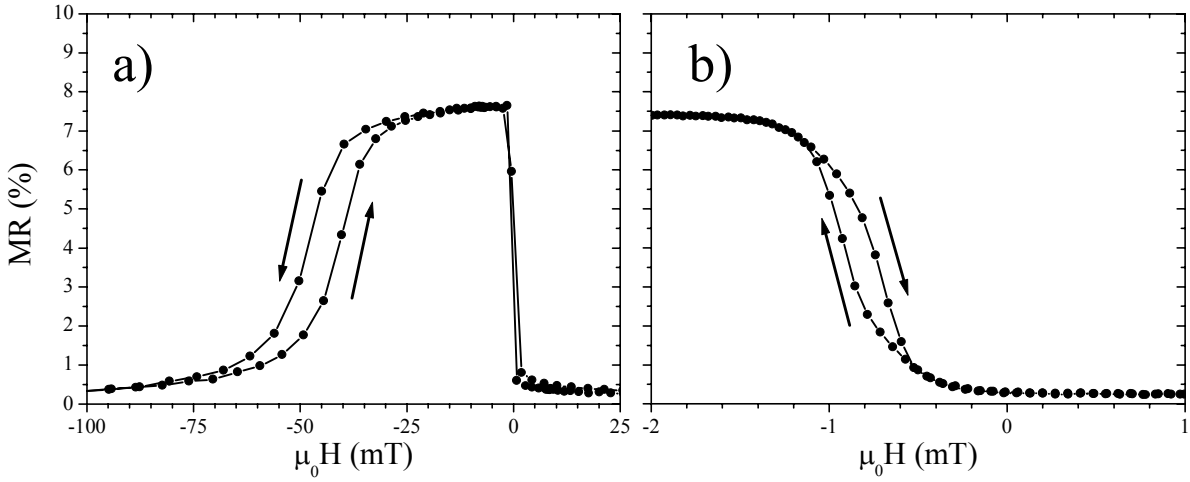

Figure 6.30: MR curve measured from a IrMn spin valve showing the a) major loop and b) minor loop.

6.2.3.2 Crystal Structure

The reflection observed at 41.3° was associated with the IrMn layer, while the reflection at 44.0° is seen as the combined reflection for fcc NiFe/Cu/CoFe (111) peak (see Figure 6.31). The lack of any other reflections, other than at 42.8°, indicated that the IrMn spin valve system had a (111) texture. The (111) texture is preferred due to the higher GMR effect [Cho98] and H_{eb} [vDr00] observed in IrMn spin valves with this texture. The Cu and CoFe

layers grew lattice matched with the NiFe buffer/free layer as indicated by the presence of a single (111) reflection at 44.0°. The (111) reflection at 44° for NiFe/Cu/CoFe layers was shifted by 0.3° in comparison to the (111) reflection of the NiFe/Cu/Co/FeMn layers of the FeMn spin valve (see Section 6.2.2.2). The IrMn layer did not grow lattice matched with the NiFe/Cu/CoFe trilayer, as was the case with FeMn spin valve (see Figure 6.28).

The bulk of the research to date on IrMn thin films has identified this (111) reflection from the IrMn layer as a disordered fcc IrMn alloy [Fuk97] [Dev98], but a ordered fcc $IrMn_3$ crystal structure has also been reported in IrMn thin films [Yam74]. The presence of the cubic-Mn (330) peak at 42.8° indicated that the ordered $IrMn_3$ was the structure for the IrMn in this spin valve. There was an excess amount of Mn present (5 atm%), target composition $Ir_{20}Mn_{80}$, if the $IrMn_3$ phase had grown during the sputter deposition.

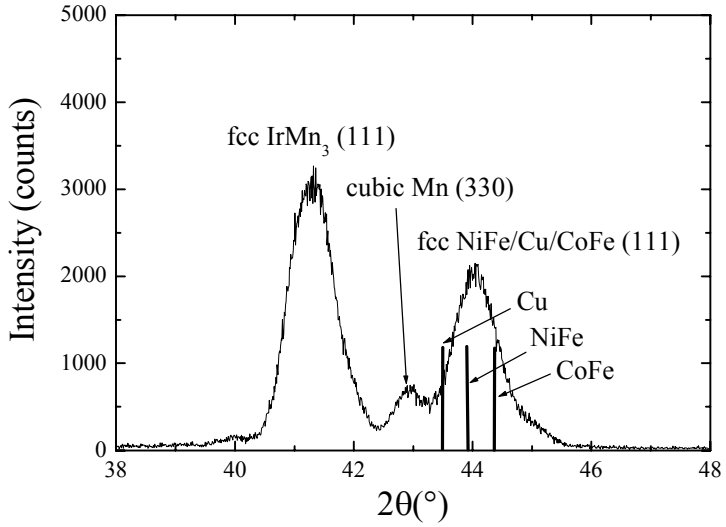

Figure 6.31: X-ray diffraction pattern of a IrMn spin valve. The solid lines in the diffraction pattern represent the expected positions for the (111) reflection of fcc-Cu, fcc-NiFe, and fcc-CoFe.

6.2.3.3 Temperature Dependence of GMR and Exchange Bias Effect

The blocking temperature for the IrMn spin valve system was determined to be 190°C. (see Figure 6.32). This is a large improvement over the NiO and FeMn spin valve systems, but this T_b still was at the limit of the specified maximum temperature of 190°C. The measured T_b was significantly lower than the T_b commonly reported in literature for IrMn of 230°C [Led99]. The main limitation to blocking temperature was again the loss of magnetic order with increasing temperature and not interdiffusion. The MR effect showed a linear dependence over the entire temperature range in contrast to FeMn and NiO (see Figure 6.32) The MR effect had dropped to only 5.1% at 170°C from 7.5% at RT indicating sufficient MR effect for the temperature range up to 150°C.

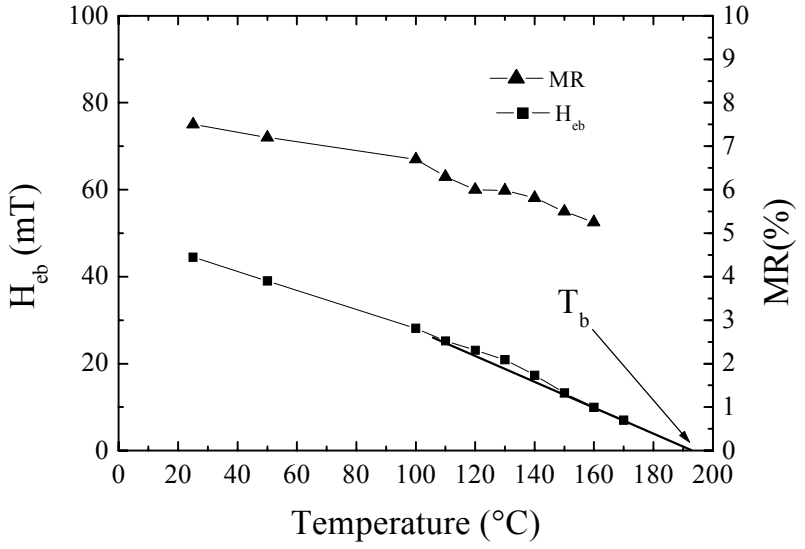

Figure 6.32: Temperature dependence of the MR and H_{eb} of IrMn spin valve.

6.2.4 PtMn Spin Valve System

A PtMn antiferromagnet has a much higher T_b of 380°C according to literature than either NiO, FeMn or IrMn [Mao00]. PtMn also shows excellent corrosion resistance in comparison to FeMn. The only major drawback is the requirement of a high temperature anneal (200-300°C / several hours) to transform PtMn from the nonmagnetic disordered fcc phase into the ordered antiferromagnetic fct phase. The antiferromagnetic fct phase of PtMn exists from 41 to 66 atm% Mn [Kré68] [Ric74]. $Pt_{50}Mn_{50}$ was the standard alloy composition for the PtMn spin valves studied in this dissertation.

This particular PtMn spin valve system had the following structure: Si/SiO_2/Ta/ NiFe/PtMn/CoFe/Cu/CoFe/NiFe/Ta. The standard spin valve deposition conditions are summarized in Section 3.14. A Ta/NiFe buffer is used to induce a (111) texture in the spin valve stack. The uniaxial anisotropy of the free layer is initially set perpendicular to the bias direction in the free layer by changing the direction of the magnetic bias field prior to deposition of this layer. The PtMn spin valve was annealed under vacuum at 200-300°C for several hours under a high applied magnetic field (~1T) to transform the disordered fcc phase into the ordered antiferromagnetic fct phase.

6.2.4.1 Magnetoresistive Characteristics

An MR effect of 6.1% and a H_{eb} of 42 mT were measured from the PtMn spin valve after the post-deposition anneal (see Figure 6.33). The H_e was measured to be 0.75 mT which is an indication of high ferromagnetic coupling. The H_{c1} was found to be 0.9 mT, which indicated a parallel anisotropy axis orientation between free and pinned layer. The uniaxial anisotropy axis orientation of the free layer was changed during the high-temperature anneal [Bar01].

The coercivity of the pinned layer in the PtMn spin valve, H_{c2} = 41 mT, greatly increased in comparison to that of the FeMn (see Figure 6.27) and IrMn spin valve systems (see Figure 6.30). A high Hc_2 has also been reported in other studies of PtMn spin valves [Sai97]. The cause of the higher induced anisotropy in PtMn is not yet understood, but it is apparently related to the fct crystal structure of PtMn. FeMn and IrMn have disordered fcc crystal structure while NiMn and PtMn have the a ordered fct structure [Sch99].

This difference in coercivity was quantified by Pokhil, et al. [Pok99], by comparing NiFe/IrMn and NiFe/NiMn bilayers. NiMn had induced uniaxial anisotropy that is 100 times

higher than that of the intrinsic uniaxial anisotropy in single NiFe layer while IrMn had only induced a uniaxial anisotropy that was 6-8 times higher than the intrinsic uniaxial anisotropy. These results could also applied to PtMn since both NiMn and PtMn belong to the same class of fct AFMs. A ordered fct AFM must in some way, not yet understood way, induce a larger uniaxial anisotropy in the pinned layer in comparison to the disordered fcc AFM.

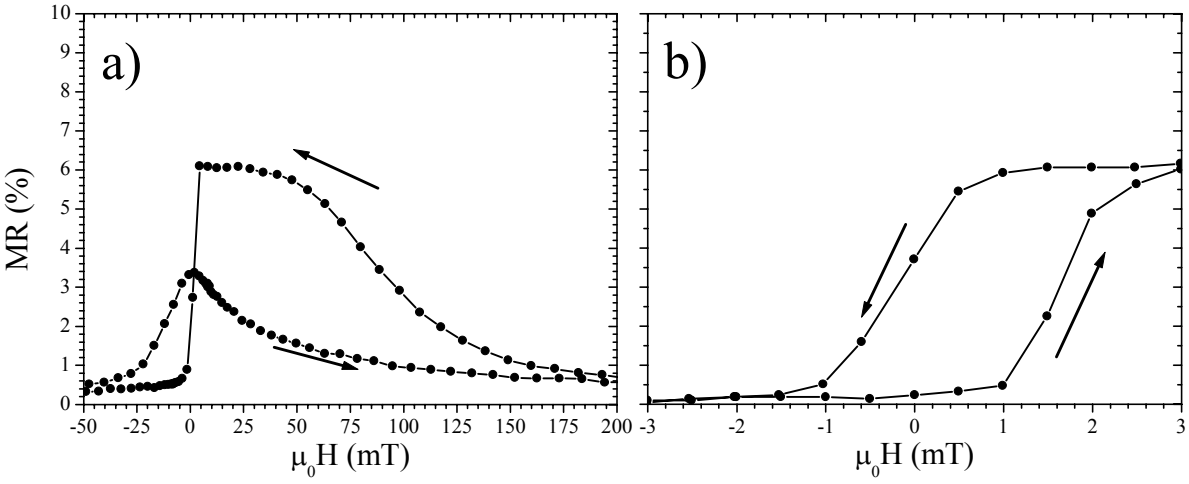

Figure 6.33: MR curve measured from a PtMn spin valve showing the a) major loop and b) minor loop.

6.2.4.2 Fcc to Fct Transformation

XRD measurements were performed on as-deposited and annealed PtMn wafer samples to confirm the transformation from a disordered fcc structure to a ordered fct structure. A high temperature anneal (200-300°C / several hours) was required to transform the PtMn from the fcc to the fct phase. The as-deposited PtMn spin valve stack showed a strong (111) texture (see Figure 6.34). Prior to the anneal the PtMn fcc (111) reflection was observed at 39.8° and the NiFe/Cu/CoFe fcc (111) peak at 43.8°. This corresponded to a lattice parameter of 0.391 nm for fcc PtMn and 0.358 nm for the fcc NiFe/Cu/CoFe trilayer. This is virtually identical to values stated in literature [Pok01] [Mao00]. After the anneal the PtMn (111) peak shifted to 40.2° indicating that the full transformation of PtMn into the antiferromagnetic fct phase. The location of the NiFe/Cu/CoFe fcc (111) reflection remained the same despite the high temperature anneal. The difference in intensity between the peaks is due to the large thickness of the PtMn layer in comparison to the rest of the spin valve stack.

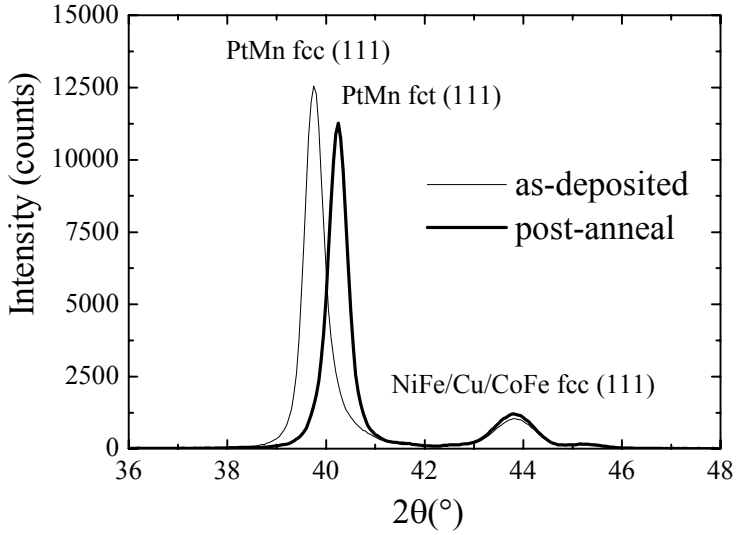

Figure 6.34: X-ray diffraction pattern of a PtMn simple spin valve in the as-deposited and the annealed state.

6.2.4.3 Temperature Dependence of GMR and Exchange Bias Effect

The exact value for T_b of PtMn could not be determined from these measurements due to the temperature limitation of the sample heating stage (max. temp. 170°C). According to literature the T_b PtMn should be approximately 380°C [Mao00]. The T_b of the PtMn spin valve could not be determined by the temperature de MR measurements. The H_{eb} has dropped from 49 mT at 25°C to 37 mT at 170°C (see Figure 6.35). The MR linearly dropped to 5.9 % at room temperature to 3.5 % at 170°C indicating sufficient MR effect up to 150°C. PtMn has a sufficient T_b up to 150°C, but the H_{eb} of the PtMn spin valve was simply not sufficient to meet exchange bias criteria (H_{eb}>>100 mT).

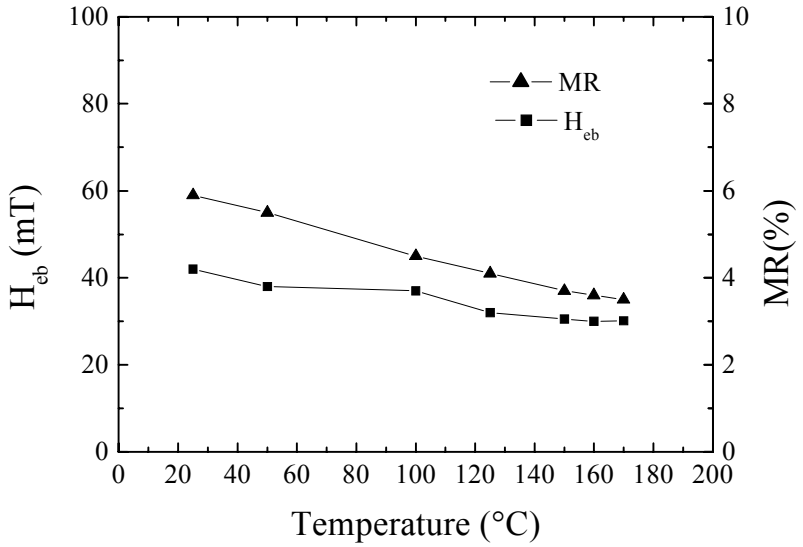

Figure 6.35: Temperature dependence of the MR and H_{eb} of a PtMn spin valve.

6.2.5 PtMn Spin Valve System with SAF

The PtMn simple spin valve showed the highest T_b (T_b>>190°C) among the previously studied spin valves, but had insufficient H_{eb} up to 190°C and large hysteresis in the MR curve. The most common solution to these problems was the insertion of a Synthetic AntiFerromagnet (SAF) in the PtMn spin valve structure. The H_{eb} in a spin valve can be increased fourfold and the large hysteresis is reduced with the inclusion of a SAF in the spin valve stack (see Section 2.7). The appropriate spin valve system must have a H_{eb} >>100 mT to insure an magnetic field operating window of 10-100 mT as proven experimentally in Section 6.1.3 The PtMn spin valve system with SAF was deposited on the same Cyberite sputtering system under the same deposition conditions as the PtMn simple spin valve (see Section 6.2.4). The only difference is the addition of a Ru spacer layer and CoFe reference layer in the spin valve stack (SAF structure).

6.2.5.1 Magnetoresistive Characteristics: As-deposited

The PtMn spin valve with SAF was found to have an MR effect of 6.0% and a H_{ex} of 140 mT prior to the anneal as seen in Figure 6.36a. H_{ex} is a measurement of the exchange biasing due to SAF and not simply the pinned layer (see Section 2.7). The H_{saf} was measured at 63 mT for this sample. A bias direction already exists in the SAF despite the lack of exchange biasing from the AFM layer. This is due to the antiferromagnetic coupling between the pinned layer and the reference layer. H_e was measured to be 0.69 mT, which is an indication of ferromagnetic orange-peel coupling. H_{c1} was 0.25 mT for the free layer due to crossed axis anisotropy orientation between the free layer and reference layer. The H_{c2}, coercivity of the reference layer, was measured to be only 1 mT. H_{c2} represents the coercivtity of the reference layer instead of the pinned layer in a spin valve with SAF. The coercivity of the pinned layer H_{c3} could not be measured with normal MR, but should be on the same order of magnitude as the reference layer.

The MR curve showed an unusual switching of the bias direction in the SAF at low field value of only 22 mT. Normally an unbiased SAF must be brought into saturation to change the bias direction [Len99]. The switching of the bias direction of the SAF at 22 mT can be best described through a detailed description of the magnetization directions in the individual layers of the SAF (see Figure 6.36). The MR measurement began at zero field with the field direction anti-parallel to the bias direction of the SAF. As the field increased to positive values, The magnetization of the reference layer was parallel to the free layer and therefore no MR was measured.

The sudden jump in the MR value at 22 mT could only be explained by an anti-parallel alignment between the magnetization of the free layer and the reference layer. The magnetization of the pinned layer must have been pulled into the direction of the applied field. The reference layer magnetization immediately switched to anti-parallel orientation to pinned layer due to the antiferromagnetic interlayer coupling across the Ru space layer. Upon going to negative field values, the bias direction in the SAF was now the same as the direction of the applied field and the measured MR effect dropped to a minimum.

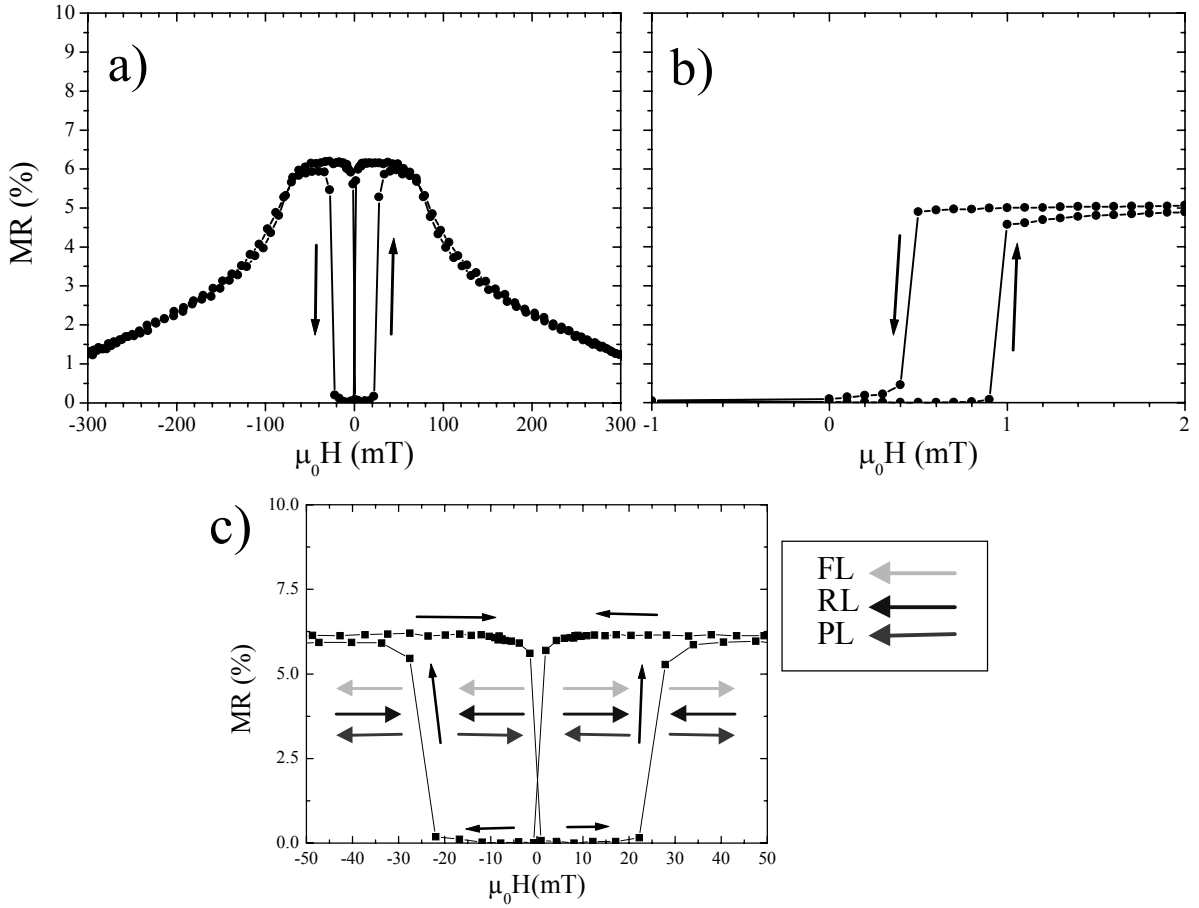

Figure 6.36: MR Curve measured from a PtMn spin valve with SAF in the as-deposited state showing the a) major loop and b) minor loop. c) This measurement at lower field strength illustrates the magnetization direction of each ferromagnetic layer in the spin valve in relation to the MR curve.

The pinned layer magnetization again rotated in the direction of the applied field at -22 mT and the reference layer magnetization reoriented itself 180° to the pinned layer. The magnetization of the free and reference layer was again in the anti-parallel orientation resulting in a rise of the measured MR. It was not possible to switch the bias direction by applying a field 90° to the original bias direction (see Figure 6.37) as is possible with other unbiased SAF systems [Len99]. The fact that the bias direction could only be changed 180° and not 90° seemed to indicate that a uniaxial anisotropy played a role in the unusual hysteresis behavior.

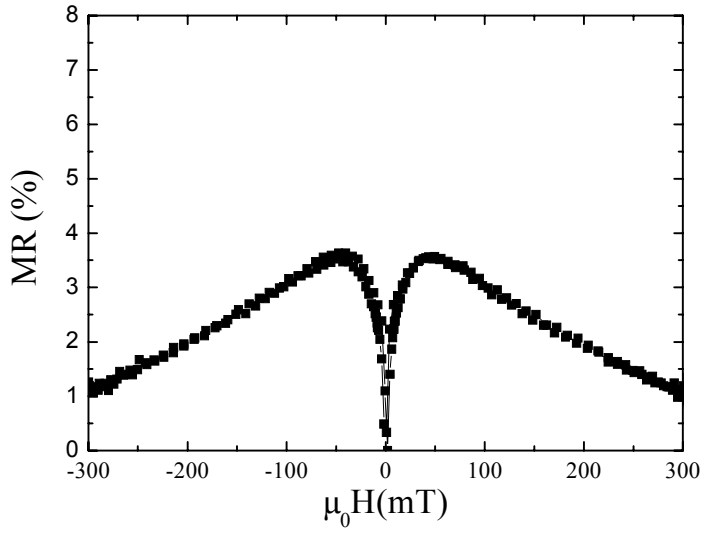

Figure 6.37: MR curve measured from a PtMn spin valve with SAF in the as-deposited state measured 90° to easy axis.

6.2.5.2 Simulation: Low Field Change in Bias Direction

This flipping of the bias direction of the SAF at only 22 mT was an unexpected but not unexplainable result. A larger uniaxial anisotropy in the pinned layer combined with a larger magnetic moment in the pinned layer than in the reference layer could explain the low field change in the bias direction. The applied field would first pull the magnetization of the pinned layer in the direction of the applied field due to it's larger magnetic moment, but the rotation of the pinned layer magnetization would be delayed due to the large uniaxial anisotropy in the pinned layer.

The MR curve of an as-deposited PtMn spin valve with SAF was simulated using the free energy model for a spin valve with SAF described in Section 5.3 to test this hypothesis. The resistance change parameter for spin-dependent scattering was set at 6% for ΔR_r and 0.05% for ΔR_r (see Eq 5.12). The CoFe bulk saturation value of 1.91 T [Jil91] was used for M_p and M_r and an averaged saturation value magnetization value of 1.245 T was used for the NiFe/CoFe sandwich free layer. The AMR effect plays no role in this switching behavior so it was neglected in this simulation. The other simulation parameters are listed below:

Layer 1: Pinned Layer
Saturation Magnetization (M_p): 1.91 T
Unidirectional Anisotropy (K_{eb}): 0 (no unidirectional anisotropy prior to the anneal)
Direction of the Unidirectional Anisotropy: 0°
Uniaxial Anisotropy ($K_p^{uniaxial}$): 8.50×10^{-6} Jm^{-2}
Direction of the Uniaxial Anisotropy: 0°
Interlayer coupling (J_{SAF}): -7.34×10^{-4} Jm^{-2} (coupling coefficient for Ru in the 1st antiferromagnetic maximum)

Layer 2: Reference Layer
Saturation Magnetization (M_r): 1.91 T
Uniaxial Anisotropy ($K_r^{uniaxial}$): $1.91\times10^{-6}Jm^{-2}$
Direction of the Uniaxial Anisotropy: 0°
Interlayer coupling (J_{int}): 4.30×10^{-6} Jm^{-2} (orange peel coupling)

Layer 3: Free Layer
Saturation Magnetization (M_f): 1.245 T
Uniaxial Anisotropy ($K_f^{uniaxial}$): 3.89×10^{-7} Jm^{-2}
Direction of the Uniaxial Anisotropy: 0°

$K_p^{uniaxial}$ had to be set to a value approximately four times larger than the expected value of 1.90×10^{-6} Jm^{-2} to reproduce the change in the pinned layer magnetization direction at the correct field value. The uniaxial anisotropy $K_p^{uniaxial}$ in the pinned layer was expected to be on the same order of magnitude as the uniaxial anisotropy of the reference layer $K_r^{uniaxial}$. The switching point of the pinned layer occurred at the same point, 22 mT, with this large uniaxial anisotropy value (see Figure 6.38) as in the experimental results (see Figure 6.36). PtMn does induce a high uniaxial anisotropy in the adjacent ferromagnetic [Pok01], but the PtMn layer in this case was still in the nonmagnetic fcc phase. The nonmagnetic fcc-PtMn layer adjacent to the pinned layer must have therefore induced a coercivity increase in the CoFe pinned layer in order to explain low field change in the bias direction.

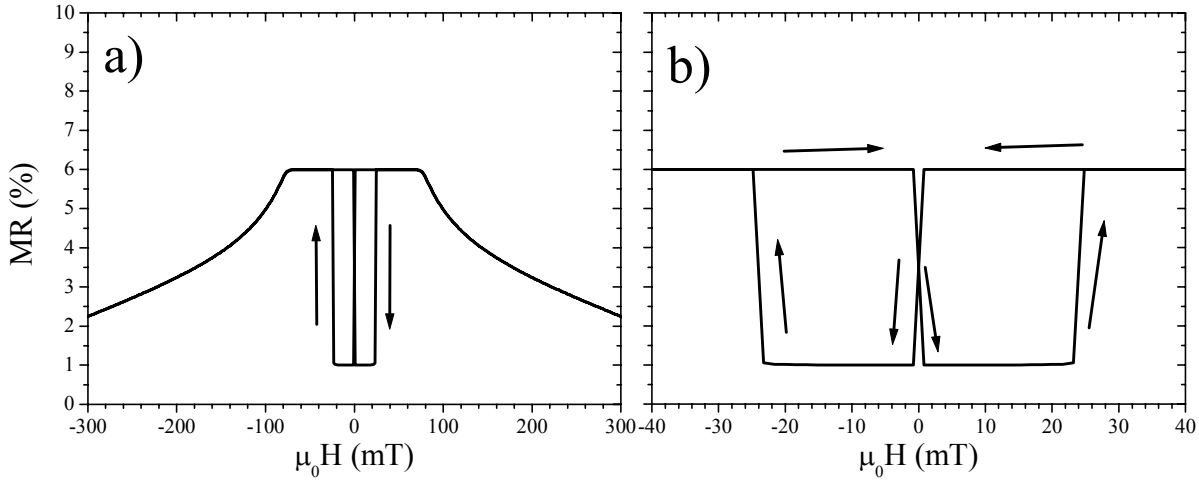

Figure 6.38: a) Major loop and b) minor loop from a simulated MR curve measured from a PtMn with SAF in the as-deposited state.

6.2.5.3 Magnetoresistive Characteristics: Post Anneal

After the high-temperature anneal the PtMn spin valve with SAF had an MR effect of 6.3% and a H_{ex} of 190 mT as seen in Figure 6.39. The H_{eb} and H_{saf} were determined to be 180 mT and 105 mT, respectively. The hysteresis H_{c2} in the major loop of the MR curve had been reduced to 5 mT. H_{c2} was determined to 40 mT by an AGM measurement (not shown), which matched the measured H_{c2} of the pinned layer from the PtMn simple spin valve (see Figure 6.33).

The H_e was measured at 0.75 mT and the H_{c1} at 0.4 mT as seen in Figure 6.39. The H_e has slightly increased in comparison to the value prior to the anneal. This was probably due to interdiffusion during the anneal, which lead to an increase in the interface roughness and subsequently increase in the ferromagnetic orange-peel coupling. The higher H_{c1} indicated that the uniaxial anisotropy axis in the free layer was now parallel to the bias direction. It is now no longer possible to change to bias direction of the SAF due to the exchange biasing of the pinned layer.

The rise in the MR effect at bump in the MR curve (see Figure 6.39) was due to a scissoring motion of the pinned and reference layer magnetizations (see Section 2.5.4) The pinned layer was no longer completely fixed in one direction by the exchange bias effect and

begins to rotate in the direction of the applied field. The reference layer magnetization will attempt to remain in an anti-parallel alignment to the pinned layer magnetization because of the antiferromagnetic coupling across the Ru spacer layer.

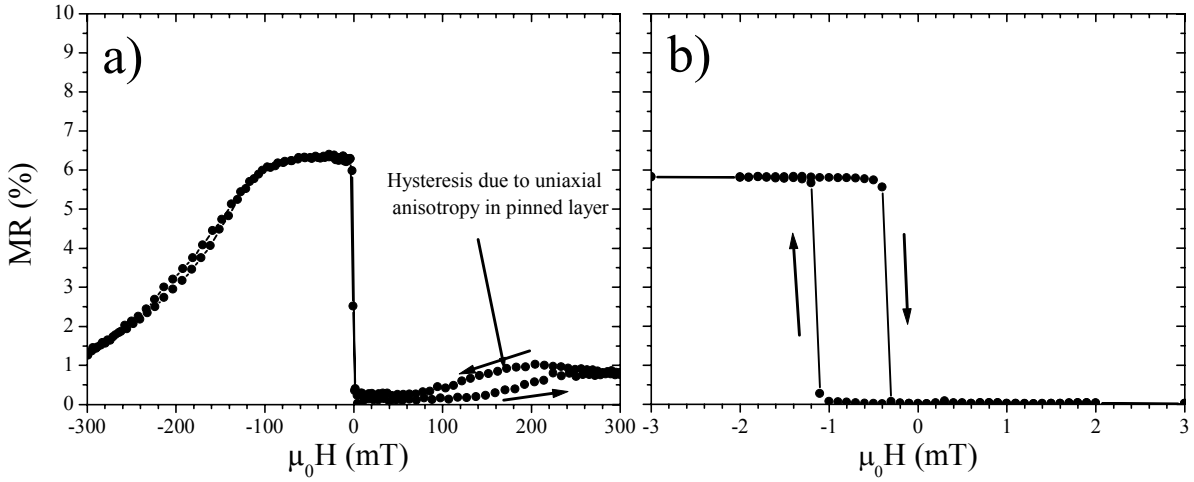

Figure 6.39: MR curve measured from a post-anneal PtMn spin valve with SAF sample.

The hysteresis in the MR curve that appears near this bump in the MR curve, indicated in Figure 6.39, was due to a large uniaxial anisotropy in the pinned layer. The detriments of a high uniaxial anisotropy in the pinned layer becomes evident upon increasing the maximum field value of the MR measurement to 400 mT (Figure 6.40). There is not only an enlargement of the hysteresis in the field value, but also a hysteresis in the magnitude of the MR effect. A hysteresis of large magnitude only appears when the applied field strength is increased to field values that are much larger than the H_{eb} of the spin valve as in Figure 6.40. The MR rises to 1.5% until reaching the zero field value. Upon going to negative field values, MR jumps to only 5.4% rather than the previously measured 6.3%. The full MR value is only restored in the spin valve upon going into magnetic saturation of the SAF at –500 mT and then reducing the applied field to zero. A uniform magnetization direction is restored in the pinned layer, thus uniform bias direction in the SAF, upon going into magnetic saturation in the same direction as the direction of the unidirectional anisotropy.

The reason for this mixed magnetic state, domains with different bias directions, is a uniaxial anisotropy distribution in the pinned layer. This explained by taking into account that the uniaxial anisotropy coefficient $K_p^{uniaxial}$ is of the same order of magnitude as the exchange bias energy coefficient K_{eb}. A number of grains in the pinned layer will have a $K_p^{uniaxial} > K_{eb}$ and other grains will have $K_p^{uniaxial} < K_{eb}$ (see Figure 6.40). A percentage of the magnetic domains in the pinned layer will remain in the applied field direction because of the high uniaxial anisotropy. This happens when the field direction is anti-parallel to the bias direction and the field strength is decreased below the H_{eb} of the spin valve (see Figure 6.40). A percentage of the magnetic domains will be reoriented by the unidirectional anisotropy in the bias direction at this point. There now exists a mixed magnetic state in the SAF with regions of opposite magnetization directions in the pinned layer. The magnetization direction in individual domains will be dictated by which anisotropy component is the strongest.

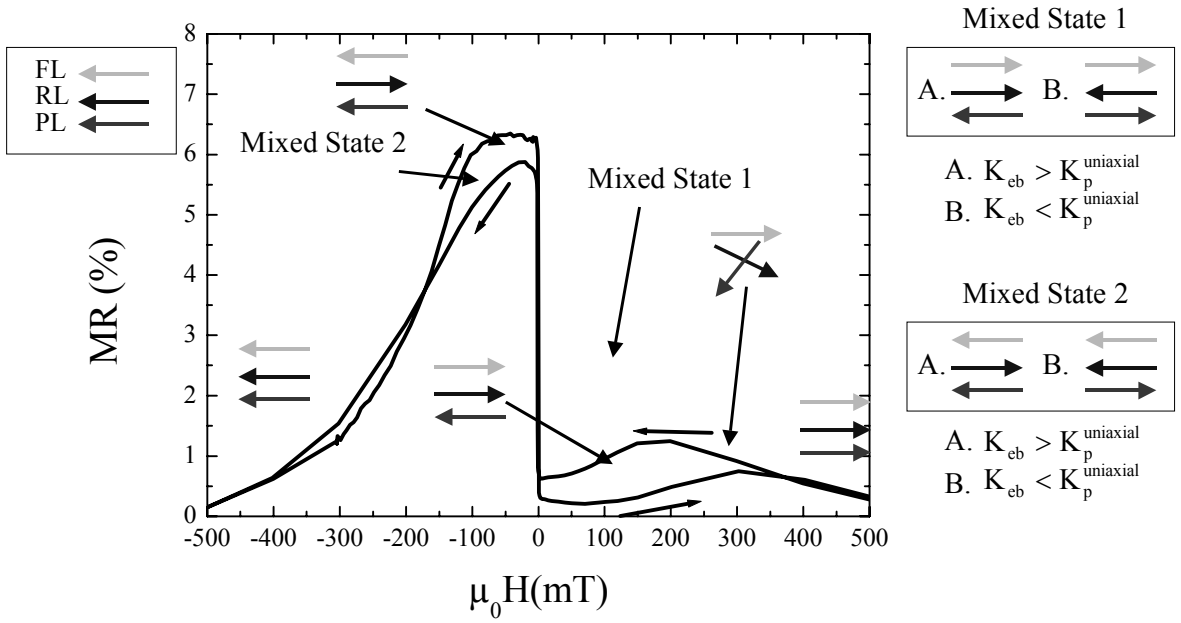

Figure 6.40: MR curve measured from a post-anneal PtMn spin valve with SAF sample with measurement field strength increased to a maximum of ±500 mT.

6.2.5.4 Simulation of the Post Anneal MR Curve

The post-anneal MR curve of the PtMn spin valve with SAF was simulated by turning on the unidirectional anisotropy (K_{eb} = 2.01×10^{-5} Jm^{-2}) in the simulation described in Section 6.2.5.2. The uniaxial anisotropy in the reference layer ($K_r^{uniaxial}$ = 7.5×10^{-6} Jm^{-2}) and the free layer ($K_f^{uniaxial}$ = 1.25×10^{-6} Jm^{-2}) were increased because of undefined changes caused by the high-temperature anneal under a high magnetic field [Rij94]. The interlayer coupling between the free layer and reference layer has also been slightly increased (J_{int}= 4.67×10^{-6} Jm^{-2}) due to the interdiffusion during the anneal. The uniaxial anisotropy in the pinned layer ($K_r^{uniaxial}$ = $9.77\times10^{-5}Jm^{-2}$) was increased one order of magnitude due to the presence of the neighboring fct PtMn AFM.

All of the features of the experimental MR curve are duplicated in the simulated MR curve except for the size of hysteresis near the bump in the positive field direction,. The differences between the experimental and simulated MR curves was in the terms of the magnitude of H_{saf}, H_{eb} and the H_{ex} in the simulated MR curve. The simulated MR curve had an H_{saf} of 170 mT and an H_{ex} of 205 mT (see Figure 6.41) in comparison to the experimental values of 105 mT for H_{saf} and 180 mT for H_{eb}.

There were two possible answers to the differences between the experimental and simulation MR curves. The first possibility was an incorrect value for the K_{eb}, but reducing the unidirectional anisotropy value in the simulation lead to a strange hysteresis behavior that was physically unrealistic. The second possible explanation was a reduction in the antiferromagnetic interlayer coupling in the SAF due to a change in the spacer layer thickness.

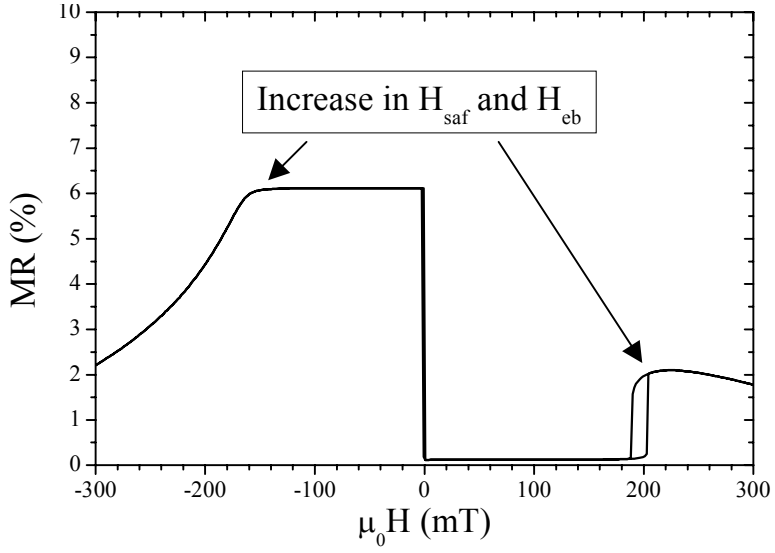

Figure 6.41: Simulated MR curve of PtMn spin valve with SAF after high-temperature anneal.

The PtMn samples undergo a long term anneal, 300°C for several hours, which results in interdiffusion between the different layers in the spin valve. Interdiffusion has been observed in other anneal studies of PtMn spin valves with a SAF conducted at comparable temperatures and over shorter periods of time, e.g. 200-350°C for 10 min [And00]. The interlayer coupling value at the first anti-ferromagnetic maxima is very sensitive to changes of only a few tenths of a nm in the spacer layer thickness [Par90]. The interdiffusion could have slightly changed the effective thickness of the Ru spacer layer in the SAF. The J_{SAF} was decreased to 4.75×10^{-5} Jm^{-2} in order to have the correct H_{saf} value as seen in Figure 6.42.

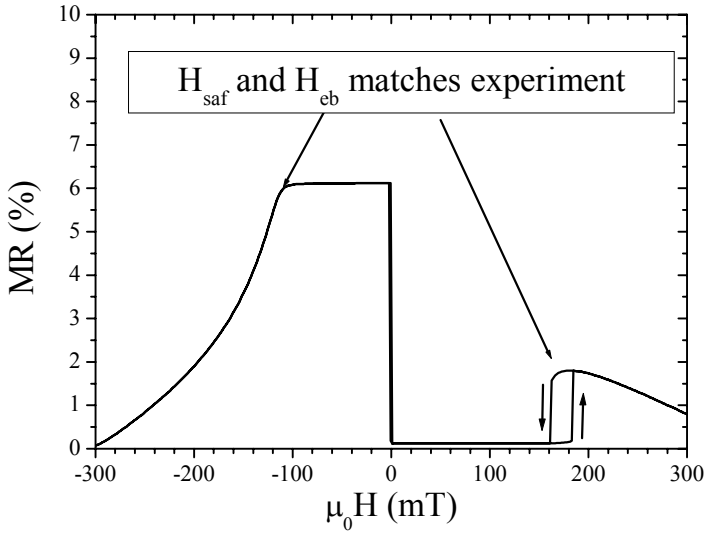

Figure 6.42 Simulated MR curve of post-anneal PtMn spin valve with SAF sample with the reduced interlayer coupling.

6.2.5.5 Temperature Dependence of the GMR and Exchange Bias Effect

The blocking temperature for PtMn with SAF could not be determined directly from the MR measurements for the same reasons as with the PtMn simple spin valves (see Section 6.2.4.4). The H_{ex} has dropped from 198 mT to 169 mT (see Figure 6.43). The H_{ex} is sufficient at 170°C to ensure a stable operating range up to 100 mT. The MR had dropped from 6.4 % at room temperature to 3.5% at 170°C. Extrapolation of the plot out to 190°C

indicated that sufficient MR effect would remain over specified temperature range. PtMn with SAF showed both sufficient H_{eb} and MR effect up to the 150°C and a high T_b to ensure the thermal stability of the bias direction up to 190°C.

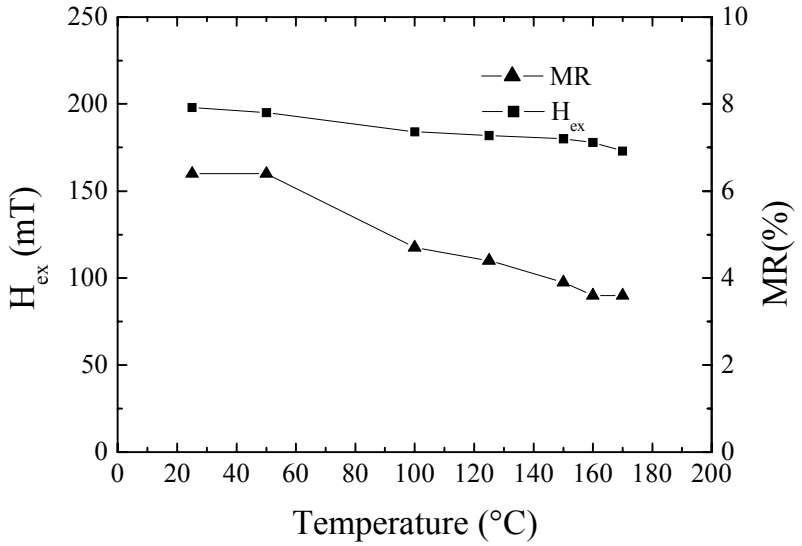

Figure 6.43: Temperature dependence of the MR and H_{eb} for PtMn spin valve. H_{ex} is plotted here due to the difficulty in determining H_{eb} directly from the MR curve measured from a spin valve with SAF.

6.2.6 Comparison Between the Different Spin Valve Systems

A general comparison was made between the different spin valve studied in the previous sections. This comparison was made considering based the following points listed below:

- MR Signal: MR > 3% in specified temperature range [-40°C to 150°C]
- Thermal Stability: T_b >>190°C to ensure stability of bias direction.
- Exchange Bias: H_{eb} > 100 mT in the specified temperature range [-40°C to 150°C]
- Processability: compatibility with existing semiconductor processes

The first step in this evaluation was a direct comparison between the temperature dependence of the MR effect between the different spin valves systems. The normalized MR effect for each spin valve system was plotted as function of temperature up to 170°C to allow this direct comparison. The measured MR effect for the NiO and FeMn spin valve showed a drastic drop in magnitude up to 150°C. The IrMn, PtMn and PtMn with SAF spin valve systems showed sufficient MR effect up to 150°C (see Figure 6.44).

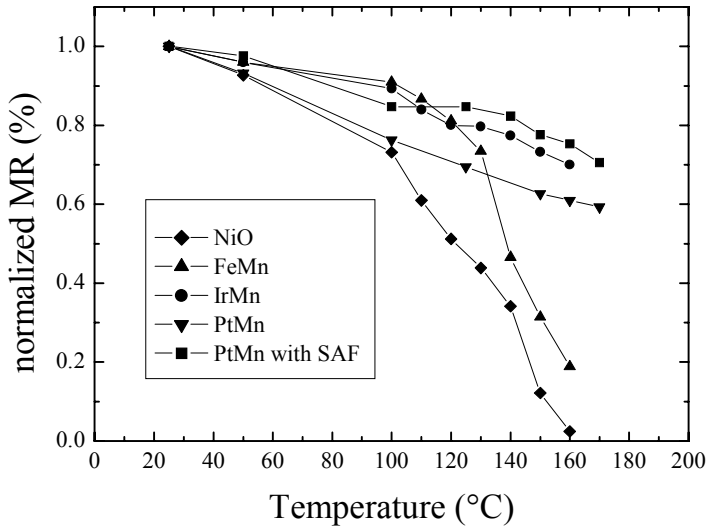

Figure 6.44: Comparison of the temperature dependence of the MR effect measured from NiO, FeMn, IrMn, PtMn and PtMn spin valve with SAF.

The normalized H_{eb} effect for each spin valve system was plotted together as function of temperature as seen in Figure 6.45. This was done to directly illustrate which spin valve had the highest T_b and the highest H_{eb} over the specified temperature range. FeMn and NiO had a T_b of only 140°C and IrMn had a T_b of only 190°C that makes these suitable for applications with a less rigid temperature regime. The PtMn and PtMn with SAF spin valves showed the highest T_b. This was more than enough to ensure a stable bias direction above 190°C.

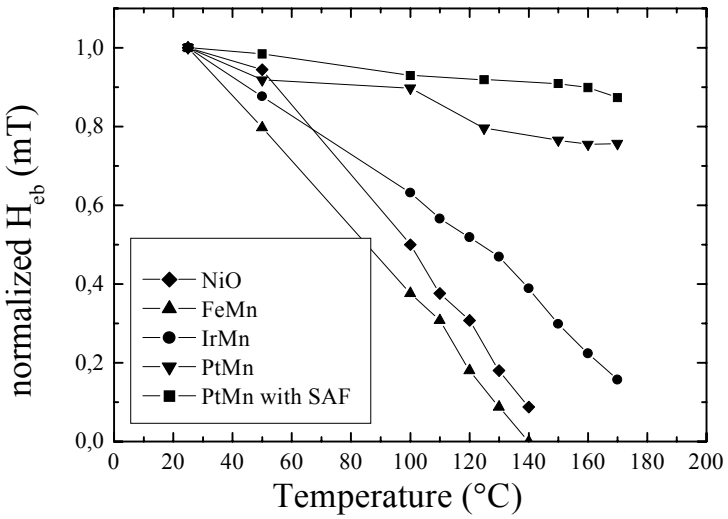

Figure 6.45: Comparison of the H_{eb} dependence on temperature between NiO, FeMn, IrMn, PtMn and PtMn with SAF spin valves. H_{ex} was plotted rather than H_{eb} in the case of PtMn spin valve with SAF.

The PtMn simple spin valve had did not have sufficient H_{eb} at 150°C and a relatively large uniaxial anisotropy in the pinned layer (41 mT) in comparison to the previously studied spin valve stacks (see Figure 6.35). The insertion of a SAF in PtMn spin valve system reduced the hysteresis in the MR curve and lead to a fourfold increase in the H_{eb} of the spin valve. The PtMn with SAF spin valve had a H_{eb} of 180 mT and the hysteresis in the major loop of the MR curve H_{c3} had been reduced from 40 mT in the simple spin valve to 5 mT in the spin valve with SAF (see Table 10.3).

The photolithography process compatibility of a spin valve system was also a major concern when considering the patterning of a sensor element. NiO may have a good corrosion resistance thus good compatibility with existing wet processes in the patterning steps, but was difficult to deposit in the correct (111) NiO phase without very precise control of the Ar partial pressure [Tie00]. FeMn showed poor corrosion resistance, which leads to a large amount of degradation during the patterning of the sensor. The IrMn and PtMn spin valve systems had superior corrosion resistance to FeMn, but PtMn requires a long-term anneal step for the fcc to fct phase transformation. The long-term anneal would length the time required for the processing of the sensor element. A simplified comparison list based upon the previously stated criteria points is given in Table 6.3.

Table 6.3: Criteria list: comparison between the studied spin valve systems.

Spin Valve	Sufficient MR Signal	Thermal Stability	Operating Range	Processability
NiO	No	No	No	No
FeMn	Yes	No	No	No
IrMn	Yes	No	No	Yes
PtMn	Yes	Yes	No	Yes*
PtMn SAF	Yes	Yes	Yes	Yes*

*requires additional anneal

6.2.7 Summary: Selection of Spin Valve System

A wide range of spin valves with different antiferromagnets (NiO, FeMn, IrMn, PtMn) were studied with standard MR measurements to determine the magnetic parameters (MR effect, H_{eb}, H_e, H_{c1}, H_{c2}) of each system. The most important experimental results are listed below:

- A (111) texture was a common feature in all the spin valve systems studied that exhibited a high GMR effect and H_{eb}.
- The incorporation of the SAF in a spin valve stack lead to an increase in H_{eb} and H_{saf} of the spin valve without any actual increase in the strength of the antiferromagnetic interlayer coupling or the exchange bias in the spin valve. This was seen in the increase of the plateau region in the MR curve, a measure of H_{saf}, after the annealing of the spin valve necessary for the transformation of fcc PtMn to antiferromagnetic fct phase.
- The hysteresis in the major loop of an MR curve measured from a PtMn spin valve with SAF is due to K_{eb} being on the same order of magnitude as $K_p^{uniaxial}$ and a $K_p^{uniaxial}$ distribution in the pinned layer.
- The PtMn spin valve with SAF had the highest H_{eb} and MR over the specified temperature range [-40°C bis 150°C].

6.3 Multiple Deposition: Lift-off Method

6.3.1 Description of the Method

Multiple deposition of the spin valve stack on a wafer was seen as the simplest solution for creating four different bias directions on a single chip. The multiple deposition of a spin valve on selected areas of a chip is made possible through the use of the lift-off process. The basic steps in the lift-off method are shown in Figure 6.46 for the example of a two-fold deposition. In part a) photoresist is applied to the substrate via spincoating and windows or forms are patterned into the photoresist with photolithography techniques. This is done to allow deposition of the spin valve directly on the wafer. After the deposition under an applied field (see part b), the photoresist is dissolved in an acetone bath, (see part c) and the spin valve stack not in direct contact with the substrate is lifted-off the substrate hence the term "lift-off method". The next step is the 2nd application of a photoresist layer and 2nd deposition of a spin valve stack as shown in part d. Finally, the photoresist is again removed (see part e) The result is a neighboring spin valve stacks with opposite bias directions. This process is repeated then two times to have four different bias directions on a single chip.

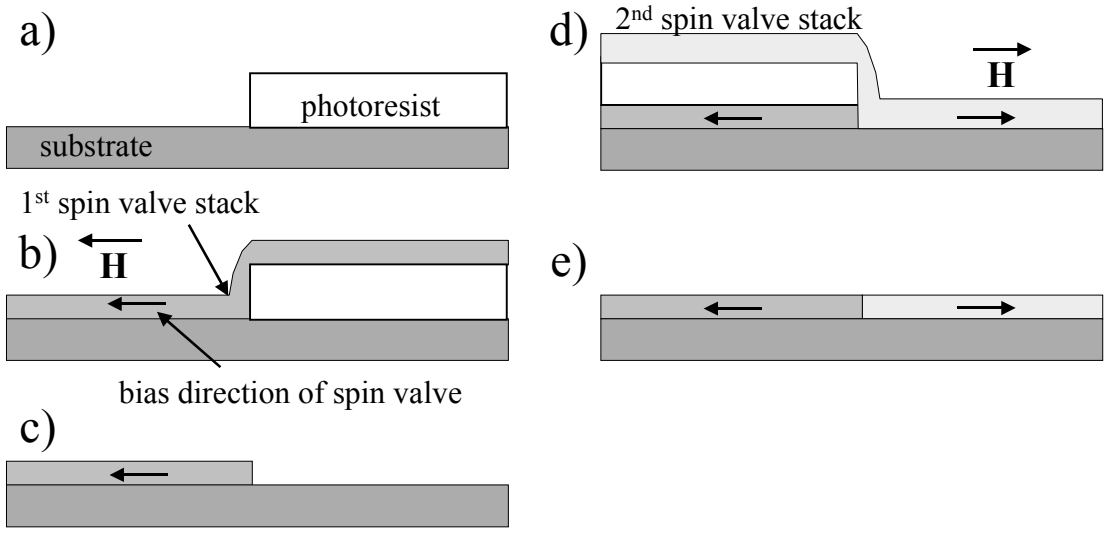

Figure 6.46: Lift-off process used to achieve two bias directions on single chip with a) spincoating of photoresist, b) 1st deposition of spin valve stack, c) removal of the photoresist with acetone, d) the 2nd spincoating of photoresist on wafer and deposition of the spin valve stack on the substrate, and e) final removal of the photoresist with acetone.

6.3.2 Test of the Lift-off Method

The lift-off method was tested by depositing two test squares with opposite bias directions on a single wafer (see Figure 6.47). The deposition and photolithography parts of the experiment were performed at IFW-Dresden. This has been achieved by a two-fold deposition of a NiO spin valve stack in an applied magnetic field of 50 mT and use of the lift-off method shown in Figure 6.46. The NiO spin valve used in this experiment is described in Section 6.2.1. The bias direction in the upper test squares is shifted 180° with respect to the

bias direction of the lower test squares (see Figure 6.47a). This is seen in the MR curve measured from both sets of test squares plotted together in Figure 6.47b. The MR effect was the same at 3.8% in both bias directions, but the H_{eb} was 5 mT in the 1st deposited spin valve stack and 3 mT in the 2nd deposited spin valve stack. The difference in the H_{eb} between the 1st and 2nd deposition was explained through the presence of contaminants introduced to the wafer surface between the 1st and 2nd depositions.

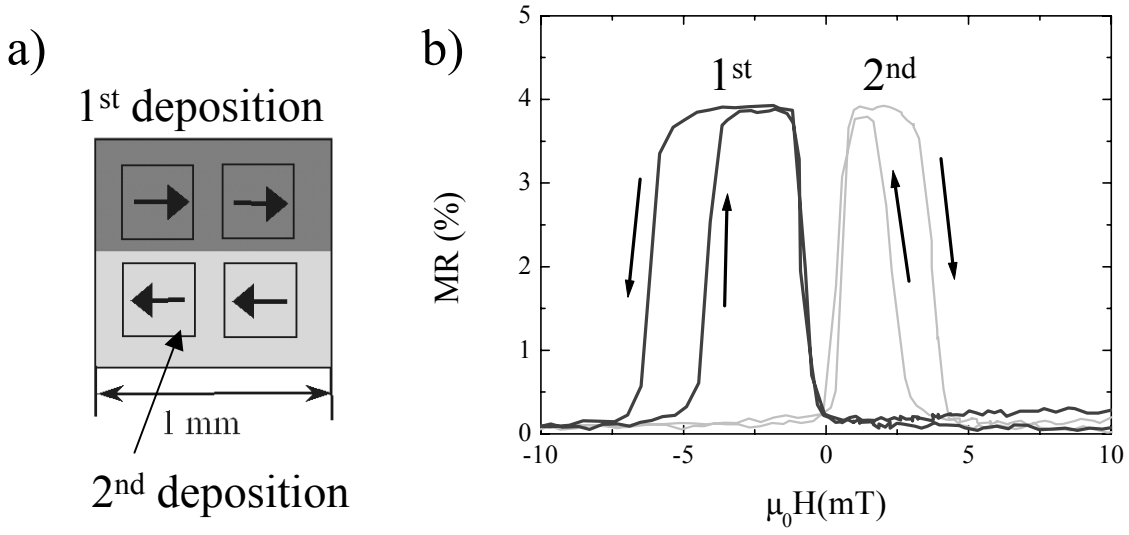

Figure 6.47: Two-fold deposition of NiO on the µm scale where a) is the patterned wafer chip deposited and b) the MR curves measured from the test squares.

Problems with the Lift –off Method

There are several problems associated with the use of the lift-off method for the fabrication of a demonstrator GMR angle sensor. Slight variations in layer thickness between two depositions and the presence of the contaminants deposited on the substrate during removal of photoresist can result in differences in the resistance and magnetic properties of the spin valve thin films. A variation in the intrinsic resistance between two half-bridges in a Wheatstone bridge circuit can lead to a large offset and a possible voltage drift over a temperature range of –40 to 150°C. This offset drift would only increase with a four-fold deposition required and result in a drastic increase in the angular error.

Another drawback with the lift-off method is it's incompatibility with the PtMn spin valve system. A PtMn antiferromagnet requires an anneal of 200-300°C for several hours to transform into the antiferromagnetic fct phase (see Section 6.2.6). If an anneal is performed on a angle sensor fabricated by the lift-off method, all of the meanders in the Wheatstone bridge would have the same bias direction.

6.3.3 Summary: Lift-off Method

Multiple deposition of the spin valve stack on a substrate and subsequent patterning with the lift-off process was seen as the simplest solution to create four different bias directions on a single chip. The major points of the analysis of the lift-off method are given below:

- Two different bias directions on a single chip were successfully created through the multiple deposition of a NiO spin valve system and use of the lift-off method.
- Variation in the H_{eb} resulted from either contamination of the substrate surface between the deposition runs or slight thickness variations between the two spin valve stacks.

6.4 Ion Irradiation Method

The exchange bias effect can be modified in magnitude and direction by He^+ ion irradiation under an applied magnetic field. This has already been demonstrated in He^+ ion irradiation experiments performed on FeMn/NiFe bilayers by Mewes, et al. [Mew00a], and Mougin, et al. [Mou01a]. Depending on the ion dosage, the H_{eb} of the samples can either be enhanced or reduced through the ion irradiation process. Theoretically the ion irradiation could then be used to locally change the bias direction of AFM layer in structured meanders of a Wheatstone bridge element enabling the creation of a GMR angle sensor. In the first section, ion irradiation was used for the first time to change the bias direction in actual spin valve structures rather than just AFM/FM bilayers. This method was then tested on patterned meanders of a FeMn spin valve. This work was done in cooperation with the University of Kaiserslautern and IPHT-Jena.

6.4.1 Ion Irradiation of FeMn and IrMn Spin Valves

The bias direction of both FeMn and IrMn spin valve samples were reoriented by irradiation with He^+ ions. The FeMn spin valve was deposited on a Shamrock 150 PVD system and was of the following structure: Si/SiO_2/Ta(5)/NiFe(6)/Co(3)/Cu(3)/Co(3.6)/ FeMn(10)/Ta(5). All layer thicknesses are given in nm. This FeMn spin valve had an MR effect of 8% and H_{eb} of 50 mT. The IrMn spin valve is the same as IrMn spin valve system described in Section 6.2.3 The IrMn spin valve had an MR effect of 7.5 % and H_{eb} of 45 mT.

FeMn and IrMn spin valve samples, 10 by 10 mm^2 in size, were placed in an ion-optical bench. The He^+ ions were produced by a Penning type source and accelerated to 10 kV. Varying the ion current (10–100 nA) and irradiation time (3-120s) changed the ion dosage. An ion dosage range of 2×10^{13}-10^{16} ions/cm^2 was used in the experiment. The ion dosage range had been previously determined through previous experiments on FeMn/NiFe bilayers [Mou01a]. The equipment used for the ion irradiation of the spin valves was located at Universität Kaiserslautern. During the ion irradiation a magnetic field of 100 mT was applied anti-parallel to the original bias direction. The spin valve sample was irradiated at a single ion dosage with a spot size of approximately 1 mm in diameter. The ion beam after the first ion beam was moved to another location on the sample to avoid overlap with the previously irradiated area.

6.4.1.1 Characterization of Ion Irradiated Samples with MOKE

MOKE was the only available method that could determine the change in the magnitude and direction of the exchange bias in the ion irradiated samples due to the small size of the irradiated area, 1 mm in diameter. The laser beam of the MOKE apparatus was scanned over the surface of sample in 1 mm steps and the hysteresis loops were made at each step. The change in the MR effect as a function of ion dosage could not be determined due to previously mentioned size limitations. Only the MOKE measurements made on the spots irradiated at 3×10^{14} ions/cm^2 and 1×10^{16} ions/cm^2 ion dosages are shown in Figure 6.48.

It was possible with a ion dosage of 3×10^{14} ions/cm^2 to reverse the bias direction of the FeMn spin valve as seen in Figure 6.48a. The applied field direction during the ion irradiation is indicated in the Figure. The H_{eb} was 50 mT prior to the ion irradiation treatment and actually increased to 70 mT after the ion irradiation reoriented the bias direction. No exchange bias was measured in the sample at an ion dosage of 1×10^{16} ions/cm^2. It was also

possible to reverse the bias direction in the IrMn spin valve, but not with the same degree of success (Figure 6.48b). At an ion dosage of 3×10^{14} ions/cm^2, the bias direction had reversed, but the H_{eb} has decreased from 40 mT in the pre-ion irradiation state to 25 mT. The ion dosage was optimized for FeMn AFM not for a IrMn AFM. No exchange bias was measured in the IrMn spin valve at an ion dosage of 1×10^{16} ions/cm^2.

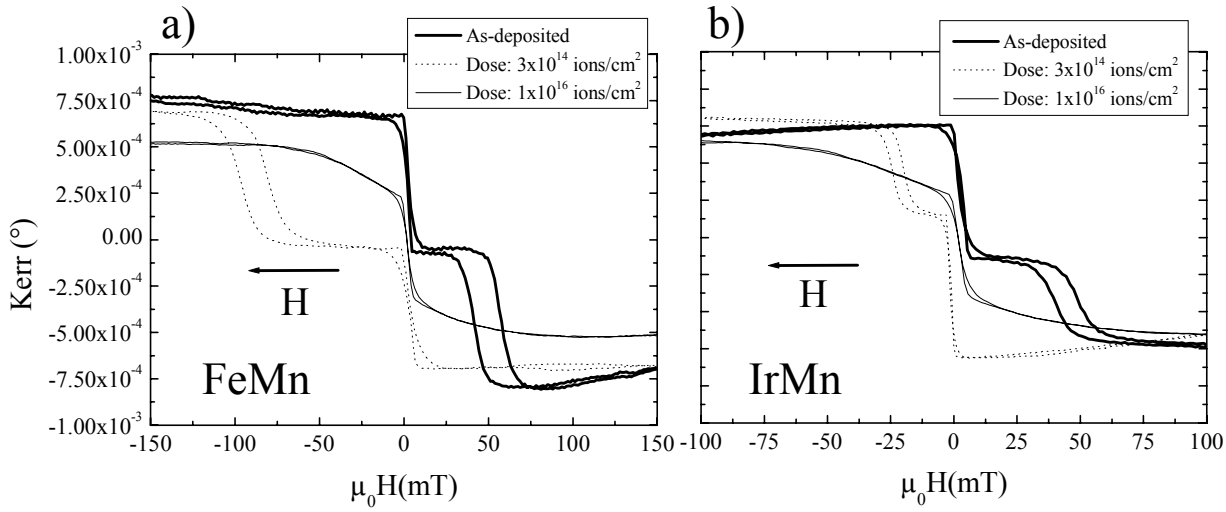

Figure 6.48: MOKE measurements made on a) FeMn spin valve samples and b) IrMn spin valve samples in the as-deposited state and irradiated at an ion dosage of 3×10^{14} ions/cm^2 and 1×10^{16} ions/cm^2.

The experimental results can be best understood in terms of ion-induced defect creation in the AFM layer and with help of the domain state model [Now00] (see Section 2.5.5). According to the domain state model, the exchange bias effect is proportional to the number of AFM domain walls which is dependent upon the number of defects in the volume of AFM. The He^+ ion irradiation created interstitial vacancies in the volume of the AFM layer. In the case of He^+ ions accelerated at 10 kV, the majority of the nuclear collisions occur at 90 nm depth below the surface of the spin valve stack [Zie85]. The AFM/FM interface is only 15 nm below the surface of the sample so the majority of the defects will not be in the volume of the AFM layer. but rather deep in the substrate layer. This allowed for a more controlled change in the defect density of the AFM layer. The irradiation of the spin valve with He^+ ions under a magnetic field creates new defects in the volume of the AFM, which in turn creates new domain walls with a spin orientation in the same direction as the applied magnetic field. Eventually the number of domains with a opposite spin orientation created by the ion irradiation are greater in number than the pre-existing domain state. This results in a change in the bias direction of the spin valve.

The increase in the defect density of the AFM layer also explains the increase in H_{eb} in the FeMn spin valve to 70 mT at an ion dosage of 1×10^{16} ions/cm^2. The domain state created by the ion-induced defects had a net magnetization with the opposite spin orientation greater than that in the as-deposited state. An increase in H_{eb} was not seen in the ion irradiated IrMn spin valves at an ion dosage of 1×10^{16} ions/cm^2. The H_{eb} had been reduced to 25 mT in the case of IrMn spin valve. The ion dosage used in this study was optimized for FeMn spin valve system, but not for IrMn spin valve system. The disappearance of the exchange bias at an ion dosage of 1×10^{16} ions/cm^2 in the FeMn spin valves and IrMn spin valves resulted from the loss of long-range order in the AFM lattice with the increase in defect density caused by the ion irradiation.

6.4.2 Ion Irradiation of a Patterned Spin Valve Sample

The ion irradiation method has also been applied to changing the bias direction in a spin valve meander patterned into a Wheatstone bridge circuit. Previous experiments had shown that it was possible to micropattern the bias direction in FeMn/NiFe bilayers through windows in a photoresist layer [Mou01b] [Fass02]. The structuring of the spin valve sample was done at IPHT-Jena. Four meanders were milled out of the spin valve stack by ion beam etching in order to create the Wheatstone bridge. In the second step a photo-resist pattern was deposited to protect the parts of the Wheatstone bridge in which the bias direction should remain unchanged. The two spin valve meanders not covered by photoresist were irradiated at an ion dosage of 6×10^{14} ions/cm^2 under an applied field of 100 mT as illustrated in Figure 6.49. The applied magnetic field during the ion irradiation has to have a field value strength greater than the H_{eb} of the spin valve in order to reorient the bias direction of the pinned layer.

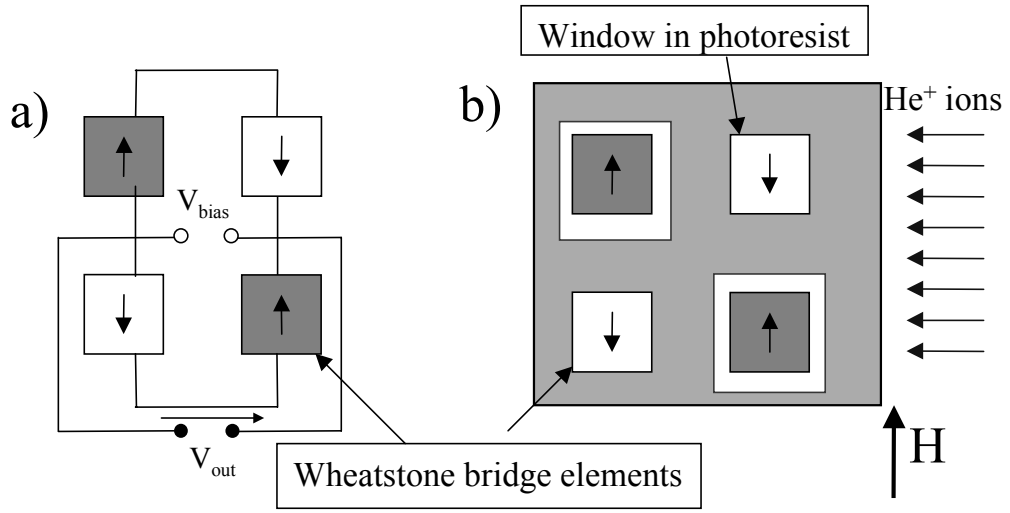

Figure 6.49: Ion irradiation of half bridge element in Wheatstone bridge circuit through a window in the photoresist to reorient the bias direction of the spin valve. The arrows indicate the bias direction in that part of the Wheatstone bridge circuit.

The Wheatstone bridge circuit showed an MR effect of only 5.5 %, as calculated from the bridge signal ($MR = \Delta V/V_{bias}$) (see Figure 6.50a) after the ion irradiation. This was a drop of 2.5 % in comparison to the MR effect (8%) prior to ion irradiation and patterning of the FeMn spin valve. The loss of MR could be attributed to either the loss of homogenous bias direction due to high temperature steps during the patterning of the spin valve or intermixing at the FM/NM interface induced by the ion irradiation, which led to an increase in the amount of spin-independent scattering.

The rotation curve of the bridge signal measured at 5 mT exhibited sinusoidal behavior indicating the existence of two bias directions in the Wheatstone bridge, but had a large offset of 0.25 V. The cosine deviation, also angular error, was determined by performing an arctan analysis of the output signal as shown in Eq. (2.27). The arctan analysis requires both a sine and cosine signal to determine an angle, but only a single Wheatstone bridge element was irradiated in this experiment to reduce the number of photolithography steps. The sine signal had to be created from the original bridge signal. First the offset was removed from the bridge signal and the data set shifted 90° to create a sine output signal.

The cosine deviation began at a maximum of ±11.8° and then decreased to a minimum of ±3.0° at 7 mT (see Figure 6.50b). The cosine deviation then begins to increase to maximum of ±14.1° at 38 mT. The reason for the decrease in cosine deviation error up to 7 mT was the

applied field overcoming the influence of the interlayer coupling on the magnetization in the free layer as previously described in Section 6.1.2. The cause of the increase in cosine deviation above 7 mT was the rotation of the pinned layer magnetization in the direction of the applied field below the H_{eb} of the spin valve system (see Section 6.1.3). This is indicated by the drop in the MR with increasing applied field (see Figure 6.50b).

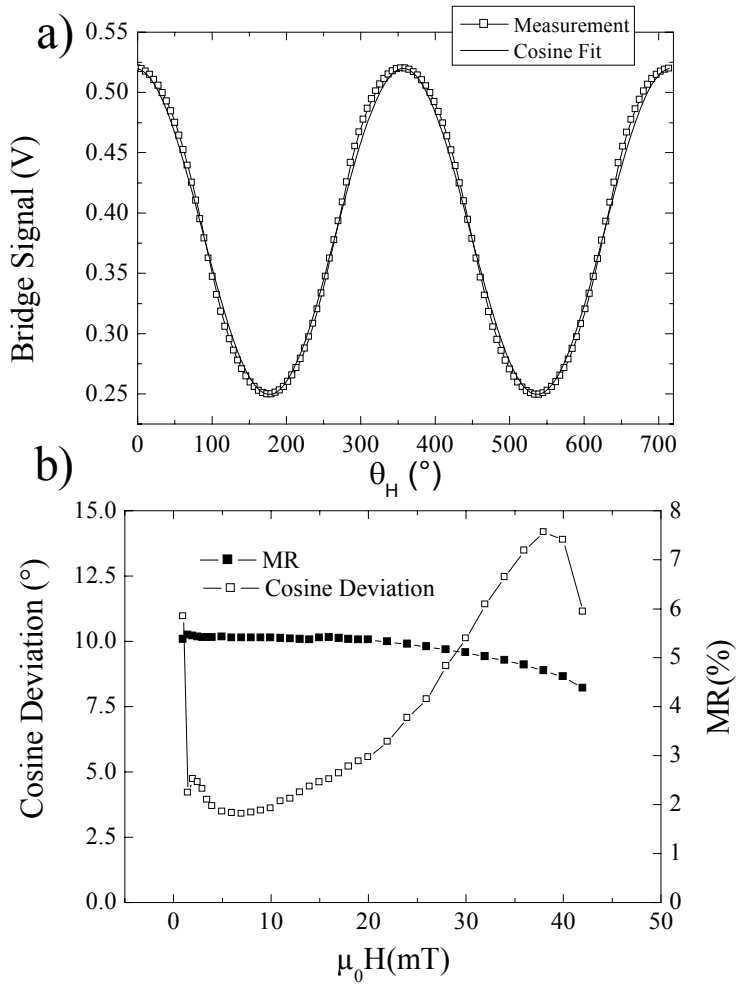

Figure 6.50: a) Bridge signal rotation curve measured at 5 mT from ion irradiated FeMn spin valve meander and b) cosine deviation of the bridge signal and MR effect of the entire Wheatstone bridge circuit as a function of applied field.

Problems with the Ion Irradiation Method

There are many inherent problems with the ion irradiation method despite the success in changing the bias direction in a spin valve meander. It is not possible to reorient the bias direction with the same dosage in different directions (0°, 90°, 180°, 270°) to the original bias direction and have the same H_{eb} [Mou01a]. The ion dosage must be optimized for every bias direction in order to achieve the same H_{eb} in each part of the Wheatstone bridge circuit. The ion irradiation method has also not yet been successfully tested on the PtMn antiferromagnets [Fas01].

The stability of the ion induced defects at elevated operating temperatures is also questionable. Point defects can be annealed out of the system through a low temperature anneal. An anneal of FeMn/NiFe bilayers at 230°C showed a reduction in the H_{eb} due to the vacancy removal in the AFM layer [Mou01a]. The magnitude of the exchange bias could change over time at elevated temperatures, e.g. at 190°C. All magnetic parameters of spin

valve must remain unchanged in the specified operating temperature range for a GMR angle sensor.

6.4.3 Summary: Ion Irradiation Method

The ion irradiation method was seen as a unique method by which to locally change the bias direction in spin valve meanders. This method was used successfully to change the bias direction of AFM layer in wafer samples and patterned meanders of a Wheatstone bridge circuit. A summarized analysis of the experimental results is presented below:

- The bias direction in FeMn and IrMn spin valves was successfully reoriented with use of He^+ ion irradiation at a dosage of 3×10^{14} ions/cm^2 and under an applied magnetic field of 100 mT.
- A Wheatstone bridge circuit with opposite bias directions, 180° difference in direction in the spin valve meanders, was created via the ion irradiation.
- The change in the direction and magnitude of the exchange bias effect induced by the ion irradiation provided additional experimental support for the domain state model of exchange bias.

6.5 Laser-writing Method

The bias direction of a spin valve can be changed on a μm scale by heating a spin valve above the T_b of the AFM layer with a laser and cooling down under an applied magnetic field. The heating of spin valve sample with a laser to "write" the unidirectional anisotropy in one direction will be referred to as "laser-writing" throughout this dissertation. The concept of laser-writing is not a new idea. This method was first proposed by Glazer, et al. [Gla72], for possible application in magnetic memory and tested by Salanskii, et al. [Sal74], on Mn/NiFe bilayers. The use of a laser to imprint four different bias directions in a spin valve meander structure on a single chip was seen as the most promising method for fabrication of a GMR 360° angle sensor. Experimental results showing the use of laser to change the bias direction in actual spin valve structures are presented for the first time in this dissertation.

The first step in testing the laser-writing method was the irradiation of FeMn and IrMn simple spin valves with a KrF excimer laser over a range of laser energies. The goal was to find the minimum laser energy necessary to heat the spin valve above the T_b of the AFM. The reorientation point, minimal laser energy necessary for the change of the bias direction, could be determined by observing the change in MR effect in relation to the original bias direction. The change in magnetic properties (MR and H_{eb}) and microstructure in the laser irradiated spin valves were studied in detail with AGM, XRD, GIXR, and AES. The results of these studies were used to explain the change in the MR effect and H_{eb} after the reorientation of the bias direction. The microstructure changes induced by the laser-writing were used to explain the degradation in the GMR effect with the increase in laser energy. The behavior of the exchange bias effect in the laser irradiated spin valves was explained with help of the domain state model.

The second part of the laser-writing study centered on the application of this method to reorienting the bias direction of a PtMn spin valve with an SAF. Two physical effects present in a PtMn spin valve with SAF, high induced uniaxial anisotropy in the pinned layer and antiferromagnetic interlayer coupling in the SAF, were viewed as possible obstacles in the reorientation of the bias direction in this spin valve system during laser-writing. The exact role of these physical effects in the reorientation process was deduced through the laser irradiation of PtMn simple spin valves (no antiferromagnetic interlayer coupling) and IrMn spin valves with SAF (no induced uniaxial anisotropy).

6.5.1 Laser Writing of FeMn and IrMn Simple Spin Valves

A KrF excimer laser, described in Section 3.2.2, was used to irradiate FeMn (see Section 6.2.2) and IrMn (see Section 6.2.3) spin valve samples in the energy range of 0-20 mJ. The laser energy values were converted into a % values to allow comparison between different types of lasers. The applied field strength was set at 30 mT and the applied field direction 90° to original bias direction during the laser-writing of the spin valve samples. The standard sample size was 10 mm by 10 mm wafer piece. This was necessary to allow the characterization of the samples by XRD, AGM and AES.

The expected changes in the magnetic properties of the spin valve after a 90° reorientation of the bias direction can be best understood by considering MR measurements made parallel and perpendicular to the bias direction of a spin valve. The maximum MR measured perpendicular to the original bias direction is approximately half the maximum MR measured in the parallel orientation (see Figure 6.51). If the FeMn spin valve is heated above 150°C, T_b of FeMn, by the laser irradiation, the pinned layer magnetization will reorient in the direction of the applied field and be reoriented 90° in relation to the original bias direction upon cooling

down. If the same MR measurements are repeated after the reorientation of the bias direction, the maximum MR overall should now be found 90° to the original bias direction.

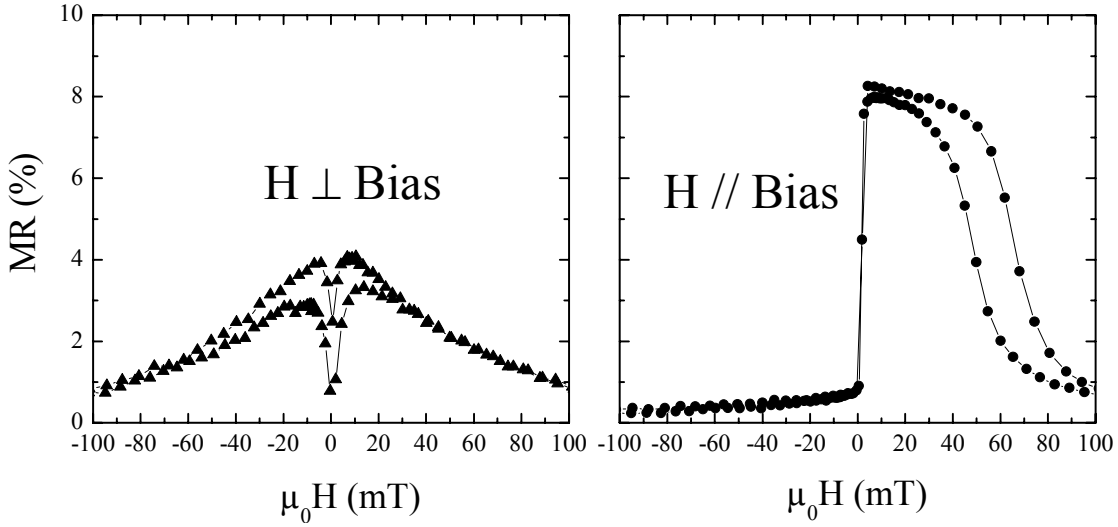

Figure 6.51: MR plots measured from an FeMn spin valve sample both perpendicular and parallel to the bias direction of the spin valve.

6.5.1.1 FeMn Spin Valve: 90° Reorientation

A FeMn simple spin valve (see Section 6.2.2) was the first spin valve system tested with the laser writing process. The FeMn spin valves used in these studies are described in Section 6.2.3. The maximum MR effect is plotted for both the parallel and perpendicular orientations as a function of % laser energy as seen Figure 6.52. The expression " MR ⊥ orig. Bias" refers to an MR measurement made perpendicular to the original bias direction and " MR // orig. Bias" to an MR measurement made parallel to the original bias direction. The H_{eb} is also plotted as a function of % laser energy. The H_{eb} is determined from an MR measurement made in the parallel orientation and after the reorientation of the bias direction from the MR measurement made in the perpendicular orientation. H_{eb} can only be determined from a MR measurement made parallel to the bias direction. Various MR curves measured from laser irradiated FeMn samples are presented in Figure 6.53.

The bias direction in the FeMn spin valve remained unchanged upon irradiation at 0.75% laser energy as seen in Figure 6.52 and Figure 6.53. The bias direction in the pinned layer was only partially reoriented in the new direction as seen in the examination of the MR curve measured at 1.25% laser energy (see Figure 6.53). The MR effect was 6% in the new bias direction. The temperature in the sample during the laser irradiation at 1.25% laser energy had to be above the T_b of FeMn, 140°C, in order for a change in the bias direction to occur. At 2% laser energy, the bias direction was found to be completely reoriented as indicated by an MR effect of 8%.

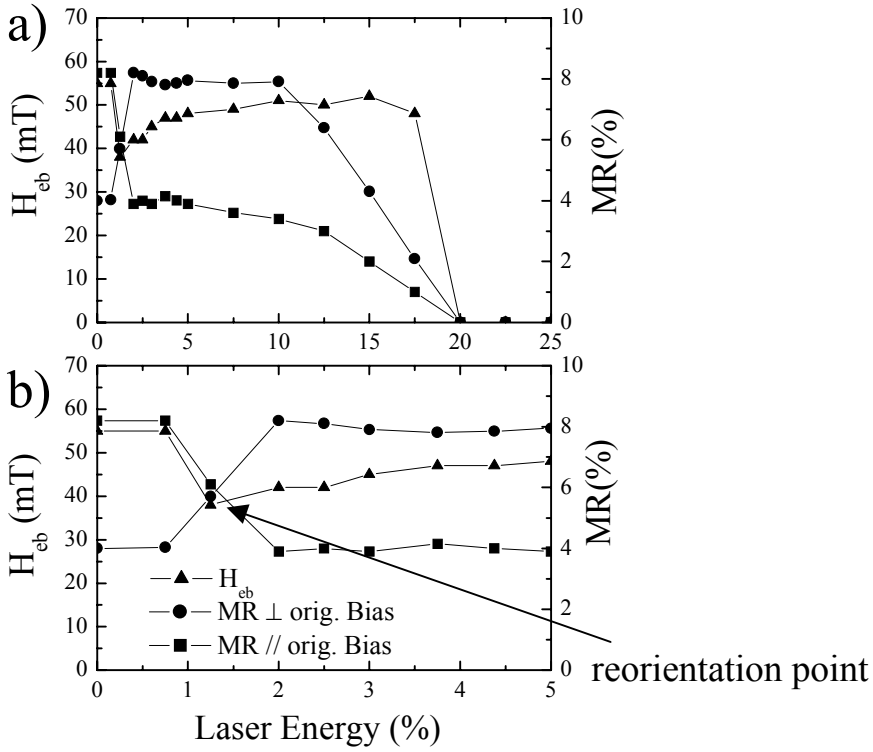

Figure 6.52: Change in the MR effect and H_{eb} of the FeMn spin valve as a function of % laser energy plotted a) over the entire laser energy range and b) close-up of the reorientation point.

The H_{eb} was found to drop to 38 mT after the reorientation at 2% laser energy. The H_{eb} did increase to 50 mT with increasing % laser energy, but never reached the as-deposited value of 55 mT. The cause of the drop in H_{eb} was not related to a T_b distribution otherwise the H_{eb} would have increased with increasing laser energy. This gradual change in the bias direction with increase in % laser energy was indicative of a T_b distribution in the FeMn layer [Ara98] and will be discussed in more detail in Section 6.5.2.1.

The MR effect dropped to 6.4% at 10-12.5% laser energy (see Figure 6.52). The MR continually decreased to 2.5% at 15% laser energy (Figure 6.52) and to zero at 20% laser energy. This loss of MR effect was indicative of microstructure changes in the spin valve stack. Surprisingly the H_{eb} in the same laser energy range remains fairly constant at approx. 50 mT. This result was unexpected considering that a drop in the MR effect usually coincides with a drop in the H_{eb}. This has been observed in most thermal degradation studies of FeMn and IrMn spin valves [Iwa97][Sai98][Mae98]. This mystery will be examined in detail in later in Sections 6.5.4 and 6.5.5.

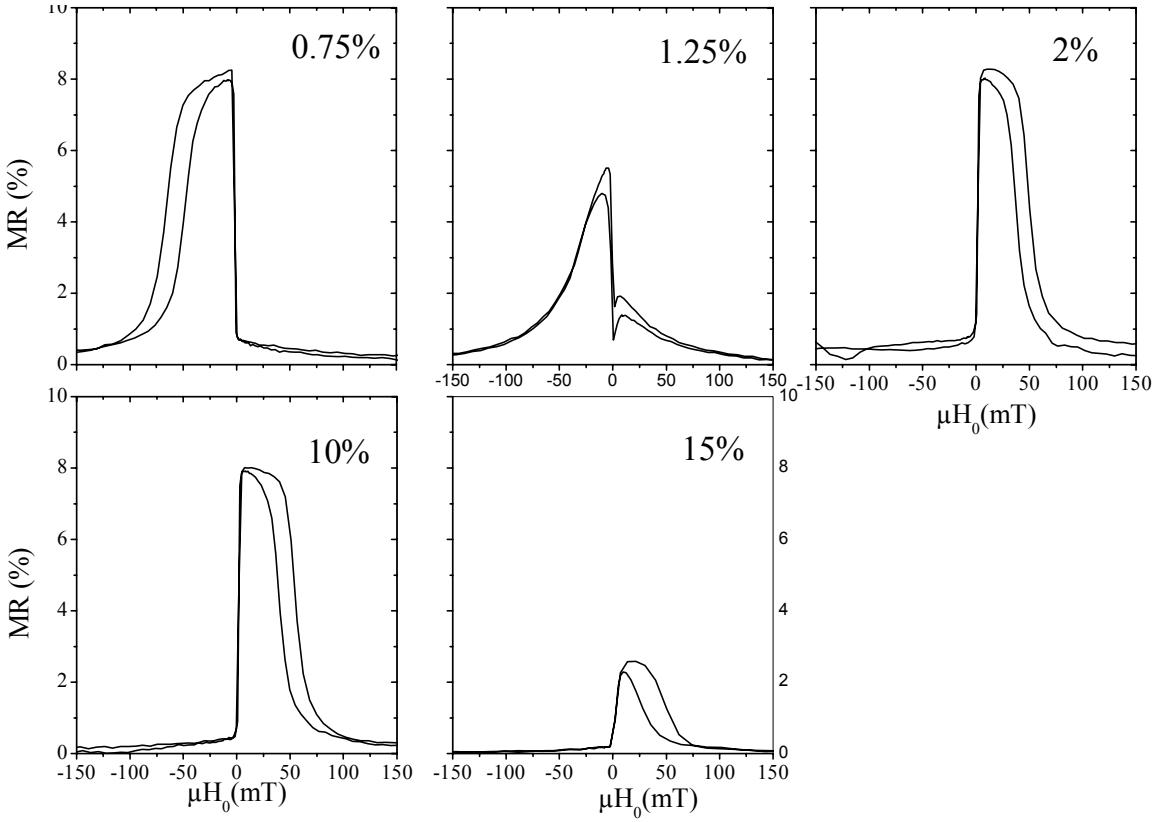

Figure 6.53: MR curves measured from FeMn spin valve samples irradiated at 0.75%, 1.25%, 2%, 10%, and 15% laser energy.

6.5.1.2 FeMn Spin Valve: 0° and 180° Reorientation

The laser writing process must be able to reorient the bias direction 90°, 180° and 270° to original bias direction with no or minimal loss in the MR or H_{eb}. This is a necessary condition for any reorientation method used in the fabrication of a demonstrator GMR 360° angle sensor with four different bias directions on a single chip. FeMn samples were irradiated in the 0-5 % laser energy range under an applied field of 30 mT where the bias direction was set 0° and 180° to the original bias direction. The MR measurements were made with the applied field direction both parallel and perpendicular to the bias direction same as in the 90° reorientation experiments. These measurements were directly compared to the MR measurements from the 90° reoriented experiments. Only the maximum MR measured in the bias direction is plotted rather than the maximum MR from parallel and perpendicular measurement orientations (see Figure 6.54a and b). This format is used to better distinguish between the experimental results from a 0°, 90° and 180° reorientation. For example the 0° reorientation has a maximum MR of zero in the bias direction since the free layer and pinned magnetization are parallel to each other (see Figure 6.54c and d), but switched to 7.8% upon the reorientation of the bias direction. The maximum MR for a 0°, 90° and 180° reorientation should be the same after reorientation point.

The MR effect in the 0° reorientation remained constant at approx. 7.8 % over the entire laser energy range, but the H_{eb} showed a drop from 55 mT (as-deposited state) to 45 mT at 2% laser energy and gradually increased to 48 mT at 5% laser energy (see Figure 6.54). This was the only indication that the spin valve had reached a temperature above the T_b of FeMn. The 90° reorientation showed a drop in MR to 6.0% at 1.25% laser energy and increased to 8% MR after reaching 2% laser energy. In the 180° reorientation the MR also dropped to 6.2

% MR at 1.25% laser energy and then increased again to 7.8% MR at 2% laser energy. The H_{eb} showed a drop from 55 mT to 27 mT at 2% laser energy and gradually increased to 48 mT at 5% laser energy (see Figure 6.54).

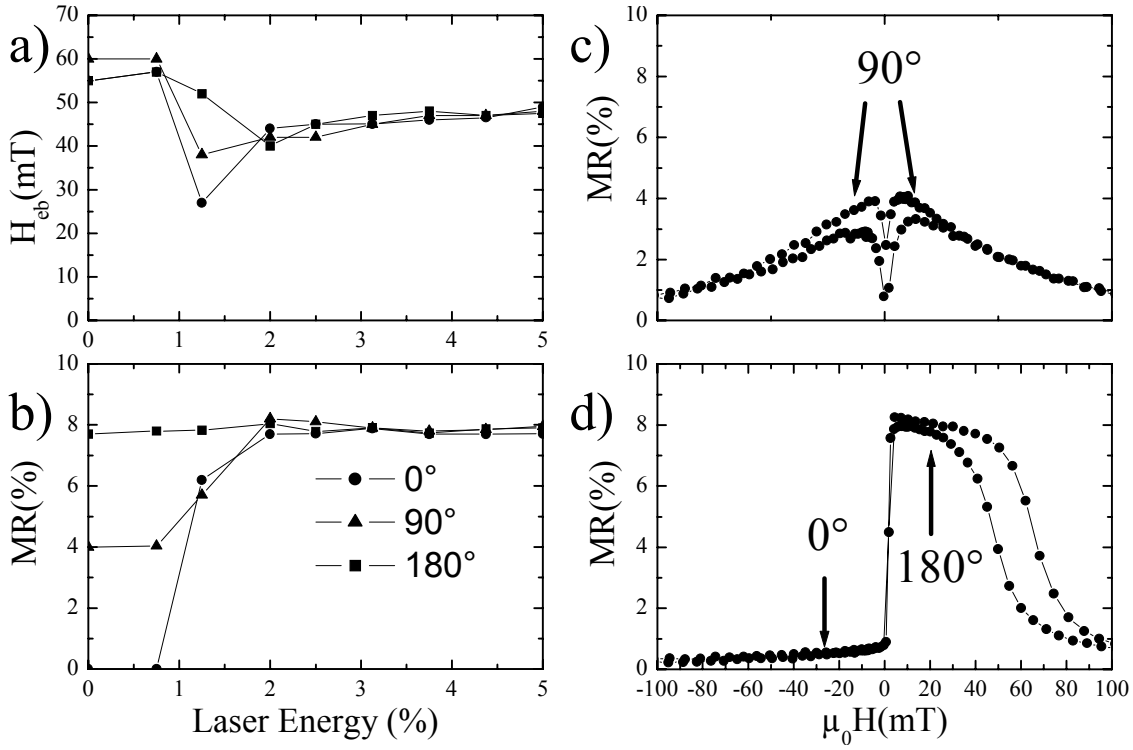

Figure 6.54: Comparison of the change in a) H_{eb} and b) MR of FeMn spin valve as function of % laser energy for the 0°, 90° and 180° reorientation. Representative MR plots measured c) ⊥ and d) // to the bias direction have been included to show the expected maximum MR for 0°, 90° and 180° orientations.

The reorientation point for the 180° case was only visible in the change in the H_{eb} after the reorientation point was reached. The laser energy necessary for reorientation of the pinning direction was identical in all cases: 0.75-2% laser energy. The H_{eb} and MR approached the same value, after 2% laser energy, regardless of the previous orientation of the bias direction. These results showed that the reorientation of the bias direction in simple spin valves such as FeMn or IrMn is independent of the direction of the applied field during the laser writing process when sufficient % laser energy was applied during the laser-writing.

6.5.1.3 IrMn Spin Valve: 90° Reorientation

The results from the laser writing of the IrMn spin valves were similar to those seen in the laser-writing of FeMn spin valves (see previous Section). The IrMn spin valves used in these studies are described in Section 6.2.3. The % laser energy necessary for reorientation of the bias direction was found to be 2.5-3.75% laser energy range (see Figure 6.55b). The temperature reached in the IrMn spin valve had to be above 190°C, T_b of IrMn, in order to change the bias direction. The gradual change in the MR effect and correspondingly in the bias direction was again attributed to a T_b distribution in the AFM layer [Ara98].

The MR effect was only slightly reduced to 7.4% from 7.5% and the H_{eb} dropped to 25 mT from 45 mT after reorientation point. The MR dropped to 6.2% at 15% laser energy and dropped further to zero at 20% laser energy range. The onset of the GMR reduction (12.5-

15% laser energy) was at higher % laser energy than in the case of the FeMn (10-12.5% laser energy). The IrMn spin valve used CoFe as the material for the pinned layer and the interdiffusion barrier in the free layer instead of Co. A CoFe is less prone to intermixing with Cu than the pure Co layer [Zet98]. The H_{eb} increased up to 38 mT with an increase to 8.75% and remained constant until the complete disappearance of the GMR effect.

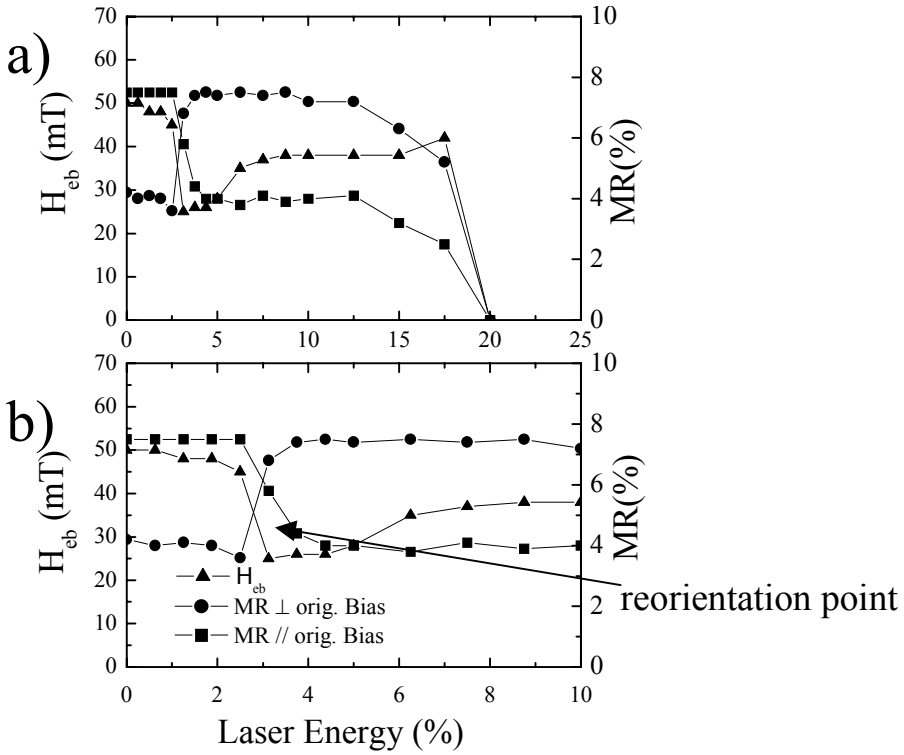

Figure 6.55: Change in the MR effect and H_{eb} of the IrMn spin valve as a function of % laser energy plotted a) over the entire laser energy range and b) close-up of the reorientation point.

6.5.1.4 Laser Writing Process: Unanswered Questions

There were several unanswered questions that arose after a detailed examination of the experimental results from the laser-writing of the FeMn and IrMn spin valves. These questions are summarized below:

- The gradual transition and loss of H_{eb} near the reorientation point. Was this a result of a T_b distribution in the AFM layer?
- The complete loss of GMR and exchange bias effect at 17.5% laser energy. Was the exchange bias effect still present in the spin valve and was simply not detectable by a MR measurement?
- The reduction in the GMR effect in the laser energy range: 12.5-17.5% laser energy. Which microstructural changes lead to a reduction in the spin-dependent scattering?
- The stability of the exchange bias in the same laser energy range (12.5-17.5% laser energy) as the reduction of GMR effect. Why did the exchange bias remain stable?

The experimental results presented in the following sections were devoted to the explanation of these unanswered questions.

6.5.2 Reorientation Point: Gradual Change in Bias Direction

6.5.2.1 Blocking Temperature Distribution

The gradual reorientation of the bias direction over the laser energy range of 0.75-2%(FeMn) and 2.25-3.75% (IrMn) can best be understood by assuming a T_b distribution in the AFM layer. The measured blocking temperature T_{b_meas} is an averaged value of the entire AFM layer, but each grain has its own T_b. This leads to a T_b distribution in the AFM layer [Ara98]. Let us assume a T_b distribution of ±10°C in the AFM layer with a T_{b_meas} of 140°C. As illustrated in Figure 6.56 one third of the grains have a $T_b > T_{b\_meas}$(140°C), one third with $T_b < T_{b\_meas}$, and approx. equal to T_{b_meas}.

If the AFM is heated to a temperature of 120°C by the laser, all of the grains will retain the same bias direction as indicated Figure 6.56a. After the laser energy is increased to near T_{b_meas} (140°C) the grains with a $T_b > T_{b\_meas}$ will retain the original bias direction (see Figure 6.56b). This corresponds to the situation seen in Figure 6.52 for the laser irradiation of a FeMn spin valve at 1.25% laser energy. The bias direction was partially reoriented in the new direction resulting in the MR drop to 6%. There would only be a homogeneous bias direction in the spin valve upon heating to a temperature of above 160°C which is above the T_b distribution range (see Figure 6.56c). This happened when the % laser energy reached 2% in the case of the FeMn spin valve (see Figure 6.52) as indicated by the measured MR effect of 8%.

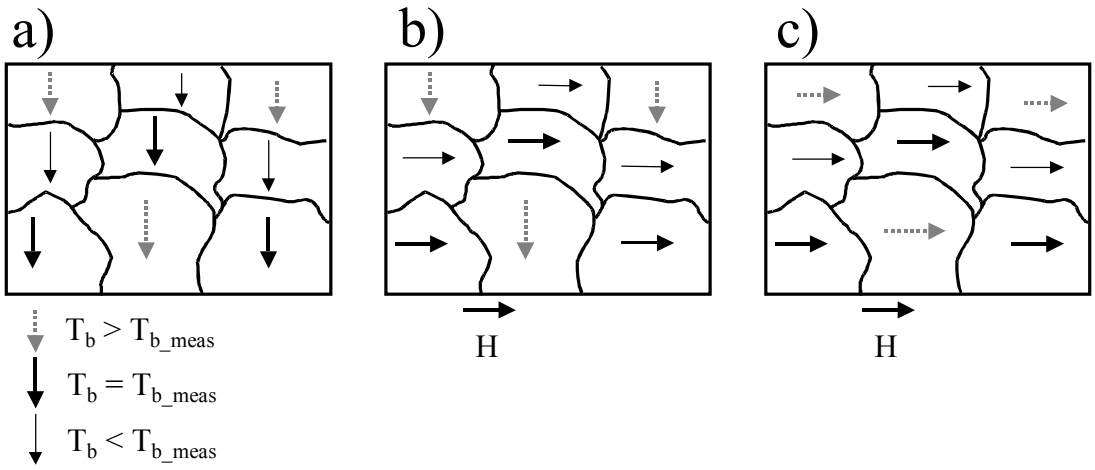

Figure 6.56: Diagram illustrating the T_b distribution after heating to a temperature a) of 120°C where all of the grains have the same bias direction, b) of 140°C where 2/3 of the grains are reoriented in the new bias direction and c) above 160°C all where of the grains have the same bias direction.

6.5.2.2 Loss of H_{eb} after Reorientation of Bias Direction

The drop in the H_{eb} after the reorientation of the bias direction and gradual rise with increasing % laser energy could be attributed to two different possible causes. The first possible cause is insufficient temperature during the laser anneal to overcome the problem of the T_b distribution. Insufficient time during the laser anneal to allow for reorientation of the net magnetization in either the AFM or FM layer was seen as another possible reason for the loss of H_{eb}.

The continuing influence of a T_b distribution can be ruled out by considering the temperature reached in the spin valve during the laser anneal. The maximum temperature in

the spin valve stack reached during the laser irradiation can not be determined by conventional temperature measurement methods due to the extremely small area irradiated and the time scale of the laser pulse: 20 ns. It is however possible to establish a rough relationship of % laser energy vs. temperature by considering the different T_b of the different AFM irradiated in each spin valve system. Each spin valve system consist of metallic thin films of different material and layer thicknesses, but this can be neglected when considering thin metallic films that are a few tens of nm in thickness [Bon00].

The FeMn (140°C), IrMn (190°C), and PtMn (380°) spin valves each had a different T_b (see Table 10.3). The experimental results for reorientation of PtMn antiferromagnet are presented later in Section 6.5.6. A rough plot of % laser energy versus temperature was created from this data as shown in Figure 6.57. The temperature reached in the spin valve irradiated at 10% laser energy above 400°C in order to allow the reorientation of the bias direction in the PtMn spin valves. These experimental results will be shown later in Section 6.5.6. The H_{eb} reached saturation at 10% laser energy of until loss of the GMR effect at 20% laser energy. If temperature had played a significant role in the reduction of the exchange bias effect, H_{eb} should have continually increased with increasing laser energy until it reached the H_{eb} measured in the as-deposited state (55 mT).

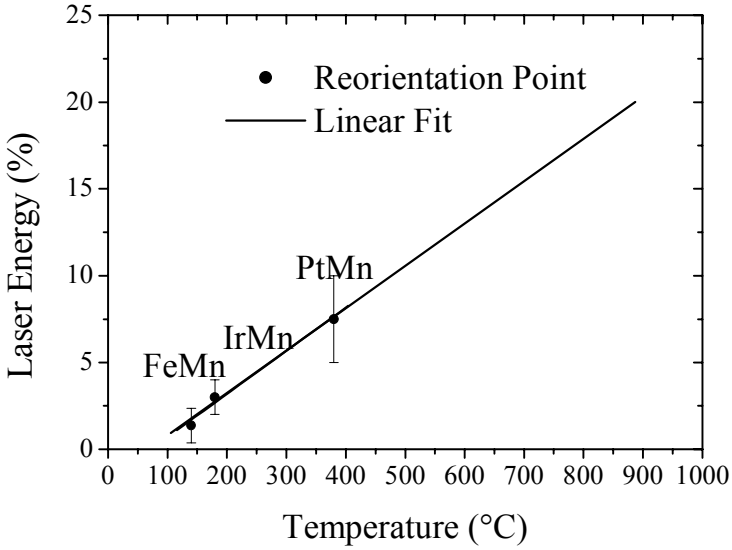

Figure 6.57: % Laser energy as a function of temperature as determined by comparison with the T_b of the individual antiferromagnets.

The laser pulse time probably played the biggest role in the reduction of the H_{eb}. The domains in the AFM may have not had enough time to reorient in the direction of magnetic field. The time above the T_b can be roughly estimated by considered the time scale of the laser pulse and experimental results presented by Boneberg, et al. [Bon00], on laser annealed 40 nm thick Cu thin films. Boneberg determined a time-dependent temperature profile in the Cu thin film using time-resolved reflectivity measurements. The heat generated by a Nd:YAG laser with pulse time of 7 ns dissipated within 20 ns. The time at the maximum temperature (T_{max}) during the laser irradiation was approximately only 2 ns. These quoted times are from the irradiation of Cu film at laser energy setting below the melting point of the Cu thin film. Similar results in the laser irradiation of other metallic thin films have also been reported [Zav75][Tsa86][Bis99]. The time above T_{max} due to the laser irradiation by a KrF excimer laser (pulse time of 20 ns) of spin valve thin films cannot be longer the pulse time.

This hypothesis was tested by performing a field cool on a FeMn spin valve sample irradiated at 5% laser energy. If the field cool could restore the original H_{eb} in the sample, then the reduction in the H_{eb} after the reorientation could be attributed to the limited time

above T_b during laser irradiation. The field coil settings were 160°C for 30 min. under 500mT field. The applied field direction during the field cool was set in the same direction as the original bias direction. The MR curves are shown measured from a FeMn spin valve before and after the field cool (see Figure 6.58). The H_{eb} was restored to the 60 mT where it had previously been only 42 mT, which is higher than the H_{eb} measured in the as-deposited sample, 55 mT. These results conclusively proved that when the time scale of heating was time played a decisive role in the reduction exchange bias effect after the reorientation of the bias direction when the heating time was on the ns scale.

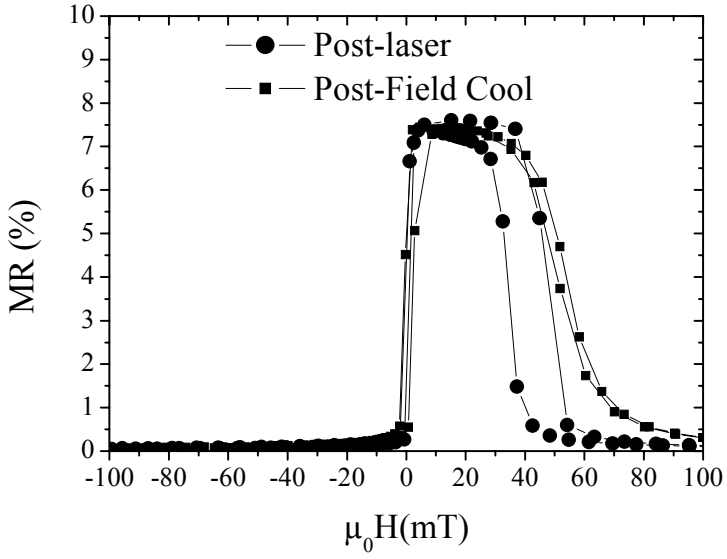

Figure 6.58: Restoration of exchange bias effect in FeMn spin valve irradiated at 5% laser energy with a field cool.

6.5.3 Source of GMR and Exchange Bias Effect Loss

The gradual loss of the MR effect up to 20% laser energy and the abrupt loss of the H_{eb} effect at 20% laser energy in the FeMn and IrMn spin valves did not fit the expected behavior. It was expected that the MR effect and H_{eb} would simultaneously reduce in magnitude as the laser irradiation induced interdiffusion in the spin valve stack. This was the typical behavior of H_{eb} and the GMR effect in FeMn and IrMn spin valves subjected to long term anneals (200-300°C for several hours) [Iwa97][Mae98][Sai98].

The GMR effect may no longer be present in the spin valve, but pinned layer may still be have been exchange biased by the neighboring AFM layer. Magnetization measurements by an AGM from spin valve samples irradiated at or above 20% laser energy would determine if the exchange bias effect was still present. AES depth profiling of the same samples could determine the degree of interdiffusion between the different layers in the spin valve stack as a function of % laser energy during the irradiation.

6.5.3.1 Magnetization Characterization with AGM: FeMn and IrMn

The AGM measurements were made from three different FeMn samples: as-deposited, irradiated at 17.5% laser energy and at 20% laser energy. The magnetization measurement of the reference sample showed the expected H_{eb} of 55 mT (see Figure 6.59). At 17.5% laser energy the H_{eb} reduced to 50 mT, which was identical to the H_{eb} as determined by MR measurements made on the same sample. The magnetization curve measured from the sample irradiated at 20% laser energy showed a hysteresis loop characteristic of a single

ferromagnetic layer with a low H_c. There was no sign of asymmetric shift due to exchange biasing of the ferromagnetic pinned layer. This was an indication that microstructural changes occurred not only in the Co/Cu/NiFe layers but also in the FeMn layer of the spin valve. Massive interdiffusion must have occurred in the spin valve stack to cause the disappearance of both the H_{eb} and MR effect.

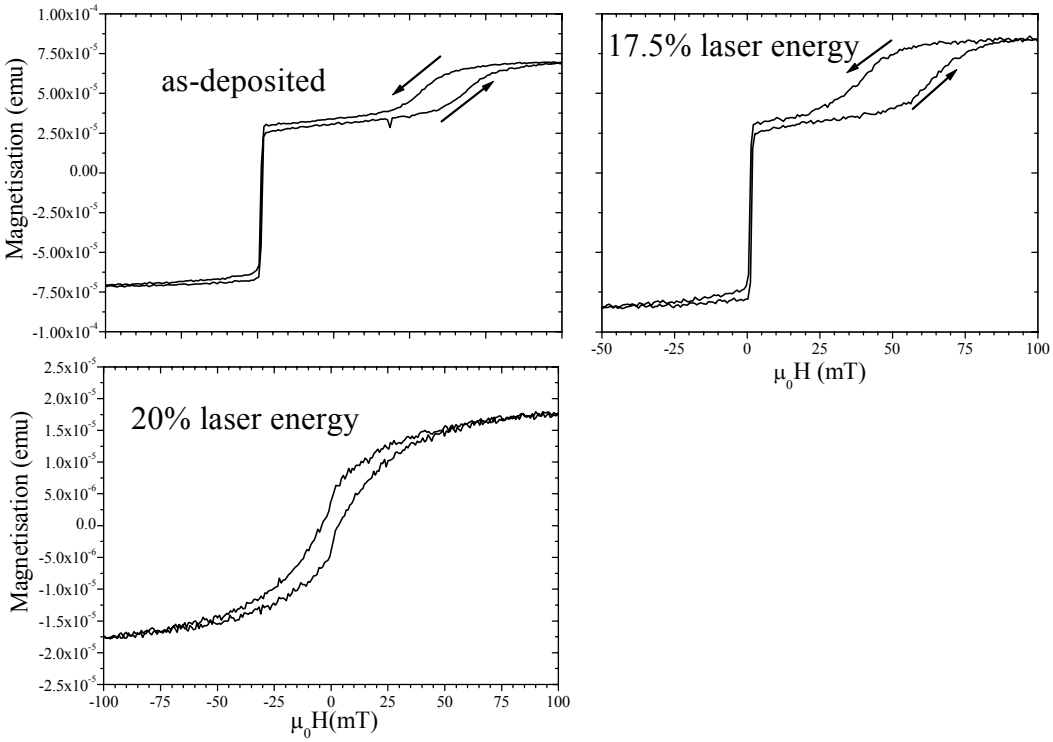

Figure 6.59: Magnetization curves measured from a FeMn spin valve in the as-deposited state and irradiated at 17.5% and 20% laser energy.

The same AGM measurements were repeated on three different IrMn spin valve samples: as-deposited, irradiated at 17.5% laser energy, and irradiated at 20% laser energy. The AGM measurement of the as-deposited sample had the expected H_{eb} of 45 mT (see Figure 6.60). At 17.5% laser energy the H_{eb} was reduced to 40 mT again the same value as determined by MR measurements (see Figure 6.60). This mirrored the results of the AGM measurements of the FeMn spin valves (see Figure 6.59). The magnetization curve from the IrMn spin valve sample irradiated at 20% laser energy as seen in Figure 6.60. showed paramagnetic behavior, which was indication of massive microstructural changes in the spin valve stack.

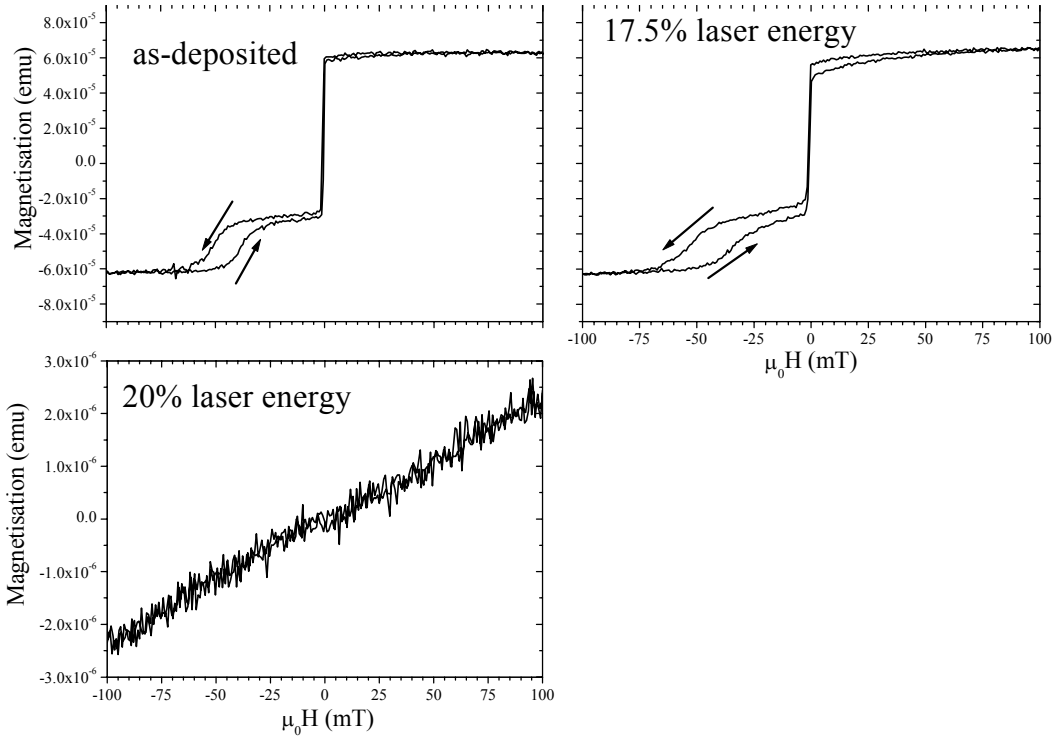

Figure 6.60: Magnetization curves measured from IrMn spin valves in the as-deposited state and irradiated at 15% and 20% laser energy.

6.5.3.2 AES Depth Profiling

AES depth profiling measurements were performed to determine the amount of interdiffusion in the spin valve stack as a function of the laser energy in both FeMn and IrMn spin valve samples. Four different FeMn samples and four different IrMn samples were analyzed by AES: an as-deposited sample and samples irradiated at three laser energy settings (15%, 17.5% and 20% laser energy). The AES depth profiles are presented together for the IrMn spin valve as seen in Figure 6.61 for a better overview of the differences in depth profiles between the different samples. Reference spectra [Muh97] were used to determine the sputter rates of the individual element. The AES settings used for the depth profiling are described in Section 4.2.3.

There were no discernible differences in the AES depth profiles from the as-deposited sample and the IrMn samples irradiated at 15% and 17.5% laser energy. The AES depth profile from the 20% laser energy sample showed the complete intermixing of IrMn, Cu, CoFe and NiFe layers. Only the Ta layer remained intact in the spin valve stack. This explained the complete lack of MR and exchange bias in the spin valve after irradiation at 20% laser energy. There are simply no more defined layers in the spin valve stack. AES depth profiles of the FeMn spin valves irradiated at the same % laser energy showed the same results (not depicted). The expected scenario was a gradual interdiffusion of the different elements into the neighboring layers in the spin valve stack with increasing laser energy as shown in anneal studies of IrMn and FeMn spin valves [Isa97][Mae98][Sai98]. In this case there was an abrupt transition from the original spin valve structure at 17.5% energy to complete intermixing at 20% laser energy.

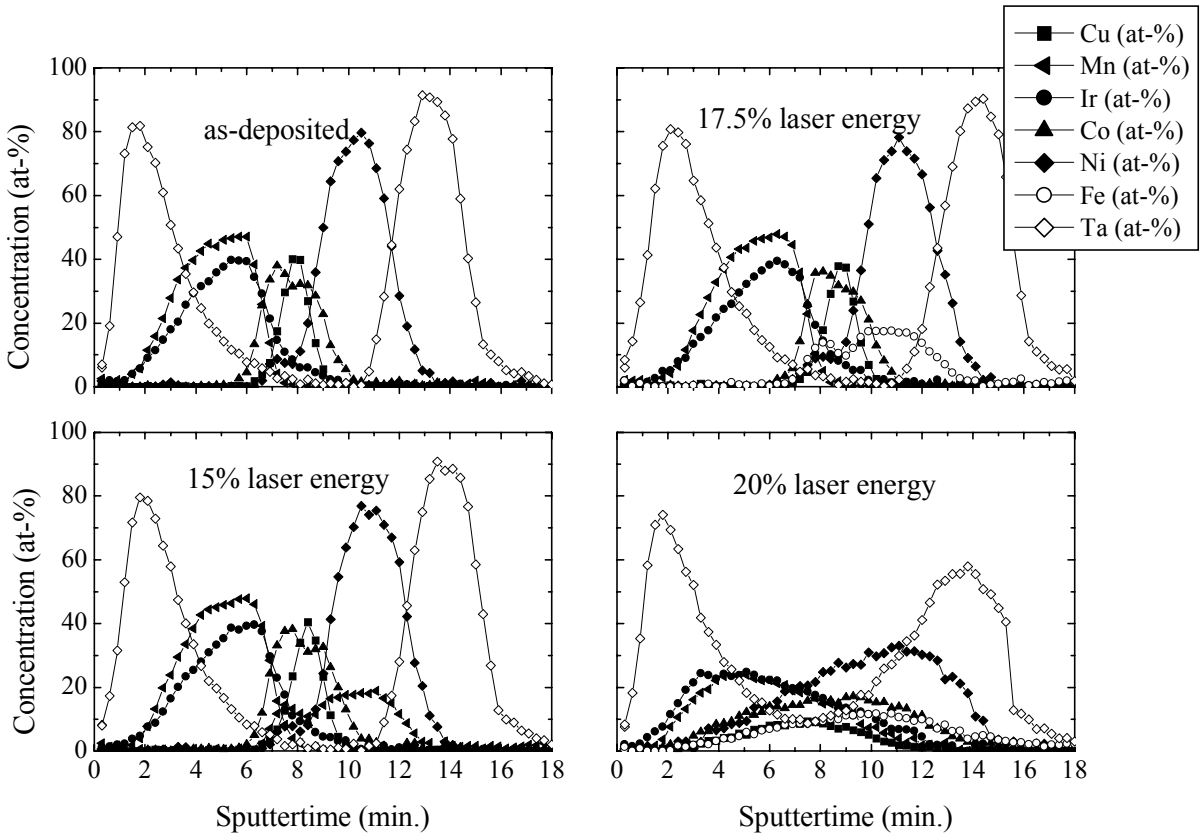

Figure 6.61: AES depth profiles from IrMn spin valves in the as-deposited case and irradiated at 15% laser energy, 17.5% laser energy, and 20% laser energy.

The Full Half Mean Width (FHMW) was determined for the respective peaks of Ir, Mn, Co, Cu, and Ni in the AES depth profile (see Table 6.4). The FHMW of a peak is proportional to the layer thickness. The FHMW of a peak would increase if any amount of interdiffusion had occurred in these samples prior to the complete intermixing of the spin valve stack at 20% laser energy. The FHMW for Ni, Co, and Cu peaks in the AES depth profiles from the samples irradiated at 15% laser energy and 17.5% laser energy showed only a slight increase in FHMW and therefore the layer thickness. This supposed increase in layer thickness was however below the resolution limit of AES. The escape depth of the Auger electrons is on the order of the layer thicknesses of the spin valves [Bru92].

FeMn spin valves showed similar results to those of IrMn (see Table 6.5). The FHMW for every element were almost identical upon comparison between the as-deposited and 17.5% laser energy samples. This again indicated the lack of interdiffusion between the layers in the spin valve. The reduction in the GMR effect up to 17.5% laser energy indicated that some amount of interdiffusion had taken place, but this could not be confirmed due the resolution limits of AES depth profiling.

Table 6.4: FHMW for the Ir, Mn, Co, Cu and Ni peaks in the AES depth profiles measured from laser irradiated IrMn spin valves.

Sample	Ir	Mn	Co_1	Cu	Co_2	Ni
% laser energy	min.	min	min	min	min	min
Reference	3.30	2.97	1.52	1.07	1.01	2.43
15%	3.53	3.17	1.63	1.17	1.10	2.52
17.5%	3.52	3.16	1.65	1.15	1.15	2.61

Table 6.5: FHMW for the Fe, Mn, Co, Cu and Ni peaks in the AES depth profiles measured from laser irradiated FeMn spin valves.

Sample	Fe	Mn	Co_1	Cu	Co_2	Ni
% laser energy	min.	min	min	min	min	min
Reference	3.12	2.93	1.49	1.06	1.29	1.85
15%	3.20	3.05	1.51	1.14	1.34	1.98
17.5%	3.21	3.06	1.50	1.16	1.37	2.01

The abrupt transition from a intact spin valve structure at 17.5% laser energy to complete intermixing at 20% laser energy was a surprising result considering the small difference in % laser energy. If the temperature increased linearly as shown in Figure 6.55 this would indicate a temperature of approx. 780°C at 17.5% laser energy and 880°C at 20% laser energy. Such a drastic change in layer structure of spin valve cannot be explained by simple grain boundary diffusion with a temperature increase of only 100°C. Up to this point there had been no appreciable interdiffusion observed in the laser irradiated spin valves (See Table 6.4 and Table 6.5). It is for all practical purposes impossible to predict which of the many possible reaction products resulted from the intermixing of all of these elements. The spin valve stack contains several different elements including, Co, Cu, Fe, Ir, Mn, Ni, and Ta.

It was curious to note that Ta passivation layer was the only element to remain fairly stable in the sample irradiated at 20% laser energy (see Figure 6.61). This layer is oxidized through exposure to air to form Ta_2O_5. The Ta_2O_5 is probably more stable at higher temperatures than pure Ta. This is supported by the fact that the Ta buffer layer intermixed with the rest of the spin valve stack. The complete intermixing of the spin valve stack at 20% laser energy explained the simultaneous loss of the both the exchange bias and GMR effect in the spin valve stack. This did not however explain the stability of the exchange bias effect and the gradual loss of the GMR effect up to the irradiation at 20% laser energy.

6.5.4 Source of the GMR Effect Reduction

The GMR effect was seen to gradually reduce with increasing laser energy up to the complete intermixing of the spin valve stack. This was in the range of 12.5-20% laser energy, in the case of FeMn, and 15%-20% laser energy in case of the IrMn spin valves (see Figure 6.52 and Figure 6.55). There are four different commonly cited causes for the loss of GMR effect in annealed spin valves. These four reasons are summarized below:

Mn diffusion from the AFM layer: Mn diffusion from the AFM layer to the FM/NM interface has been cited as a source of the GMR reduction in annealed FeMn and IrMn samples (e.g. 200-300°C for several hours) [Mae98][Sai98][Zet98]. The presence of the Mn at the NM/FM interface changes the spin arrangement at the interface thereby reducing the spin dependent scattering [Mae98].

Ni diffusion from the free layer: Diffusion of Ni from the free layer to Cu spacer layer has often been cited as major issue in the thermal stability of the spin valves in the 200-300°C temperature range [Coe96] [Koo96]. This is a primary reason for the place of a Co layer between the NiFe free layer and Cu spacer layer.

Transformation of Metastable Phases: It is possible to induce a transformation of one of the metastable phases in the spin valve stack, e.g. fcc Co to hcp Co through a long-term anneal [Zet98]. The presence of noncubic phases in the spin valve would result in an increase in spin-independent scattering and a decrease in the GMR effect [Koo96].

Intermixing of Co and Cu at the interfaces: The alloying of Co or CoFe alloys with Cu at the interfaces in spin valve stack. This has been found to increase the amount of spin-independent scattering in the FeMn and IrMn spin valves and thus a reduction in the GMR effect [Sai98][Mae98].

Mn and Ni diffusion can immediately be discounted as a possible source of the GMR loss. The AES depth profiling had no diffusion of Mn or Ni to neighboring layer in the spin valve stack prior to complete intermixing at 20% laser energy (see Figure 6.61). This left only the points 3 and 4 as possible explanations for the GMR loss. The goal of the next set of experiments was to determine which of these two mechanisms were responsible for the loss of the GMR effect. XRD measurements were made on the laser irradiated samples to determine if any phase changes had occurred in the spin valve stack. The change in resistance and interlayer coupling as a function of % laser energy were studied to give an indication of any minor structural changes that were not immediately visible in AES or XRD measurements. Reflectometry measurements were performed to determine the change in interface roughness with increase in % laser energy.

6.5.4.1 Structural Analysis with XRD

XRD analysis was performed on the laser irradiated spin valves to determine if phase changes had occurred as a result of the laser irradiation. This phase change could account for the reduction in GMR effect (See point 3 in previous section). XRD measurements were made on FeMn and IrMn samples in the as-deposited state and on samples irradiated at every laser energy setting. Only the XRD diffraction patterns from the as-deposited sample and samples irradiated at 17.5% and 20% laser energy are presented in Figure 6.62 and Figure 6.63.

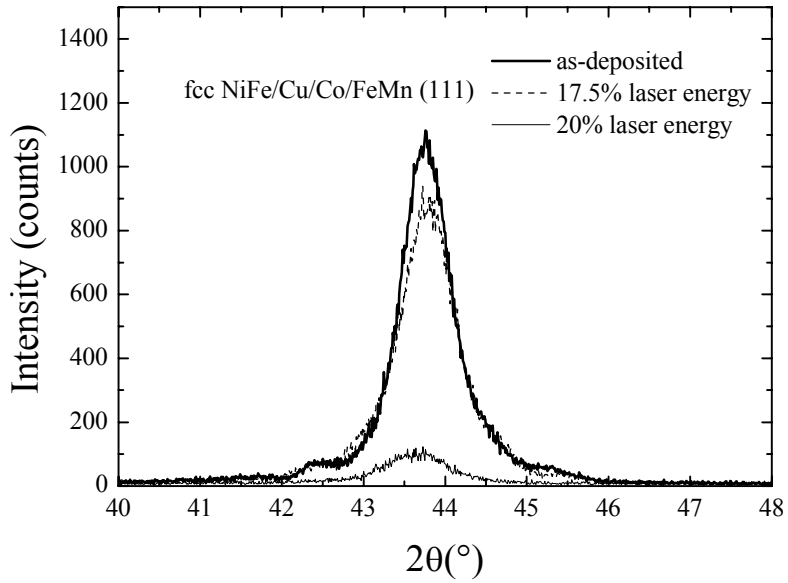

Figure 6.62: X-ray diffraction pattern from a FeMn spin valve sample in the as-deposited state and samples irradiated at 17.5% laser energy and 20% laser energy.

In the FeMn as-deposited sample, the combined (111) reflection for NiFe/Cu/Co/FeM was present at 43.7° (see Figure 6.62), which is the same position as previously reported (see Figure 6.28). The (111) reflection did not shift after the laser irradiation at 17.5% laser energy. No other reflections were present in the XRD diffraction pattern. This indicated that no transformations of any of the metastable phases, e.g. fcc Co, had occurred in the spin valve stack. At 20% laser energy the peak intensity had dropped to 100 counts and the (111)

reflection had shifted to 43.5°. This shift in the reflection position and loss of intensity was due to the large-scale intermixing of the different spin valve layer as determined by AES depth profiling (see Section 6.5.3.2).

The analysis of the XRD diffraction patterns from the laser irradiated IrMn spin valves produced similar results to that of FeMn spin valves. The (111) reflection for fcc NiFe/Cu/CoFe is present at 43.9°, the (330) reflection for cubic Mn at 42.9°, and the cubic $IrMn_3$ (111) peak at 41.2° (see Figure 6.61) as seen in other XRD measurements (see Figure 6.63). The (111) reflection for NiFe/Cu/CoFe and IrMn after irradiation at 17.5% laser energy had remained in the same position. There was no change in reflection position or the appearance of new reflections to indicate the transformation of any metastable phases.

At 20% laser energy a drastic change was noted in the XRD diffraction pattern in the position and number of the reflections. There are now only two reflections at 41.5° and 43.5°, present in the diffraction pattern where there were previously three reflections. The shift in the reflection position and reduction in number of reflections was an indication of massive changes in the crystal structure of the spin valve. A transformation of a metastable phase can be ruled out as source of the GMR reduction prior to complete intermixing of the spin valve stack.

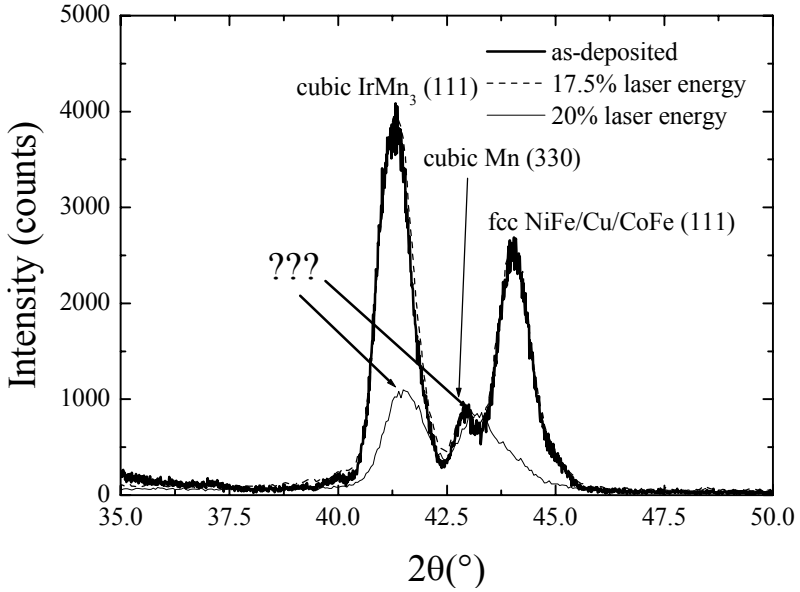

Figure 6.63: X-ray diffraction pattern taken from a IrMn spin valve sample in the as-deposited state and irradiated at 17.5% laser energy and 20% laser energy.

6.5.4.2 Change in Resistance: Indication of Interdiffusion

Closer analysis of the changes in resistance with increase in % laser energy point to the presence of interdiffusion in the spin valve stack at the same time as the decrease in the MR effect. The resistance of the spin valve as function of laser energy is shown in Figure 6.64. In the case of FeMn, the sheet resistance began at 4.4 ohm in the as-deposited case and remained in the range of 3.9-4.4 Ohms up to 12.5% laser energy range. The MR effect dropped to 6.4% at 12.5% laser energy without any noticeable increase in the resistance. The resistance at 15% laser energy suddenly jumped to 7.35 Ohm and the MR effect had further dropped to 4.2%. This trend continued until 20% laser energy was reached after which no more MR effect measured in the sample. The resistance has risen to 13.3 Ohm at this point.

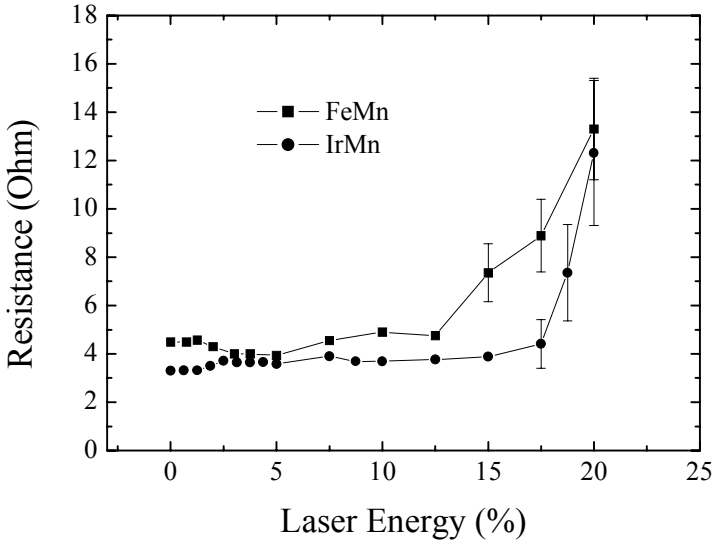

Figure 6.64: Change in resistance of FeMn and IrMn spin valve as a function of the % laser energy.

The change in the resistance of the IrMn spin valves as a function of % laser energy showed a similar behavior to that of FeMn (see Figure 6.64). The resistance began at 3.3 Ohm in the as-deposited case and remained roughly constant in the range of 3.3-3.8 ohms from 2-15 % laser energy. At 15% laser energy the resistance had slight risen to 4.4 Ohm and the MR effect had dropped to 6.2% The MR effect continually dropped in the laser energy range 15-20% while the resistance rose to 12.3 Ohm. At 20% laser energy the entire spin valve was intermixed resulting in a drastic increase in the resistance of the spin valve.

The rise in resistance with increasing % laser energy prior to complete intermixing of the spin valve stack is a sign of the interdiffusion in the spin valve stack. This is a common effect associated with long term anneal studies in the temperature range of 200-300°C of FeMn and IrMn spin valves [Iwa97][Mae98][Sai98], NiMn spin valves [Tsu99] and PtMn spin valves [Mao00][Tak00]. Large-scale interdiffusion in spin valves was usually reported in annealing studies of spin valves; but AES analysis had shown that the spin valve layers remain completely intact up to 20% laser energy (see Figure 6.61). The level of intermixing taking place in both the IrMn and FeMn spin valves must be on an extremely small scale (sub-nm) to not be detectable by the AES depth profiling.

The difference between the FeMn spin valves to IrMn spin valves in reference to the onset of the resistance increase and MR reduction was attributed to the use of CoFe rather Co in the pinned layer and free layer interdiffusion barrier of the IrMn spin valve. Zeltser, et al.[Zel98], studied the effects of long-term anneals (200-300°C/2hr) on the GMR effect in FeMn spin valves with Co and CoFe layers. The spin valves with Co layers showed an increase in the resistance at 210°C while the spin valve samples with a CoFe layer remained unchanged up to 250°C [Zel98]. The Co in CoFe alloy form was probably less prone to intermixing with the neighboring Cu layer than pure Co.

6.5.4.3 Change in Interlayer Coupling

The increase in interlayer coupling in the same regime as that of the GMR reduction (FeMn: 12.5%-17.5% laser energy; IrMn: 12.5%-17.5% laser energy) gave an indication of the actual structural changes in the spin valve stack. The change in the H_e is a sign of the strength of the ferromagnetic interlayer coupling as stated in Section 2.5.5. In most of the spin valves studied in this dissertation, orange-peel ferromagnetic coupling was the dominant

coupling mechanism. The strength of the orange-peel interlayer coupling is a related to two-dimensional sinusoidal interface waviness or interface roughness σ of the spacer layer as seen in Eq (2.16).

The H_e of FeMn remained constant at 1.1 mT in the range from 0-10% laser energy (see Figure 6.65). The H_e rose to 1.77 mT at 12.5% laser energy and continued to rise to 3.11 mT with a further increase in laser energy to 17.5%. Analysis of the H_e data from the laser-irradiated IrMn spin valves showed similar results. The H_e remained constant at 0.6 mT up to 12.5% laser energy (see Figure 6.65). At 12.5% laser energy, the H_e had slightly risen to 0.75 mT and at 17.5% laser energy the H_e has risen to 1.55 mT. The rise in interlayer coupling occurs at the same % laser energy as the onset of the GMR reduction in both the laser irradiated FeMn and IrMn spin valves (see Figure 6.52 and Figure 6.55). Interlayer coupling and spin-dependent scattering are probably more sensitive to microstructural changes at the FM/NM interface than electrical conductivity of the entire spin valve stack. The resistance increase usually lagged behind the increase in interlayer coupling and the reduction of the GMR effect in relation of % laser energy.

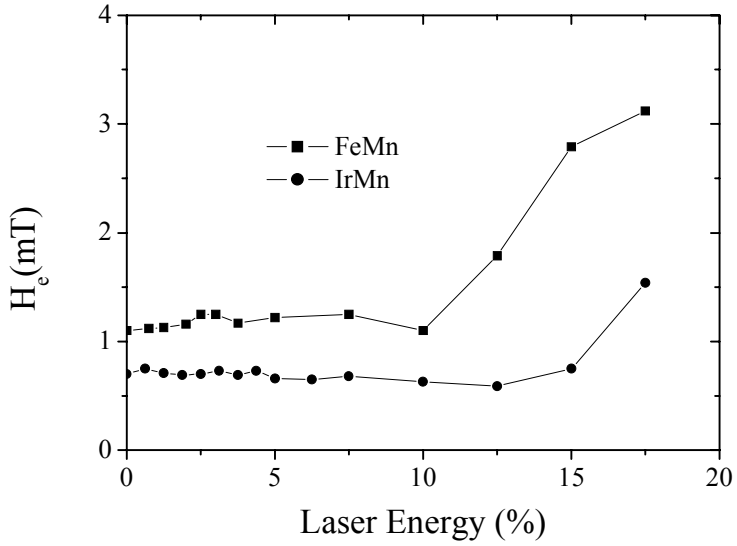

Figure 6.65: Change in H_e of FeMn and IrMn spin valves as a function of % laser energy.

6.5.4.4 Reflectometry: Change in the Interface Roughness

Reflectometry measurements were made on five different FeMn spin valve samples to quantify the change in interface roughness in the spin valve stack. These five samples were a as-deposited sample and samples irradiated at 10%, 12.5%, 15% and 17.5% laser energy. The settings of the X-ray diffractometer setup used for XRR are described in Section 4.2.2. The X-ray reflectometry diffraction patterns are presented in Figure 6.66. The reflectometry diffraction pattern from the as-deposited sample and sample irradiated at 10% and 12.5% laser energy showed very little difference in terms of the Bragg peak position and the clarity of peak. This is not surprising in the case of the sample irradiated at 10% laser energy, but the GMR reduction (see Figure 6.52) and increase in interlayer coupling (see Figure 6.64) began at 12.5% laser energy. The resistance in laser irradiated FeMn spin valves however first began to increase at 15% laser energy (see Figure 6.65).

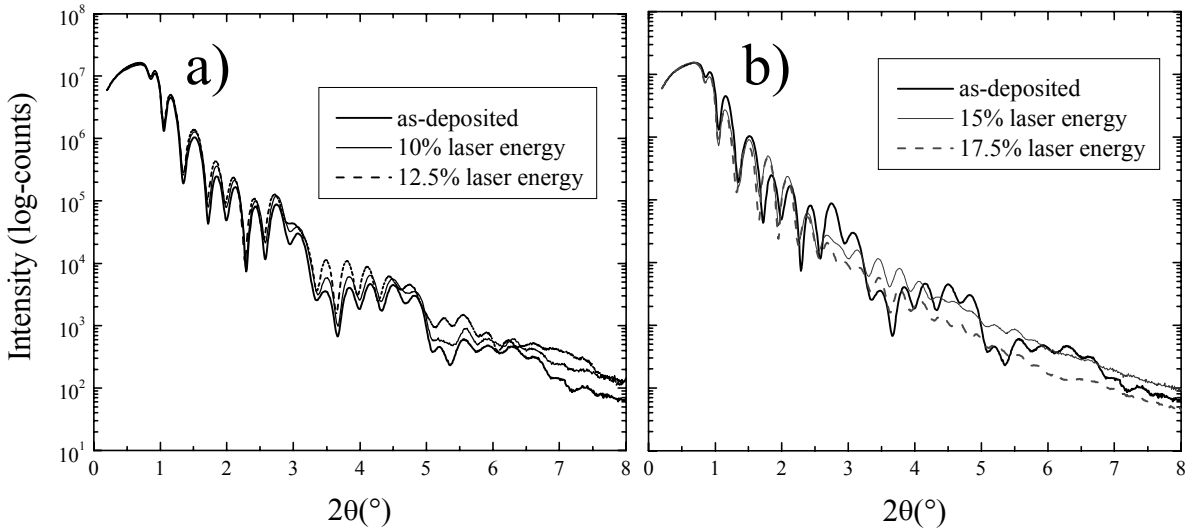

Figure 6.66: Reflectometry diffraction patterns from a FeMn spin valve in the as-deposited state (left and right plots) and a) samples irradiated at 10% and 12.5% and b) at 15% and 17.5% laser energy.

The optical differences between the as-deposited and laser irradiated samples (15% and 17.5%) in the diffraction patterns were evidence of the increase in the interface roughness (see Figure 6.66). The interface roughness had increased from 0.36 nm in the as-deposited spin valve sample to 0.70 nm in the sample irradiated at 17.5% laser energy. The differences are best seen in the oscillations at 2.7° and 4.7°, which are associated with the Co/Cu/Co/NiFe part of the spin valve stack. The clarity and the intensity of the Bragg peaks from the laser irradiated spin valves (15% and 17.5%) were greatly reduced in comparison those of the as-deposited sample. The increase in interface roughness matched the increase in resistance seen at 15% laser energy (see Figure 6.64), but lagged behind the onset of the GMR loss (see Figure 6.65) and an increase in interlayer coupling seen at 12.5% laser energy. There may have been a sufficient amount of intermixing occurring at 12.5 % laser energy to increase the amount of spin-independent scattering but an insufficient amount to be detected by XRR.

6.5.4.5 Source of GMR Reduction: Intermixing at FM/NM interface

The intermixing at the NM/FM interface in the spin valve, Co/Cu interface in the case of FeMn and CoFe/Cu in the case of IrMn, was determined to be the source of the GMR loss in the laser irradiated spin valves. There are numerous other possible reasons (Mn diffusion, Ni diffusion, Co phase transformation), but these GMR loss mechanisms were ruled out based on the experimental results from AES depth profiling, and XRD measurements. AES depth profiles had shown no Mn or Ni had diffused to other layers in the spin valve stack (see Figure 6.61). XRD diffraction patterns of the FeMn spin valves (see Figure 6.62) and IrMn spin valves had indicated no change in crystal structure after the laser irradiation (see Figure 6.63). The only structural change detected was an increase in the interface roughness as shown by the reflectometry measurements (see Figure 6.66). The reduction of the GMR effect in the FeMn and IrMn laser irradiated spin valves (see Figure 6.52 and Figure 6.55) with increasing laser energy coincided with the increase in the interlayer coupling, resistance and interface roughness of the spin valve.

The alloying of Co and Cu at the FM/NM interface in spin valves has been found to reduce the MR effect in spin valves [Sai98] [Mae98]. The solubility of Co in Cu increases upon going above 422°C according the Co-Cu phase diagram [Nis84]. The GMR reduction in the laser irradiated FeMn spin valves began above 10% laser energy (see Figure 6.52).

This corresponded to a temperature of 500°C according to Figure 6.57. Spin-dependent scattering has been shown to primarily occur at the FM/NM interface in magnetic multilayers. This was experimentally confirmed by Parkin, et al. [Par93], where the placement of Co layer at the NiFe/Cu interface in a NiFe/Cu/NiFe/FeMn spin valve increased the MR effect from 2.9% to 6%. The formation of a CoCu alloy at the interface results in an increase in the amount of spin-independent scattering in a spin valve as illustrated in Figure 6.57. These results support the existing research that spin-dependent scattering occurs primarily at the FM/NM interface and not in the bulk of a FM layer of magnetic multilayers.

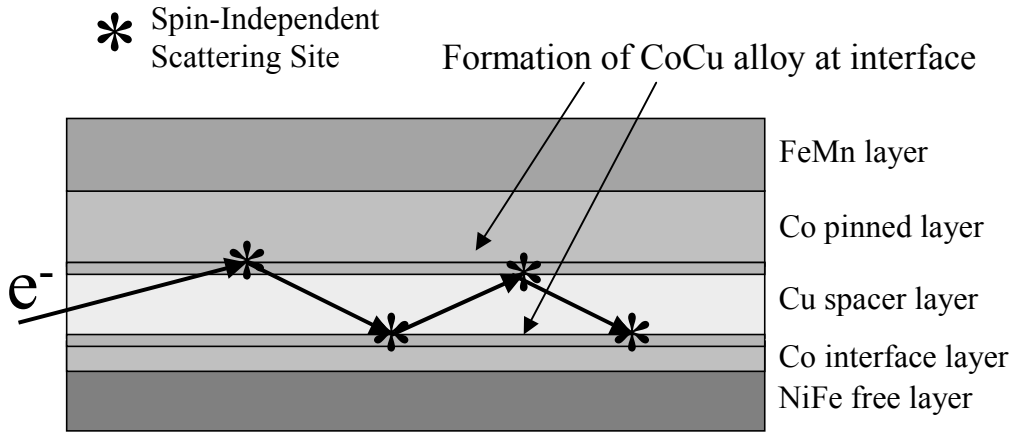

Figure 6.67: Illustration showing the intermixing at Co/Cu interface that leads to an increase in the spin-independent scattering.

6.5.5 Domain State Model: Stability of the Exchange Bias Effect

The H_{eb} of the laser irradiated FeMn (50 mT) and IrMn (40 mT) spin valves remained constant with the increase in % laser energy (12.5-20% laser energy range for FeMn and 15%-20% laser energy range for IrMn). The GMR effect gradually reduced in the same laser energy range. These experimental results contrasted with those seen in typical annealing studies (200-300°C for several hours) of FeMn and IrMn spin valves. The H_{eb} of a spin valve in these anneal studies decreased with increasing anneal time simultaneously with a reduction in the GMR effect [Sai98][Iwa97]. This however only occurs when the time scale of the anneal is sufficient to allow Mn diffusion from the AFM into the rest of the spin valve. The pulse time for the excimer laser is only 24 ns. There is no Mn diffusion to the other layers in the laser irradiated spin valves below 20% laser energy according to the AES depth profiles of the laser irradiated spin valves (see Figure 6.61).

A recent model for the exchange bias effect, the domain state model [Now00] [Now02], was used to explain the behavior of the exchange bias effect in laser irradiated spin valves. According to the domain state model, the defect density in the volume of the AFM layer determines the magnitude of the exchange bias effect and not the AFM/FM interface microstructure (See Section 2.6.4). AES depth profiling (see Figure 6.61) and XRD diffraction patterns (see Figure 6.62) showed that there were no changes in the microstructure of the AFM layer. There was only an increase in the interfacial intermixing seen in the increase in the interface roughness from 0.36 nm (as-deposited state) to 0.70 nm (17.5% laser energy) as determined by reflectometry measurements (see Figure 6.66). The laser irradiation of the FeMn spin valves and IrMn spin valves produced no change in the volume of the AFM layer of the spin valve only intermixing at the interfaces with spin valve stack. It was therefore, according to the domain state model, not surprising that no reduction in the exchange bias effect occurred with the increase in interface roughness.

The validity of the domain state model has already been supported by numerous published results. The H_{eb} of a AFM/FM bilayer has been to increase by increasing the number of defects in the volume of AFM layer. Experiments of this type were done by He^{+} ion irradiation of FeMn/NiFe bilayers [Mou01] [Fas02] and FeMn and IrMn spin valves (see Section 6.4) and the oxidation of CoO in CoO/Co bilayers through increase in the oxygen partial pressure during deposition [Mil00] [Kel02a]. It was also possible to observe the exchange bias effect over a non-magnetic spacer layer placed between ferromagnetic and antiferromagnetic thin film. This type of interaction was seen in experiments using spacer layers of Ag, Au and Cu between a FM/AFM bilayer [Mew00b][Gök97]. This indicates that exchange bias stems from long-range interaction rather than a short-range interaction or interface effect and fits the behavior of the exchange bias observed in the laser irradiated spin valves.

6.5.5.1 Field Cool Experiment

A simple experiment was conceived to test the validity of the domain state model in relation to intermixing at the FM/NM interface in the laser-irradiated spin valves. A field cool (see Section 6.1.1) on a FeMn spin valve irradiated at 17.5% laser energy should restore the H_{eb} to the original value of 55 mT if the exchange bias effect was not dependent on the AFM/FM interface microstructure. This was the same type of experiment as described in Section 6.5.2.2. The FeMn sample irradiated at 17.5% laser energy was annealed at 160°C for 2 hr. under a applied magnetic field of 500 mT at 90° to the bias direction imprinted by the laser-writing. The temperature of 160°C was selected to avoid any smoothening of the interfaces in the spin valve that typically results in anneals conducted above 200°C [Zel98]. After the anneal the MR had risen from 2.2% to 2.5% and the H_{eb} had risen from 50 mT to 60 mT. The increase in the MR effect was probably due to an AMR contribution since the current-bias orientation had shifted 90° after the field cool (see Section 6.1.1.1).

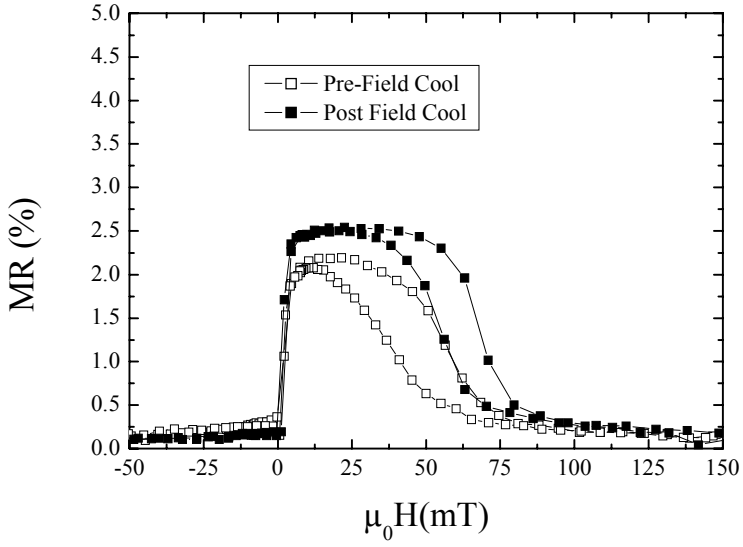

Figure 6.68: MR curve measured from a FeMn spin valve irradiated at 17.5% laser energy and after an anneal of 160°C for 30 min. under a 500 mT applied field.

The H_{eb} of the spin valve sample (60 mT) after the field cool was higher than the H_{eb} of a as-deposited spin valve sample (55 mT) despite the interface mixing. The increase in the H_{eb} in comparison to the as-deposited values was due to the bias direction being more homogeneously oriented in the pinned layer. The bias direction in a spin valve sample

deposited under an applied magnetic field is not as uniform as that bias direction induced in a spin valve by a field cool.

The anneal during the field cool can be ruled out as the source of the exchange bias increase. Any anneal would remove any point defects in the AFM volume, rather than inducing new ones. This was observed in the anneal studies of ion irradiated NiFe/FeMn bilayers where an anneal of 230°C lead to removal of the point defects in the AFM and a slight reduction in the H_{eb} of the bilayer [Mou01a]. Also a decrease in the defect density in the AFM would lead to a decrease in the H_{eb} of the spin valve rather than increase. The exchange bias effect was unaffected by the small amount of the intermixing at the AF/FM interface. The domain state model correctly predicts the behavior of the exchange bias effect in the case of the laser irradiated spin valves.

6.5.6 Laser Writing Experiments: PtMn Spin Valve with SAF

The laser writing method had been successfully applied to reorienting the bias direction in FeMn and IrMn spin valve, but had not yet been tested on the PtMn spin valve with SAF. PtMn spin valve with SAF samples were irradiated with the KrF excimer laser over a laser energy range of 0%-25% with the applied field of 30 mT in one set of experiments and 120 mT in a second set of experiments. The applied field direction was set 90° to original bias direction. Another set of PtMn samples was irradiated at a set % laser energy of 12.5% under an applied field varying from 30-275 mT. The H_{ex} is plotted in the reorientation graphs rather than H_{eb} due to the difficulty in determining an accurate value for H_{eb} directly from an MR measurement.

6.5.6.1 PtMn with SAF: 90° Reorientation under 30 mT and 120 mT Applied Magnetic Field

The 90° reorientation of the bias direction in the PtMn spin valve with SAF under 30 mT applied field produced unusual results in comparison to the previous laser-writing experiments (see Sections 6.5.1). The maximum overall MR effect of the sample remained at the pre-laser state value of 5.5% until the reaching a laser energy of 8.75% (see Figure 6.69). The MR effect in this patterned PtMn spin valve sample was somewhat lower than in the unpatterned state (see Section 6.2.5), (5.5% vs. 6.3%) due to effects with the photolithography and etching steps in the patterning. The reorientation point was in the 8.75-10% laser energy range. It had shifted in comparison to the reorientation point of FeMn or IrMn due to higher T_b of PtMn (380°C).

The MR dropped to 1.9 % at this point in both measurement orientations and remained at this MR value approximately until reaching 15% laser energy (see Figure 6.69). Above 15% laser energy no more MR effect was measured in the sample. This was due to complete intermixing of different layers in the spin valve. The H_{ex} had dropped from 180 mT at 5% laser energy to 140 mT at 8.75% laser energy shortly after the reorientation and remained in the range of 134-145 mT until reaching 17.5% laser energy (see Figure 6.69). The loss of the MR effect after a reorientation of the bias direction was an unexpected result considering the previous experience with the FeMn and IrMn spin valves. No MR loss had been seen in the laser irradiated FeMn and IrMn samples after the reorientation of the bias direction (see Figure 6.52 and Figure 6.55).

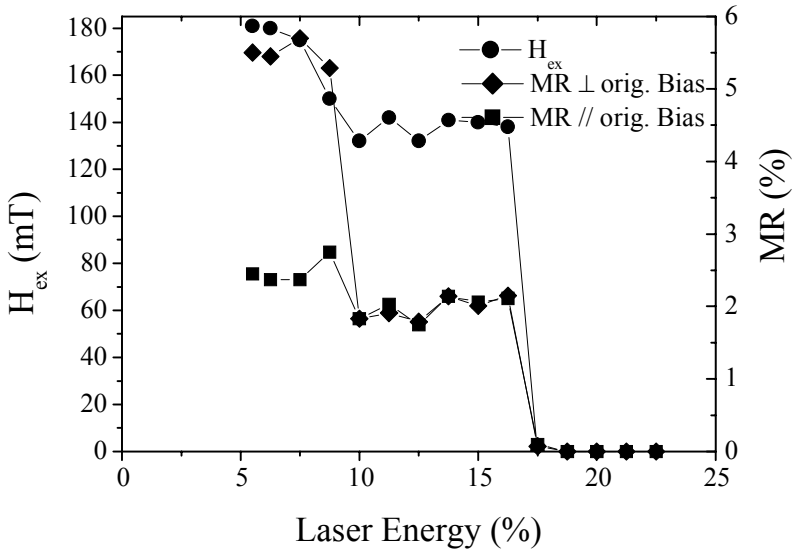

Figure 6.69: MR effect and H_{ex} of the PtMn spin valve with SAF as a function of % laser energy under 30 mT applied magnetic field.

The applied field was increased to 120 mT in an attempt to more homogeneously orient the bias direction during the laser-writing. The reorientation point was again in the range of 8.75-10% laser energy. This time the MR effect after the reorientation was measured to be 4.1% in the perpendicular orientation and 2.0% in the parallel orientation at 10% laser energy (see Figure 6.70). The H_{ex} was measured at 150 mT, which was a slight increase of 10 mT in comparison to the H_{ex} measured in a sample irradiated under 30 mT at the same % laser energy (see Figure 6.69).

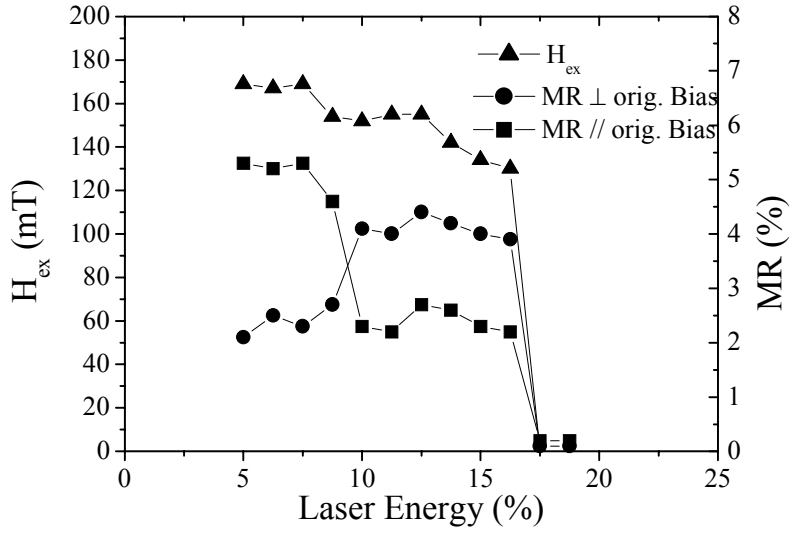

Figure 6.70: MR effect and H_{eb} of the PtMn spin valve with SAF as a function of the laser energy under 120 mT applied field.

The reason for the increase in the MR effect was a more defined bias direction in the spin valve. This is evident upon comparison between the MR rotation curves measured from a as-deposited sample and samples irradiated at 12.5% laser energy under 30 mT and 120 mT applied field as seen in Figure 6.71. The pre-laser showed a maximum MR effect of 5.3% at 270°. The rotation curve from the sample irradiated under an applied field of 30 mT showed a large plateau from 100° to 260° in the MR rotation curve and had a maximum MR effect of 1.9%. This indicated that the bias direction in the spin valve was not uniformly defined.

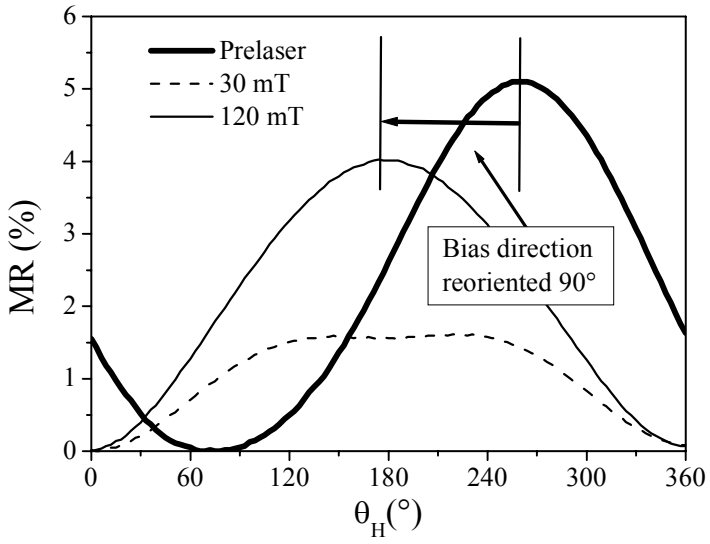

Figure 6.71: MR rotation curves from PtMn spin valve with SAF samples in pre-laser state and two samples irradiated at 12.5% laser energy under a 30 mT and 120 mT applied field respectively. MR rotation curves were measured at 10 mT.

After the laser irradiation under a 120 mT applied direction, the spin valve had a MR effect of 4.0% at 170°. This corresponded to a 100° shift of the bias direction from the pre-laser state. The pinned layer in the spin valve obviously has a more homogeneously defined bias direction at this point. The MR curve measured from samples irradiated at 12.5% laser energy showed no defined bias direction in the SAF of the spin valve (not shown). This explained the drop in MR effect and H_{ex} after the reorientation in the bias direction of the PtMn spin valve with SAF.

A comparison of the MR curves measured from a pre-laser sample and one irradiated under a field of 120 mT showed some differences in the magnitude of the MR effect and the curve form. The H_{saf} had however been reduced to 75 mT from 105 mT (pre-laser). The H_{c2} had drastically increased after the reorientation of the bias direction from 10 mT to almost 25 mT (see Figure 6.72a). There was also a hysteresis of 0.5% MR effect in the MR curve. Such an effect had only been previously observed when the SAF had been brought into a magnetic saturation ($\mu_0 H > 300$ mT) (see Figure 6.40). These characteristics were typical of MR curves measured from PtMn spin valve samples irradiated at a % laser energy above the reorientation threshold. The MR curve measured 90° to bias direction from the laser irradiated sample also showed a hysteresis in terms of the MR effect (see Figure 6.72b).

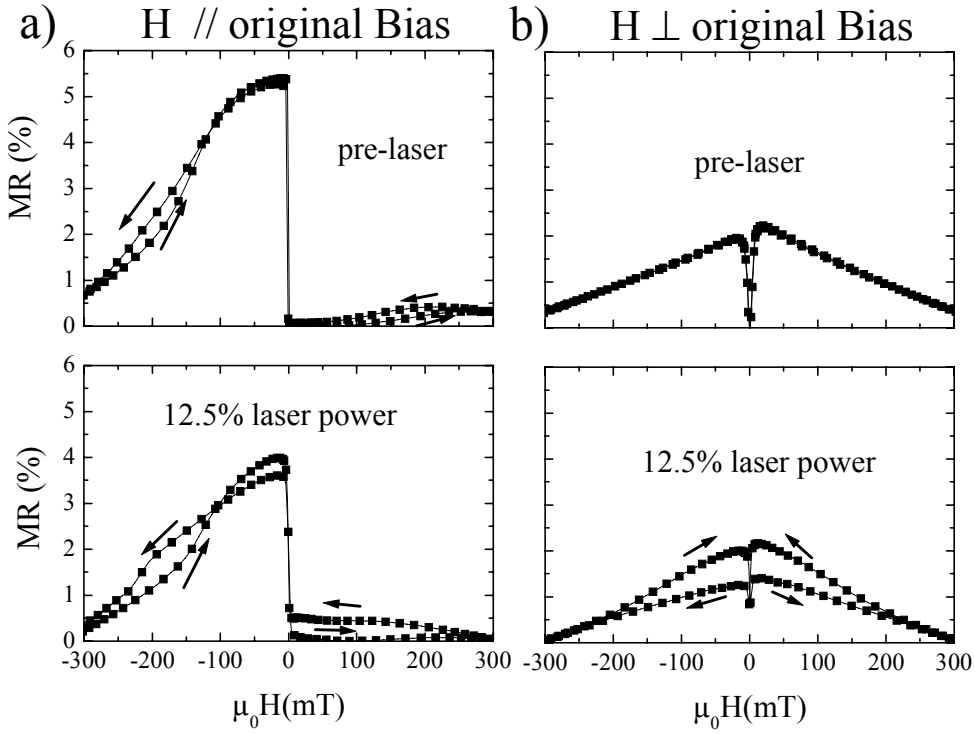

Figure 6.72: MR curve measured from a PtMn spin valve with SAF in the pre-laser state and from sample irradiated at 12.5% laser energy under 120 mT applied field a) parallel to the bias direction and b) perpendicular to bias direction

6.5.6.2 PtMn with SAF: Field Dependence of Laser-writing Process

The applied field dependence of the laser writing was explored by repeating the laser-writing process at a set laser energy of 12.5% under an applied field varying from 20-275 mT. The purpose of this experiment was to better align the bias direction by increasing strength of the magnetic applied field during the laser-writing. The applied field dependence of the laser writing process in PtMn with SAF became clear by plotting the MR in both the parallel and perpendicular orientations as a function of the applied field (Figure 6.73). The MR effect measured from samples irradiated under a 30 mT applied field was virtually identical in both orientations: 2.2 % parallel orientation and 2.08% in the perpendicular orientation. At 100 mT the MR effect in the parallel and perpendicular orientation is 1.86% and 3.81%, respectively. The MR in the parallel orientation increased to 2.4% and 4.31% in the perpendicular orientation after laser-writing under an applied field of 275 mT. The MR loss had been reduced by increasing the applied field strength to 275 mT, but the unusual hysteresis was still present in the MR curve.

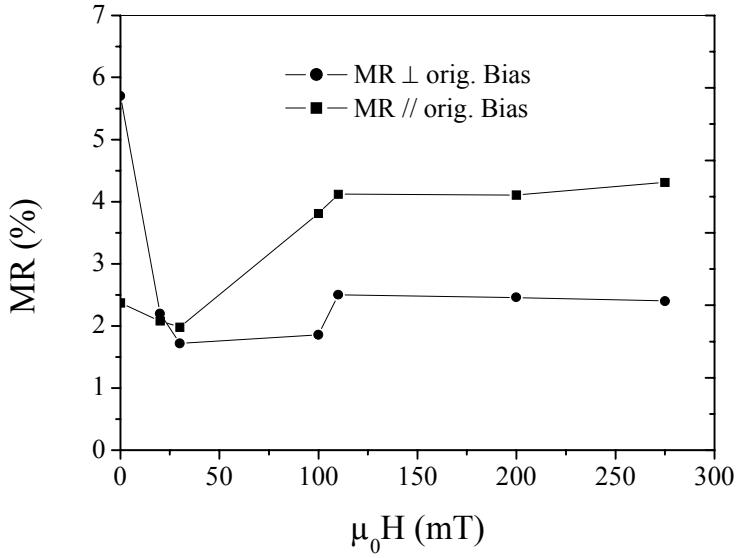

Figure 6.73: MR and H_{ex} from PtMn with SAF irradiated at 12.5% laser energy plotted as a function of the applied field during laser writing process.

The cause of the MR loss after the bias direction reorientation could stem from two different physical effects (induced uniaxial anisotropy and antiferromagnetic interlayer coupling) that are still present in the spin valve above the T_b of the PtMn antiferromagnet. These two physical effects are summarized below:

- **Induced uniaxial anisotropy in the pinned layer:** Antiferromagnets are known to induce a uniaxial anisotropy in the pinned layer of a spin valve. Pokhil, et al. [Pok99], showed that the induced uniaxial anisotropy in NiMn and IrMn spin valves were still present in the pinned layer of spin valve upon heating to temperature above the T_b of the antiferromagnet. PtMn is of the same class of antiferromagnets as NiMn.
- **Antiferromagnetic interlayer coupling in the SAF:** The antiferromagnetic interlayer coupling in the SAF is known to exist above the T_b of PtMn. SQUID magnetization measurements made on PtMn spin valves with an SAF at 380°C showed the existence of antiferromagnetic interlayer coupling at this temperature [Kel02b].

Either or both of these two physical effects could be pose a hindrance to the reorientation of the bias direction in the laser-writing process. The role of the antiferromagnetic interlayer coupling in the laser-writing process will be explored in Section 6.5.7 and that of the induced uniaxial anisotropy in Section 6.5.8.

6.5.7 Antiferromagnetic Interlayer Coupling and the Reorientation Process

Antiferromagnetic interlayer coupling in the SAF of the PtMn spin valve system could have hindered the reorientation of the bias direction during the laser-writing process. This hypothesis was tested by reorienting the bias direction with the laser writing process in a spin valve system with SAF that had an induced uniaxial anisotropy that was much lower in magnitude than that of PtMn: an IrMn spin valve system with SAF. It should be possible to reorient the bias direction of an IrMn spin valve with SAF since this had already been successfully done via the current setting method [Gie01].

A IrMn spin valve system with SAF used for this experiment was of the following structure: Si/SiO_2/Ta(5)/NiFe(7.2)/Co(1)/Cu(3)/CoFe(2)/Ru(0.8)/CoFe(2.5)/IrMn(10)/Ta(5).

The deposition conditions are the same as those described for the IrMn spin valve system in section 6.2.3 except for the addition of CoFe layer (reference layer) and a Ru layer (spacer layer in the SAF) in the spin valve stack. The IrMn spin valve with SAF had a MR effect of 5.5% H_{ex} of 138 mT, H_{eb} of 200 mT, and H_{saf} of 60 mT. The samples were irradiated at 12.5% laser energy under an applied magnetic field varied from 30-275 mT.

The experimental results mirrored those of the laser-writing experiments with PtMn up to the applied field of 200 mT. At an applied field of 30 mT, the MR effect in the expected bias direction had dropped from 5.5% MR effect in the pre-laser state to 3.5% MR effect. The sample did not appear to have a defined bias direction (see Figure 6.74 and Figure 6.75a). At 120 mT applied field the MR was still only 4.3% in comparison to 5.5% in the as-deposited state and a hysteresis was present in the MR curve (see Figure 6.75a & b). The MR curve at 200 mT applied field was similar in curve form to the MR curve measured from the as-deposited state except for small differences in the MR effect, H_{eb}, H_{ex} and H_{saf} (see Figure 6.75 a & d). The rise in the MR effect can be attributed to the AMR contribution caused by the change in the current-bias orientation. The H_{eb} had decreased to 150 mT, H_{ex} to 100 mT and H_{saf} to 40 mT. The reduction in H_{eb}, H_{ex} and H_{saf} can be traced to the time limitation problems with the bias direction reorientation (see Section 6.5.2.2).

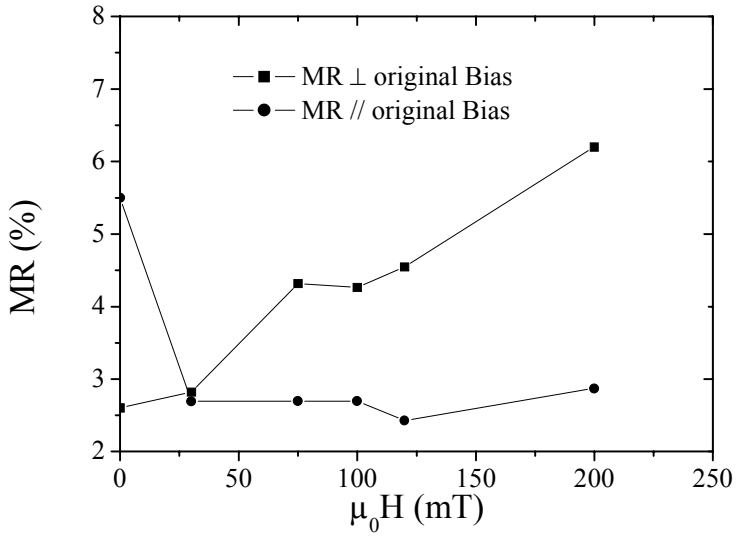

Figure 6.74: MR effect from IrMn spin valve with SAF as a function of the applied field during laser writing at 12.5% laser energy.

The reduction of the MR effect and H_{ex} in the PtMn spin valve with SAF after laser-writing at lower magnetic field values (30-120 mT) is due to antiferromagnetic coupling in the SAF. The SAF must be brought completely into saturation during laser-writing to overcome the antiferromagnetic coupling. This occurs at 200 mT in the case of the IrMn spin valve with SAF. Saito, et al. [Sai99], had shown that the magnetic saturation value for antiferromagnetic interlayer coupling of the Co/Ru/Co trilayer set at 1st antiferromagnetic maximum was still 220 mT at 300°C. If the magnetization of the pinned layer is only partially reoriented to the applied field, the unidirectional anisotropy will also not be uniformly oriented upon cooling down below T_b. These results did not explain the MR reduction and hysteresis behavior in MR curves measured from the PtMn spin valves with SAF irradiated under applied fields above 200 mT.

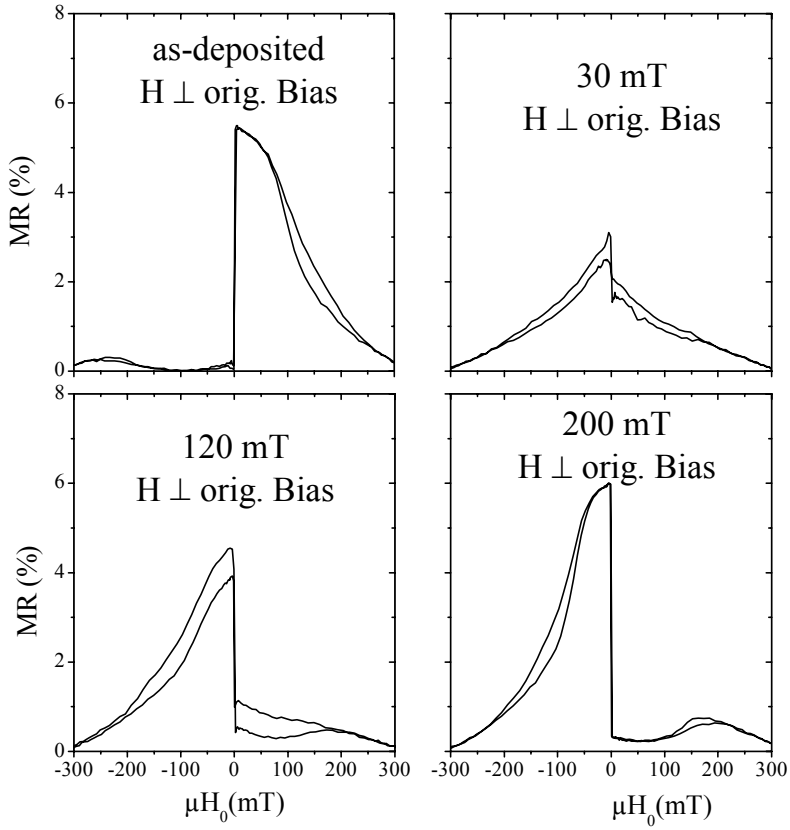

Figure 6.75: MR curves measured from IrMn spin valve with SAF in the as-deposited state and laser-written at 12.5% laser energy under 30 mT, 120 mT and 200 mT applied field after a 90° reorientation of the bias direction.

6.5.8 Induced Uniaxial Anisotropy of PtMn and the Reorientation Process

An induced uniaxial anisotropy in the pinned layer of the PtMn spin valve was seen as a possible cause for the MR reduction and the large increase in the hysteresis in the MR curves in the laser-writing of the PtMn spin valves with SAF under higher applied fields ($\mu_0 H$>200 mT). This MR loss and hysteresis increase came in the 90° reorientation case, but the bias direction was reoriented 180° with minimal loss in MR and no increase in the hysteresis (see Figure 6.76). The inability to reorient the bias 180° with no MR loss indicated that the reorientation of the bias direction was hindered by an effect that is uniaxial nature. These results are in direct contrast to those from laser-writing of FeMn and IrMn simple spin valves (see Sections 6.5.1.1 and 6.5.1.2) and the IrMn spin valve with SAF (see Figure 6.75) where no loss in the GMR effect was induced through the laser-writing process in the 90° reorientation case.

The exchange bias effect is always associated with an increase or inducement of a uniaxial anisotropy in the pinned layer of a spin valve (See Section 2.5.4). Pokhil, et al. [Pok99], had shown in the study of NiFe/NiMn and NiFe/IrMn bilayers that the induced uniaxial anisotropy remained above the Tb of both NiMn and IrMn AFMs. These published results can also be applied to PtMn antiferromagnets since NiMn is of the same class of antiferromagnets as PtMn (see Section 1.5.5). The unidirectional anisotropy may have been reoriented in the direction of the applied magnetic field by the laser-writing process, but the induced uniaxial anisotropy would retained in it's original orientation. This would have an adverse effect on the rotation of the magnetization in the pinned layer during the laser writing or the

magnetization reversal process during a MR measurement. The induced uniaxial anisotropy previously was thought to be coupled on the unidirectional anisotropy in all spin valve systems.

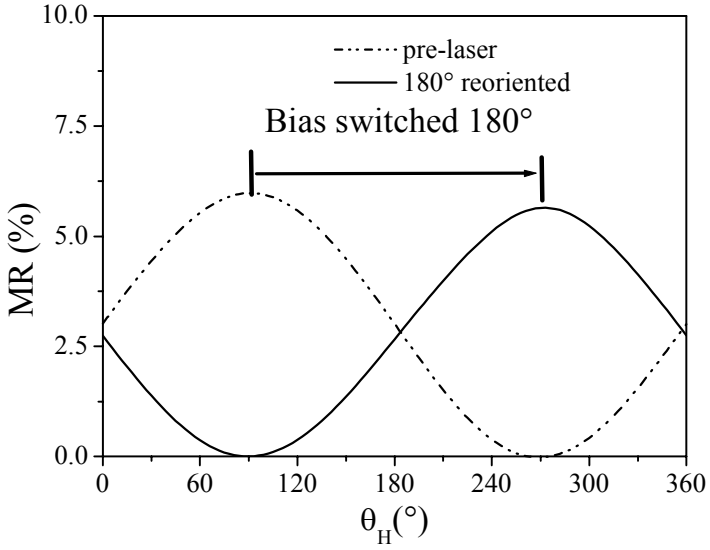

Figure 6.76: MR rotation curves measured from PtMn spin valve with SAF samples irradiated at 12.5% laser energy under 275 mT applied with the bias direction reoriented 90°and 180°. MR rotation curves were measured at 10 mT.

6.5.8.1 PtMn Simple Spin Valves: 90° Reorientation

PtMn spin valves, as described in Section 6.2.4, were irradiated at 12.5% laser energy under an applied field of 30-275 mT. The MR effect measured parallel and perpendicular to the original bias direction was plotted as a function of % laser energy in Figure 6.77. At 30 mT applied field, the MR effect dropped to 4.9% in the parallel measurement orientation and rose to 5.3% from 2.9% in the perpendicular measurement orientation. With increasing applied field the MR effect continued to drop to 4% at 75 mT when measured in the expected bias direction. The MR effect rose to almost 5% MR effect after increasing the applied field to 275 mT.

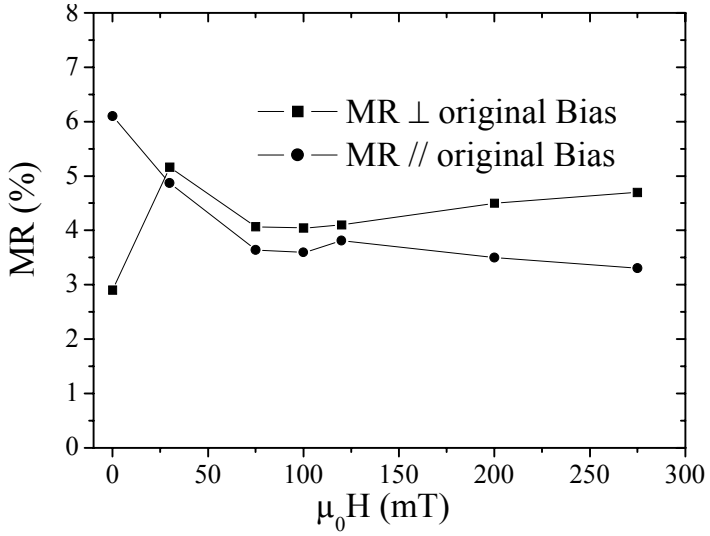

Figure 6.77: MR effect of a PtMn spin valve as a function of the applied field during laser writing from the parallel and perpendicular measurement orientations. Laser writing was done at 12.5% laser energy.

The MR effect in the parallel orientation was only 0.2-1.0% lower than in the perpendicular orientation at every applied field strength during the laser writing process. Examination of MR measurement from a PtMn sample irradiated under 275 mT applied field and post-anneal sample showed the drastic differences in the two MR curve forms (see Figure 6.78). First the maximum MR has dropped to 4 % after the reorientation of the bias direction. The MR curve also lost the plateau feature to the MR curve and assumed more of a saw-toothed form. The hysteresis in the MR curve measured from the PtMn spin valve was much higher than those measured from the IrMn and FeMn spin valves (see Figure 6.52 and Figure 6.55).

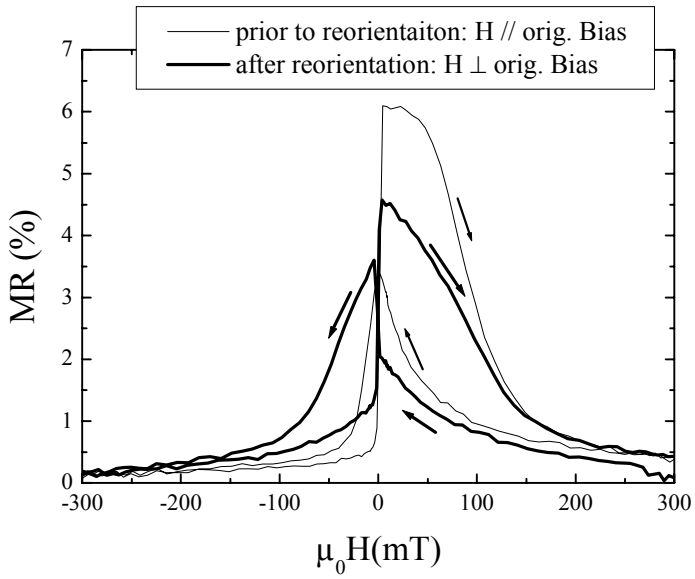

Figure 6.78: MR curve measured from a PtMn spin valve prior to laser-writing and a sample irradiated at 12.5% laser energy under 275 mT applied field.

The reorientation problems in this case cannot be attributed to temperature being below the T_b of the PtMn or applied field not being strong enough to reorient the magnetization in the pinned layer. At 15 % laser energy the temperature in the spin valve is well above 380°C (see Figure 6.57). The H_{c2} of 41 mT was much less than the applied field of 275 mT used during the laser-writing process. Based on these results the induced uniaxial anisotropy in the pinned layer was identified as the source of the MR reduction during the laser-writing of PtMn spin valves at higher applied fields ($\mu_0 H > 200$ mT).

6.5.9 Induced Uniaxial Anisotropy: FeMn and IrMn Antiferromagnets

The goal of this section was to explain the success in reorienting the bias direction in FeMn and IrMn simple spin valves compared to apparent inability to reorient bias direction in the PtMn simple spin valves without a significant loss in MR effect. There are obvious differences in the strength of the induced uniaxial anisotropy upon comparison between the FeMn and IrMn antiferromagnets and that of PtMn antiferromagnets. The H_{c2}, measure of the induced uniaxial anisotropy, of the FeMn spin valve (6 mT) and IrMn spin valves (6.5 mT) was seven times smaller than that of the PtMn spin valves (41 mT). It is a well-known fact that the fct class of antiferromagnets induce a uniaxial anisotropy is an order of magnitude larger that of the fcc class of antiferromagnets [Pok99].

A closer examination of the Hc_2 of the laser irradiated FeMn and IrMn spin valves as a function of laser energy was necessary to see if induced uniaxial anisotropy in this class of

antiferromagnets truly rotated with the unidirectional anisotropy upon the reorientation of the bias direction. The H_{c2} should remain the same after the reorientation of the bias direction if the induced uniaxial anisotropy is coupled on the exchange bias effect. H_{c2} is always determined from the MR curve measured parallel to the bias direction of the spin valve (see Figure 6.79). This was the same method used to determine the H_{eb} in all of the previous laser-writing experiments. The H_{eb} as function of % laser energy was included to allow direct correlation with the reorientation of the exchange bias direction.

In the case of FeMn, the H_{c2} started at 6 mT and dipped down to 3-3.5 mT in the 1.25-3% laser energy range (see Figure 6.79). H_{c2} is now determined from the MR measurement made in the new bias direction. The drop in the H_{c2} at this point is due to the mixed state of the bias direction near the reorientation point of the FeMn layer and coincides exactly with the change in H_{eb} (see Figure 6.79). The H_{c2} increased to 5-6 mT in the range from 3-12% laser energy. The H_{c2} of IrMn showed a similar behavior. The H_{c2} remained constant at 6.5 mT in the 0-1.25 % laser energy range and dipped down to 3 mT at 2.5% laser energy (Figure 6.79). This corresponded to the reorientation point of the IrMn spin valve as seen in the change in H_{eb}. The H_{c2} then rose steadily to 5 mT at laser energy of 5%. The H_{c2} remained in the 5-6.5 mT range from 5-15% laser energy.

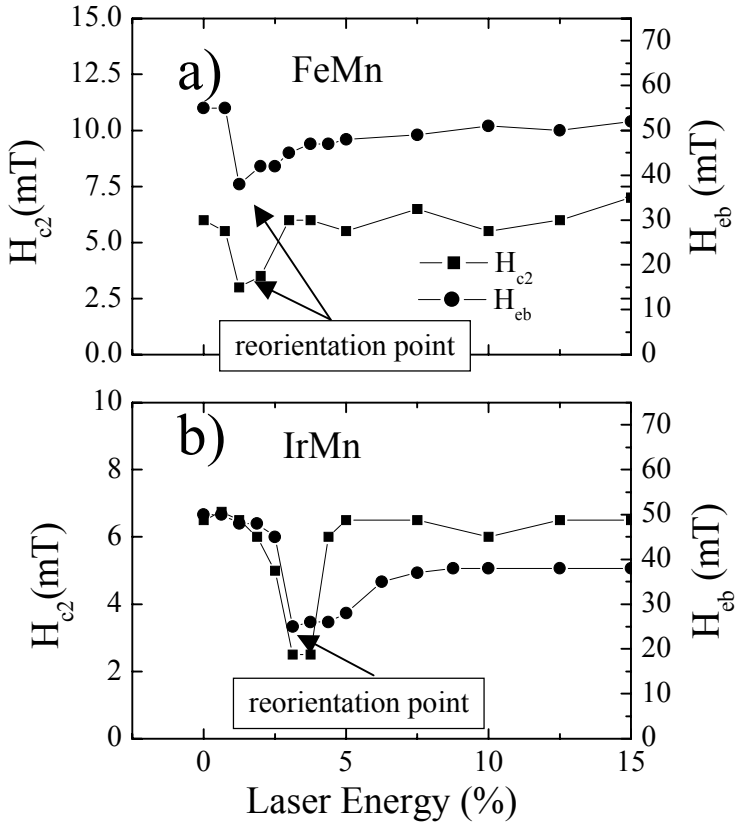

Figure 6.79: Plot of H_{c2} and H_{eb} as a function of % laser energy in laser irradiated FeMn and IrMn spin valves.

These results suggest that the induced uniaxial anisotropy present in FeMn and IrMn spin valves are coupled on the exchange bias effect. H_{c2} had the same value before and after the reorientation in the spin valve despite the change in the bias direction. The induced uniaxial anisotropy in the PtMn spin valve system is not coupled in the exchange bias effect otherwise the laser-writing experiments with PtMn simple spin valves (see Figure 6.77) would have mirrored the results from the laser writing of FeMn and IrMn spin valves (see Figure 6.52 and Figure 6.55).

The only large difference between the PtMn spin valve and the FeMn and IrMn spin valves is the crystal structure (PtMn: fct, FeMn & IrMn: fcc). If the uniaxial anisotropy stems the crystal structure of the PtMn antiferromagnet, the anisotropy axis could only be changed through a long term anneal (several hours; T>300°C) under a applied field. This would allow a reordering of the crystal lattice to take place. The uniaxial anisotropy induced by an disordered fcc AFMs and ordered fct AFMs can be placed in two different categories based on the results presented in Section 6.5.8 and this Section.

- Induced uniaxial anisotropy in the pinned layer of spin valves due fcc disordered AFMs (FeMn and IrMn). This uniaxial anisotropy is coupled on the exchange bias effect.
- Induced uniaxial anisotropy in the pinned layer of spin valves with fct ordered AFMs (PtMn). This uniaxial anisotropy is not coupled on the exchange bias effect.

6.5.10 Summary: Laser-Writing Method

The laser-writing method was proven to be the simplest and most reliable method, based on the presented experimental results, to imprint four different bias directions in a patterned spin valve sample. The successful development of this method was a critical step in the fabrication of a demonstrator GMR 360° angle sensor. The laser-writing method was tested on FeMn, IrMn and PtMn simple spin valves and on IrMn and PtMn spin valves with an SAF. The change in microstructure of the laser irradiated spin valves were studied in detail with AGM, XRD, XRR and AES. The results of these studies were used to explain the change in the MR effect and H_{eb} after the reorientation of the bias direction. The major highlights of this research are summarized below:

- The bias direction of FeMn and IrMn simple spin valves was reoriented through use of an excimer laser with minimal loss in GMR effect and exchange bias effect.
- Intermixing at the Co/Cu interface (FeMn spin valves) or CoFe interface (IrMn spin valves) was identified as source of the GMR reduction prior to complete intermixing of the entire spin valve stack at 20% laser energy. These experimental results supported the common notion that the majority of the spin-dependent scattering occurs at the NM/FM interface rather than in the bulk of the FM layer.
- The magnitude of the exchange bias effect was found to be independent of microstructural changes at the FM/AFM interface caused due to the laser irradiation in the 12.5%-20% laser energy range both the FeMn and IrMn spin valves. These results correlated well with the domain state model for exchange bias, which states that the defect density in the volume of the AFM determines the magnitude of the exchange bias.
- The loss of MR effect (1-2% MR loss) and H_{eb} in the laser irradiated PtMn spin valves with SAF was caused by the influence of antiferromagnetic interlayer coupling in the SAF and the induced uniaxial anisotropy of the PtMn during reorientation of the bias direction. Both of these effects remain present upon heating the spin valve above the T_b of PtMn. The influence of the antiferromagnetic interlayer coupling can be overcome by laser-writing under an applied field that is above the magnetic saturation of the SAF.
- The uniaxial anisotropy induced by fcc disordered antiferromagnets (FeMn, IrMn) was found to be coupled on the exchange bias effect.
- The uniaxial anisotropy induced by fct ordered antiferromagnets (PtMn) was not coupled on the exchange bias effect and did not change direction upon reorientation of the bias direction in the PtMn spin valve.

Demonstrator of a 360° GMR Angle Sensor

The creation of a demonstrator GMR 360° angle sensor, an important milestone in the BMBF Leitprojekt "Magneto-Elektronik", was made possible with the research presented in this dissertation. A GMR angle sensor can be applied in most cases where wear-affected potentiometric techniques, Hall and AMR sensors are used today. Examples are pedal position, engine control (e.g. throttle valve position, crankshaft or camshaft angle), transmission control, active suspension damper systems, head lamp levelling, seat position and other automotive applications. A GMR 360° angle sensor would allow for more design freedoms due to a larger possible airgap, higher signal-to-noise ratio and removing the need of a magnetic pole wheel in the design. A possible automotive application is shown in Figure 7.1. A GMR angle sensor in this application can be used for absolute determination of the angle of the steering wheel over a 360° range. This information is necessary for use in automotive safety systems such as ABS or Electronic Stability Program (ESP).

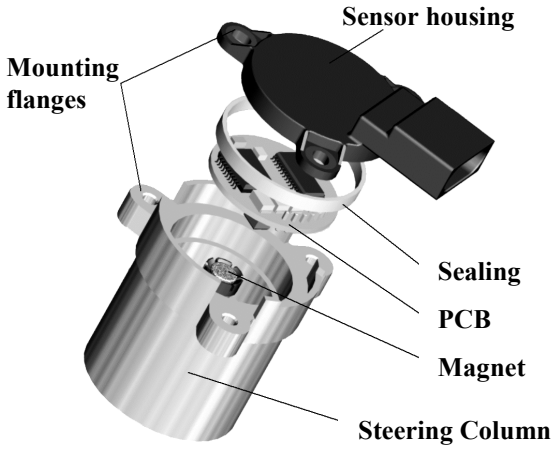

Figure 7.1: Example of a possible application for a GMR 360° angle sensor.

The information gleaned from the experimental results presented in the dissertation was directly applied to the development of a demonstrator GMR 360° angle sensor. The PtMn spin valve system with SAF was the spin valve system selected for use in this demonstrator. The sensor element was designed using rules learned from the study of the cosine deviation factors. The sensor was fabricated using standard semiconductor processes and the laser-writing method was used to imprint four different bias directions in the patterned spin valve structure. This demonstrator was subsequently tested to determine the accuracy at room temperature.

7.1 Design and Fabrication

A sensor layout design was based upon information learned from the study of the cosine deviation factors (see Section 6.1). The AMR effect was found to compensate the cosine deviation due to ferromagnetic coupling when the current direction was placed perpendicular to the bias direction (see Figure 7.2a) [Joh01]. A sensor element was designed that utilized the ⊥ current-bias orientation to minimize the cosine deviation. This involves a meander design where the length of meander is elongated in x-direction in preference to the y-direction, as seen in Figure 7.2b. If the bias direction is set ⊥ to the elongated meander direction, then the majority of the MR signal will originate from the ⊥ current-bias orientation, rather than the // current-bias orientation, in turn reducing the cosine deviation.

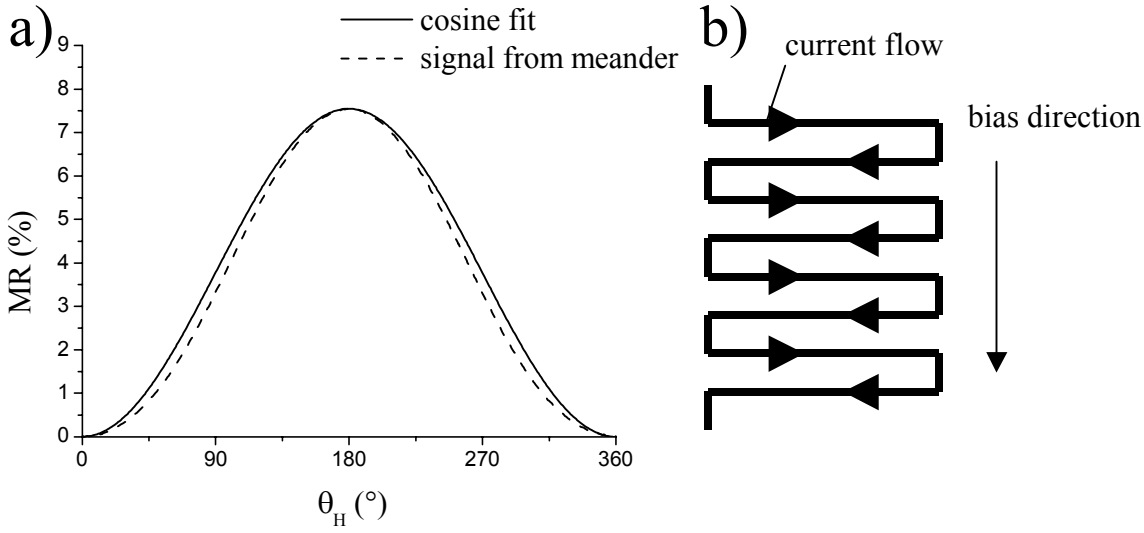

Figure 7.2: a) MR rotation curve measured from a spin valve in the ⊥ current-bias orientation and b) meander design with the bias direction set ⊥ to the long side of the meander.

The fabrication of the sensor element, with the exception of the spin valve deposition, was performed in the clean room facilities located at the Corporate R&D Center of Robert Bosch GmbH. Standard photolithography processes were used to structure the spin valve stack into the sensor element. The sensor element layout is presented in Figure 7.3a. The Wheatstone bridge circuit on the left delivers the cosine signal for the angle sensor, and the Wheatstone bridge on the right delivers the sine signal. The two individual meanders in a single Wheatstone bridge circuit were irradiated with a KrF excimer laser at the optimal laser power through a NiFeCr photomask under an applied magnetic field (see Figure 7.3b). This process was repeated another three times so that there was a total four different bias directions (0°, 90°, 180° and 270°) in two different Wheatstone bridge circuits. The use of a laser for the fabrication of a GMR angle sensor element is described in more detail in the following reference: [Joh02b].

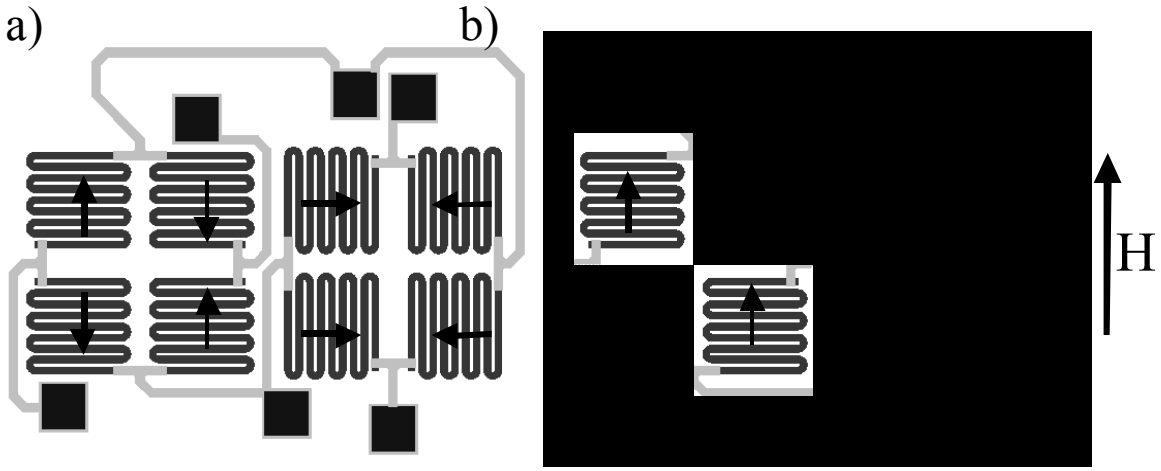

Figure 7.3: a) Layout design of a GMR 360° angle sensor element with the bias directions of the half-bridge elements indicated on the meanders and the b) laser writing of two meanders in the Wheatstone bridge circuit through a photomask to reorient the bias direction in the spin valve under an applied field.

7.2 Demonstrator in Operation

The output signal from the demonstrator GMR 360° angle sensor was at room temperature measured in the 0-100 mT field range to determine the sensor accuracy. The angular error was calculated by taking the arctan of the cosine and sine output signals from the sensor element as seen in Eq. (2.27), and by then taking the difference between the reference and measured angle. A MR rotation measurement made at 20 mT from the demonstrator is shown in Figure 7.4a with the angular error plotted over a 360° range. Amplitude and offset compensations are performed on both the cosine and sine output signals to achieve a low angular error of ±1°. A picture showing the display of the demonstrator is seen in Figure 7.4b. These initial results were very promising. A GMR angle suitable for the automotive applications will surely be developed with further optimization of the sensor design and fabrication process.

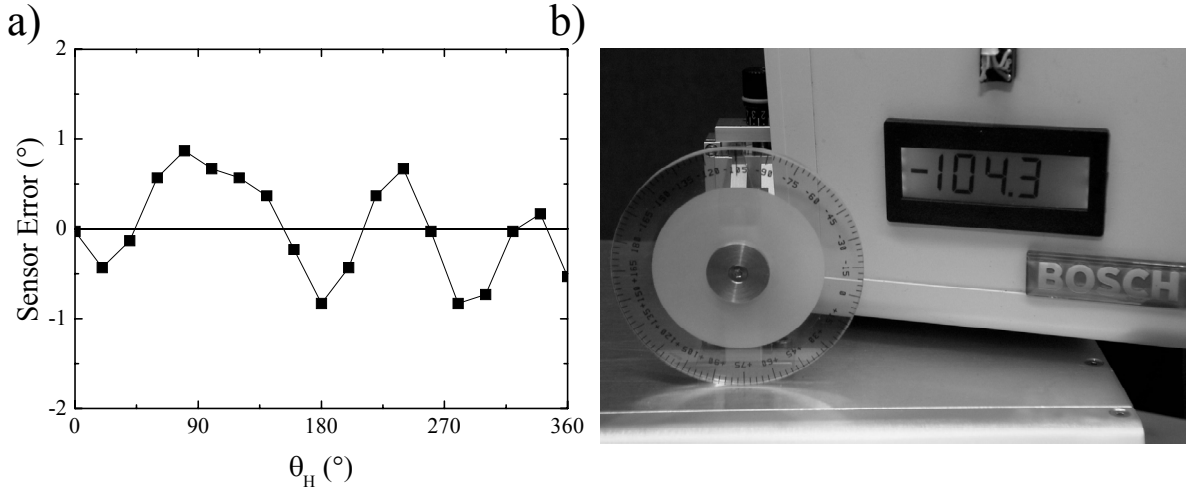

Figure 7.4: a) Angular error of the demonstrator GMR 360° angle sensor calculated from a MR rotation curve measured at 20 mT as a function of applied field direction and b) picture of the demonstrator display showing the measured angle.

Summary of Conclusions

8.1 Summary

The primary motivation for the dissertation "Spin Valve Systems for Angle Sensor Applications" was the development of the basic technology necessary for the creation of a demonstrator GMR 360° angle sensor. Two basic specifications for the sensor operation provided the starting point for the analysis of the different spin valve systems. The angle sensor must be able to operate in a (1) magnetic field range of 10-100 mT and (2) over the given temperature range [-40°C to 150°C]. An additional criteria was the goal to keep the angular error of the sensor to a minimum, e.g. ±1°. Three main goals for this dissertation were defined in order to develop a demonstrator GMR 360° angle sensor that fulfilled the previously described sensor specifications. These goals are summarized below:

Identification of the physical effects that cause a deviation from the cosine dependence of the GMR effect in a spin valve.

- Analysis of the thermal stability of five different spin valve systems (NiO, FeMn, IrMn, PtMn, PtMn with SAF).

Development of a method for local reorientation of the bias direction in a spin valve on a µm scale.

There are many scientific and technological highlights contained in this dissertation. The most important highlights are summarized below:

1. Identification of the physical effects that cause a deviation from the cosine dependence of the GMR effect as (1) Anisotropic Magneto-Resistance (AMR) effect (see Section 6.1.1), (2) interlayer coupling (see Section 6.1.2) and (3) rotation of the pinned layer magnetization in the direction of the applied field at field values below the exchange bias field value H_{eb} (see Section 6.1.3) through comparison between experiment and simulation [May02].

2. Classification of the studied spin valve systems (NiO, FeMn, IrMn, PtMn, PtMn with SAF) according to thermal stability (see Section 6.2.6). PtMn spin valve with SAF was shown to have the best thermal stability of the studied spin valves.

3. Successful application of the studied methods (lift-off, ion irradiation, laser-writing) in achieving different bias directions in a patterned spin valve samples. The use of the laser-writing method to change the bias direction of the spin valve is presented for the first time in this dissertation (see Section 6.5.5)

4. Determination of the source of the GMR reduction in the laser irradiated spin valves as intermixing at the Co/Cu interface (FeMn spin valves) and CoFe/Cu interface (IrMn spin valves), respectively (see Section 6.5.4).
5. Clarification of the stability of the exchange bias effect in the laser irradiated valves through use of the domain state model for exchange bias. (see Section 6.5.5)
6. Fabrication of a demonstrator GMR 360° angle sensor using the laser-writing method. (see Section 6.5.7)

It is important to note that the development of a demonstrator angle sensor was not possible without a deeper scientific understanding of the physical effects in a spin valve system (exchange bias, GMR effect, interlayer coupling). This is seen below in the detailed description of the aforementioned major highlights of this dissertation.

The deviation factors from the cosine dependence of the GMR effect were identified as AMR effect, ferromagnetic interlayer coupling at low fields ($\mu_0 H < 1/6\text{th } H_{eb}$) and rotation of the pinned layer magnetization in the applied field direction below the H_{eb} ($\mu_0 H > 1/6\text{th } H_{eb}$) of a spin valve. The AMR effect was found to add an additional cosine-squared resistance signal to the GMR effect, which was dependent on the angle between the current and the magnetization in each ferromagnetic layer in the spin valve. The interlayer coupling between the free and pinned layer influences the direction of the free layer magnetization. The magnitude of the deviation is dependent on the strength and sign of the interlayer coupling and the strength and direction of the applied field. The rotation of the pinned layer in the direction of the applied field below the H_{eb} of the spin valve was seen as the primary factor limiting the magnetic field operating window of the GMR 360° angle sensor. A simulation program developed by Dr. Ulrich May [May02] and based on a free energy model of a spin valve [Die00][Tie02] was used to verify the experimental results. A cosine deviation was observed in the simulated measurements when the direction of the current, strength of the interlayer coupling, or the strength of the applied field was varied. The good correlation between experiment and theory confirmed the accuracy of the free energy model used as the basis for the simulation.

The temperature dependence of the MR and H_{eb} of five different spin valve systems (NiO, FeMn, IrMn, PtMn, PtMn with SAF) was studied in great detail. The results were used to classify the spin valves according to thermal stability. The PtMn was identified as the only antiferromagnet with sufficient blocking temperature T_b to meet the temperature specifications. PtMn has a T_b of 380°C as cited in literature [Mao00], which allows for a stable bias direction at elevated temperatures (T>190 °C). The stability of the bias direction was further increased with the incorporation of a SAF in the spin valve stack. The PtMn spin valve with SAF showed the highest H_{eb} and MR over the given temperature range [-40°C to 150°C].

An important step in the fabrication of demonstrator GMR 360° angle sensor was development of a method for reorientation of the bias direction in a spin valve on a µm scale. Lift-off, ion irradiation and laser-writing methods were three methods that were analyzed in terms of their effectiveness in achieving opposite bias directions on a µm scale with minimal degradation in the spin valve properties. The bias direction was successfully achieved or reoriented on a µm scalar with all three methods. The results using a laser to locally reorient the bias direction in actual spin valves were presented for the first time in literature in this dissertation.

The reduction of the GMR effect in laser irradiated spin valve samples, prior to complete intermixing of the layers, was explained through analysis of the spin valve microstructure. No microstructural changes such as interdiffusion between the different layers or phase transformation were detected up to the complete intermixing of the spin valves. This was confirmed by Auger Electron Spectroscopy (AES) depth profiling or X-Ray Diffraction

increase in the interface roughness of the spin valve stack (0.36 nm to 0.72 nm) as shown by reflectometry measurements. The increase in interface roughness coincided with an increase in the sheet resistance and interlayer coupling of the spin valve. These results were indicative of intermixing of Co and Cu at the Co/Cu interface (FeMn spin valves) and CoFe and Cu at CoFe/Cu interface (IrMn spin valves). This interface intermixing was seen as the source of the GMR reduction. Spin-dependent scattering was shown to mainly occur at the interface between the FerroMagnetic (FM) layers and NonMagnetic (NM) spacer layer and not in the bulk of the FM layer based on these experimental results.

The domain state model for exchange bias explained the stability of the exchange bias effect in the laser irradiated FeMn and IrMn spin valves. This was despite the intermixing occurring at every interface in the spin valve stack. According to the domain state model, the number of defects in the volume of the AntiFerroMagnetic (AFM) layer mainly determines the magnitude of the exchange bias effect rather than defects at the AFM/FM interface. The irradiation of an FeMn spin valve with He^+ ions increased the defect density in the volume of the AFM and correspondingly increased the H_{eb} of the spin valve. The laser irradiation induced intermixing only at the interfaces in the spin valve stack, which caused no change in the H_{eb} of the spin valve. These experimental results provided additional support for the validity of the domain state model for exchange bias.

The wealth of information obtained through the detailed analysis of the experimental results was directly applied to the development of a demonstrator GMR 360° angle sensor. A sensor layout was designed to reduce the amount of cosine deviation from AMR effect and interlayer coupling. The PtMn spin valve with SAF was the spin valve system used in the demonstrator. The laser-writing method was used to imprint the bias directions in the different spin valve meanders of the Wheatstone bridge circuit. An important milestone of the BMBF "Leitprojekt Magneto-Elektronik" was reached with the development of a demonstrator GMR 360° angle sensor.

8.2 Future Work

Applied Research

A certain amount of applied research and development is necessary before the possible use this sensor in an automotive environment. The rotation measurements as a function of temperature must be performed to determine the temperature dependence of the angular error. Accelerated lifetime studies must be conducted on the packaged angle sensors in order to confirm the stability of the bias direction after processing of the spin valve stack deposited on a wafer. Studies of the sensor in actual operation are final step before possible application of this sensor in automotive systems.

Basic Research

The further study of ion and laser irradiated spin valves with spectroscopy methods such as X-ray Magnetic Circular Dichroism Spectro-Microscopy (XMCD) or neutron diffraction will certainly provide more insight into the physical origin of the exchange bias effect. XMCD even allows the measurement of element-specific magnetization curves. Such research studies could answer questions regarding the actual importance of the interfacial spin structures on the exchange bias effect by varying the defect density in the volume of the AFM (ion irradiation) or modifying the AFM/FM interface structure (laser-writing). High Resolution Transmission Electron Microscopy (HR-TEM) could be used to relate the exact microstructural changes to the change in the spin structure within the volume of the AFM and at the AFM/FM interface.

The same set of experiments could also shed light on the origin of the induced uniaxial anisotropy in ordered face-centered-tetragonal (fct) antiferromagnets. A better understanding of the induced uniaxial anisotropy in the PtMn antiferromagnet is of technological importance to the GMR 360° angle sensor application. There may be visible differences in the spin structure in the volume or interfacial spin structures of disordered face-centered-cubic (fcc) antiferromagnets and ordered fct antiferromagnets after the bias direction is reoriented by either ion irradiation or laser-writing. Models of the exchange bias effect in ordered fct antiferromagnets cannot be developed without knowledge of the physical origin of this induced uniaxial anisotropy. These experiments may finally lead to the creation of an exchange bias model that fully explains the existing experimental data on the exchange bias effect.

Zusammenfassung und Ausblick

9.1 Zusammenfassung

Die Hauptmotivation für die Doktorarbeit "Spin Valve Systems for Angle Sensor Applications" war die Entwicklung der Basistechnologie für die Herstellung eines 360° Winkelsensors-Demonstrators basierend auf dem "Giant Magneto-Resistance" (GMR) Effekt. Für die Auswahl eines geeigneten Spinvalve-Systems bezüglich der Anwendung als Winkelsensor sind zwei Kriterien von besonderer Bedeutung: Anwendung in 1.) einen Magnetfeldbereich von 10-100 mT und 2.) in Temperaturbereich von [-40°C bis 150°C]. Ein zusätzliches Kriterium war das Ziel, den Winkelfehler des Demonstrators so klein wie möglich, z.B. unter ±1°, zu halten. Um einen GMR Winkelsensor Demonstrator entwickeln zu können, der die vorgegebenen Spezifikationen erfüllt, werden die folgenden Hauptziele definiert:

- Identifikation der physikalischen Effekte, die eine Abweichung von der Kosinus-Abhängigkeit des GMR Effektes in einem Spinvalve-System verursachen.
- Auswahl eines thermisch stabilen Spinvalve-Systems von fünf unterschiedlichen Spinvalve-Systemen (NiO, FeMn, IrMn, PtMn, PtMn with SAF).
- Entwicklung einer Methode zur lokalen Umorientierung der Biasrichtung eines Spinvalve (µm-Skalar).

Die wichtigsten wissenschaftlichen und technologischen Erkenntnisse des Kapitels "Results and Discussion" dieser Dissertation sind hier kurz zusammengefasst:

1. Als Ursache für die Abweichung vom Kosinusverhalten konnten, durch Vergleich von Experiment und Simulation [May02], die folgende Effekte identifiziert werden: (1) Der "Anisotropic Magneto-Resistance" (AMR) Effekt (s. Abschnitt 6.1.1), (2) die Zwischenschichtkopplung (s. Abschnitt 6.1.2) und (3) die Rotation der Magnetisierung der gepinnten Schicht in Richtung des angelegten Feldes unterhalb der Exchange Bias Wertes H_{eb} (s. Abschnitt 6.1.3)

2. Unterschiedliche Materialsysteme (auf Basis von NiO, FeMn, IrMn, PtMn) wurden bezüglich Temperaturstabilität untersucht und bewertet. Die höchste Temperaturstabilität wurde mit einem PtMn Spinvalve mit "Synthetic Anti-Ferromagnet" (SAF) erreicht (s. Abschnitt 6.2.6).

3. Unterschiedliche Methoden (Lift-off, Ionenbeschuss und Lasereinschreiben) um die Biasrichtung eines Spinvalve im µm-Skalar einzustellen, wurden untersucht. Einschreiben mit der Lasermethoden wurde in dieser Arbeit zum ersten mal erfolgreich durchgeführt (s. Abschnitt 6.3, 6.4 und 6.5).

4. Als Ursache für die Reduktion des GMR-Effekts bei den laserbestrahlten Spinvalves wurde eine Vermischung der Co/Cu (FeMn Spinvalve) beziehungsweise CoFe/Cu Grenzfläche (IrMn Spinvalve) nachgewiesen (s. Abschnitt 6.5.4).

5. Unter Verwendung des „Domain-State" Modells konnte die Stabilität des Exchange Bias Effektes in laserbestrahlten Spinvalves für Exchange Bias beschrieben werden (s. Abschnitt 6.5.5).

6. Es wurde ein Demonstrator eines GMR 360° Winkelsensors entwickelt. (s. Abschnitt 7.1 & 7.2).

Es ist wichtig zu unterstreichen, dass die Entwicklung dieses Sensor-Demonstrators ohne ein tieferes wissenschaftliches Verständnis der physikalischen Effekte in einem Spinvalve-System (Exchange Bias, GMR Effekt, Zwischenschichtkopplung) nicht möglich gewesen wäre.

Als wesentliche Gründe dafür, dass der Verlauf des GMR Effektes als Funktion der äußeren Feldrichtung von einem kosinusförmigen Verlauf abweicht, wurden der AMR Effekt, die ferromagnetische Zwischenschichtkopplung im Falle niedriger Felder ($\mu_0 H < 1/6^{th}\ H_{eb}$), beziehungsweise die Rotation der gepinnten Schichtmagnetisierung in Richtung des angelegten Feldes im Falle höherer Felder ($\mu_0 H > 1/6^{th}\ H_{eb}$) identifiziert. Der AMR-Beitrag ist in jeder ferromagnetischen Schicht abhängig vom Winkel zwischen Strom und Magnetisierung und addiert sich zu dem GMR Effekt als ein zusätzliches, kosinusquadratförmiges Signal hinzu. Die durch diese Zwischenschichtkopplung verursachte Kosinusabweichung ist von der Stärke und dem Vorzeichen der Kopplung sowie der Stärke des angelegten Feldes abhängig. Der magnetische Arbeitsbereich des GMR 360° Winkelsensors wird bei großen äußeren Feldern durch die Stabilität der Magnetisierungsrichtung der gepinnten Schicht oder H_{eb} begrenzt. Ein auf dem Freie-Energie-Modell [Die00][Tie02] basierendes Simulations-Programm entwicklet bei Dr. Ulrich May [May02] bildete die experimentell gefundene Kosinusabweichung nach, die im Experiment durch Variation der Stromrichtung, der Stärke der Zwischenschichtkopplung oder des Betrages des angelegten Feldes verursacht wird. Die Übereinstimmung zwischen Experiment und Theorie bestätigte, dass sich das Freie-Energie-Modell als analytisches Werkzeug in diesem Bereich einsetzen lässt.

Um das geeignete Spinvalve-System für die Winkelsensoranwendung zu finden, wurde die Temperaturabhängigkeit des MR Effektes und des H_{eb} für fünf verschiedene Materialsysteme (NiO, FeMn, IrMn, PtMn, PtMn mit SAF) detailliert untersucht. PtMn war hierbei der einzige „Anti-Ferro-Magnet" (AFM), der die Temperaturanforderungen erfüllen konnte. Die „Blocking"-Temperatur T_b von PtMn ist deutlich größer als 190° C. In der Literatur finden sich Werte für T_b von 380°C [Mao00]. Allerdings wurde hier nur durch Integration eines SAF in den Schichtstapel ein ausreichendes H_{eb} bei erhöhten Temperaturen erreicht. Das PtMn Spinvalve-System mit SAF hat die höchsten H_{eb} und MR über die spezifizierten Temperaturbereich [-40°C bis 150°C] gezeigt.

Ein notwendiger Schritt bei der Herstellung eines 360° GMR Winkelsensors Demonstrator ist die Umorientierung der Biasrichtung. Dazu wurden die Methoden Lift-off, Ionenbeschuss und Lasereinschreiben getestet. Das Ziel von unterschiedlichen Biasrichtungen in einen Spinvalve-System mittels aller drei studierten Methoden wurde erfolgreich erreicht. Ergebnisse zur Umorientierung des Biasrichtung eines Spinvalves mittels Laserbestrahlung wurden erstmalig im Rahmen dieser Dissertation veröffentlicht.

Die Reduzierung des GMR Effekts nach der Laserbehandlung konnte durch eine detaillierte Analyse der mikrostrukturellen Änderungen erklärt werden. Analysen durch Auger Elektronen Spektroskopie (AES) zeigten keine signifikante Änderung der Schichtdicken. Die Röntgenbeugungs-Messungen ergaben keine Hinweise auf eine Phasenänderung des Spinvalve Stapels durch die Bestrahlung. Allerdings wurde durch

Röntgen-Reflektometrie-Messungen eine geringe Zunahme der Grenzflächenrauhigkeit (von 0.36 nm auf 0.72 nm) an der FerroMagnetischen/NichtMagnetischen (FM/NM) Grenzfläche beobachtet. Die Zunahme der Grenzflächenrauhigkeit durch Vermischung an den Grenzflächen, geht einher mit einer Zunahme des Widerstands dem Auftreten der Zwischenschichtkopplung, sowie der Reduktion des MR. Die Grenzflächendurchmischung von Co und Cu in dem FeMn Spinvalve und CoFe und Cu in dem IrMn Spinvalve führt zu einem beträchtlichen Abfall der spinabhängigen Streuung. Durch diese Ergebnisse wurde gezeigt, dass die spinabhängige Streuung hauptsächlich an der FM/NM Grenzfläche der Spinvalve Struktur und nicht im Inneren der FM Schicht auftritt.

Die Stabilität der Exchange Bias trotz Vermischung an der AFM/FM Grenzfläche kann mit dem „Domain-State“ Modell erklärt werden. Entsprechend dem „Domain-State“ Modell, wird die Größe des Exchange Bias von der Anzahl der Defekte im Volumen der AFM Schicht und nicht von der Anzahl der Defekte an der AFM/FM Grenzfläche bestimmt. Ionenbeschuss von FeMn Spinvalves mit He^+ Ionen erzeugt zusätzliche Defekte im Volumen des AFM. H_{eb} erhöht sich aufgrund des Zunahme der Defektdichte. Die Laserbestrahlung hingegen führt zu einer Durchmischung an der AFM/FM Grenzfläche. Diese experimentellen Ergebnisse bestätigen somit die Gültigkeit des Domain State Modells für Exchange Bias.

Die durch die detaillierte Analyse des Spinvalve-Systems gewonnenen Informationen wurden direkt auf die Herstellung des GMR 360° Winkelsensor Demonstrator angewandt. Ein Sensorlayout wurde so entworfen, dass die Kosinusabweichung aufgrund von AMR und Zwischenschichtkopplung reduziert wird. Die Methode des Lasereinschreibens wurde verwendet, um die Biasrichtung der Mäander von den zwei Wheatstoneschen Brücken-Schaltungen auf einem Spin Valve Sensorchip aus PtMn mit SAF einzuschreiben. Mit der Entwicklung dieses GMR 360° Winkelsensor Demonstrators wurde dennoch ein wichtiger Meilenstein des BMBF Leitprojekts "Magneto-Elektronik" erreicht.

9.2 Zukünftige Fragestellungen und Ausblick

Angewandte Forschung

Ein gewisses Maß an angewandten Forschung und Entwicklung an der GMR Winkelsensor ist vor möglicher Verwendung in einer Automobilumgebung notwendig. Um die Temperaturabhängigkeit des Sensorfehlers zu bestimmen, müssen Rotationsmessungen als Funktion der Temperatur durchgeführt werden. Beschleunigte Lebensdauerstudien an verpackten Winkelsensoren sollten die Stabilität der Biasrichtung in einen Spin Valve bestätigen. Studien über den Sensor in tatsächlichem Betrieb sind letzter Schritt vor möglicher Bewerbung dieses Sensorenelements in Automobilsensorensystemen.

Grundlagenforschung

Weitere Untersuchungen an Ionen-bestrahlten und Laser-bestrahlten Spinvalves mit Methoden wie der magnetischen zirkularen Dichroismus-Spectro-Mikroskopie (XMCD) oder der Neutronenbeugung, würden sicher weitere Einblicke in den physikalischen Ursprung des Exchange Bias liefern. XMCD erlaubt sogar die Messung der Element-aufgelösten Magnetisierung. Solch eine Untersuchung könnte, z.B. durch Variation der Defektdichte des Volumens des AFM (durch Ionenbeschuss) oder Modifizieren der AFM/FM Grenzflächen Rauhigkeit (durch Lasereinschreiben) zeigen, inwieweit die Grenzflächen- Spinstrukturen einen Einfluss auf dem Exchange Bias haben. Hochauflösende Transmission Elektronen Mikroskopie (HR-TEM) könnte die genauen mikrostrukturellen Änderungen im Volumen des AFM und an der AFM/FM Grenzfläche aufklären.

Dieselben Versuche könnten auch zur Klärung des Ursprungs der induzierten uniaxialen Anisotropie in geordneten "face-centered-tetragonal“ (fct) Antiferromagneten beitragen. Ein

besseres Verständnis der induzierten uniaxialen Anisotropie im PtMn Antiferromagnet ist von technologischer Bedeutung für die GMR 360° Winkelsensoranwendung. Mit den diskutierten Methoden sollte es möglich sein, sichtbare Unterschiede in der Spinstruktur im Volumen oder an den Grenzflächen von ungeordneten "face-centered-cubic" (fcc) Antiferromagneten und geordneten fct Antiferromagneten, aufzulösen, nachdem die Biasrichtung entweder durch Ionenbeschuss oder Laser-Schreiben verändert worden ist. Modelle, die das Exchange Bias in geordneten fct-Antiferromagneten beschreiben, können nicht ohne Kenntnis des physikalischen Ursprungs der induzierten uniaxialen Anisotropie entwickelt werden. Diese Untersuchungen könnten schließlich zu einem Exchange Bias Modell führen, das die vorhandenen experimentellen Daten geschlossen erklären kann.

Appendices

Table 10.1: Overview of the different spin valve systems studied in this dissertation

Type of Spin Valve	Spin Valve Stack
FeMn (FeMn1) (Section 6.1.1)	Si/SiO_2/Ta/NiFe/CoFe/Cu/CoFe/NiFe/FeMn/Ta
FeMn (FeMn2) (Section 6.1.2)	Si/SiO_2/Ta/NiFe/CoFe/Cu/CoFe/NiFe/FeMn/Ta
FeMn (FeMn3) (Section 6.1.2)	Si/SiO_2/Ta/NiFe/CoFe/Cu/CoFe/NiFe/FeMn/Ta
FeMn (FeMn4) (Section 6.1.2)	Si/SiO_2/Ta/NiFe/CoFe/Cu/CoFe/NiFe/FeMn/Ta
NiO (Section 6.2.1)	Si/SiO_2/NiO/NiFe/Cu/NiFe
FeMn (Section 6.2.2)	Si/SiO_2/Ta/NiFe/Co/Cu/Co/FeMn/Ta/Cu
IrMn (Section 6.2.3)	Si/SiO_2/Ta/NiFe/CoFe/Cu/CoFe/IrMn/Ta
PtMn (Section 6.2.4)	Si/SiO_2/Ta/NiFe/PtMn/CoFe/Cu/CoFe/NiFe/Ta
PtMn with SAF (Section 6.2.5)	Si/SiO_2/Ta/NiFe/PtMn/CoFe/Ru/ CoFe/Cu/CoFe/NiFe/Ta
IrMn with SAF (Section 6.5.7)	Si/SiO_2/Ta/NiFe/CoFe/Cu/CoFe/Ru/CoFe/IrMn/Ta

Table 10.2: Free energy coefficients for each spin valve system analyzed in Section 6.2

Spin Valve	K_{eb}	J_{int}	$K_f^{uniaxial}$	$K_p^{uniaxial}$	$K_r^{uniaxial}$
	J/m^2	J/m^2	J/m^2	J/m^2	J/m^2
NiO	4.86×10^{-5}	4.32×10^{-6}	1.62×10^{-6}	4.05×10^{-6}	N/A[a]
FeMn	1.38×10^{-4}	6.73×10^{-6}	1.53×10^{-7}	7.539×10^{-6}	N/A[a]
IrMn	1.72×10^{-4}	7.75×10^{-6}	3.63×10^{-7}	1.24×10^{-5}	N/A[a]
PtMn	2.01×10^{-4}	4.67×10^{-6}	2.80×10^{-6}	9.77×10^{-5}	N/A[a]
PtMn with SAF (as-deposited)	N/A[b]	4.30×10^{-6}	3.89×10^{-7}	[c]8.500×10^{-6}	1.91×10^{-6}
PtMn with SAF (post-anneal)	[d]2.01×10^{-4}	4.67×10^{-6}	1.25×10^{-6}	[d]9.77×10^{-5}	7.50×10^{-6}

[a]Only spin valves with a SAF have a reference layer.
[b]PtMn with SAF in the as-deposited state has no unidirectional anisotropy.
[c]Determined by simulation.
[d]Assumed to be the same as the pinned layer in the PtMn simple spin valve.

Table 10.3: Magnetic properties of each spin valve system studied in Section 6.2.

Spin Valve	MR	H_{eb}	H_{ex}	H_{saf}	T_b	H_e	H_{c1}	H_{c2}	H_{c3}
	%	mT	mT	mT	°C	mT	mT	mT	mT
NiO	4.1	9	N/A[a]	N/A[a]	145	0.8	0.1	1.5	N/A[a]
FeMn	7.9	55	N/A[a]	N/A[a]	140	1.1	0.1	6	N/A[a]
IrMn	7.5	45	N/A[a]	N/A[a]	190	0.8	0.1	6.5	N/A[a]
PtMn	6.1	42	N/A[a]	N/A[a]	380[b]	0.75	0.9	41	N/A[a]
PtMn SAF (as-deposited)	6.0	N/A[c]	140	60	N/A	0.69	0.25	4[d]	1
PtMn SAF (post-anneal)	6.4	180	190	105	380[b]	0.75	0.4	41[e]	5

[a] This magnetic parameter exists only for spin valves with SAF.
[b] Taken from literature.
[c] No exchange bias present since PtMn is not in the antiferromagnetic fct phase.
[d] Determined by simulation.
[e] Assumed to be the same as the simple PtMn spin valve.

Table 10.4: List of abbreviations used in this disseration

Abbreviation	Explanation
AAF	Artificial AntiFerromagnet
ABS	Anti-Blocking System
AES	Auger Electron Spectroscopy
AFM	Antiferromagnetic or Antiferromagnet
AGM	Alternating Gradient Magnetometer
AMR	Anisotropic Magneto-Resistance
ASIC	Application Specific Integrated Circuit
BSV	Bottom Spin Valve
CCD	Charge Coupled Device
CIP	Current in Plane
CMR	Colossal Magnetoresistance
CPP	Current Perpendicular to Plane
CVD	Chemical Vapor Deposition
ESP	Electronic Stability Program
FL	Free Layer
FM	Ferromagnetic
GMR	Giant Magneto-Resistance
HDD	Hard Disk Drive
HR-TEM	High Resolution Transmission Electron Microscopy
IBD	Ion Beam Deposition
MBE	Molecular Beam Epitaxy
MOKE	Magnetic Optical Kerr Effect
MR	Magnetoresistance
MRAM	Magnetic Random Access Memory
NM	NonMagnetic
PCB	Printed Circuit Board
PL	Pinned Layer
PVD	Physical Vapor Deposition

RKKY	Ruderman-Kittel-Kasuya-Yosida
RL	Reference Layer
SAF	Synthetic Antiferromagnet
SQUID	Super Conducting Quantum Interference Device
TMR	Tunnel Magnetoresistance
TSV	Top Spin Valve
UHV	Ultra High Vacuum
UV	Ultra Violet
VDC	Vehicle Dynamics Controls
VSM	Vibrating Sample Magnetometer
XMCD	X-ray Magnetic Circular Dichroism
XRD	X-Ray Diffraction
XRR	X-Ray Reflectometry

Table 10.5: List of commonly used variables and symbols in this dissertation

Symbol/Variable	Explanation (page number reference)	Units
Bias	bias direction of the spin valve	-
CD	amount of Cosine Deviation of a MR rotation curve from a optimal cosine curve (p. 46)	deg.
ΔR_{AMR}	resistance change due to the AMR effect (p. 6)	ohm
ΔR_{GMR}	resistance change due to the GMR effect (p. 56)	ohm
ΔR^{i}_{GMR}	fit parameters for the resistance change due to the GMR effect between the i-th and the i+1-th layer (p. 56)	ohm
ΔR^{p}_{GMR}	resistance change due spin-dependent scattering between the pinned and free layer (p. 57)	ohm
E_{eb}	free energy term for the unidirectional anisotropy (p. 20)	Jm^{-2}
E_H	free energy term for the applied field (p. 55)	Jm^{-2}
E_{int}	free energy term for the interlayer coupling between the free layer and pinned layer (p. 19)	Jm^{-2}
E_{SAF}	free energy term for the antiferromagnetic coupling between the pinned and reference layer	Jm^{-2}
$E_f^{uniaxial}$	free energy term for the uniaxial anisotropy in the free layer (p. 17)	Jm^{-2}
$E_p^{uniaxial}$	free energy term for the uniaxial anisotropy in the pinned layer (p. 17)	Jm^{-2}
$E_r^{uniaxial}$	free energy term for the uniaxial anisotropy in the reference layer (p. 57)	Jm^{-2}
H_{c1}	coercivity field value of the free layer (p. 15)	mT
H_{c2}	coercivity field value of the pinned layer (p. 15)	mT
H_{c3}	coercivity field value of the reference layer (p. 29)	mT
H_e	interlayer coupling field value between free and pinned layer (p. 15)	mT
H_{eb}	exchange bias field value (p. 15)	mT
H_{ex}	measure of the asymmetry of an MR curve measured from a spin valve with SAF (p. 29)	mT
H_{saf}	antiferromagnetic interlayer coupling field value (p. 29)	mT
J_{int}	coefficient for interlayer coupling between the free layer and	Jm^{-2}

	pinned layer (p. 18)	
J_{SAF}	coefficient for interlayer coupling in the SAF (p. 29)	Jm^{-2}
K_{eb}	exchange bias or unidirectional anisotropy coefficient (p. 20)	Jm^{-2}
$K_f^{uniaxial}$	uniaxial anisotropy coefficient of the free layer (p. 16)	Jm^{-2}
$K_p^{uniaxial}$	uniaxial anisotropy coefficient of the pinned layer (p. 17)	Jm^{-2}
$K_r^{uniaxial}$	uniaxial anisotropy coefficient of the reference layer (p. 57)	Jm^{-2}
M_f	saturation magnetization for the free layer (p. 17)	T
M_{FM}	magnetization of ferromagnetic thin film	T
M_p	saturation magnetization for the pinned layer (p. 17)	T
MR	resistance change due to applied magnetic field (p. 5)	in %
μ_0	induction constant (p. 9)	H/m
M_r	saturation magnetization for the reference layer	T
$R_\perp$	resistance with the current $\perp$ to the applied direction (p.6)	ohm
$R_{//}$	resistance with the current // to the applied direction (p.6)	ohm
R_1, R_2, R_3 and R_4	resistance elements in a wheatstone bridge circuit (p. 31)	ohm
R_{ap}	resistance for the anti-parallel state (p. 13)	ohm
R_p	resistance for the parallel state (p. 13)	ohm
T_b	blocking temperature, Néel temperature of AFM thin film (p. 21)	°C
t_f	t_f thickness of the free layer (p. 17)	nm
t_{FM}	thickness of the FM layer	nm
T_N	Néel temperature of AFM (p. 20)	°C
t_p	t_p thickness of the pinned layer (p. 17)	nm
t_r	t_r thickness of the reference layer (p. 57)	nm
θ_{eb}	direction of the unidirectional anisotropy (p. 20)	deg.
θ_f	direction of the magnetization in the free layer (p. 17)	deg.
θ_H	direction of applied magnetic field (p. 5)	deg.
θ_p	direction of the magnetization in the pinned layer (p. 17)	deg.
θ_r	direction of the magnetization in the reference layer (p. 57)	deg.
$\theta_f^{uniaxial}$	direction of the uniaxial anisotropy in the free layer (p. 17)	deg.
$\theta_p^{uniaxial}$	direction of the uniaxial anisotropy in the pinned layer (p. 17)	deg.
$\theta_r^{uniaxial}$	direction of uniaxial anisotropy in the reference layer (p. 57)	deg.
V_B	applied bias voltage on the wheatstone bridge (p. 31)	volts
V_{cos}	cosine output signal from 360° angle sensor (p. 32)	volts
V_{out}	output signal from the Wheatstone bridge (p. 31)	volts
V_{sin}	sine output signal from 360° angle sensor (p. 32)	volts

Citations

[And00] G. W. Anderson, M. Pakala and Y. Huai. Spin Valve Thermal Stability: Interdiffusion versus Exchange Biasing. *IEEE Trans. Magn*. **36**, 2605-2607 (2000).

[Ant94] T. C. Anthony, J. A. Brug and S. Zhang. Magnetoresistance of symmetric spin valve structures. *IEEE Trans. Magn*. **30**, 3819-3821, (1994).

[Ara98] S. Araki, M. Sano, M. Ohta, Y. Tsuchiya, K. Tsuichiya, H. Morita and M. Matsuzaki. The distribution of blocking temperature in NiFe-Ru_xRh_yMn bilayers. *IEEE Trans. Magn*. **34**, 1426-1428 (1998).

[Arn97] C. S. Arnold, M. Dunlavy and D. Venus. Magnetic susceptibility measurements of ultrathin films using the surface magneto-optic Kerr effect: optimization of the signal-to-noise ratio. *Rev. Sci. Inst*. **68**, 4212-4216 (1997).

[Bai88] M. Baibich, J. Broto, A. Fert, F. N. van Dau, F. Petroff, P. Eitenne, G. Creuzet, A. Friederich and J. Chazelas. Giant magnetoresistance of (001)Fe/(001)Cr magnetic superlattices. *Phy. Rev. Lett.* **61**, 2472-2475 (1988).

[Bar01] L. Baril, D. Mauri, J. McCord, S. Gider and T. Lin. Thermal relaxation of the free layer anisotropy in spin valves. *J. Appl. Phys.* **89**, 1320-1324 (2001).

[Bar90] J. Barnas, A. Fuss, R. E. Campley, U. Walz, P. Grünberg and W. Zinn. Layered magnetic structures: magnetoresistance due to antiparallel alignment. *Vac*. **41**, 1241-1243 (1990).

[Bas01] D. Basting. *Excimer Laser Technology: laser sources, optics, systems, and applications*. Lambda Physik Göttingen (2001).

[Bau01] S. Baunack, S. Menzel, W. Brückner and D. Elefant. AES depth profiling multilayers of 3d transition metals. *Appl. Sur. Sc.* **179**, 25-29 (2001).

[Bea00] R. Beach, M. Pinarbasi, and M. Carey. AP-pinned spin valve GMR and magnetization. *J. Appl. Phys*. **87**, 5723-5725 (2000).

[Ben95] M. Benaissa, P. Humbert, H. Lefakis, J. Werckmann, V. S, Speriosu and B. A. Gurney. Structural characterization of Co in sputtered Ta/Co/Ta thin-film sandwiches. *J. Magn. Magn. Mater*. **148**, 15-16 (1995).

[Ber99] A. E. Berkowitz and K. Takano. Exchange Anisotropy – a review. *J. Magn. Magn. Mat*. **200**, 552-570 (1999).

[Bin89] G. Binasch, P. Grünberg, F. Saurenbach and W. Zinn. Enhanced magnetoresistance in layered magnetic structures with antiferromagnetic interlayer exchange. *Phys. Rev. B*. **39**, 4828-4830 (1989).

[Bis99] J. Bischof, M. Reinmuth, J. Boneberg, S. Herminghaus, T. Palberg and P. Leider. Behavior of Thin Metallic Films Upon Melting with a ns Laser. *SPIE* **2777**, 119-127 (1999).

[Bon00] J. Boneborg, J. Bischof and P. Leiderer. Nanosecond time-resolved reflectivity determination of the melting of metals upon pulsed laser annealing. *Opt. Com.* **174**, 145-149 (2000).

[Bor95] J. A. Borchers, R. W. Erwin, S. D. Berry, D. M. Lind, J. F. Ackner, E. Lochner

and D. Hilton. Long-range magnetic order in Fe_3O_4//NiO superlattices. *Phys. Rev. B* **51**, 8276-8286 (1995).

[Bri83] D. Briggs and M. P. Seah. *Practical Surface Analysis by Auger and X-ray Photoelectron Spectroscopy*. Whiley Science New York (1983).

[Bru92] C. Brundle. *Encyclopedia of Materials Characterization*. Batteroworth-Heineman Boston (1992).

[Bru93] P. Bruno. Interlayer exchange coupling: a unified physical picture. *J. Magn. Magn. Mater.* **121**, 248-252 (1993).

[But02] W. H. Butler, O. Heinonen and X. G. Zhang. *The Physics of Ultra-High-Density Magnetic Recording*. Springer Berlin (2002).

[Cad00] U. Caduff, H. Schweren and H. Kittel. Low Cost Angle Sensor for Multi-purpose Applications. *SAE Conf. Proc.*, (2000).

[Car92] M. J. Carey and A. E. Berkowitz. Exchange anisotropy in coupled films of NiFe with NiO and Co_x Ni_{1-x}. *Appl. Phys. Lett.,* **60**, 3060-2 (1992).

[Cho97] G. Choe and S. Gupta. NiFe underlayer effect on exchange coupling field and coercivity in NiFe/FeMn films. *IEEE Trans. Man.* **33**, 3691-3693 (1997).

[Cho98] G. Choe, A. Tsoukatos and S. Gupta. Growth of giant magnetoresistive spin valves with strong exchange bias field. *IEEE Trans. Magn.* **34**, 867-869 (1998).

[Cle97] W. Clemens, H. A. M. van den Berg, G. Rupp, W. Schelter, M. Vieth and J. Wecker. Contactless pontentiometer, based on giant magnetoresistance sensors. *J. Appl. Phy.* **81**, 4310-4312, (1997).

[Coe96] R. Coehoorn. Giant mangetoresistance in exchange-biased spin-valve structures and its application in read heads. *Magnetic Thin Films and Industrial Application*. 65-331 (1996). Springer Verlag.

[Dau93] J. M. Daughton and Y. J. Chen. GMR Materials for low field applications. *IEEE Trans. Magn.* **29**, 2705-2710 (1993).

[Dau94] J. M. Daughton, J. Brown, E. Chen, R. Beech, A. Pohm and W. Kude. Magnetic field sensor using GMR multilayer. *IEEE Trans. Magn.* **30**, 4608-4610 (1994).

[dBe96] H.A. M. van den Berg, W. Clemens, G. Gieres, G. Rupp, W. Schlelter and M. Vieth. GMR sensor scheme with artificial antiferromagnetic subsystem. *IEEE Trans. Magn.* **32**, 4624-4626 (1996).

[dBo88] F. R. de Boer, R. Boom, W. C. M. Mattens, A. R. Miedama and A. K. Kiessen. *Cohesion in Metals*. Amsterdam North Holland (1988).

[dBo95] D. K. G. de Boer , A. J. G Leenaers and W. W. van den Hoogenhof. Glancing-incidence X-ray analysis of thin-layered materials. *Phil. Res. Mat. Ana.* **3**, 5-19 (1995).

[Dev98] A. J. Devasahayam, P. J. Sides and M. H. Kryder. Magnetic, temperature and corrosion properties of NiFe/IrMn exchange couple. *J. Appl. Phys.* **83**, 7216-7218 (1998).

[dHa02] O. de Haas. Private communication (2002).

[Die00] B. Dieny, M. Li, S. Liao, C. Horng and K. Ju. Quantitative interpretation of the magnetoresistive response (amplitude and shape) of spin valves with synthetic antiferromagnetic pinned layers. *J. Appl. Phys.* **87**, 3415-3420 (2000)

[Die91] B. Dieny, V. S. Speriouso, S. S. P. Parkin, B. A. Gurney, D. R. Wilhoit and D. Mauri Giant magnetoresistance in soft ferromagnetic multilayers. *Phys. Rev. B* **43**, 1297-1301 (1991).

[Die93] B. Dieny, B. Gurney, S. Lambert, D. Mauri, S. Parkin, V. Speriosu and D. Wilhoit. Magnetoresistive sensor based on the spin-valve effect. *US Patent*

5206590 (1993).

[Die94] B. Dieny. Giant magnetoresistance in spin-valve multi-layers. *J. Magn. Magn. Mat.* **136**, 335-359 (1994).

[Dim98] D. V. Dimitrov, C. Prados, C. Y. Ni, G. C. Hadjipananyis and J.Q. Xiao. Magnetoresistance in NiCoO/Py/Cu/Py spin valves. *J. Magn. Magn. Mater.* **189**, 25-31 (1998).

[Duc96] J. P. W. Duchateau, A. E. M. de Veirman and J. C. S. Kools. Unpublished (1996).

[Dup90] C. Dupas, P. Beauvillain, C. Chappert, J. P. Bernhard, F. Trigui, P. Veilleit, E. Velu and D. Renard. Very large magnetoresistance effects induced by antiparallel magnetization in two ultrathin cobalt films. *J. Appl. Phys.* **67**, 5680-5682 (1990).

[Ege95] W. F. Egelhoff, Jr., T. Ha, R. D Misra, Y. Kadmon, J. Nir, C. J. Powell, M. D. Stiles, R. D. McMichael, C. –L. Lin, J. M. Siversten, J. H. Judy, K. Takano, A. E. Berkowitz, T. C. Anthony and J. A. Brug. Magnetoresistance values exceeding 21%, in symmetric and bottom spin valves. *J. Appl. Phys.* **78**, 273-277 (1995).

[Ele01] D. Elefant, D. Tietjen L. van Loyen, I. Moench and C. M. Schneider. Dominant role of the size effect for saturation resistivity and giant magnetoresistance in Co/Cu multilayers. *J. Appl. Phys.* **89**, 7118-20 (2001).

[Ert85] G. Ertl and J. Küppers. *Low Energy Electrons and Surface Chemistry*. VCH Berlin (1985).

[Fas01] J. Fassbender. Private communication (2001)

[Fas02] J. Fassbender, S. Poppe, A. Mougin, B. Hillebrands, D. Engel, M. Jung, A. Ehresmann, H. Schmoranzer, G. Faini, K. J. Kirk and J. N. Chapman. Magnetization Reversal of Exchange Bias Double Layers Magnetically Patterned by Ion Irradiation. *Phys. Stat. Sol.* **189**, 439-447 (2002).

[Fas02b] J. Fassbender, S. Poppe, T. Mewes, J. Juraszek, B. Hillebrands, D. Engel, M. Jung, A. Ehresmann, H. Schmoranzer, K.-U. Barholz and R. Mattheis. Ion irradiation of exchange bias systems for magnetic sensor applications. To be published.

[Fla89] P. J. Flanders. An alternating-gradient magnetometer (invited). *J. Appl. Phys*. **63**, 3940-3945 (1989).

[Fuk97] H. N. Fuke, K. Saito, Y. Kamiguchi, H. Iwasaki and M. Sahashi. Spin-valve giant magnetoresistive films with antiferromagnetic Ir-Mm layers. *J. Appl. Phys* .**81**, 4004-4006 (1997).

[Gie01] G. Giebeler, J. J. M. Ruigrok and J. B. A. van Horn. Single deposition GMR sensors for rotational speed sensing. *Proc. Eurosensors XV* **2**, 144-147 (2001).

[Gla72] A. A. Glazer , A. P. Poapov and R. I. Tagirov. Thermographic Recording on a Manganese-Permalloy with Exchange Anisotropy. *JETP Lett.* **15**, 259-261 (1972).

[Gök97] N. J. Gökemeijer, T. Ambrose and C. L. Chien. Long-range exchange bias across a spacer layer. *Phys. Rev. Lett.* **79**, 4270-4273 (1997).

[Gra00] C. D. Graham. High-sensitivity magnetization measurements. *Mater. Sci. Technol.* **16**, 97-101 (2000).

[Grü86] P. Grünberg, R. Schreiber, Y. Pang, M. B. Brodsky and H. Sowers. Layer Magnetic Structures: Evidence of Antiferromagnetic Coupling of Fe layers across the Cr layers. *Phy. Rev. Lett.* **57**, 2442-2445 (1986).

[Haa00] G. Haas, M. Freitag, P. Schmollngruber, A. Johnson and A. Hütten. GMR-Sensors for Automotive Applications. *VDI Magnetoeletronic Status Sem. Conf. Proc.*, 39-44 (2000).

[Haa99] G. Haas, M. Freitag and A. Johnson. Multilayer Magnetoresistive Sensor/Bridge Circuit Arrangement. German Patent No. DE19949714 (1999).

[Har00] Hartmann. *Magnetic multilayers and Giant Magnetoresistance*. Springer Berlin (2000).

[Hec86] Hecht. *The Laser Guidebook*. McGraw-Hill New York (1986).

[Hei95] D. Heim and S. S. P. Parkin, Magnetoresistive spin valve sensor with improved pinned ferromagnetic layer and magnetic recording system using the sensor. U. S. Patent No. 5465185 (1995).

[Hos94] K. Hoshino, S. Niguchi, R. Nakatani, H. Hoshiya and Y. Sugita. Magnetoresistance and interlayer exchange coupling between magnetic layers in Fe-Mn/Ni-Fe-Co/Cu/Ni-Fe-Co multilayers. *Jpn. J. Appl. Phys.* **33**, 1327-33 (1994).

[Hua93] T. C. Huang R. Gilles and G. Will. Thin-film thickness and density determination from X-ray reflectivity data using a conventional powder diffractometer. *Thin Sol. Fil.* **230**, 99-101 (1993).

[Hwa98] D. G. Hwang, C. M. Park and S. S. Lee. Exchange Biasing in NiO spin valves. *J. Magn. Magn. Mater.* **186**, 265-276 (1998).

[Iji98] Y. Ijiri, J. A. Borchers, R. W. Erwin, S. H. Lee, P. J. van der Zaag and R. M. Wolf. Perpendicular coupling in exchange-biased Fe_3O_4/CoO superlattices. *Phys. Rev. Lett.* **80**, 608-611 (1998).

[Inf02] http://www.infineon.com/

[Iwa97] H. Iwasaki, A. T. Saito and M. Sahashi. Excellent Reliability of CoFe-IrMn spin valves. *IEEE Trans. Magn.* **33**, 2875-2877 (1997).

[Jac92] M. Jacob, G. Reiss, H. Brückl and H. Hoffmann. Electronic transport properties of giant magnetoresistance Fe/Cr multilayers. *Phys. Rev. B* **46**, 11208-11211 (1992).

[Jan57] J. P. Jan. *Solid State Physics* 5, 1-96 (1957). Academic Press New York

[JCP96] JCPDS Electronic Databank. International Center for Diffraction Data. Swarthmore, PA (1996).

[Jil91] D. Jiles. *Introduction to Magnetism and Magnetic Materials,* 1st ed. . Chapman & Hill New York (1991).

[Joh01] A. Johnson, I. Herrmann and M. Rabe. Kompensation der Winkelfehler in einen Spin Valve Mänder, German Patent Application No. DE10138757.1, (2001).

[Joh02a] A. Johnson, H. Siegle and H. Hahn. Effect of Anisotropy Influences on the Angle Dependent Resistance Changes in IrMn Spin-Valves. *Phys. Stat. Solidi A* **189**, 637-642 (2002).

[Joh02b] A. Johnson, G. Haas and G. Mörsch. Method for Adjusting Magnetization in a Layer Arrangement and use thereof. German Patent Application No. DE10117355 (2002).

[Jun95] R. Jungblut, R. Coehorn, M. T. Johnson, C. Sauer, P. J. van der Zaag, A. R. Ball and T. G. S. M. Rijks. Exchange biasing in MBE-grown $Ni_{80}Fe_{20}/Fe_{50}Mn_{50}$ bilayers. *J. Magn. Magn. Mat.* **148**, 300-306 (1995).

[Kam96] Y. Kamiguchi, K. Saito, H. Iwasaki, M. Sahashi, M. Ouse and S. Nakamura. Giant magnetoresistance and soft magnetic properties of $Co_{90}Fe_{10}$/Cu spin-valve structures. *J. Appl. Phys.* **79**, 6399-401 (1996).

[Kan01] H. Kanai, K. Noma and J. Hong. *Fujitsu Sci. Tech. J.* **37**, 174 (2001).

[Kat93] N. Kataoka, K. Saito and J. Fujimori. Magnetoresistance of $Co_{90}Fe_{10}$/Cu/Co_x Fe_{1-x}/Cu metallic multilayers. *J. Magn. Magn, Mat.* **126**, 508-509 (1993).

[Kel02a] J. Keller, P. Miltenyi, B. Beschoten, G. Güntherodt, U. Nowak and K. D. Usadel. Domain state model for exchange bias. II. Experiment. *Phys. Rev. B*

66, 014431/1-11 (2002)

[Kel02b] J. Keller. Private communication (2002).

[Ker77] J. Kerr. On rotation of the plane of polarization by reflection from the pole of a magnet. *Phil. Mag.* **3**, 321 (1877).

[Kle93] W. Kleemann. Random-field induced antiferromagnetic, ferroelectric, and structural domain states. *Int. J. Mod. Phys. B* **7**, 2469-2507 (1993).

[Koh49] M. Kohler. Theorie der magnetischen Widerstands Effekte in Metallen. *Ann. Physik* **6**, 18-21 (1949).

[Koo95] J. C. S. Kools. On the ferromagnetic interlayer coupling in exchange-biased spin-valve multilayers. *J. Appl. Phys*. **77**, 2993-2998 (1995).

[Koo96] J. C. S. Kools. Exchange Biased Spin-Valves for Magnetic Storage. *IEEE Tran. Magn*. **32**, 3165-3184 (1996).

[Koo97] N. C. Koon. Calculations of exchange bias in thin films with ferromagnetic/anti-ferromagnetic interfaces. *Phys. Rev. Lett.* **78**, 4865-4868 (1997).

[Kré68] E. Krén, G. Kadar, L. Pál, J. Sólyom, P. Szabó and T. Tarnóczi. *Phys. Rev.* **17**1, 574-576 (1968).

[Lai96] C. H. Lai, T. C. Anthony, E. Iwamura and R. L. White. The effect of microstructure and interface conditions on the anisotropic exchange fields of NiO/NiFe**.** *IEEE Trans. Magn.* **32** 3419-21 (1996).

[Lan01] J. Langer, R. Mattheis, B. Ocker, W. Maass, S. Senz D. Hesse and J. Krausslich. Microstructure and magnetic properties of sputtered spin valve systems. *J. Appl. Phys* **90**, 5126-5134 (2001).

[Lea98] J. L. Leal and M. H. Kryder. Spin valves exchange biased by Co/Ru/Co synthetic antiferromagnets. *J. Appl. Phys* **83**, 3720-3723 (1998).

[Led99] M. Lederman. Performance of Metallic Antiferromagnets for Use in Spin-Valve Read Sensors. *IEEE Tran. Magn*. **35**, 794-799 (1999).

[Len00] K.M. H. Lenssen, D. J. Adelerhof, H. J. Gassen, A. E. Kuiper, G. H. J. Somers and J. B. A. van Zorn. Robust giant magnetoresistance sensors. *Sens. & Act*. **A85,** 1-8 (2000).

[Len97] K. M. H. Lenssen, A. E. M. de Veirmann and J. J. T. M. Donkers. Inverted spin valves for magnetic heads and sensors. *J. Appl. Phys.* **81**, 4915-4917 (1997).

[Len99] K. M. H. Lenssen, A. E. T. Kuiper and F. Roozeboom. Robust GMR material system for magnetic sensors. *J. Appl. Phys.* **85**, 5531-5533 (1999).

[Lev95] P. M. Levy and S. Zhang. Our current understanding of giant magnetoresistance in transition-metal multilayers. *J. Magn. Magn. Mater.* **151**, 315-23 (1995).

[Lin93] D. M. Lind, S. P. Tay, S. D. Berry, J. A. Borchers and R. W. Erwin. Structural and magnetic ordering in iron oxide/nickel oxide multilayers by X-ray and neutron diffraction. *J. Appl. Phys*. **73**, 6886-91 (1993).

[Lin95] T. Linn, C. Tsang, R. E. Fontana and J. Kent Howard. Exchange coupled NiFe/FeMn, NiFe/NiMn, and NiO/NiFe films for stabilization of magnetoresistive sensors. *IEEE Trans. Magn*. **31**, 2585-2590, 1995.

[Mae98] A. Maesaka, N. Sugawara, A. Okabe, and M. Itabish. Influence of microstructure on thermal stability of spin-valve multilayers. *J. Appl. Phys.* **83**, 7628-34 (1998).

[Mal87] A. P. Malozemoff. Random-field model of exchange anisotropy at rough ferromagnetic- antiferromagnetic interfaces. *Phys. Rev. B* **35**, 3679-3682 (1987).

[Mal88] A. P. Malozemoff. Mechanisms of Exchange Anisotropy. *J. Appl. Phys* **63**,

3874-3879 (1988).

[Mao00] S. Mao and Z. Gao. Characterization of Magnetic and Thermal Stability of PtMn Spin Valves. *IEEE Tran. Magn.* **36**, 2860-2862, (2000).

[Mat00] R. Matheis. 10 target-PVD system as a fertile tool for development of enhanced GMR multilayer systems. *VDI Magnetoeletronic Status Sem. Conf. Proc.*, 63-67 (2000).

[Mau87] D. Mauri, H. C. Siegmann, P. S. Bagus and E. Kay. Simple model for thin ferromagnetic films exchange coupled to a antiferromagnetic substrate. *J. Appl. Phys.* **62**, 3047-3049 (1987).

[May02] U. May. Simulation program (2002).

[McC96] J. McCord, A. Hubert, J. C. S. Kools and M. C. de Noijer. Magnetization Reversals in Exchange Biased Giant Magnetoresistive Elements. *IEEE Trans. Magn.* **32**, 4803-4805 (1996).

[McG75] T. R. McGuire and R. I. Potter. Anisotropic magnetoresistance in ferromagnetic 3d alloys. *IEEE Trans. Magn.* **11,** 1018-1038 (1975).

[Mei56] W. H. Meiklejohn and C. P. Bean. New Magnetic Anisotropy. *Phys. Rev.* **102**, 1413-1414 (1956).

[Mei57] W. H. Meiklejohn and C. P. Bean. New Magnetic Anisotropy. *Phys. Rev.* **105**, 904-906 (1957).

[Mew00a] T. Mewes, R. Lopusnik, J. Fassbender, B. Hillebrands, M. Jung, D. Engel, M. Ehresmann and H. Schmoranzer. Suppression of exchange bias by ion irradiation. *Appl. Phys. Lett*. **76**, 1057-1059 (2000).

[Mew00b] T. Mewes, B. F. Roos, S. O. Demokritov and B. Hillebrands. Oscillatory exchange bias effect in FeNi/Cu/FeMn and FeNi/Cr/FeMn trilayer systems. *J. Appl. Phys.* **87**, 5064-5066, 2000.

[Mil00] P. Miltenyi, M. Gierlings, J. Keller, B. Beschoten, G. Güntherodt, U. Nowak and K D. Usadel. Diluted Antiferromagnets in Exchange Bias: Proof of the Domain State Model. *Phys. Rev. Lett.* **84**, 4224-4227 (2000).

[Mil93] B. H. Miller, E. Youjun Chen and E. Dan Dahlberg. A method of separating the giant magnetoresistance and the anisotropic magnetoresistance in multilayers. *J. Appl. Phys.* **73**, 6384-6386 (1993).

[Moo96] J. S. Moodera and R.Merservey. Ferromagnetic-insulator-ferromagnetic tunneling: Spin-dependent tunneling and large magnetoresistance in trilayer junctions. *J. Appl. Phys*. **79**, 4724-4728 (1996).

[Mot36] N. Mott and H. H. Willis. Resistance and thermoelectric properties of the transition metals. *Prov. Roy. Soc*. **A156**, 368-382 (1936).

[Mou01a] A. Mougin, T. Mewes, M. Jung, D. Engel, A. Ehresmann, H. Schmoranzer, J. Fassbender and B. Hillebrands. Local manipulation and reversal of the exchange bias field by ion irradiation in FeNi/FeMn double layers. *Phys. Rev. B* **63**, 1-4 (2001).

[Mou01b] A. Mougin, S. Poppe, J. Fassbender, B. Hillebrands, G.Faini, U. Ebels, M. Jung, D. Engel, A. Ehresmann and M. Schmoranzer. Magnetic micropattering of FeNi/FeMn exchange bias bilayers by ion irradiation. *J. Appl. Phys.* **89**, 6606-6608 (2001).

[Mul97] Multipak V5.0. Physical Electronics (1997).

[Nak94] R. Nakatani, K. Hoshino, S. Noguchi and Y. Sugita. Magnetoresistance and preferred orientation in FeMn/NiFe/Cu/NiFe sandwiches with various buffer layers. *Jpn. J. Appl. Phys.* **33**, 133-137 (1994).

[Nak97] R. Nakatani, H. Hoshiya, K. Hoshino and Y. Sugita. Relationship between film structure and exchange coupling in Mn-Ir/Ni-Fe films. *J. Magn. Magn. Mat.* **173**, 321-330 (1997).

[Née54] L. Néel. Anisotropie Magnetique Superficielle Et Surstructures D'Orientation. *J. Phys. Radium* **15**, 225 (1954).

[Née62] L. Néel. Sur le nouveau mode de couplage entre les aimantations de deux couches minces ferromagnetiques. *Comptes. Rendus* **255**, 1676 (1962).

[Née67] L. Néel. Etude théorique du couplage ferro-antiferromagnétique dans les couches minces. *Ann. Phys. Paris* **2**. 61-80 (1967).

[Név80] L. Névot and P. Croce. Caractérisation des surfaces par réflexion rasante de rayons X. Application á l'étude du polissage de quelques verres silicates. *Revue Phys. Appl.* **15,** 761-769 (1980).

[Nic94] D. M. Nicholson, W. H. Butler, X. G. Zhang, L. J. MacLaren, B. A, Gurney and V. S. Speriosu. Magnetic structure of the spin valve interface. *J. Appl. Phys.* **76**, 6805-6807 (1994).

[Nis84] T. Nishizawa and K. Ishida. The Co-Cu (Cobalt-Copper) System. *Bull. All. Ph. Diag*. **5**, 161-165 (1984).

[Nis95] K. Nishioka, G. Gangopadhyay, H. Fjiwaran and M. Parker. Hysteresis and interaction between the magnetic layers in spin valves. *IEEE Trans. Magn.* **31**, 3949-3951 (1995).

[Nog99] J. Nogues and I. K. Schuller. Exchange bias. *J. Magn. Magn. Mater.* **192**, 552-570 (1999).

[Nol00] F. Nolting, A. Scholl, J. Stöhr, J. W. Seo, J. Fompeyrine, H. Siegwart, J.-P. Locquet, S. Anders, J. Lüning, E. E. Fullerton, M. F. Toney, M. R. Scheinfein and H. A. Padmore. Direct Observation of the Alignment of Ferromagnetic Spins by Antiferromagnetic Spins. *Nature* **405**, 767-769 (2000)

[Now00] U. Nowak, A. Misra and K. D. Usadel. Domain State Model of Exchange Bias. *J. Appl. Phys*. **89**, 7269-7271 (2001).

[Now02] U. Nowak, K. D. Usadel, J. Keller, P. Miltenyi, B. Beschoten and G. Güntherodt. Domain state model for exchange bias. I. Theory. *Phys. Rev. B* **66**, 014430/1-9 (2002)

[Ohl01] H. Olhdag, A. Scholl, F. Nolting, S. Anders, F. U. Hillebrecht, and J. Sthr. Spin reorientation at the antiferromagnetic NiO(001) surface in response to an adjacent ferromagnet. *Phys. Rev. Lett.* **86**, 2878-2880 (2001).

[Ohr92] Ohring. *The Materials Science of Thin Films.* Academic Press New York (1992).

[Par90] S. S. P. Parkin, N. More and K. P. Roche. Oscillations in exchange coupling and magnetoresistance in metallic superlattice structures: Co/Ru, Co/Cr, Fe/Cr. *Phys. Rev. Lett*. **64**, 2304-2407 (1990).

[Par91a] S. S. P Parkin. Systematic variation of the strength and oscillation period of indirect magnetic exchange coupling through the 3d, 4d, and 5d transition metals. *Phys. Rev. Lett*. **67**, 3598-3601 (1991).

[Par91b] S. S. P. Parkin, Z. G. Li and S. J. Smith. Giant magnetoresistance in antiferromagnetic Co/Cu multilayers. *Appl. Phys. Lett.* **58**, 2710-2712 (1991). S. S. P. Parkin, R. Bhadra, and K. P. Roche. Oscillatory Magnetic Exchange Coupling through Thin Copper Layers. *Phy. Rev. B*. **66**, 2152-2155 (1991).

[Par92] S. S. P. Parkin. Oscillation in giant magnetoresistance and anti-ferromagnetic coupling in $(NiFe/Cu)_n$ multilayers. *Appl. Phys. Lett.* **60**, 512-514 (1992).

[Par93] S. S. P. Parkin. Origin of enhanced magnetoresistance of magnetic multilayers: spin-dependent scattering from magnetic interface states. *Phys. Rev. Lett.* **71**, 1641-1644 (1993).

[Par95] M. R. Parker, H. Fujiwara, S. Hossain and W. E. Webb. *Magnetic vector model of spin-valve. IEEE Trans. Magn.* **31**, 2618-2620 (1995).

[Par96] S. S. P. Parkin and T. Rabedeau. Low field giant magnetoresistance in

sputtered permalloy/Au multilayers. Appl. Phys. Lett. **68**, 162-1164 (1996).

[Pok01] T. Pokhil, E. Linville and S. Mao. Exchange anisotropy and micromagnetic properties of PtMn/NiFe bilayers. *J. Appl. Phys.* **89**, 6588-6590, (2001)

[Pok99] T. Pokhil, S. Mao and A. Mack. Study of exchange anisotropy in NiFe/NiMn and NiFe/IrMn exchange coupled films. *J. Appl. Phys.* **85**, 4916-4918 (1999).

[Pri95] G. A Prinz. Spin-polarized transport. *Physics Today* **4**, 58-63 (1995).

[Ric74] J. A. Ricodeau. Model of the antiferromagnetic-antiferromagnetic transition in Mn_3Pt alloys. *J. Phys. F* **4**, 1285-1303 (1974).

[Rij94] T. G. S. M. Rijks, W. J. M Jonge, W. Folkerts, J. C. S. Kools and R. Coehorn. Magnetoresistance in NiFe/Cu/NiFe/FeMn spin valves with low coercivity and ultrahigh sensitivity. *Appl. Phys. Lett*. **65**, 916-918 (1994).

[Rij95] Th. G. S. M. Rijks, R. Coehoorn, M. J. M. de Jong and W. J. M. de Jong. Semiclassical calculations of the anisotropic magnetoresistance of NiFe-based thin films, wires, and multilayers. *Phy. Rev. B.* **51**, 283-291, (1995).

[Sai97] M. Saito, Y. Kakihara, T. Watanabe and N. Hasegawa. Exchange Coupling between antiferromagnetic PtMn and ferromagnetic films. *J. Magn. Soc. Jpn.* **21**, 505-508 (1997).

[Sai98] A. T. Saito, H. Iwasaki, Y. Kamiguchi, H. N. Fuke and M. Sahashi. Activation energy of interdiffusion and interface structure for CoFe/Cu spin-valves**.** *IEEE Trans. Magn.* **34**, 1420-1422 (1998).

[Sai99] M. Saito, N. Hasegawa, F. Koike, H. Seki and T. Kuriyama. PtMn single and dual spin valves with synthetic ferrimagnet pinned layers. *J. Appl. Phys.* **85**, 4928-4930 (1999).

[Sal74] N. M Salanskii, V. A. Seredikin, V. A. Burmakin and A. V. Nabatov. Stabilization of microdomain configurations in two-magnetic films. *Sov. Phys. JETP* **38**, 1011-1012 (1974).

[Sch99] T. C. Schulthess and W. H. Butler. Coupling mechanisms in exchange biased films. *J. Appl. Phys.* **85**, 5510-5515 (1999).

[Scha94] R. Schad. C. D. Potter, P. Belien, G. Verbanck, V. V. Moschalkov and Y. Bruynseraede. Giant magnetoresistance in Fe/Cr superlattices with very thin Fe layers. *Appl. Phys. Lett.* **64**, 3500-3502 (1994).

[She96] J. X. Shen and M. T. Kiel. Exchange Coupling in NiO and NiFe thin films. *J. Appl. Physics* **79**, 5008-5010 (1996).

[Smi51] J. Smit. Magnetoresistance of Ferromagnetic Metals and Alloys at Low Temperatures. *Physica* **16**, 612 (1951).

[Spe91] V. S. Speriosu, B. Dieny, S. Metin, P. Number, B. A. Gurney, and H. Lefakis. Nonoscillatory magnetoresistance in Co/Cu/Co layered structures with oscillatory coupling. *Phys. Rev. B* **44**, 5358-5361 (1991).

[Spo96] J. K. Spong, V. S. Speriosu, R. E. Fontana, Jr., M. M. Dovek and T. L. Hylton. Giant magnetoresistive spin valve bridge sensor. *IEEE Trans. Magn*. **32**, 366-371 (1996).

[Sta00] R. L. Stamps. Topical Review: Mechanisms for exchange bias. *J. Phys. D.: Appl. Phys*. **33**, R247-R268 (2000).

[Sto48] E. C. Stonier and E. P. Wohlfarth. A Mechanism of Magnetic Hysteresis in Heterogeneous Alloys. *Phil. Trans. R. Soc. London A Math. Phys. Sci* **240A**, 599-642 (1948).

[Sun98] J. Z. Sun, L. Krusin-Elbaum, A. Gupta, G. Xiao, P. R. Duncombe and S. S. P. Parkin. Magnetotransport in doped manganate perovskites. *IBM. J. Res. Develop.* **42**, 89-102 (1998).

[Tak00] M. Takiguchi, S. Isii, E. Makino and A. Okabe. Thermal Degradation of spin valve multilayers caused by Mn migration. *J. Appl. Phys.* **87**, 2469-2471

(2000).

[Ter87] T. Terashima and Y. Bando. Formation and magnetic properties of artificial superlattice of CoO-Fe_3O_4. *Thin Sol. Films* **152**, 455-463 (1987).

[Tie00] T. Tietjen. Private Communication (2000).

[Tie02] T. Tietjen, D. Elefant and C. M. Schneider. Rotation Angle Sensors Based On Spin Valves – A Modeling Approach. *J Appl. Phys.* **18**, 182-189 (2002)

[Tsa86] J. Y. Tsao, S. T. Picraux, P. S, Peercy and M. A. Thompson. Direct measurements of liquid/solid interface kinetics during pulsed- laser-induced melting of aluminum. *Appl. Phys. Lett*. **48**, 278-80 (1986).

[Tsu99] I. F. Tsu and K. J. Duxstad. Thermal Reliability of NiMn-based spin valves. *J. Appl. Phys.* **85**, 5858-5861 (1999).

[Umb66] H. Umbayashi and Y. Ishikawa. J. Phys. Soc. Japan **21**, 1281-1283 (1966).

[vDr00] J. van Driel, F. R. Boer, K. M. H. Lenssen and R. Coehoorn. Exchange biasing by $Ir_{19}Mn_{81}$: Dependence on temperature, microstructure, and antiferromagnetic layer thickness. *J. Appl. Phys*. **88**, 975-982 (2000).

[Wil68] C. H. Wilts and F. B. Humprey. Magnetic Anisotropy in flat Ferromagnetic Films: A Review. *J. Appl. Phys.* **19**, 1191-1200 (1968).

[Yam71] T. Yamaoka, M. Mekata, and H. Takaki. *J. Phys. Soc. Japan* **31**, 301-303 (1971).

[Yam99] H. Yamane, J. Mita and M. Kobayashi. Spin-Valve Film for Sensitive Giant Magnetoresistive Sensor Using AC Bias Magnetic Field. *Mat. Tran. JIM* **40**, 186-192 (1999)

[Zav75] T. E. Zavecz, M. A. Saifi and M. Notis. Metal reflectivity under high-intensity optical radiation. *Appl. Phys. Lett.* **26**, 165-168 (1975).

[Zel98] A. M. Zeltser, K. Pentek, M. Menyhard and A. Sulyok. Thermal Stability of CoFe, Co, and NiFe/Co spin valves. *IEEE Trans. Magn.* **34**, 1417-1419 (1998).

[Zie85] J. F. Ziegler, J. P. Biersack and U. Littmark. *The Stopping and Range of Ions in Solids.* Pergamon New York/Oxford (1985).

[Zor94] G. M. Zorn. Siemens analytical application note Nr. 337 (1994).

ACKNOWLEDGMENTS

I wish to express my thanks and gratitude to my "Doktorvater," Prof. Dr. Horst Hahn, for his guidance during my studies. He has always been supportive of my work and gave me the freedom to fully explore the different research areas associated with spin valves. I would also like to thank my "Zweitbetreuer," Prof. Dr. Fuess, for spending the time to read through my dissertation and for the use of the X-ray diffraction equipment in the Structure Research Department. Next I would like to thank Prof. Dr. Rauh and Prof. Dr. Tschudi for agreeing to serve on my thesis committee and for an unbiased evaluation of my dissertation.

I would like to extend my deepest thanks to all of my colleagues in the Magnetic Sensors Group at the Corporate R&D Center of the Robert Bosch GmbH. First, my thanks to both Dr. Gunther Haas and Dr. Martin Freitag for extending me the opportunity to write a dissertation on such an interesting topic as spin valves. Dipl.-Ing. Ingo Herrmann and Dr. Hartmut Kittel were always ready to help with the measurement setups and in understanding magnetic angle sensors. Dipl.-Physiker Peter Schmollngruber and Dr. Paul Farber helped with the sensor processing and Dr. Henrik Siegle capably guided the "Magneto-Elektronik Leitprojekt". My thanks also goes to Helmut Besser for helping build any holder was necessary for this project and Rudolf Galster for the fabrication of the sensor chips. My appreciation also goes to Dr. Gilbert Mörsch and Dipl.-Physiker Thomas Schwarz for helping me learn how to operate an excimer laser. The simulation program developed by Dr. Ulrich May helped me to explain many different experimental results. Furthermore I would like to say that both Uli and Dipl.-Physiker Maik Rabe showed patience with me by answering the many questions that I asked them over the past few years.

I have also benefited from the help and friendship of several colleagues from the TU-Darmstadt. Dr. Christian Alof, Dr. Mohammed Ghafari, Dr. Stahl and Dipl.-Ing. Jörg Ebert from the Thin Films Department provided important instruction in the use of the Siemens diffractometer and held many helpful discussions in the area of GMR thin films with me. I would especially like to thank Dr. Joachim Brötz for his help with the reflectometry measurements and the insightful explanations of X-Ray Reflectometry. I would also like to thank any other "Doktoranden," Ph.D. students, and anyone else at the TU-Darmstadt that may helped me during my dissertation.

I would like to thank Dr. Roland Matheis, Dipl.-Physiker Kai-Uwe Barholz and co-workers of the "Institut für Physikalische Hoch Technologie Jena", Kathy O'Donnell of NEXX Systems LLC and Brian Sylvia and Bill Sproul of Reactive Sputtering, Inc. for the supply of the spin valves samples studied in this dissertation. I would like to express my gratitude to Dipl.-Physiker Tim Mewes, Dr. Jürgen Fassbender and Prof. Dr. Hilldebrandt of Universität Kaiserslautern for the use of the ion irradiation results presented in this dissertation.

The collaborative work with the "Institut für Festkörperphysik and Werkstoff-wissenschaft" Dresden, IFW-Dresden was an example of good teamwork. Dipl.-Physiker Detlev Tietjen developed the free energy model that was used to simulate MR measurements and MR rotation measurements. Dr. Dieter Elefant was responsible for organizing the AGM and AES measurements and Dr. Stefka Zutova help was invaluable to the completion of the lift-off experiments.

The list of acknowledgements would not be complete without thanking my parents for their moral support and encouragement. They came to Germany several times to check up on their son. This included one important visit during following very serious knee surgery.

In addition to all of this personal support, I was supported financially by the "BMBF Magneto-Electronik Projekt".

Resume

Name:	Andrew Scott Johnson
Date of Birth:	26.05.72
Place of Birth:	Cincinnati, Ohio. USA
Nationality:	USA

Education

2/99-12/03 **Dr.-Ing. Materialwissenschaft "Materials Science"**
Darmstadt University of Technology, Darmstadt, Germany.
Thesis Topic: " Spin Valve System for Angle Sensor Applications"
Advisor: Professor Horst Hahn. FB Dünne Schichten "Thin Films"

8/95-8/97 **Masters of Science in Metallurgical Engineering**
Purdue University, West Lafayette, Indiana U.S.A.
GPA: 3.8/4.0.
Thesis Topic: "Phase Development in Pt/SiGe Alloy Layers"
Advisor: Professor Eric Kvam

9/90-6/95 **Bachlors of Science in Materials Engineering**
International Engineering Program - German Focus.
University of Cincinnati, Cincinnati, Ohio U.S.A.
GPA: 3.4/4.0. Major GPA: 3.6/4.0.

Employment

2/99-12/03 **Robert Bosch GmbH, Corporate R&D, Dept. Physical Technologies (FV/FLT) Stuttgart, Germany**
Research Staff: Responsible for the analysis of spin valve system for application in magnetic angle sensors and development of the process central to fabrication of demonstrator angle sensor. Worked in inter-disciplinary team involved in sensor design, thin film development and strategic planning of the project. Conducted liaison work with partner universities, research institutes and other external industry partners.

8/97-12/98 **Max-Planck Institut für Metallforschung Fulbright Enterprise Scholarship Program, Stuttgart, Germany**
Visiting Scientist. Examined Ge quantum dot structures on Si substrates with electron microscopy to determine the strain state at Ge/Si interface. Research conducted in cooperation with Purdue University.

8/95-8/97 **Purdue University, School of Materials Science and Engineering, West Lafayette, Indiana**
Research Assistantship. Studied the phase development of Pt metallizations on SiGe alloy layers with electron microscopy and x-ray diffraction. Part of thesis work conducted at Max-Planck Institut für Metallforschung.

List of Publications

1. A. Johnson, H. Siegle, and H. Hahn. Effect of Anisotropy Influences on the Angle Dependent Resistance Changes in IrMn Spin-Valves. *Physica Status Solidi A* **189**, 637-642 (2002).
2. U. May, A. Johnson and H. Siegle. Verfahren zur Einstellung oder lokalen Veränderung einer Magnetisierung in einer Schicht einer magnetoresistiven Schichtanordnung, Heizstempel zum Anheizen der magnetoresistiven Schichtanordnung und deren Verwendung. Patent No. EP-1378950-A1 (2002).
3. A. Johnson, G. Haas, and G. Mörsch. Method for Adjusting Magnetization in a Layer Arrangement and use thereof. Patent No. DE10117355, WO-2002082111A1 (2002).
4. A. Johnson, I. Herrmann, und M. Rabe. Kompensation der Winkelfehler in einen Spin Valve Mänder. Patent No., DE-10138757-A1: (2001).
5. A. Johnson, D. Tietjen, C. M. Schneider, and H. Hahn. Angle Rotation Properties of FeMn Spin Valves, *Proc. Eurosensor XIV* (2000).
6. G. Haas, M. Freitag, P. Schmollngruber, A. Johnson, and A. Hütten. GMR-Sensors for Automotive Applications. *VDI Magnetoeletronic Status Seminar Conf. Proc*., 39-44 (2000).
7. G. Haas, M. Freitag, and A. Johnson. Multilayer Magnetoresistive Sensor/Bridge Circuit Arrangement. German Patent No. DE19949714 (1999).

List of Presentations

1. A. Johnson, H. Siegle, and H. Hahn. Effect of Anisotropy Influences on the Angle Dependent Resistance Changes in IrMn Spin-Valves. Poster. *Seeheim Conference on Magnetism 2001*.
2. A. Johnson, D. Tietjen, C. M. Schneider, and H. Hahn. Angle Rotation Properties of FeMn Spin Valves. Presentation. *Eurosensor XIV* (2000).
3. A. Johnson, D. Tietjen, C. M. Schneider, and H. Hahn. Angle Rotation Properties of FeMn Spin Valves. Poster. *EMSA 2000* (2000).

Eidesstattliche Erklärung

Hiermit erkläre ich an Eides Statt, dass ich diese Dissertation selbständig und nur mit den angegebenen und erlaubten Hilfsmitteln angefertigt habe.

Ich habe bisher noch keinen Promotionsversuch unternommen.

Darmstadt, den 31. Oktober 2004

Andrew Johnson